Topology and symmetry-breaking in the strong light-matter coupling regime

Valerii Kozin

Faculty of Physical Sciences
University of Iceland
2021

TOPOLOGY AND SYMMETRY-BREAKING IN THE STRONG LIGHT-MATTER COUPLING REGIME

Valerii Kozin

180 ECTS thesis submitted in partial fulfillment of a
PhD Scientiarum degree in Physics

Advisor
Ivan Shelykh

Faculty Representative
Oddur Ingólfsson

PhD committee
Ivan Shelykh (supervisor)
Ivan Iorsh
Hafliði Gíslason
Viðar Guðmundsson

Opponents
Iacopo Carusotto
Leonid Golub

Faculty of Physical Sciences
School of Engineering and Natural Sciences
University of Iceland
Reykjavik, 08 2021

Topology and symmetry-breaking in the strong light-matter coupling regime
Topology and symmetry-breaking in the strong light-matter coupling regime
180 ECTS thesis submitted in partial fulfillment of a PhD degree in Physics

Faculty of Physical Sciences
School of Engineering and Natural Sciences
University of Iceland
Dunhagi 3
IS-107, Reykjavik, Reykjavik
Iceland

Telephone: 525 4000

Bibliographic information:
Valerii Kozin, 2021, Topology and symmetry-breaking in the strong light-matter coupling regime, PhD thesis, Faculty of Physical Sciences, University of Iceland.

Printing: Háskólaprent, Fálkagata 2, 107 Reykjavík
Reykjavik, Iceland, 08 2021

Abstract

The physics of light-matter interactions is a rapidly developing research area at the junction between condensed matter physics and quantum optics. Depending on the strength of the light-matter interaction the systems behave very differently. In the current thesis, we mainly (but not exclusively), focus on the regime of (ultra)strong light-matter interaction. Typically, the strong coupling regime implies the employment of various low-dimensional semiconductor structures embedded into a microcavity, or irradiation by a strong laser field, or considering cold atoms, trapped in the vicinity of a waveguide. In the current thesis, we investigate various quantum systems and phenomena in the (ultra)strong coupling regime, including:

1)topological insulator based on a two-dimensional array of dressed quantum rings;

2)the new type of a polariton $\mathbb{Z}$ topological insulator;

3)Bose-Einstein condensate in a tilted polariton ring;

4)chiral waveguide quantum optomechanics;

5)the new type of a Hall effect for composite particles (excitons), that we refer to as the anomalous exciton Hall effect;

6)transition metal dichalcogenide polaritons in the presence of free carriers;

and other related phenomena.

Útdráttur

Eðlisfræði víxlverkunar ljóss og efnis þróast hratt sem rannsóknarsvið á mörkum þéttefnisfræði og skammtaljósfræði. Hegðun eðlisfræðikerfa þar sem þessi víxlverkun á við er mjög mismunandi og fer eftir styrkleika þess. Í þessari ritgerð, skoðum við aðallega svið ofursterkrar víxlverkunar ljóss og efnis án þess að einskorða okkur við það. Svið ofursterkrar víxlverkunar ljóss og efnis gefur almennt til kynna notkun á ýmsum lágvídda hálfleiðarakerfum, ágeislun með sterku leysissviði, eða kaldar frumeindir í gildru nálægt bylgjuleiðurum. Ritgerð þessi fjallar um rannsóknir okkar á mismunandi skammtakerfum og fyrirbærum í sviði ofursterkrar kúplunar, svo sem:

1) grenndareinangrara byggða á tvívíðri grind af ágeisluðum skammtahringjum;

2) nýja tegund $\mathbb{Z}$ grenndareinangrara byggða á ljósskauteindum;

3) Bose-Einstein þéttingu í hallandi hring ljósskauteindahring;

4) skammtaljósaflfræði með hendnum bylgjuleiðara;

5) nýja tegund Hallhrifa fyrir samsettar eindir (örveindir), sem við köllum afbrigðileg Hallhrif örveinda;

6) hliðarmálms díkalkogeníða (TMD) ljósskauteindir í nærveru frjálsra rafbera;

og fleiri tengd fyrirbæri.

Acknowledgements

First of all, I would like to thank my scientific supervisor Prof. Ivan Shelykh for formulating very interesting and challenging scientific problems and sharing his deep understanding of condensed matter physics. I highly appreciate all the knowledge I got during my PhD studies and during informal meetings at Prof. Ivan Shelykh's place.

The years I spent in Reykjavik were unforgettable, Iceland is a wonderful country to live and work in. It was a real pleasure to work with my colleagues in the Shelykh group. Particularly, I thank Ivan Iorsh, Oleg Kibis, Anton Nalitov, Skender Morina, Helgi Sigurdsson, Vanik Shahnazaryan, Luciano Ricco, Yuri Marques, Yurii Krivosenko, Alexey Yulin, Ivan Vrubel, Roman Polozkov, Dmitry Gulevich, Dmitry Yudin, Stanislav Kolodny, Kevin Dini for the productive cooperation and all the pleasant time spent together. Especially, I would like to thank Ivan Iorsh (ITMO University) and Oleksandr Kyriienko (University of Exeter) for careful advising, and sharing their non-standard ways of thinking. I also express my gratitude to our scientific partners from abroad for fruitful collaboration.

It was a great pleasure to do science and to teach students at the University of Iceland. Also, I am grateful to ITMO University and NORDITA for their hospitality during my visits.

I would like to gratefully acknowledge the financial support from the Icelandic Research Fund and Eimskip Fund for my PhD scholarship, and H2020 project CoExAn for funding the visits to institutions abroad.

Finally, and most importantly, I would like to thank my wife Daria, and my family for the vast help and encouragement in all the beginnings. Especially, I would like to thank my grandfather Valerii P. Kozin for opening the world of physics for me.

Contents

1 Introduction

The field of strong light-matter interactions is one of the rapidly developing areas of contemporary physics, situated on the boundary of quantum optics and condensed matter physics. Working in this field requires a deep comprehension of the microscopic principles for both the electromagnetic field and matter constituent. When the interaction rate between the material subsystem and electromagnetic field exceeds all possible decay rates of the system, the perturbative treatment of the irradiation impact on the system properties ceases to work, because the matter-light system becomes a hybrid entangled object. Conventionally, there are several approaches to implement strong light-matter coupling. For example, embedding semiconductor structures into an optical cavity leads to resonant coupling between the cavity mode and the matter excitations. If the matter excitations are bosonic, then the resulting hybrid quasiparticles are referred to as "polaritons". Another way to implement (ultra)strong coupling, is the cold atoms set-ups. Namely, if the cold atoms are trapped in the vicinity of a waveguide, then the atoms can interact with each other by means of exchanging photons through the waveguide which results in the hybridization between the atomic and photonic subsystems. Alternatively, the regime of strong light-matter coupling can be achieved by "dressing" the system – i.e. by applying a high-frequency driving field, which modifies the properties of the system, if one studies only the stroboscopic dynamics in the prethermal regime. The concept of driving is widely spread in quantum physics and is used, for instance, to modify the spectrum of nanostructures or to create so-called discrete time crystals that break discrete time-translation symmetry.

The current thesis consists of two main parts. The first part is devoted to the theoretical study of optical and transport properties of semiconductor quantum wells and 2D materials, being in the regime of strong light-matter coupling. The second part is devoted to studying various symmetry-breaking phenomena that take place in the systems of cold atoms. In the *introductory chapter*, the general description of the systems under consideration and the mathematical methods are presented.

Chapter 2 is devoted to the transport properties of a two-dimensional array of interconnected quantum rings, dressed by hight-frequency circularly polarized light. It is demonstrated that the artificial gauge field that is induced by the radiation leads to the opening of bandgaps that may host topologically protected edge states. Also, in this chapter, the effects of a linearly polarized dressing field on a single quantum ring with the Rashba spin-orbit coupling are studied.

Chapter 3 is devoted to the topological metamaterials, based on exciton-polariton rings. We show, that the interplay of Zeeman splitting with the photonic analog of spin-orbit coupling (the transverse-electric–transverse-magnetic (TE-TM) splitting) inherently present in this system leads to the appearance of synthetic U(1) gauge field and the opening of topologically nontrivial spectral gaps.

In *Chapter 4* we theoretically and experimentally studied the effect of pseudo magnetic field originating from the polaritonic analog of spin-orbit coupling (TE-TM splitting) on a polariton condensate in a ring-shaped microcavity (polariton ring). The effect gives rise to a stable four-leaf pattern around the ring as seen from the linear polarization measurements of the condensate photoluminescence. This pattern is found to originate from the interplay of the cavity potential, energy relaxation, and TE-TM splitting in the ring. Our observations are compared to the dissipative one-dimensional spinor Gross-Pitaevskii equation with the TE-TM splitting energy which shows good qualitative agreement.

In *Chapter 5* we show, that the atoms harmonically trapped in the vicinity of a chiral waveguide exhibit quantum phase transitions and the emergence of the multicomponent Schrödinger cat ground states in the regime of strong optomechanical coupling. We found a rigorous mathematical mapping between the quantum optomechanical systems in a waveguide geometry and the generalized Quantum Rabi Model describing the light-matter interaction of a multilevel atom in a cavity. As a result, we revealed a hidden unconventional $\mathbb{Z}_N$ symmetry in the optomechanical systems consisting of N atoms and demonstrate that the self-organization of atoms in the vicinity of the photonic waveguide maps to a super-radiant quantum phase transition occurring in the Rabi model which is accompanied by the spontaneous breaking of the $\mathbb{Z}_N$ symmetry. These findings bridge the fields of ultrastrong light-matter coupling and optomechanics. We demonstrated, that the proposed phenomena can be observed in state-of-the-art experiments with cold atoms.

Chapter 6 is devoted to the transport properties of bright and dark excitons in a disordered (doped) quantum well in the presence of a magnetic field. The regimes of weak and strong magnetic fields are studied. The latter corresponds to the so-called magneto-excitons. We have shown, that in both cases the exciton flow deflects due to the scattering of the excitons with the induced dipole moment on electrically charged impurities. This mechanism resembles the anomalous Hall effect, and for this reason, we call the proposed phenomenon the anomalous exciton Hall effect.

In *Chapter 7* we consider the 2D TMD material in an optical microcavity in the presence of free carriers, that are injected by the gate. Exploiting the fact that the free carriers modify the excitonic response of the system due to the formation of exciton-polarons, we have shown that the optical nonlinearity stemming from both the exciton-exciton interaction and (b) phase-space filling effects can be efficiently controlled by the gate voltage.

In the last chapter (*Conclusions*) we give a brief summary of the thesis with concluding remarks. After *Conclusions*, we list 7 publications on which this thesis is based. Some of the text and figures from the listed publications have been reused in this thesis with the permission of the publisher (Copyright (2021) by the American Physical Society).

1.1 Quantum wells, quantum wires, and quantum dots

A significant part of this thesis is devoted to optical phenomena in semiconductor microstructures, and in this section, we give a brief description of the main types of semiconductor microstructures.

Three main types of semiconductor microstructures can be distinguished: quantum wells, quantum wires, and quantum dots, the latter sometimes being called artificial atoms. The study of these structures not only opens up new pages of electronic engineering but is also accompanied by discoveries of a fundamental nature. Quantum wells can be constructed by inserting a thin layer of one type of semiconductor material between two layers of another with a different band gap. Let us consider, for instance, a thin layer of GaAs with a smaller band-gap surrounded by two layers of AlGaAs with a large bandgap. Let us assume that the change in material occurs along some direction and therefore the potential well is along this particular direction. Since the bandgap of the surrounding AlGaAs is greater than that of the contained material, a quantum well is created in the GaAs region. This change in band energy across the structure plays a role in the potential well a carrier would feel, hence low energy carriers can be confined in such a well, see Fig. 1.1.

An electron (hole) in the conduction (valence) band can be trapped in the potential well created in the structure and the available states are particle-in-a-box-like. Those carriers can have discrete energy eigenstates within the quantum well. For instance, there are available states in the conduction band such that an electron can have lower energy within the well than it could have in the surrounding AlGaAs region. In a similar way, holes in the valence band can also be confined to the top of potential wells created in the valence band.

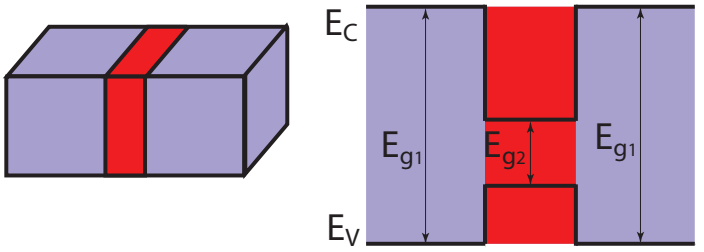

Figure 1.1: The sketch of a semiconductor heterojunction: the band structure diagram in a quantum well of GaAs in between AlGaAs.

The concept of the quantum well was proposed in 1963 independently by Zhores Alferov and R.F. Kazarinov and by Herbert Kroemer and [1]. Development of the semiconductor heterojunction for optoelectronics resulted in Nobel Prizes for Zhores

Alferov and Herbert Kroemer in 2000. If the motion of the carriers is confined in an additional direction, the motion of electrons in the structure will remain free only in the single direction and such structure is called a quantum wire. By confining the carriers in all three spatial dimensions we get a quantum dot. In *Chapters* 2-5 of the current thesis, we discuss various effects, taking place in quantum wells and quantum wires.

1.2 Strong coupling between classical light and quantum matter

In this section, we discuss the interaction between a classical electromagnetic field and various systems, described by quantum mechanics as, for example, semiconductor nanostructures, discussed in the previous section. The results, presented in this section, are relevant for *Chapters* 2, 5, and 6 of the current thesis.

1.2.1 Interaction between quantum systems and light

The concept of gauge fields is pivotal in fundamental physics and forms the grounds of the Standard Model of particle physics. The best-known example is an electromagnetic field, described by two vector fields: $\mathbf{E}$ and $\mathbf{B}$. An electromagnetic field is an Abelian $U(1)$ gauge field, and it can be coupled to any Hamiltonian, describing charged matter, by means of the so-called minimal substitution

$$\hat{p}_\mu \to \hat{p}_\mu - qA_\mu \tag{1.1}$$

with q being the particle's charge, $\hat{p}_\mu = i\hbar\partial_\mu = i\hbar(c^{-1}\partial/\partial t, \nabla)$ being the 4-momentum operator, and $A_\mu = \eta_{\mu\nu}A^\nu$ being components of the 4-potential which transforms under the action of global transformations from the adjoint representation of the $U(1)$ gauge group (here $\eta_{\mu\nu} = \mathrm{diag}(1, -1, -1, -1)$ is the metric tensor of the flat 4-dimensional Minkowski space). The 4-potential $A^\mu = (\phi/c, \mathbf{A})$ contains all the information about the corresponding (classical) electric and magnetic fields, that are given by

$$\mathbf{B}(\mathbf{r}, t) = \nabla \times \mathbf{A}(\mathbf{r}, t), \tag{1.2}$$

$$\mathbf{E}(\mathbf{r}, t) = -\nabla\phi(\mathbf{r}, t) - \frac{\partial \mathbf{A}(\mathbf{r}, t)}{\partial t}, \tag{1.3}$$

and they are invariant under the following gauge transformation $A^\mu \to A^\mu - \partial^\mu\chi$, where χ is an arbitrary smooth function of coordinates and time.

Particles interact with an electromagnetic field due to the presence of charge ($\hat{p}_\mu \to \hat{p}_\mu - qA_\mu$) which defines the strength of the interaction. At a fundamental level, in

quantum electrodynamics (QED), the charge value is the only parameter, defining the strength of the interaction. For the case of electrons/positrons with charge $q = \mp e$, one may construct the following combination

$$\alpha = \frac{1}{4\pi\varepsilon_0}\frac{e^2}{\hbar c} \approx \frac{1}{137}, \tag{1.4}$$

which plays the role of the dimensionless coupling constant, called the fine-structure constant. Here $\hbar = h/(2\pi)$ is the reduced Planck constant, c is the speed of light, and ε_0 is the electric constant or permittivity in a vacuum. It should be noted, that this constant is not actually a constant in the following sense: its value depends on the energy scale Λ at which it is measured. In particular, at low energies $\alpha(\Lambda \approx 0) \approx 1/137$, whereas at the energy scale of the weak interaction (about 90 GeV, the Z-boson mass), the experiments yield a greater value $\alpha(\Lambda \approx 90\ GeV) \approx 1/127$. This dependence is known as "running of the coupling" and it goes far beyond the scope of the current thesis because here we focus on low-energy non-relativistic phenomena in condensed matter physics. The value of the coupling constant is quite small, that is why a perturbation theory with respect to α works very well in quantum electrodynamics. However, in condensed matter physics one deals with effective theories – low-energy approximations of QED. In such effective theories, the corresponding effective coupling constants could be tuned by varying the parameters of a system under consideration. Thus the regime of strong coupling could be achieved, which is one of the main topics of the current thesis, where we study the interaction between matter excitations and photons (or phonons) in the regime of strong coupling.

Let us demonstrate the minimal coupling scheme with specific examples. For a system of N charged non-relativistic particles interacting with an external electromagnetic field the Hamiltonian reads

$$\hat{H} = \sum_{i=1}^{N}\left[\frac{1}{2m}\left(\hat{\mathbf{p}}_i - q\mathbf{A}\left(\mathbf{r}_i, t\right)\right)^2 + q\phi\left(\mathbf{r}_i, t\right)\right]. \tag{1.5}$$

This Hamiltonian preserves the gauge symmetry if one demands that the wave function transforms under the gauge transformation too. For example, for the case of a single particle this transformation reads $\psi(\mathbf{r}, t) \to \psi(\mathbf{r}, t)e^{iq\chi(\mathbf{r},t)/\hbar}$, where $\chi(\mathbf{r}, t)$ is the same as in $A_\mu \to A_\mu - \partial_\mu\chi$. The Hamiltonian can be transformed to the following form, where the interaction part is separated from the free part, suitable for a linear response approach which will be used in the future paragraphs

$$\hat{H} = \sum_{i=1}^{N}\frac{\hat{\mathbf{p}}_i^2}{2m} + \int d^3x\left[-\mathbf{j}_A(\mathbf{r})\cdot\mathbf{A}(\mathbf{r}, t) + qn(\mathbf{r})\phi(\mathbf{r}, t) - \frac{q^2}{2m}n(\mathbf{r})\mathbf{A}^2(\mathbf{r}, t)\right] \tag{1.6}$$

with the density operator $n(\mathbf{r})$ and the current operator $\mathbf{j}_A(\mathbf{r})$ defined by

$$n(\mathbf{r}) = \sum_{i=1}^{N} \delta\left(\mathbf{r} - \hat{\mathbf{r}}_i\right), \tag{1.7}$$

$$\mathbf{j}_A(\mathbf{r}) = \frac{q}{2m} \sum_{i=1}^{N} \left[\left(\hat{\mathbf{p}}_i - q\mathbf{A}(\mathbf{r},t)\right)\delta\left(\mathbf{r} - \hat{\mathbf{r}}_i\right) + \delta\left(\mathbf{r} - \hat{\mathbf{r}}_i\right)\left(\hat{\mathbf{p}}_i - q\mathbf{A}(\mathbf{r},t)\right)\right]. \tag{1.8}$$

In the presence of an electromagnetic field the current operator $\mathbf{j}_A(\mathbf{x})$ is the sum of two terms – paramagnetic+diamagnetic:

$$\mathbf{j}_A(\mathbf{x}) = \mathbf{j}(\mathbf{x}) - \frac{q^2}{m}\mathbf{A}(\mathbf{x})n(\mathbf{x}), \tag{1.9}$$

here first term (paramagnetic) is the current operator in the absence of an electromagnetic field $\mathbf{j}(\mathbf{x})$ (for $\mathbf{A} = 0$), and the second term is the diamagnetic contribution.

Another important example to consider is a single quantum particle bound by some potential $V(r)$ (for example, a single-electron atom) in the presence of near-monochromatic light with a characteristic wavelength much larger than the localization length of the particle's wavefunction. Let us use the radiation gauge which implies $\phi(\mathbf{r},t) = 0$ and $\nabla\mathbf{A}(\mathbf{r},t) = 0$, in this case $\mathbf{E}(\mathbf{r},t) = -\dot{\mathbf{A}}(\mathbf{r},t)$. Since the light field doesn't change significantly on the scale of the quantum system under study, the Hamiltonian reads

$$\left\{-\frac{\hbar^2}{2m}\left[\nabla - i\frac{q}{\hbar}\mathbf{A}\left(\mathbf{r}_0,t\right)\right]^2 + V(r)\right\}\psi(\mathbf{r},t) = i\hbar\frac{\partial\psi(\mathbf{r},t)}{\partial t} \tag{1.10}$$

where $\mathbf{r}_0$ is the average position of the particle. Now we perform the following gauge transformation

$$\psi(\mathbf{r},t) = \exp\left[\frac{iq}{\hbar}\mathbf{A}\left(\mathbf{r}_0,t\right)\cdot\mathbf{r}\right]\tilde{\psi}(\mathbf{r},t) \tag{1.11}$$

after which we arrive at the following Hamiltonian for $\tilde{\psi}$

$$i\hbar\dot{\tilde{\psi}}(\mathbf{r},t) = \left[\hat{H}_0 - \hat{\mathbf{d}}\cdot\mathbf{E}\left(\mathbf{r}_0,t\right)\right]\tilde{\psi}(\mathbf{r},t) \tag{1.12}$$

where $\hat{\mathbf{d}} = q\mathbf{r}$ is the dipole moment operator and

$$\hat{H}_0 = \frac{\hat{\mathbf{p}}^2}{2m} + V(r). \tag{1.13}$$

This Hamiltonian $\hat{H}_0 - \hat{\mathbf{d}}\cdot\mathbf{E}(\mathbf{r}_0,t)$ describes the interaction between a classical light field and a quantum two-level system and will be extensively used in the next subsections.

1.2.2 Lasers: weak light-matter coupling

The next few subsections will be devoted to the interaction between a classical monochromatic light field and matter. Such fields are typically produced by *lasers* (light amplification by stimulated emission of radiation) or *masers* (microwave amplification

by stimulated emission of radiation), invented by N. Basov, A. Prokhorov, and C. Townes, which brought them the Nobel Prize in Physics in 1964. In this section, we will briefly overview the semiclassical theory of lasers. Interestingly, that in order to describe the operation of lasers that produce classical light we will need to invoke the notion of photons – quanta of light, each having energy $h\nu$ and obeying Planck's law. They were introduced by A. Einstein and M. Planck. Following the historical path, we will employ the notion of photons before giving a strict theoretical description of them in the framework of Quantum Electrodynamics (will be presented in the subsequent sections of *Introduction*). Ordinary lasers operate in the weak light-matter coupling regime, which implies that the coupling between light and matter doesn't significantly change the parameters of the matter subsystem. In this subsection, we will assume that the condition of the weak coupling is fulfilled.

Let us consider a medium, consisting of identical two-level systems with energy levels $E_1 < E_2$. This medium interacts with a thermal bath of photons of frequency ν_0. The photon bath is at equilibrium at fixed temperature T. The photons are assumed to be in resonance with the two-level systems, i.e $h\nu_0 = E_2 - E_1$, all other frequencies are assumed to be irrelevant for our consideration. We denote the occupations of the ground and excited states as $N_{1,2}$, respectively. A. Einstein proposed the following equation for the occupations

$$\frac{dN_2}{dt} = -A_{21}N_2 + N_1 B_{12} u_{\text{Planck}}(\nu_0) - N_2 B_{21} u_{\text{Planck}}(\nu_0), \tag{1.14}$$

where

$$u_{\text{Planck}}(\nu) = \frac{8\pi h\nu^3}{c^3} \frac{1}{\exp\left(\frac{h\nu}{k_B T}\right) - 1} \tag{1.15}$$

is the energy density of the photons with frequency ν at temperature T. The RHS of the equation (1.14) consists of three terms, each of which will be discussed separately. The first term $-A_{21}N_2$ corresponds to *spontaneous emission* of photons and the so-called "Einstein's A-coefficient" A_{21} defines the probability of the two-level system to fall from the excited to state to the ground state with the emission of a photon. The second term $N_1 B_{12} u_{\text{Planck}}(\nu_0)$ corresponds to *photon absorption*, and the so-called "Einstein's B coefficient" B_{12} defines the probability of absorbing a photon with subsequent transmission from the ground state to the excited state. Finally, the third term $-N_2 B_{21} u_{\text{Planck}}(\nu_0)$ corresponds to *stimulated emission*, i.e. when a two-level, being in the excited state, meets a photon with the frequency $h\nu_0 = E_2 - E_1$ and emits an exactly the same photon as the one it meets. After this process, the two-level system turns out to be in the ground state, and there are two identical photons – the initial one and the one, produced by the two-level system. We note, that due to the fact that $N = N_1 + N_2 = \text{const}$ one has $dN_1/dt = -dN_2/dt$.

To derive the relations between Einstein's coefficients, let us assume that the matter subsystem is brought to equilibrium with light, and thus it has the same temperature T. Then one has $dN_2/dt = 0$ and $N_2/N_1 = \exp\left[-(E_2 - E_1)/(k_B T)\right] =$

$\exp[-h\nu_0/(k_BT)]$ according to the Boltzmann distribution. This immediately yields: $B_{12} = B_{21}$ (or, more generally $B_{21}/B_{12} = g_1/g_2$, where $g_{1,2}$ are the multiplicities (degeneracy) of the respective energy levels), and $A_{21}/B_{21} = 8\pi h\nu_0^3/c^3$. Thus, the study of the thermal equilibrium between photons of a certain frequency and a set of two-level systems allowed us to derive the useful relation between Einstein's coefficients without knowing the microscopic details of the mechanism of the light-matter interaction.

Now let us consider a bunch of identical (coherent) photons with frequency ν_0, passing through the medium along the z-axis. In the discussion of the nonequilibrium physics below, we do not take into account the effect of thermal photons, which does not qualitatively affect the presented results. The change in intensity, as the beam passes through a thin slice of width dz of the medium, reads

$$dI = \text{ (rate of stim. emissions per vol. - rate of absorptions per vol.) } \times h\nu_0 \times dz =$$
$$= (N_2B_{21} - N_1B_{12})\frac{I}{c}h\nu_0 dz \tag{1.16}$$

where we neglected spontaneous emission (it will be added later phenomenologically), and we used the following relation between intensity and energy density: $I = uc$. Here we do not assume that the two-level systems are in equilibrium with the photons. So far we did not include the process of spontaneous emission in the equation above because during this process the two-level systems emit photons with the same frequency ν_0 (most likely), however, they are not identical (not coherent) to the photons we consider, and thus, even though they have the same frequency, the do not enter the quantity u of interest. Solving the equation above with respect to $I(z)$, keeping in mind that $B_{21} = B_{12}$, one gets

$$I(z) = I(0)e^{\gamma z}, \tag{1.17}$$

where γ is the "gain coefficient", given by

$$\gamma = (N_2 - N_1)\,B_{21}\frac{h\nu_0}{c}. \tag{1.18}$$

Now let us include the losses due to spontaneous emission (and other processes) by introducing a phenomenological coefficient α in the expression for $I(z)$:

$$I(z) = I(0)e^{(\gamma-\alpha)z}. \tag{1.19}$$

For $\gamma > \alpha$, the intensity of the light will increase as it passes through the medium (optical gain).

Now we may formulate the two conditions of operation of a laser: (a) optical gain – gain>losses ($\gamma > \alpha$); (b) positive feedback. If we forget for a moment about losses, then the condition (a) transforms to $\gamma > 0$, which requires $N_2 > N_1$ (known as "population inversion"), but at thermal equilibrium, the Boltzmann distribution dictates $N_2 < N_1$, which makes impossible lasing in two-level systems at thermal equilibrium.

To achieve the condition $\Delta N = N_2 - N_1 > 0$, one, therefore, needs to "pump" the medium, typically by illuminating with another incoherent (thermal) light source or by passing an electric current through the medium. If we include a pump term, the rate equation becomes

$$\dot{N}_2 = -N_2 B_{21} u - A_{21} N_2 + N_1 B_{12} u + P \tag{1.20}$$

where the pumping term P represents the rate of excitation to level 2.

To provide the positive feedback required for lasing, one should put the medium in an optical cavity (resonator), represented, in the simplest form, by two reflecting surfaces that reflect light back and forth. A thoughtful discussion of optical resonators will be given in the future sections of *Introduction*.

Let us switch back to the bunch of coherent photons, discussed above, but now they pass through the medium, which is sandwiched between two mirrors, placed at $z = 0$ and $z = L$. The initial intensity of the photons equals I_0. The two mirrors are imperfect and their reflectance (effectiveness in reflecting radiant energy) is equal to $R_{1,2}$, respectively.

After the first trip from the left mirror at $z = 0$ to the right one at $z = L$, the intensity is:

$$I_0 \exp[(\gamma - \alpha)L]. \tag{1.21}$$

It is then reflected by the right mirror so that when the beam returns to $z = 0$, its intensity, right after the second reflection by the left mirror, reads

$$I_0 \exp[2(\gamma - \alpha)L] R_1 R_2. \tag{1.22}$$

For steady-state operation, one must require that the intensity doesn't change after one round-trip i.e.

$$I_0 = I_0 \exp\left[2\left(\gamma_{th} - \alpha\right) L\right] R_1 R_2 \tag{1.23}$$

where γ_{th} is the "threshold gain coefficient", which is equal to the gain required to just balance the total losses (scattering in the gain medium and leakage through the mirrors), and it reads

$$\gamma_{th} = \alpha - \frac{1}{2L} \ln\left(R_1 R_2\right) \tag{1.24}$$

If one pumps the gain medium more, so that the population inversion ΔN grows such that $\gamma > \gamma_{th}$, then the intensity will grow. However, the rate of stimulated emission increases too, which will decrease ΔN until the condition $\gamma = \gamma_{th}$ is reached. This is the feedback mechanism that always keeps $\Delta N = \Delta N_{th}$ in the steady-state regime. We remind that $\gamma = \Delta N B_{21} h\nu_0 / c$.

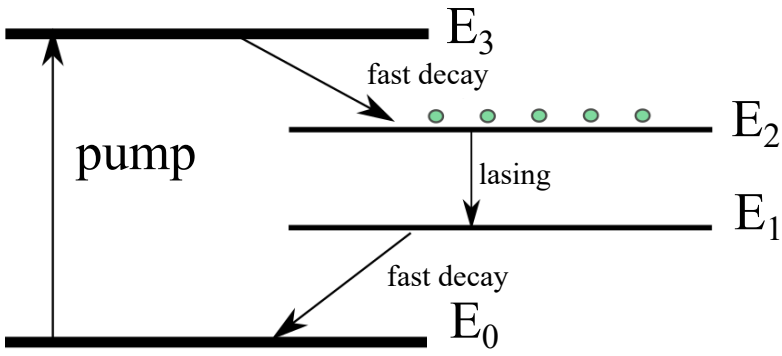

Figure 1.2: The scheme of operation of a 4-level laser. This scheme can be realised in Nd^{3+}:YAG laser, where the dopants – triply ionized Nd^{3+} replaces a small fraction of the Y ions in the yttrium aluminum garnet (YAG). Here the transitions $E_3 \to E_2$ and $E_1 \to E_0$ are non-radiative and are accompanied with phonon emission. The role of E_0, E_1, E_2, E_3 levels is played by ${}^4I_{9/2}$, ${}^4I_{11/2}$, ${}^4F_{3/2}$, ${}^4F_{5/2}$ levels of Nd^{3+}, respectively. E_0 is the ground state of Nd^{3+}. We note, that level E_1 is (almost) not occupied neither at thermodynamic equilibrium, nor during the laser operation.

The pump term introduced above implies that there are other energy levels in the gain medium since it does not conserve the total number of occupied states $N_1 + N_2$. Let us consider the scheme of operation of a 4-level laser, as illustrated in Fig 1.2 (see the description in the caption). Here, the pump excites atoms to level 3 ("pump band") from the ground state (level 0). From level 3 the atoms rapidly relax to level 2 ("upper laser level"). The lasing transition occurs between level 2 and level 1 ("lower laser level"). From level 1 the atoms rapidly relax to the ground state. The lifetimes of the transitions $3 \to 2$ and $1 \to 0$ are much shorter than the lifetime of the lasing transition $2 \to 1$, i.e.

$$\tau_{21} \gg \tau_{32}, \tau_{10} \tag{1.25}$$

This ensures that the population inversion is maximized when pumped, because $N_2 \gg N_1$ and therefore $\Delta N \approx N_2$. In this case, the equation for the occupation numbers becomes

$$(\dot{\Delta N}) = P - \Delta N \left(B_{21} u + A_{21}\right). \tag{1.26}$$

In steady-state $(\dot{\Delta N}) = 0$, and due to the positive feedback $\Delta N = \Delta N_{th}$, hence

$$u = \left(\frac{P}{\Delta N_{th}} - A_{21}\right) \frac{1}{B_{21}} = \frac{1}{\Delta N_{th} B_{21}} \left(P - \frac{\Delta N_{th}}{\tau_{21}}\right), \tag{1.27}$$

where we expressed the lifetime via Einstein's A coefficient as $\tau_{21} = 1/A_{21}$. Finally, using that $I = uc$, we obtain the following expression for the coherent emission

$$I = \frac{c}{\Delta N_{th} B_{21}} \left(P - P_{th}\right), \tag{1.28}$$

where the threshold value of the pump

$$P_{th} = \frac{\Delta N_{th}}{\tau_{21}}. \tag{1.29}$$

Thus, the output intensity of a laser is zero (or, strictly speaking, is small) if the pump intensity is below the threshold $P < P_{th}$, and grows linearly with P after the threshold $P > P_{th}$. Lasers possess a number of unique features: their emission is coherent, they can have high temporal and spatial coherence, which allows them to emit light with a very narrow spectrum and focus the beam to a tight spot. In the next few subsections, we will discuss the interaction between laser radiation and matter.

1.2.3 Two-level system interacting with classical light

Strong light-matter interaction is the main topic of the current thesis. One of the simplest models that allow for the analytical description of the regime of interest is a quantum two-level system (TLS) interacting with classical light, which is relevant, for example, for studying quantum dots, irradiated by a monochromatic laser field. Such field configuration can be described by the following expression

$$\mathbf{E}(\mathbf{r},t) = \mathbf{E}_0 \cos(\omega_L t - \mathbf{kr}) = \frac{\mathbf{E}_0}{2}(e^{-i\omega_L t + i\mathbf{kr}} + e^{i\omega_L t - i\mathbf{kr}}) = \mathbf{E}^{(+)}(\mathbf{r},t) + \mathbf{E}^{(-)}(\mathbf{r},t), \tag{1.30}$$

where $\mathbf{E}_0$ denotes the field amplitude, and ω_L is the light's frequency. The Hamiltonian of the two-level system reads

$$\hat{H}_{TLS} = E_{GS}|g\rangle\langle g| + (E_{GS} + \hbar\omega_0)|e\rangle\langle e|, \tag{1.31}$$

where $|g\rangle$ ($|e\rangle$) denotes the ground (excited) state, with the energies E_{GS} and $E_{GS} + \hbar\omega_0$, respectively. We may safely set the ground state energy to zero ($E_{GS} = 0$).

To describe the interaction of the TLS with the electromagnetic field of the laser beam we employ the dipole approximation, which is valid if the wavelength of the field is much larger than the size of the TLS, which is assumed to be localized around the point $\mathbf{r}_0$. In this case, the interaction is described by the following term in the full Hamiltonian

$$\hat{H}_{TLS-F} = -\hat{\mathbf{d}}\mathbf{E}(\mathbf{r}_0,t), \tag{1.32}$$

where $\hat{\mathbf{d}}$ denotes the dipole moment operator of the TLS

$$\hat{\mathbf{d}} = \mathbf{d}_{eg}^*\sigma_- + \mathbf{d}_{eg}\sigma_+ = \hat{\mathbf{d}}^{(+)} + \hat{\mathbf{d}}^{(-)}, \tag{1.33}$$

where $\sigma_- = |g\rangle\langle e|$, $\sigma_+ = |e\rangle\langle g|$. We set $\mathbf{d}_{ee} = \mathbf{d}_{gg} = 0$, which is valid for symmetric quantum dots. In addition to that, we assume that $\mathbf{d}_{eg}^* = \mathbf{d}_{eg}$. Thus, for the system's

total Hamiltonian is

$$\hat{H} = \hat{H}_{TLS} + \hat{H}_{TLS-F} = \hbar\omega_0\sigma_+\sigma_- - \hat{\mathbf{d}}\mathbf{E}(\mathbf{r}_0, t) = \\ \hat{H}_{TLS} - \hbar\Omega\cos(\omega_L t - \mathbf{k}\mathbf{r}_0)(\sigma_- + \sigma_+), \tag{1.34}$$

where we introduced the Rabi frequency, which is the coupling constant measuring the strength of light-matter interaction in this system

$$\Omega = \mathbf{d}_{eg}\mathbf{E}_0/\hbar, \tag{1.35}$$

and $\sigma_+\sigma_- = |e\rangle\langle e|$.

Let us start our analysis by applying the time-dependent perturbation theory, assuming that we are in the regime of weak light-matter coupling (Ω is small). The TLS is initially prepared in some state $|i\rangle$ and we take the initial time to be $t = -\infty$. The perturbation is switched on adiabatically, i.e.

$$\hat{H}_{TLS-F} \to -e^{\varepsilon t}\hat{\mathbf{d}}\mathbf{E}(\mathbf{r}_0 = \mathbf{0}, t) = e^{\varepsilon t}\hat{V}_0\cos\omega_L t = \frac{1}{2}e^{\varepsilon t}\hat{V}_0 e^{i\omega_L t} + \frac{1}{2}e^{\varepsilon t}\hat{V}_0 e^{-i\omega_L t}, \tag{1.36}$$

where we picked $\mathbf{r}_0 = \mathbf{0}$ for simplicity, and we are studying the dynamics at times much smaller than $1/\varepsilon$ (ε is small). It should be noted, that the approach where the interaction turns on abruptly yields the same results in this case. We want to study the $|i\rangle \to |f\rangle$ transition probability $P_{f\leftarrow i}(t)$ under the action of the time-dependent perturbation. It can be shown, that if we are close to the resonance, then the two terms in Eq. (1.36) correspond to the processes of stimulated emission and absorption, respectively, and can be considered separately. Let us focus on absorption, i.e. we choose the perturbation to be $(1/2)e^{\varepsilon t}\hat{V}_0 e^{-i\omega_L t}$. The transition probability to first order in perturbation theory is given by

$$P_{f\leftarrow i}(t) = |c_f^{(1)}(t)|^2 = |-\frac{i}{\hbar}\int_{-\infty}^{t}\langle f|\hat{V}_0|\mathrm{i}\rangle e^{i\omega_{fi}t'}\frac{1}{2}e^{\varepsilon t'}e^{-i\omega_L t'}dt'|^2 = \\ = \frac{1}{4\hbar^2}\frac{e^{2\varepsilon t}}{(\omega_{fi}-\omega_L)^2+\varepsilon^2}|\langle f|\hat{V}_0|\mathrm{i}\rangle|^2, \tag{1.37}$$

where $\hat{V}_0 = -\hat{\mathbf{d}}\mathbf{E}_0$ here is the time-independent part of the perturbation. Applying the identity

$$\lim_{\varepsilon\to 0}\frac{2\varepsilon}{(\omega_{fi}-\omega_L)^2+\varepsilon^2} \to 2\pi\delta(\omega_{fi}-\omega_L) \tag{1.38}$$

to the transition rate $R_{f\leftarrow i} = d(|P_{f\leftarrow i}(t)|^2)/dt|_{\varepsilon\to 0}$, we obtain Fermi' Golden Rule

$$R_{f\leftarrow i} = \frac{2\pi}{4\hbar^2}|\langle f|\hat{V}_0|i\rangle|^2\delta(\omega_{fi}-\omega_L). \tag{1.39}$$

It is important to note, that since $|V_{fi}|^2 = |V_{if}|^2$, we get the detailed balance equation, stating that for two discrete states the transition rates $|i\rangle \to |f\rangle$ and $|f\rangle \to |i\rangle$ are

the same. Averaging the transition rate $R_{f\leftarrow i}$ over all possible directions of the unit vector $\mathbf{n} = \mathbf{E}_0/E_0$, one gets

$$\langle R_{f\leftarrow i}\rangle_{\rm dir} = \frac{2\pi}{4\hbar^2}\langle|\mathbf{d}_{fi}\mathbf{E}|^2\rangle_{\rm dir}\delta\left(\omega_{fi}-\omega_L\right) = \frac{2\pi E_0^2}{4\hbar^2}\langle|\mathbf{d}_{fi}\mathbf{n}|^2\rangle_{\rm dir}\delta\left(\omega_{fi}-\omega_L\right) = \frac{2\pi E_0^2}{4\cdot 3\hbar^2}|\mathbf{d}_{fi}|^2\delta\left(\omega_{fi}-\omega_L\right), \tag{1.40}$$

where we used the fact that $\langle n_i n_j\rangle_{\rm dir} = \delta_{ij}/3 \implies \langle|\mathbf{d}_{fi}\mathbf{n}|^2\rangle_{\rm dir} = |\mathbf{d}_{fi}|^2/3$. The total energy density of the electromagnetic wave at $\mathbf{r}_0$ is $u_{EM}(\mathbf{r}_0,t) = 2u_E(\mathbf{r}_0,t)$, where $u_E(\mathbf{r}_0,t) = \varepsilon_0\mathbf{E}(\mathbf{r}_0,t)^2/2 = (\varepsilon_0 E_0^2/2)\cos^2\left(\omega_L t - \mathbf{k}\mathbf{r}_0\right)$, and we recall now that for a plane EM wave $\mathbf{B}_0 = c^{-1}[(\mathbf{k}/k)\times\mathbf{E}_0]$. Averaging the total energy density over one period $T = 2\pi/\omega_L$, we obtain

$$\langle u_{EM}\rangle_{\rm period} = \frac{1}{T}\int_{t_0}^{t_0+T} u_{EM}(\mathbf{r}_0,t)dt = \frac{1}{2}\varepsilon_0 E_0^2 \tag{1.41}$$

from where one immediately gets the spectral energy density function (energy density per unit frequency)

$$u(\nu) = \frac{1}{2}\varepsilon_0 E_0^2\delta(\nu-\nu_L), \tag{1.42}$$

which satisfies $\int_0^{+\infty} u(\nu)d\nu = \langle u_{EM}\rangle_{\rm period}$. Thus, the transition rate can be expressed as

$$\langle R_{f\leftarrow i}\rangle_{\rm dir} = \frac{|\mathbf{d}_{fi}|^2 u(\nu_{fi})}{2\cdot 3\varepsilon_0\hbar^2} \tag{1.43}$$

and we have

$$B_{12} = B_{21} = \frac{|\mathbf{d}_{fi}|^2}{2\cdot 3\varepsilon_0\hbar^2} \tag{1.44}$$

Interestingly enough, that the semiclassical theory we used above is able to predict the rates of absorption and stimulated emission (Einstein's B_{12} and B_{21} coefficients, respectively), but not the rate of spontaneous emission (Einstein's A-coefficient). The latter can be routinely calculated using the Wigner-Weisskopf method in QED. However, as we derived in the previous subsection, Einstein's A-coefficient can be expressed via Einstein's B-coefficients by considering a thermal equilibrium between light and matter, which yields

$$A_{21} = \frac{8\pi h\omega_{fi}^3}{c^3}B_{21} = \frac{\omega_{fi}^3|\mathbf{d}_{fi}|^2}{3\pi\varepsilon_0\hbar c^3}. \tag{1.45}$$

Einstein's coefficients, calculated in the framework of QED, coincide with our results, listed above.

Let us now try to solve the problem analytically without invoking the perturbation theory. The interaction term $\hat{H}_{TLS-F}$ in the total Hamiltonian can be expanded as

$$\hat{H}_{TLS-F} = -\hat{\mathbf{d}}^{(+)}\mathbf{E}^{(+)}(\mathbf{r}_0,t) - \hat{\mathbf{d}}^{(-)}\mathbf{E}^{(-)}(\mathbf{r}_0,t) - \hat{\mathbf{d}}^{(+)}\mathbf{E}^{(-)}(\mathbf{r}_0,t) - \hat{\mathbf{d}}^{(-)}\mathbf{E}^{(+)}(\mathbf{r}_0,t). \tag{1.46}$$

To investigate this expression we switch to the interaction picture, where the operators acquire time dependence.

$$\begin{aligned}\hat{H}^{(int)}_{TLS-F} &= e^{\frac{i\hat{H}_{TLS}t}{\hbar}}\hat{H}_{TLS-F}e^{-\frac{i\hat{H}_{TLS}t}{\hbar}} = \\ &- \hat{\mathbf{d}}^{(+)(int)}\mathbf{E}^{(+)}(\mathbf{r}_0,t) - \hat{\mathbf{d}}^{(-)(int)}\mathbf{E}^{(-)}(\mathbf{r}_0,t) \\ &- \hat{\mathbf{d}}^{(+)(int)}\mathbf{E}^{(-)}(\mathbf{r}_0,t) - \hat{\mathbf{d}}^{(-)(int)}\mathbf{E}^{(+)}(\mathbf{r}_0,t),\end{aligned} \tag{1.47}$$

where $\hat{\mathbf{d}}^{(\pm)(int)} = \hat{\mathbf{d}}^{(\pm)}e^{\mp i\omega_0 t}$, and we remind that $\mathbf{E}^{(\pm)}(\mathbf{r}_0,t) \sim e^{\mp i\omega_L t}$, thus the first two terms oscillate at frequency $e^{\pm i(\omega_L+\omega_0)t}$, while the last two terms oscillate at frequency $e^{\pm i\Delta t}$, where $\Delta = \omega_L - \omega_0$. In the case when the laser beam is slightly detuned from the TLS transition frequency, i.e when $|\Delta| = |\omega_L - \omega_0| \ll \omega_L + \omega_0$, we can discard the rapidly oscillating terms ($\sim e^{\pm i(\omega_L+\omega_0)t}$) and leave only the slowly oscillating terms ($\sim e^{\pm i\Delta t}$). This approach is called the rotating wave approximation (RWA), and it is justified by noting that on any appreciable time scale, the discarded terms will average to zero. Therefore, in the RWA we have (we pick $\mathbf{r}_0 = \mathbf{0}$ for convenience)

$$\hat{H}^{RWA}_{TLS-F} = -\hat{\mathbf{d}}^{(+)}\mathbf{E}^{(-)}(\mathbf{r}_0=\mathbf{0},t) - \hat{\mathbf{d}}^{(-)}\mathbf{E}^{(+)}(\mathbf{r}_0=\mathbf{0},t) = -\frac{\hbar\Omega}{2}(\sigma_- e^{i\omega_L t} + \sigma_+ e^{-i\omega_L t}). \tag{1.48}$$

Thus, in the RWA the total Hamiltonian takes the form

$$\hat{H}^{RWA} = \hbar\omega_0\sigma_+\sigma_- - \frac{\hbar\Omega}{2}(\sigma_- e^{i\omega_L t} + \sigma_+ e^{-i\omega_L t}). \tag{1.49}$$

To investigate the system's dynamics, we expand the wavefunction in the basis states

$$|\psi\rangle = c_g|g\rangle + c_e|e\rangle, \tag{1.50}$$

where $c_{g,e}$ are time dependent coefficients. Thus, the Schrödinger equation results in the following system of equations for the coefficients $c_{g,e}$

$$\begin{aligned}\frac{\partial c_g}{\partial t} &= +i\frac{\Omega}{2}e^{i\omega_L t}c_e, \\ \frac{\partial c_e}{\partial t} &= -i\omega_0 c_e + i\frac{\Omega}{2}e^{-i\omega_L t}c_g.\end{aligned} \tag{1.51}$$

The time dependence in the coefficients of the system of linear differential equations above can be eliminated by introducing $c_e(t) = a_e(t)e^{-i\omega_L t}$. After that, the equations are readily solved and the general solution reads

$$\begin{aligned}c_g(t) &= e^{i\frac{\Delta t}{2}}\left[c_g(0)\cos\frac{\Omega_R t}{2} - i\frac{\Delta c_g(0) - \Omega c_e(0)}{\Omega_R}\sin\frac{\Omega_R t}{2}\right], \\ c_e(t) &= e^{i\frac{\Delta t}{2}}\left[c_e(0)\cos\frac{\Omega_R t}{2} - i\frac{\Delta c_e(0) - \Omega c_g(0)}{\Omega_R}\sin\frac{\Omega_R t}{2}\right]e^{-i\omega_L t},\end{aligned} \tag{1.52}$$

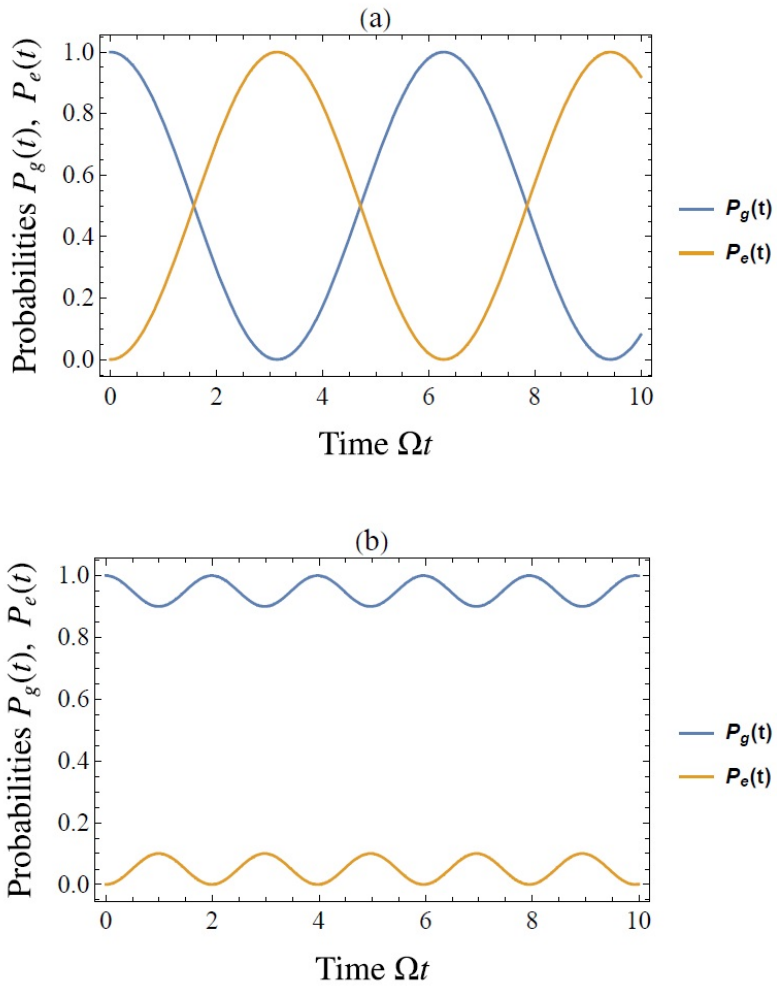

Figure 1.3: The time dynamics of ground (red curve) and excited (blue curve) state population for the detuning values (a) $\Delta = 0$, (b) $\Delta = 3\Omega$.

where we introduced the generalized Rabi frequency

$$\Omega_R = \sqrt{\Omega^2 + \Delta^2}. \tag{1.53}$$

For the case when the system is initially prepared in the ground state, $c_g(0) = 1$, and $c_e(0) = 0$. In this case, the time evolution of the ground and excited-state populations read

$$\begin{aligned} P_g(t) &= |c_g(t)|^2 = \cos^2 \frac{\Omega_R t}{2} + \frac{\Delta^2}{\Omega_R^2} \sin^2 \frac{\Omega_R t}{2}, \\ P_e(t) &= |a_e(t)|^2 = \frac{\Omega^2}{\Omega_R^2} \sin^2 \frac{\Omega_R t}{2}. \end{aligned} \tag{1.54}$$

In Fig. 1.3 the time evolution of the populations is presented. We clearly see that the populations of the two levels oscillate at frequency Ω_R. If the frequency of the laser field is perfectly matched with the resonant frequency of the TLS (i.e. $\Delta = 0$) one sees the population oscillate with the highest possible amplitude equal to one (Rabi flopping). Increasing the detuning Δ, the magnitude of the oscillations Ω^2/Ω_R^2 decreases while their frequency $\Omega_R = \sqrt{\Omega^2 + \Delta^2}$ increases.

1.2.4 Avoided crossing: dressed states

If we apply the unitary transformation $\hat{U} = exp(i\omega_L t|e\rangle\langle e|)$ to the Hamiltonian $\hat{H}^{RWA}$ from the previous section we will get rid of the time dependence in the Hamiltonian:

$$\tilde{H} = \hat{U}\hat{H}^{RWA}\hat{U}^\dagger + i\hbar\frac{\partial \hat{U}}{\partial t}\hat{U}^\dagger = -\hbar\Delta\sigma_+\sigma_- - \frac{\hbar\Omega}{2}(\sigma_- + \sigma_+), \tag{1.55}$$

which can be rewritten as a matrix

$$\tilde{H} = \begin{bmatrix} -\hbar\Delta & -\hbar\Omega/2 \\ -\hbar\Omega/2 & 0 \end{bmatrix}. \tag{1.56}$$

We note, that even though the transformation $\hat{U}$ is unitary, it does change the eigenvalues of the Hamiltonian due to the term $i\hbar\dot{\hat{U}}\hat{U}^\dagger$. The eigenvalues of the Hamiltonian are (they are closely related to Floquet energies, that will be discussed later):

$$E_{1,2} = -\frac{\hbar\Delta}{2} \mp \frac{\hbar\Omega_R}{2} \tag{1.57}$$

and the eigenvectors read

$$\begin{aligned} |1\rangle &= \cos\theta|g\rangle + \sin\theta|e\rangle, \\ |2\rangle &= -\sin\theta|g\rangle + \cos\theta|e\rangle, \end{aligned} \tag{1.58}$$

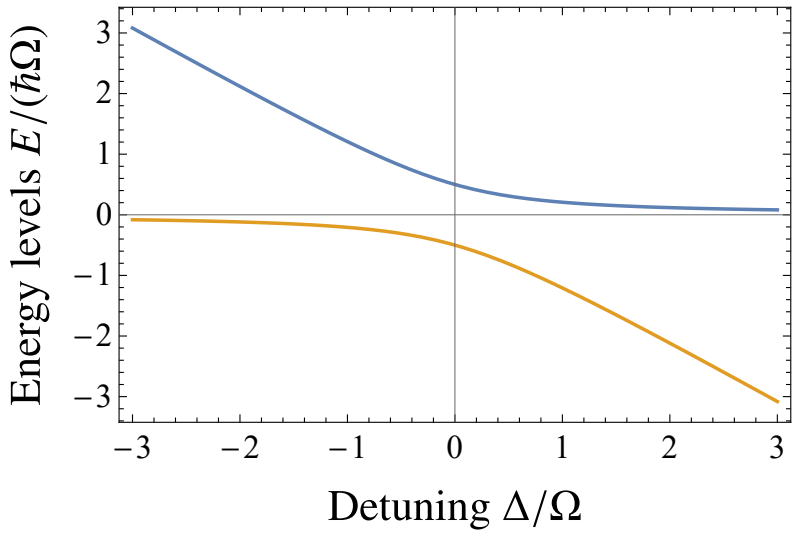

Figure 1.4: The energies of dressed states as a function of detuning Δ.

where

$$\tan\theta = \frac{\Omega}{\Delta + \Omega_R}, \tag{1.59}$$

so we see that the periodic laser field mixes (hybridizes) the two states of the TLS and renormalizes the spectrum of the system, which is referred to as "dressing". We see that for zero detuning ($\Delta = 0$) one has $E_{1,2} = \mp\hbar\Omega_R/2$, and, correspondingly, for vanishing light-matter coupling strength $E_{1,2} = 0$. Now, if we recall that we obtained these energies $E_{1,2}$ after making the unitary transformation $\hat{U} = exp(i\omega_L t|e\rangle\langle e|)$, we will see that after switching back to the original basis $\{|g\rangle, |e\rangle\}$ one has four oscillating exponentials with frequencies $\pm E_{1,2}$ and $\omega_L \pm E_{1,2}$ in the decomposition of the total wave function (we remind that for $\Delta = 0$ one has $\omega_L = \omega_0$). This fact can be interpreted (with caution, this interpretation is of a qualitative nature) as splitting of the two original energy levels $\{0, \omega_0\}$ into the quadruplet $\{0 \pm E_{1,2}, \omega_0 \pm E_{1,2}\}$. We note, that the value of the splitting $|E_2 - E_1|$, in this case, is the same for the ground and excited states and thus the corresponding fluorescence spectrum is the Mollow triplet. As we will see in the future chapters, in the full quantum description one has more than three emission lines (if we focus on two subsets with N and $N+1$ photons, then there are four emission lines) that, however, merge into a Mollow triplet at relatively high intensities ($N \gg 1$) where one may choose to not distinguish between N and $N+1$ photons.

In the Fig. 1.4 we show the energies of the dressed states as a function of the detuning Δ. The light-matter coupling leads to hybridization of the eigenstates, which is pronounced the most at the resonance ($\Delta = 0$). We clearly see that when the detuning is

large compared to the coupling strength Ω, the TLS almost doesn't feel the presence of the dressing field. However, realistic systems always have losses (for example, the bath of the free space modes), which imposes certain limitations on the conditions of the onset of the strong-light matter coupling regime. To account for the losses we add an imaginary part to the excited state energy $\omega_0 \to \omega_0 - i\Gamma$. In this case, the difference between the real parts of the eigenenergies at the point of avoided crossing is given by

$$\mathrm{Re}(E_2 - E_1) = \begin{cases} \hbar\sqrt{\Omega^2 - \Gamma^2}, & \Omega > \Gamma \\ 0, & \Omega \leq \Gamma \end{cases} \tag{1.60}$$

and the corresponding broadenings (imaginary parts with the minus sign) read

$$\gamma_{1,2} \equiv -\,\mathrm{Im}(E_{1,2}) = \begin{cases} \hbar\Gamma/2, & \Omega > \Gamma \\ \frac{\hbar}{2}(\Gamma \pm \sqrt{\Gamma^2 - \Omega^2}). & \Omega \leq \Gamma \end{cases} \tag{1.61}$$

Thus, in order to achieve the regime of strong light-matter coupling the following two conditions must be met: (a) the coupling strength is greater than the broadening $\Omega > \Gamma$ so that there is a non-zero difference between the real parts of the eigenenergies (avoided crossing), and (b) difference between the real parts of the eigenenergies is greater than the sum of the broadenings of the corresponding states, i.e. $\mathrm{Re}(E_2 - E_1) = \hbar\sqrt{\Omega^2 - \Gamma^2} > \gamma_1 + \gamma_2 = \hbar\Gamma$. The condition (b) is stronger than (a), thus finally the regime of strong light-matter coupling in the system under consideration is achieved when $\Omega > \sqrt{2}\Gamma$.

To conclude, in the last two subsections section we discussed the near-resonant interaction between a two-level system and a classical light field in the presence of losses due to the leakage of the energy in the free-space modes. In the future sections of *Introduction*, we will consider a TLS placed in an optical resonator and we will account for the quantum nature of the electromagnetic modes of the cavity in the framework of the quantum Rabi model.

1.2.5 Dressed 2DEG

In the previous subsection, we described the interaction between a quantum two-level system and classical monochromatic light. Now we proceed with studying a more sophisticated set-up, namely, a 2-dimensional electron gas (2DEG) in the presence of a monochromatic light field. A 2DEG is formed, for example, in doped quantum wells. If we neglect the influence of the field on the spin degrees of freedom of the electrons and limit our consideration to the case of a parabolic dispersion, then the problem can be solved exactly [50]. The Hamiltonian of a 2DEG dressed by a linearly polarized monochromatic light, written in the effective mass approximation, reads

$$\hat{H}(t) = \frac{\left[\hat{\mathbf{p}} - q\mathbf{A}(t)\right]^2}{2m}, \tag{1.62}$$

where m is the effective mass. The light field is assumed to be at normal incidence on the surface of the 2DEG, thus one may omit the spatial dependence in the light field. In the radiation gauge $\mathbf{E}(t) = -\dot{\mathbf{A}}(t)$ and the vector potential reads

$$\mathbf{A}(t) = \frac{\mathbf{E}_0}{\omega} \cos \omega t. \tag{1.63}$$

We assume that the frequency $\omega = 2\pi/T$ of the light is far from resonant electron frequencies corresponding to interband electron transitions, thus, in the effective mass approximations one may treat 2DEG as a bunch of free electrons, which is justified by Landau's Fermi-liquid theory. Since a free electron cannot absorb a photon because this process would violate the energy and momentum conservation laws, the only possible remaining source of absorption involves third parties, such as phonons or impurities. To estimate the energy absorption rate due to scattering events we invoke the Drude model, which allows calculating the conductivity in the frequency domain (see detailed derivation in the next section) $\sigma(\omega) = \sigma_0/(1 - i\omega\tau)$, where $\sigma_0 = ne^2\tau/m$ and τ is the mean free time between collisions with impurities and/or phonons (electron relaxation time). Knowing the conductivity, one immediately gets the current density $\mathbf{j} = \mathrm{Re}[\sigma(\omega)\mathbf{E}_\omega]$, here $\mathbf{E}_\omega \propto e^{-i\omega t}$ and $\mathbf{E}(t) = \mathrm{Re}[\mathbf{E}_\omega]$. Finally, the collisional absorption of the electromagnetic field by conduction electrons is given by the expression

$$Q = \frac{1}{T} \int_0^T \mathbf{j}(t)\mathbf{E}(t)dt = \frac{E_0^2}{2} \frac{\sigma_0}{1 + (\omega\tau)^2}, \tag{1.64}$$

where Q is the period-averaged field energy absorbed by conduction electrons per unit time and per unit area. Thus, we demand that ω satisfies the inequality

$$\omega\tau \gg 1, \tag{1.65}$$

which provides that the intraband (collisional) absorption of wave energy by conduction electrons is negligibly small.

According to the Floquet theorem, that will be discussed in details in the next subsection, for a periodic in time Hamiltonian there exist solutions to the corresponding time-dependent Schrödinger equation $i\hbar\dot{\psi}(t) = \hat{H}(t)\psi(t)$ of the form

$$\psi_\alpha(t) = e^{-i\epsilon_\alpha t/\hbar}\phi_\alpha(t), \tag{1.66}$$

where $\phi_\alpha(t)$ are the periodic *Floquet modes* with period $T = 2\pi/\omega$, and ϵ_α are the quasienergy levels. The quasienergy levels are constants in time, but only uniquely defined up to multiples of $\hbar\omega$. Any solution of the Schrödinger equation with the Hamiltonian $\hat{H}(t)$ can be decomposed into

$$\Psi(t) = \sum_\alpha c_\alpha \psi_\alpha(t), \tag{1.67}$$

where the coefficients c_α are determined by the initial wavefunction $\Psi(0) = \sum_\alpha c_\alpha \psi_\alpha(0)$. In the case of the Hamiltonian given by Eq. (1.62) the Floquet modes and quasienergies can be found analytically and they read

$$\phi_\alpha(\mathbf{r}, t) = \exp\left[-i\left(\frac{E_0^2 q^2}{8m\omega^3\hbar}\sin 2\omega t - \frac{q\mathbf{E}_0\mathbf{k}}{m\omega^2}\sin\omega t\right)\right]\chi_{\mathbf{k}}(\mathbf{r}), \tag{1.68}$$

where $\chi_{\mathbf{k}}(\mathbf{r}) = S^{-1/2}\exp(i\mathbf{kr})$, here S is the normalization area, $\mathbf{k} = (k\cos\theta, k\sin\theta)$ in polar coordinates, and the the corresponding quasienrgies read

$$\epsilon_\alpha = \epsilon_{\mathbf{k}} + \frac{E_0^2 e^2}{4m\omega^2\hbar}, \tag{1.69}$$

where $\epsilon_{\mathbf{k}} = \hbar^2\mathbf{k}^2/(2m)$ is the spectrum of the bare 2DEG. We see that the dressing field does not modify the shape of the spectrum in this case, however, as we will see later, for many other systems this is not the case. It should be stressed that the averaged over the field period $T = 2\pi/\omega$ mechanical momentum of the dressed electron coincides with the canonical momentum of the bare electron

$$\frac{1}{T}\int_0^T \langle\psi_{\mathbf{k}}(\mathbf{r}, t)\,|(\hat{\mathbf{p}} - q\mathbf{A}(t))|\,\psi_{\mathbf{k}}(\mathbf{r}, t)\rangle\, dt = \hbar\mathbf{k} \equiv \mathbf{p}, \tag{1.70}$$

where $\psi_{\mathbf{k}}(\mathbf{r}, t) = e^{-i\epsilon_\alpha t/\hbar}\phi_\alpha(\mathbf{r}, t)$ is the corresponding wave function of the dressed electron state, satisfying the Floquet theorem.

The problem of a driven non-interacting 2DEG with a parabolic dispersion, discussed in this section had an exact analytical solution, however, it is quite rare that a periodically driven quantum system admits an analytical solution. In the next subsection, we will discuss in detail the Floquet-Magnus approach, allowing one to approximately account for the dressing field in the high-frequency regime. In the current thesis, this approach will be used, in particular, in order to construct the effective Hamiltonian for dressed ring-shaped nanostructures (quantum rings) with spin-orbit coupling.

1.2.6 Floquet engineering and Magnus expansion

One of the possible ways to achieve the regime of strong light-matter coupling is to apply a high-frequency laser field to a sample. This approach is called Floquet engineering. It turns out, that under certain conditions the behavior of a periodically driven system can be governed by a static effective Hamiltonian, which resembles the initial Hamiltonian of the system (without driving) but with renormalized parameters (such as the bandgap width or the shape of the spectrum) plus extra terms that vanish in the absence of driving. An effective static Floquet Hamiltonian may have band gaps, initially absent in the original, non-driven Hamiltonian, and these gaps may host topologically protected edge states, as will be discussed in the next subsections.

Floquet engineering poses a question of avoiding heating, caused by the drive. It is well understood how this works in non-interacting Floquet systems with single-particle energy eigenstates that lay in some finite bandwidth defined by the local couplings in the system J. Many-body states are constructed by populating these single-particle states. For such systems, if one drives at a frequency much larger than the single-particle bandwidth, $\omega \gg J$, then the drive is inefficient at exciting the single-particle states, which limits the energy absorption. Formally, we will demonstrate below that there exists a Floquet-Magnus expansion in powers of ω^{-1} which converges and can be used to construct a local, non-interacting effective Hamiltonian. By contrast, the Floquet-Magnus expansion obviously breaks down in a generic, interacting many-body when the system size is taken to infinity. However, the truncated expansion manages to capture the behavior of the many-body system at intermediate times (the so-called prethermal regime), but at late times this description breaks down and the system inevitably heats up.

Here we present the Floquet-Magnus method for systems under the influence of periodic drive, which will be applied in the current thesis to achieve the regime of strong coupling between carriers in two-dimensional materials and a high-frequency electromagnetic field. In such systems, the interaction of light and matter leads to the renormalization of the carrier spectrum, which in its turn leads to a substantial modification of various features of the system. If the frequency of the field is greater than the energy scales of the two-dimensional system, the behavior can be described by a quasistationary Hamiltonian different from the original one. The Floquet-Magnus method allows approximately calculate the quasistationary Hamiltonians. A detailed overview of this method is presented in [48], and this section summarizes the main provisions of this method.

Let the system under the action of periodic excitation be described by the Hamiltonian $\hat{H}(t)$, In this case, we can split the full Hamiltonian into two parts $\hat{H}(t) = \hat{H}_0 + \hat{V}(t)$, where $\hat{H}_0$ is the Hamiltonian of the unperturbed system (time-independent), and $\hat{V}(t) = \hat{V}(t+T)$, where $T = 2\pi/\omega$ is the period of driving. Let $\psi(t)$ be the total wave function of the system satisfying the Schrödinegr equation. According to the Floquet theorem, there exist solutions to the corresponding time-dependent Schrödinger equation (with the Hamiltonian $\hat{H}(t)$) of the form

$$\psi_\alpha(t) = e^{-i\epsilon_\alpha t/\hbar}\phi_\alpha(t), \tag{1.71}$$

where $\phi_\alpha(t)$ are the periodic *Floquet modes* with period $T = 2\pi/\omega$, and ϵ_α are the quasienergy levels. The quasienergy levels are constants in time, but only uniquely defined up to multiples of $\hbar\omega$. Any solution of the Schrödinger equation with the Hamiltonian $\hat{H}(t)$ can be decomposed into

$$\Psi(t) = \sum_\alpha c_\alpha \psi_\alpha(t), \tag{1.72}$$

where the coefficients c_α are determined by the initial wavefunction $\Psi(0) = \sum_\alpha c_\alpha \psi_\alpha(0)$.

We introduce the functions $\tilde{\psi}_\alpha(t)$:

$$\tilde{\psi}_\alpha(t) = \hat{U}(t)\psi_\alpha(t) = e^{i\hat{K}(t)}\psi_\alpha(t), \tag{1.73}$$

where $U(t)$ and $\hat{K}(t)$ are unknown unitary and Hermitian operators, respectively. Then the equation for $\tilde{\psi}_\alpha(t)$ reads

$$\begin{array}{l} i\hbar\partial_t\tilde{\psi}_\alpha(t) = \hat{H}_{\text{eff}}\tilde{\psi}_\alpha(t) \\ \hat{H}_{\text{eff}} = e^{i\hat{K}(t)}\hat{H}(t)e^{-i\hat{K}(t)} + i\left(\partial_t e^{i\hat{K}(t)}\right)e^{-i\hat{K}(t)} \end{array} \tag{1.74}$$

If we now require that H_{eff} be time-independent, this will give an equation for $\hat{K}(t)$. This equation is usually not solved exactly, but one can obtain an approximate solution by representing $\hat{H}_{\text{eff}}$ and $\hat{K}(t)$ in the form of a series

$$\hat{H}_{\text{eff}} = \sum_{n=0}^{\infty}\frac{1}{\omega^n}H_n, \quad \hat{K}(t) = \sum_{n=1}^{\infty}\frac{1}{\omega^n}K_n(t) \tag{1.75}$$

Obviously, H_0 is the Hamiltonian of the system in the absence of interaction. If now use the expansions

$$\begin{array}{l} \left(\partial_t e^{i\hat{K}(t)}\right)e^{-i\hat{K}(t)} = i\partial_t\hat{K}(t) - \frac{1}{2!}\left[\hat{K},\partial_t\hat{K}(t)\right] - \frac{i}{3!}\left[\hat{K},\left[\hat{K},\partial_t\hat{K}(t)\right]\right]\ldots \\ e^{i\hat{K}(t)}\hat{H}(t)e^{-i\hat{K}(t)} = \hat{H} + i[\hat{K},\hat{H}] - \frac{1}{2!}[\hat{K},[\hat{K},\hat{H}]]\ldots \end{array} \tag{1.76}$$

then the original equation can be split into a system of equations of a certain order in ω^{-1}. For the n-th order equation, the term K_{n+1} will be expressed in terms of $H_0,\ldots,H_n$ and $K_1,\ldots,K_n$. Having required that for any n one has $H_n = \text{const}(t)$, one can calculate sequentially H_n and K_n in any order of ω^{-1}. In particular, if the Hamiltonian can be represented in the form (driving at a specific frequency)

$$\hat{H} = \hat{H}_0 + \hat{V}e^{i\omega t} + \hat{V}^\dagger e^{-i\omega t}, \tag{1.77}$$

then the effective Hamiltonian in such a system in the first orders in the inverse frequency is written as

$$\begin{array}{l} H_{\text{eff}} = H_0 + \frac{1}{\hbar\omega}\left[V,V^\dagger\right] + \frac{1}{2\hbar^2\omega^2}\left(\left[\left[V,H_0\right],V^\dagger\right] + \left[V,\left[H_0,V^\dagger\right]\right]\right) + \\ + \frac{1}{4\hbar^3\omega^3}\left[\left[V,H_0\right],\left[H_0,V^\dagger\right]\right] + \frac{1}{4\hbar^4\omega^4}\left(\left[\left[\left[V,H_0\right],H_0\right],\left[V^\dagger,H_0\right]\right] + \text{ h.c. }\right) + \ldots \end{array} \tag{1.78}$$

and the corresponding gauge transformation $\hat{K}(t)$ is

$$\begin{array}{l} \hat{K}(t) = \frac{1}{i\hbar\omega}\left(Ve^{i\omega t} - V^\dagger e^{-i\omega t}\right) + \frac{1}{i\hbar^2\omega^2}\left(\left[V,H_0\right]e^{i\omega t} - h.c.\right) - \\ + \frac{1}{i\hbar^3\omega^3}\left(\left[\left[V,H_0\right],H_0\right]e^{i\omega t} - h.c.\right) + \ldots \end{array} \tag{1.79}$$

If it is possible to find the exact transformation $\hat{K}(t)$, leading to a to the stationary Hamiltonian H_{eff}, then its eigenfunctions $\tilde{\psi}_\alpha(t)$ evolve in time according to

$$\tilde{\psi}_\alpha(t) = e^{-i\epsilon_\alpha t/\hbar}\tilde{\psi}_\alpha(0), \tag{1.80}$$

and the total wave function can then be written as

$$\psi_\alpha(t) = e^{-i\hat{K}(t)}\tilde{\psi}_\alpha(t) = e^{-i\epsilon_\alpha t/\hbar}e^{-i\hat{K}(t)}\tilde{\psi}_\alpha(0) \tag{1.81}$$

The functions $\phi_\alpha(t) = e^{-i\hat{K}(t)}\tilde{\psi}_\alpha(0)$ are time-periodic with a period $T = 2\pi/\omega$. Thus, the solution found by the Floquet-Magnus method in an obvious way satisfies the Floquet theorem, and the eigenenergies of the quasistationary Hamiltonian correspond to the quasienergies in the Floquet problem.

Rewriting our results in the language suitable for many-body physics, a state in closed periodically driven systems will evolve as $|\Psi(t)\rangle = \sum_\alpha c_\alpha e^{-i\varepsilon_\alpha t}\,|\Phi_\alpha(t)\rangle$, where $c_\alpha = \langle\Phi_\alpha\,(t_0)\mid\psi_0\rangle$ and $|\psi_0\rangle$ is the initial state at time $t_0 = 0$. $\{|\Phi_\alpha(t)\rangle\}$ are the Floquet modes (states) with quasi-energy ϵ_α. At stroboscopic time ($t = mT$), the presented solution $|\Psi(t)\rangle$ has exactly the same form as the evolution of static systems with $\{\epsilon_\alpha\}$ playing the role of the energy spectrum and $\{|\Phi_\alpha\,(t_0)\rangle\}$ playing the role of the eigenstates.

In a generic closed nonintegrable many-body system, for realistic initial states (for example, product states), that can be experimentally prepared without the need for exponentially long (with the system size) time for preparation, thermalization is expected to occur after sufficiently-long time. This means that thermalization is also expected to occur in periodically-driven systems because $\langle\Psi(t)|\hat{O}|\Psi(t)\rangle|_{t\to\infty} \approx \sum_\alpha e^{-\beta\epsilon_\alpha}\langle\Phi_\alpha\,(t_0)\,|\hat{O}|\Phi_\alpha\,(t_0)\rangle$ should hold for a *local* observable $\hat{O}$ for some value of inverse temperature $\beta = 1/(k_{\mathrm{B}}T)$ at stroboscopic time steps. However, there is a hidden problem here since ϵ_α was defined modulo $\hbar\omega$, and such ambiguity should not manifest itself in physical quantities. The resolution of this apparent paradox is given in Ref. [52], where it was shown that $\langle\Phi_\alpha\,(t_0)\,|\hat{O}|\Phi_\alpha\,(t_0)\rangle$ is almost independent of α. This implies, that $\langle\Phi_\alpha\,(t_0)\,|\hat{O}|\Phi_\alpha\,(t_0)\rangle$ can be factored out, which is the same as saying that $k_{\mathrm{B}}T = \infty$, i.e. generic closed nonintegrable periodically driven many-body systems will thermalize to a state with infinite temperature.

Nevertheless, if the driving is chosen appropriately, heating will occur at very late times, so that the system is described by a single-particle dominated regime at short times and by a nontrivial metastable state at the intermediate time scale – a Floquet prethermal regime [56]. The slow heating processes come from higher-order terms in the Floquet-Magnus expansion, which do not affect the metastable state (an eigenstate of the truncated effective Hamiltonian). However, a lot of aspects of the driven many-body system are not yet fully understood.

1.2.7 Topological insulators and Kubo formula

When one applies an intense high-frequency laser field to a 2D (semiconductor) system, then in the regime of strong-light matter coupling the effective Hamiltonian of the system may acquire bandgaps that were initially absent in the spectrum of the

non-perturbed Hamiltonian. Under certain circumstances that are considered in the present thesis, these bandgaps may host topologically protected edge states – i.e. the modes localized at the edges of the sample and resilient to sufficiently weak perturbations such as impurities or imperfections close to the edges. In this subsection, we address the transport properties and briefly introduce the theory of topologically protected edge states. Such states are of great interest since they are responsible for the family of quantum Hall effects.

In this subsection, we closely follow the lecture notes on Quantum Hall Effect by David Tong [49]. We start with considering a particle moving on a rectangular lattice (a tight-binding model). The lattice period in the x -direction is a; the lattice period in the the y -direction is b. The energy spectrum of this system form energy bands. Within each band, states are labeled by quasimomentum which belong to the first Brillouin zone, parameterized by

$$-\frac{\pi}{a} < k_x \leq \frac{\pi}{a} \quad \text{and} \quad -\frac{\pi}{b} < k_y \leq \frac{\pi}{b} \tag{1.82}$$

The Brillouin zone is actually a torus $\mathbb{T}^2$ rather than a square since the states at the opposite edges are identical. The wavefunctions in a given band can be written using the Bloch theorem

$$\psi_{\mathbf{k}}(\mathbf{x}) = e^{i\mathbf{k}\cdot\mathbf{x}} u_{\mathbf{k}}(\mathbf{x}) \tag{1.83}$$

where $u_{\mathbf{k}}(\mathbf{x})$ is periodic on a unit cell so that $u_{\mathbf{k}}(\mathbf{x}+\mathbf{e}) = u_{\mathbf{k}}(\mathbf{x})$ with either

$$\mathbf{e} = (a, 0) \text{ or } \mathbf{e} = (0, b)$$

The systems we consider are generic and must satisfy a few simple criteria.

First, we will assume that the single-particle spectrum forms energy bands, and the corresponding Brillouin represents a torus $\mathbb{T}^2$. Under certain assumptions the derived formulas are valid in the presence of a magnetic field (in this case a magnetic Brillouin zone appears), however, the Bloch theorem must be altered in this case.

Second, we will assume that the electrons are non-interacting and the many-body states are produced by filling the single-particle spectrum accounting for the Pauli exclusion principle.

Finally, we will assume that the system is an insulator, i.e. there is a gap between bands and that the Fermi energy E_F lies in the gap.

It turns out that if these three criteria above are obeyed, one can assign an integer number (topological invariant) $C \in \mathbb{Z}$ to each band. The origin of topology is in a winding of the phase of the eigenstates as we move around the torus (Brillouin zone $\mathbb{T}^2$). This is closely related to a $U(1)$ Berry connection, defined by

$$\mathcal{A}_i(\mathbf{k}) = -i\langle u_{\mathbf{k}}| \frac{\partial}{\partial k^i} |u_{\mathbf{k}}\rangle \tag{1.84}$$

When one changes the phase of the states $|u_{\mathbf{k}}\rangle$, it corresponds to gauge transformation of the Berry connection. Having the gauge field we can construct the field strength

$$\mathcal{F}_{xy} = \frac{\partial \mathcal{A}_x}{\partial k^y} - \frac{\partial \mathcal{A}_y}{\partial k^x} = -i\langle \frac{\partial u}{\partial k^y} \mid \frac{\partial u}{\partial k^x} \rangle + i\langle \frac{\partial u}{\partial k^x} \mid \frac{\partial u}{\partial k^y} \rangle \tag{1.85}$$

The above mentioned topological invariant – the so-called first Chern number (or the TKNN invariant) is constructing by integrating $\mathcal{F}$ over the Brillouin zone $\mathbb{T}^2$

$$C = -\frac{1}{2\pi} \int_{\mathbb{T}^2} d^2k \mathcal{F}_{xy}. \tag{1.86}$$

This number is always an integer. As we will see below, the Chern number is related to the Hall conductivity σ_{xy} of a non-interacting insulator by summing over all filled bands α:

$$\sigma_{xy} = \frac{e^2}{2\pi\hbar} \sum_{\alpha} C_\alpha \tag{1.87}$$

Let's now prove this result. Our starting point is the Kubo formula for the Hall conductivity at zero temperature of a non-interacting system, which can be derived in the framework of the linear response theory

$$\sigma_{xy} = i\hbar \sum_{E_\alpha < E_F < E_\beta} \int_{\mathbb{T}^2} \frac{d^2k}{(2\pi)^2} \frac{\langle u^\alpha_{\mathbf{k}} | \hat{J}_y | u^\beta_{\mathbf{k}} \rangle \langle u^\beta_{\mathbf{k}} | \hat{J}_x | u^\alpha_{\mathbf{k}} \rangle - \langle u^\alpha_{\mathbf{k}} | \hat{J}_x | u^\beta_{\mathbf{k}} \rangle \langle u^\beta_{\mathbf{k}} | \hat{J}_y | u^\alpha_{\mathbf{k}} \rangle}{\left(E_\beta(\mathbf{k}) - E_\alpha(\mathbf{k})\right)^2} \tag{1.88}$$

where the index α labels the filled bands and β labels the unfilled bands.

To proceed, we need to define the current operator $\hat{\mathbf{J}}$. For a single electron in the presence of an electromagnetic field the current carried by the particle is $\hat{\mathbf{J}} = -e\dot{\hat{\mathbf{x}}} = -e(\hat{\mathbf{p}} + e\mathbf{A})/m$. Here we will employ a more general definition, based on the Bloch theorem

$$\hat{H}|\psi_{\mathbf{k}}\rangle = E_{\mathbf{k}}|\psi_{\mathbf{k}}\rangle \Rightarrow \left(e^{-i\mathbf{k}\cdot\mathbf{x}} \hat{H} e^{i\mathbf{k}\cdot\mathbf{x}}\right) |u_{\mathbf{k}}\rangle = E_{\mathbf{k}}|u_{\mathbf{k}}\rangle \tag{1.89}$$

$$\Rightarrow \hat{\tilde{H}}(\mathbf{k})|u_{\mathbf{k}}\rangle = E_{\mathbf{k}}|u_{\mathbf{k}}\rangle \quad \text{with} \quad \hat{\tilde{H}}(\mathbf{k}) = e^{-i\mathbf{k}\cdot\mathbf{x}} \hat{H} e^{i\mathbf{k}\cdot\mathbf{x}} \tag{1.90}$$

Then we define the current operator in terms of the Bloch Hamiltonian

$$\hat{\mathbf{J}} = -\frac{e}{\hbar} \frac{\partial \hat{\tilde{H}}}{\partial \mathbf{k}} \tag{1.91}$$

It is straightforward to check that the new definition coincides with the old one. For a free particle $\hat{H} = (\hat{\mathbf{p}} + e\mathbf{A})^2/(2m)$, which yields $\hat{\tilde{H}} = (\hat{\mathbf{p}} + \hbar\mathbf{k} + e\mathbf{A})^2/(2m)$ and the current operator of a single particle is $\hat{\mathbf{J}} = -e\dot{\hat{\mathbf{x}}}$.

With this new definition, the Kubo formula reads

$$\sigma_{xy} = \frac{ie^2}{\hbar} \sum_{E_\alpha < E_F < E_\beta} \int_{\mathbb{T}^2} \frac{d^2k}{(2\pi)^2} \frac{\langle u^\alpha_{\mathbf{k}} | \partial_y \hat{\tilde{H}} | u^\beta_{\mathbf{k}} \rangle \langle u^\beta_{\mathbf{k}} | \partial_x \hat{\tilde{H}} | u^\alpha_{\mathbf{k}} \rangle - \langle u^\alpha_{\mathbf{k}} | \partial_x \hat{\tilde{H}} | u^\beta_{\mathbf{k}} \rangle \langle u^\beta_{\mathbf{k}} | \partial_y \hat{\tilde{H}} | u^\alpha_{\mathbf{k}} \rangle}{\left(E_\beta(\mathbf{k}) - E_\alpha(\mathbf{k})\right)^2} \tag{1.92}$$

where ∂_x and ∂_y are derivatives with respect to momenta k_x and k_y. We can then write

$$\langle u_{\mathbf{k}}^{\alpha}|\partial_i \hat{\hat{H}}|u_{\mathbf{k}}^{\beta}\rangle = \langle u_{\mathbf{k}}^{\alpha}|\partial_i\left(\hat{\hat{H}}|u_{\mathbf{k}}^{\beta}\rangle\right) - \langle u_{\mathbf{k}}^{\alpha}|\hat{\hat{H}}|\partial_i u_{\mathbf{k}}^{\beta}\rangle \tag{1.93}$$

$$= \left(E_\beta(\mathbf{k}) - E_\alpha(\mathbf{k})\right)\langle u_{\mathbf{k}}^{\alpha} \mid \partial_i u_{\mathbf{k}}^{\beta}\rangle \tag{1.94}$$

$$= -\left(E_\beta(\mathbf{k}) - E_\alpha(\mathbf{k})\right)\langle \partial_i u_{\mathbf{k}}^{\alpha} \mid u_{\mathbf{k}}^{\beta}\rangle \tag{1.95}$$

After this transformation, the Kubo formula reads

$$\sigma_{xy} = \frac{ie^2}{\hbar}\sum_{E_\alpha<E_F<E_\beta}\int_{\mathbb{T}^2}\frac{d^2k}{(2\pi)^2}\langle\partial_y u_{\mathbf{k}}^{\alpha} \mid u_{\mathbf{k}}^{\beta}\rangle\langle u_{\mathbf{k}}^{\beta} \mid \partial_x u_{\mathbf{k}}^{\alpha}\rangle - \langle\partial_x u_{\mathbf{k}}^{\alpha} \mid u_{\mathbf{k}}^{\beta}\rangle\langle u_{\mathbf{k}}^{\beta} \mid \partial_y u_{\mathbf{k}}^{\alpha}\rangle \tag{1.96}$$

The sum over the unfilled bands can be rearranged as $\sum_\beta |u_{\mathbf{k}}^{\beta}\rangle\langle u_{\mathbf{k}}^{\beta}| = \mathbf{1} - \sum_\alpha |u_{\mathbf{k}}^{\alpha}\rangle\langle u_{\mathbf{k}}^{\alpha}|$. Performing summation over the unfilled bands we're left with

$$\sigma_{xy} = \frac{ie^2}{\hbar}\sum_{\alpha}\int_{\mathbb{T}^2}\frac{d^2k}{(2\pi)^2}\langle\partial_y u_{\mathbf{k}}^{\alpha} \mid \partial_x u_{\mathbf{k}}^{\alpha}\rangle - \langle\partial_x u_{\mathbf{k}}^{\alpha} \mid \partial_y u_{\mathbf{k}}^{\alpha}\rangle. \tag{1.97}$$

The resulting formula is nothing but the sum of the Chern numbers of filled bands

$$\sigma_{xy} = -\frac{e^2}{2\pi\hbar}\sum_{\alpha} C_\alpha, \tag{1.98}$$

which completes the proof.

The Chern number C can't change continuously thus the TKNN formula states that the Hall conductivity is a topological invariant. This means that if we perturb the system in some way then, as long as the topological bandgap is opened, the Hall conductivity can't change.

1.2.8 Light-induced quantum anomalous Hall effect and light-induced (synthetic) Berry curvature

In this section we introduce the theory, describing the photovoltaic anomalous Hall effect [53, 54]. This effect was confirmed experimentally in 2020 [55]. Before proceeding with the photovoltaic (quantum) anomalous Hall effect, we briefly remind the key ideas behind the ordinary Hall effect (OHE), the spin Hall effect (SHE), and the (quantum) anomalous Hall effect (AHE/QAHE). In this subsection, we focus on 2D systems.

The ordinary Hall effect manifests itself in the production of a voltage (the Hall voltage) across a conductor, transverse to an applied magnetic field perpendicular to

the current, flowing through the conductor with an applied electric field. At fields magnetic fields the classical description of the OHE yields the same results as the quantum description, however, at large magnetic fields the quantum description yields quantization of the Hall resistivity as seen in Fig. 1.5(a). This is the manifestation of the quantum Hall effect (QHE), which arises from the quantization of the motion of charged carriers in a magnetic field (Landau levels). The plateaux in the QHE owe their existence to the localization, associated with a drift motion of carriers along contours of constant disorder [49].

Now let us imagine that there is no external magnetic field, and we applied an electric field in, say, x-direction, and for some reasons (will be discussed below), carriers with opposite spins deflect in opposite directions towards the edges in addition to moving along the electric field. If the amount of carriers with opposite spins is the same, then one would have an accumulation of the opposite spins at the opposite edges of the sample in the y-direction. This is the spin Hall effect (SHE). If the sample is a ferromagnetic conductor with a non-zero magnetization, then there is spin imbalance at the Fermi level, and thus, if the same mechanism, that causes SHE, applies, then one would have a voltage drop in the y-direction in addition to spin separation. This is the anomalous Hall effect (AHE). The presence of a non-zero magnetization lifts the spin degeneracy and shifts the spin-up and spin-down density-of-state profiles, which results in spin imbalance at the Fermi level. We note that in the presence of spin-orbit coupling, the density of states (DOS) of a system changes, and thus, for example, the DOS of a 2D material with a parabolic dispersion is no longer equal to a constant in this case.

There are three main mechanisms responsible for spin separation: 1) intrinsic deflection, 2) skew scattering and 3) side jump. The later two mechanisms are related to scattering on impurities, whereas the first one (intrinsic) is due to the momentum-space Berry curvature of a perfect crystal, which typically stems from the presence of spin-orbit coupling. The skew scattering contribution is the asymmetric scattering on impurities which also stems from the spin-orbit coupling. In the modern approach to the anomalous Hall effect, the side-jump contribution defined as the difference between the full Hall conductivity and the two previously considered contributions (intrinsic and skew scattering). As will be discussed below, the intrinsic contribution to the Hall conductivity is quantized due to the topological properties of the Berry curvature, as shown in Fig. 1.5(b). Thus, if one has a perfect crystal without impurities with a non-zero intrinsic contribution to the Hall conductivity, the AHE turns into the quantum anomalous Hall effect (QAHE).

We have outlined the mechanism behind the (Q)AHE, starting from SHE. The key ingredients were spin and spin-orbit coupling. However, in condensed matter physics, one may have effective Hamiltonians with pseudospin degrees of freedom, that have nothing to do with spin but nevertheless act like spin. For example, the effective two-band description of graphene contains a pseudospin degree of freedom, which comes from the fact that an elementary cell of the lattice has a basis of two atoms (that

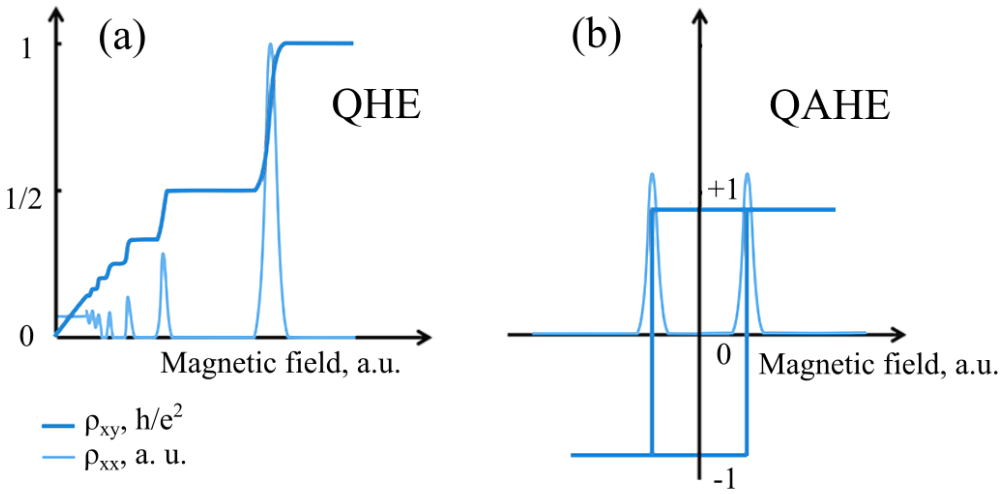

Figure 1.5: Dependence of the transverse resistance ρ_{xy} and the longitudinal resistance ρ_{xx} on the magnetic field strength for the (a) QHE and (b) QAHE. Note the presence of a hysteresis loop in the QAHE.

is why it has two bands). As a consequence, the effective Hamiltonian of graphene contains a spin-orbit-like coupling term and thus one may study the AHE physics. The aforementioned imbalance between opposite pseudospins may be reached by varying the position of the Fermi level.

Now we switch to the photovoltaic AHE, closely following the original paper [53]. We start with deriving the Kubo formula for electric transport for strongly AC-driven systems. We add the periodic AC electric field $\mathbf{A}_{\mathrm{ac}}(t+T) = \mathbf{A}_{\mathrm{ac}}(t)$ via the minimal coupling scheme, with $\Omega = 2\pi/T$ being the frequency. Besides, we add a weak DC electric field with the corresponding vector gauge potential $\mathbf{A}(t) = \mathbf{E}t$ to study the linear response. Thus, we have a time-dependent Hamiltonian $\hat{H}\left(\hbar\mathbf{k} + e\mathbf{A}_{\mathrm{ac}}(t) + e\mathbf{A}(t)\right)$, which we use to construct the Floquet operator

$$\hat{\mathcal{H}}\left(\mathbf{k}, \mathbf{A}_{\mathrm{ac}}(t), \mathbf{A}(t)\right) = \hat{H}\left(\hbar\mathbf{k} + e\mathbf{A}_{\mathrm{ac}}(t) + e\mathbf{A}(t)\right) - i\hbar\partial_t, \tag{1.99}$$

which allows us to rewrite the time-dependent Schrödinger as

$$\hat{\mathcal{H}}\left(\mathbf{k}, \mathbf{A}_{\mathrm{ac}}(t), \mathbf{A}(t)\right)|\Psi(\mathbf{k};t)\rangle = 0. \tag{1.100}$$

Employing the adiabatic approximation for the infinitesimally small DC field $\mathbf{A}(t)$, assuming that $\mathbf{A}(t)$ is an infinitesimally slow function of time, one may introduce the Floquet states, satisfying the Floquet equation

$$\hat{\mathcal{H}}\left(\mathbf{k}, \mathbf{A}_{\mathrm{ac}}(t), \mathbf{A}\right)|\Phi_\alpha(\mathbf{k};\mathbf{A},t)\rangle = \varepsilon_\alpha(\mathbf{k};\mathbf{A})\,|\Phi_\alpha(\mathbf{k};\mathbf{A},t)\rangle \tag{1.101}$$

with a periodicity $|\Phi_\alpha(\mathbf{k};\mathbf{A},t+T)\rangle = |\Phi_\alpha(\mathbf{k};\mathbf{A},t)\rangle$, where $\varepsilon_\alpha(\mathbf{k};\mathbf{A})$ are the Floquet quasi-energies, which are represented here as a sum of the dynamical phase and the Aharonov-Anandan phase (see Eq. (1.110) below). A solution of the time-dependent Schrödinger equation for a fixed $\mathbf{A}$ can be found as $|\Psi_\alpha(t)\rangle = e^{-i\varepsilon_\alpha t/\hbar}|\Phi_\alpha(t)\rangle$. If an inner product is defined as averaging over a period T:

$$\langle\langle\alpha \mid \beta\rangle\rangle \equiv \frac{1}{T}\int_0^T dt\langle\alpha(t) \mid \beta(t)\rangle, \tag{1.102}$$

then the Floquet states form an orthonormal basis, i.e., $\langle\langle\Phi_\alpha(\mathbf{k};\mathbf{A}) \mid \Phi_\beta(\mathbf{k};\mathbf{A})\rangle\rangle = \delta_{\alpha\beta}$. This orthonormal basis can be used to express a solution to the time-dependent Schrödinger as

$$|\Psi_\alpha(\mathbf{k};\mathbf{A}(t),t)\rangle = e^{-i\hbar^{-1}\int_0^t dt'\varepsilon_\alpha(\mathbf{k};\mathbf{A}(t'))}[|\Phi_\alpha(\mathbf{k};\mathbf{A}(t),t)\rangle + \sum_{\beta\neq\alpha}|\Phi_\beta(\mathbf{k};\mathbf{A}(t),t)\rangle\frac{\hbar\langle\langle\Phi_\beta(\mathbf{k};\mathbf{A}(t),t)|\frac{\partial\mathbf{A}}{\partial t}\cdot\frac{\partial}{\partial\mathbf{A}}|\Phi_\alpha(\mathbf{k};\mathbf{A}(t),t)\rangle\rangle}{\varepsilon_\beta(\mathbf{k};\mathbf{A}(t))-\varepsilon_\alpha(\mathbf{k};\mathbf{A}(t))}] \tag{1.103}$$

up to first order in $\mathbf{E} = -\dot{\mathbf{A}}$. We rewrite the

$$\langle\langle\Phi_\beta(\mathbf{k};\mathbf{A}(t))|\frac{\partial\mathbf{A}}{\partial t}\cdot\frac{\partial}{\partial\mathbf{A}}|\Phi_\alpha(\mathbf{k};\mathbf{A}(t))\rangle\rangle = \sum_{\beta\neq\alpha}\frac{\langle\langle\Phi_\beta(\mathbf{k};\mathbf{A}(t))\frac{\partial\mathbf{A}}{\partial t}\cdot\frac{\partial\mathcal{H}}{\partial\mathbf{A}}|\Phi_\alpha(\mathbf{k};\mathbf{A}(t))\rangle\rangle}{\varepsilon_\beta(\mathbf{A}(t))-\varepsilon_\alpha(\mathbf{A}(t))}. \tag{1.104}$$

Since the current operator is defined as $\hat{\mathbf{J}} = -\partial\hat{H}(\hbar\mathbf{k}+e\mathbf{A}_{\rm ac}(t)+e\mathbf{A})/\partial\mathbf{A}$, the Kubo formula for the DC conductivity in an intense AC field reads

$$\sigma_{ab}\left(\mathbf{A}_{ac}\right) = i\hbar\int\frac{d^2\mathbf{k}}{(2\pi)^2}\sum_{\alpha,\beta\neq\alpha}\frac{[f_\beta(\mathbf{k})-f_\alpha(\mathbf{k})]}{\varepsilon_\beta(\mathbf{k})-\varepsilon_\alpha(\mathbf{k})}\frac{\langle\langle\Phi_\alpha(\mathbf{k})|\hat{J}_b|\Phi_\beta(\mathbf{k})\rangle\rangle\langle\langle\Phi_\beta(\mathbf{k})|\hat{J}_a|\Phi_\alpha(\mathbf{k})\rangle\rangle}{\varepsilon_\beta(\mathbf{k})-\varepsilon_\alpha(\mathbf{k})+i\eta} \tag{1.105}$$

where $f_\alpha(\mathbf{k})$ is the distribution function of the α-th Floquet state. The distribution function is non-equilibrium in general if, say, leads attached to a finite system. The Hall conductivity σ_{xy} can be cast to the TKNN formula, introduced in the previous subsection

$$\sigma_{xy}\left(\mathbf{A}_{\rm ac}\right) = \frac{e^2}{\hbar}\int\frac{d^2\mathbf{k}}{(2\pi)^2}\sum_\alpha f_\alpha(\mathbf{k})\left[\nabla_\mathbf{k}\times\mathcal{A}_\alpha(\mathbf{k})\right]_z \tag{1.106}$$

where the light-induced Berry connection (or the light-induced Berry gauge potential) is givne by $\mathcal{A}_\alpha(\mathbf{k}) \equiv -i\left\langle\left\langle\Phi_\alpha(\mathbf{k})\left|\nabla_\mathbf{k}\right|\Phi_\alpha(\mathbf{k})\right\rangle\right\rangle$. Let us redefine the Floquet index such that now it includes the band index too: $\alpha = (i,m)$, here i labels the bands, and m is the original Floquet index. We note, that $\mathcal{A}_\alpha(\mathbf{k})$ is independent of m in contrary to the distribution function $f_\alpha(\mathbf{k})$, which depends on both indices. In equilibrium, $f_{(i,m)}(\mathbf{k}) = \delta_{m0}f_{\rm FD}\left(E_i(\mathbf{k})\right)$, where $E_i(\mathbf{k})$ is the state with momentum $\mathbf{k}$ from the i-th energy band, and $f_{\rm FD}$ is the Fermi-Dirac distribution.

Let us apply this theory to a specific material, namely, graphene, which is described by the two-band 2D Dirac Hamiltonian

$$\hat{H}(t) = \tau_z v \left[\hbar k^x + eA^x_{\rm ac}(t)\right] \sigma_x + v \left[\hbar k^y + eA^y_{\rm ac}(t)\right] \sigma_y, \tag{1.107}$$

where $\tau_z = \pm 1$ is the valley index, marking K and K' points in reciprocal space, $v \ll c$ is the Fermi velocity, and σ_i are the Pauli matrices (they represent the fact that an elementary cell of the lattice has a basis of two atoms, and they have nothing to do with spin, as discussed above). We focus on the case when the driving field is polarized field $(A^x_{\rm ac}, A^y_{\rm ac}) = (E_0/\Omega)(\cos \Omega t, \sin \Omega t)$.

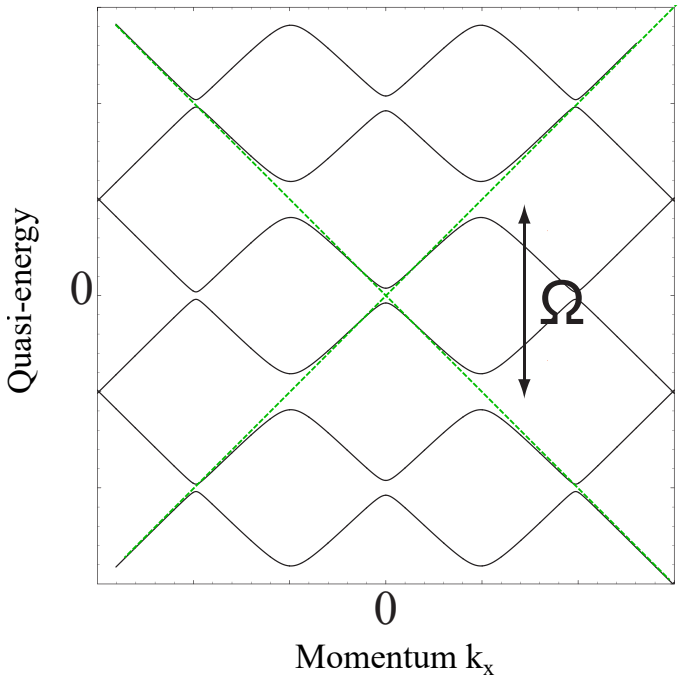

Figure 1.6: Quasi-energy spectrum of graphene, irradiated by circularly polarized light of frequency Ω (adopted form [53]). The dashed green lines show the spectrum of the unperturbed system (two Dirac bands). The sample is finite and periodic boundary conditions are imposed.

The AC field opens gaps $\omega = n \times \Omega/2$, where $n \in \mathbb{Z}$ in the quasi-energy bands as shown in Fig. 1.6. The gap at $\omega = \pm\Omega/2$ is the largest, and it also opens in the case of linearly polarized light. What is more important, there is another gap opening at $k = 0$ which appears only in the case of circularly polarized light. To see this, we note that the time-dependent Schrödinger equation can be solved analytically at $\mathbf{k} = 0$, and its solution reads

$$|\Psi_\alpha(\mathbf{k} = 0, t)\rangle \propto e^{-i\varepsilon_\alpha t/\hbar} \begin{pmatrix} 1 \\ \frac{\tilde{\varepsilon}_i \Omega}{evE_0} e^{i\Omega t} \end{pmatrix} \tag{1.108}$$

where the quasi-energies $\varepsilon_\alpha = \tilde{\varepsilon}_i + m\hbar\Omega$ with $\tilde{\varepsilon}_1 = (\sqrt{4(evE_0/\Omega)^2 + (\hbar\Omega)^2} + \hbar\Omega)/2$, $\tilde{\varepsilon}_2 = (-\sqrt{4(evE_0/\Omega)^2 + (\hbar\Omega)^2} + \hbar\Omega)/2$ The $\alpha = (1,-1), (2,0)$ bands are direct analogs of the original Dirac bands, with the light-induced gap $\Delta = 2\varepsilon_{(1,-1)} = \sqrt{4(evE_0/\Omega)^2 + (\hbar\Omega)^2} - \hbar\Omega$ between them. The quasi-energies are sums of the dynamical phase and the Aharonov-Anandan phase

$$\varepsilon_\alpha = \langle\langle \Phi_\alpha | \hat{H}(t) | \Phi_\alpha \rangle\rangle + \hbar\gamma_\alpha^{\mathrm{AA}}/T, \tag{1.109}$$

where the Aharonov-Anandan phase is given by

$$\gamma_\alpha^{\mathrm{AA}} \equiv T \langle\langle \Phi_\alpha | i\partial_t | \Phi_\alpha \rangle\rangle = \pm\pi \left\{ \left[4(evE_0/\hbar\Omega^2)^2 + 1\right]^{-1/2} - 1 \right\}, \tag{1.110}$$

here $\pm$ refers to $\alpha = (1,-1), (2,0)$, and $i = 1,2$ corresponds to the lower/upper Dirac bands, respectively. In the adiabatic limit ($\Omega \to 0$ with a fixed E_0/Ω) the Aharonov-Anandan phase approaches $\mp\pi$.

Thus, the irradiation opens a topological gap in the Dirac spectrum which leads to the (quantum) anomalous Hall effect. It manifests itself through the appearance of a photovoltaic DC Hall voltage in graphene under circularly polarized illumination.

1.3 Optical microcavities

In the previous section, we discussed how to achieve the regime of strong light-matter due to interaction between a laser field and low-dimensional nanostructures. Another possible way to achieve the desired regime is to place a nano-structure in an optical resonator, where light is trapped, for example, between two mirrors. Here we discuss different realization of optical resonators (microcavities). The results, presented in this section, are relevant for *Chapters* 3, 4, and 7 of the current thesis.

1.3.1 Distributed Bragg reflectors

The simplest possible approach to trap light is to consider a metal-coated dielectric spacer as shown in Fig. 1.7. The standing eigenmodes of such a resonator can be found by superimposing a wave moving in the positive direction of the z-axis and the reflected wave $\mathbf{E}_{||} = \mathbf{E}_{||0} e^{-i(\omega t - kz)} + r\mathbf{E}_{||0} e^{-i(\omega t + kz)} = \mathbf{E}_{||0} e^{-i\omega t} \left(e^{-ikz} + re^{ikz}\right)$, where r is the reflection coefficient. To find the reflection coefficient in the metal and the appropriate boundary conditions, we need to recall that the current density and the electrical displacement in conducting media are related to the electric field oscillating at a certain frequency $\mathbf{E}_\omega \propto e^{-i\omega t}$ by

$$\mathbf{j}_{f\omega} = \sigma(\omega)\mathbf{E}_\omega, \tag{1.111}$$

$$\mathbf{D}_\omega = \varepsilon_L(\omega)\mathbf{E}_\omega, \tag{1.112}$$

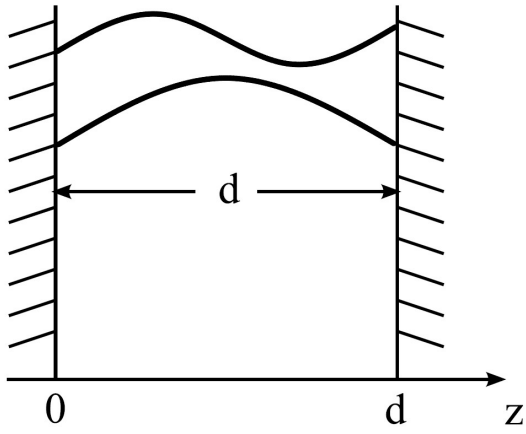

Figure 1.7: Fabry–Perot modes of a resonator, consisting of two parallel perfect metal plates.

where $\varepsilon_L(\omega)$ is the dielectric constant of the lattice (it does not include the conduction electrons), and $\sigma(\omega)$ is the metal conductivity. Here we assumed for simplicity that the medium (metal) is isotropic. Plugging this into the Maxwell equation

$$\nabla \times \mathbf{H} = \frac{\partial \mathbf{D}}{\partial t} + \mathbf{j}_f, \tag{1.113}$$

we get

$$\nabla \times \mathbf{H} = \varepsilon_L \frac{\partial \mathbf{E}}{\partial t} + \sigma \mathbf{E} = \left(\varepsilon_L + \frac{i\sigma}{\omega} \right) \frac{\partial \mathbf{E}}{\partial t} = \varepsilon \frac{\partial \mathbf{E}}{\partial t}, \tag{1.114}$$

from where it follows that the conduction band electrons can be accounted for by introducing the following complex dielectric function,

$$\varepsilon(\omega) = \varepsilon_L(\omega) + \frac{i\sigma(\omega)}{\omega}. \tag{1.115}$$

In the simplest case, the conductivity $\sigma(\omega)$ can be found from the Drude model, where it is assumed that the conduction electrons are non-relativistic non-interacting particles that move in the presence of an external electric $\mathbf{E}$ field and collide with the lattice ions. In the case, Newton's law of motion reads $\dot{\mathbf{p}} = -e\mathbf{E} - \mathbf{p}/\tau$, where τ is mean free time between electron-impurity and/or electron-phonon collisions, and m is the effective electron mass. Defining the current density as $\mathbf{j} = -en\mathbf{p}/m$ with n_e being the conduction band electron concentration, one immediately gets the following expression for the conductivity $\sigma(\omega) = \sigma_0/(1 - i\omega\tau)$, where $\sigma_0 = ne^2\tau/m$. Therefore, this approach results in the following dielectric function

$$\varepsilon(\omega) = \left(\varepsilon_L(\omega) - \frac{\sigma_0 \tau}{1 + \omega^2 \tau^2} \right) + \frac{i\sigma_0}{\omega \left(1 + \omega^2 \tau^2\right)}. \tag{1.116}$$

At low frequencies $\omega\tau \ll 1$, the dielectric function is inversely proportional to ω and is purely imaginary, $\varepsilon(\omega) \approx i\sigma_0/\omega$. At high frequencies $\omega\tau \gg 1$, one has $\varepsilon(\omega) \approx \varepsilon_L(1 - \omega_p^2/\omega^2)$, where $\omega_p^2 = e^2 n/(m\varepsilon_L)$ is the plasma frequency and we neglected the dependence of ε on ω. Knowing the dielectric function one immediately obtains the complex refractive index $n = \sqrt{\varepsilon(\omega)/\varepsilon_0}$. Finally, from the Fresnel equation one gets the reflection coefficient at normal incidence from air to the metal plate

$$r = \frac{1-n}{1+n}. \tag{1.117}$$

The measurable quantities are the reflectivity $R = |r|^2$ and the absorption coefficient $\alpha = 2\omega\,\mathrm{Im}(n)/c$ which relates to the skin depth (the distance of penetration of the optical beam into the medium) as $\delta = 2/\alpha$. At high frequencies (relevant for optics) that are less than the plasma frequency $\omega < \omega_p$ the dielectric function is purely imaginary and thus for this frequency range the reflectivity of metals $R = 1$. For the frequencies of light that exceed the plasma frequency $\omega > \omega_p$ the absorption coefficient vanishes ($\alpha = 0$) while the reflectivity drops sharply to zero followed by growth, and the metallic medium acts as a transparent dielectric. Typically, the plasma frequency belongs to the high visible or ultraviolet range. For the optical frequency range ($\omega\tau \gg 1$ and $\omega < \omega_p$) the light penetration depth is small (the absorption coefficient $\alpha = 2\omega\,\mathrm{Im}(n)/c$ is large) at normal incidence, while the real part of the complex refractive index is zero which yields the reflection coefficient $r \approx -1$.

Now we switch back to calculating the eigenmodes of the resonator, described above. Neglecting the skin depth allows one to impose the boundary condition that the value of the parallel component of the electric field must vanish on the metallic plates, i.e. $\mathbf{E}_{||}(z=0) = \mathbf{E}_{||}(z=d) = \mathbf{0}$. It is clear that this boundary condition immediately implies $r = -1$, showing consistency. Plugging the above mentioned ansatz for the eigenmodes of the resonator $\mathbf{E}_{||} = \mathbf{E}_{||0} e^{-i\omega t}\left(e^{-ikz} + re^{ikz}\right)$ one obtains the following set of eigenmodes

$$\omega_j = \frac{\pi c j}{d},\ j = 1, 2, 3\ldots \tag{1.118}$$

These eigenmodes exhibit themselves as dips (peaks) when measuring the reflectance (transmittance) of the resonator.

However, if we want to work the optical region of the spectrum, the metallic resonators described above have a very small Q-value, not exceeding a few hundred (see Fig. 1.8). Another way of trapping the light is to use distributed Bragg reflectors (DBR's). A DBR is a periodic structure composed of two types of dielectric layers: A with refraction index n_a and width $d_a = \lambda_c/(4n_a)$, and $\hat{C}$ with refraction index n_b and width $d_b = \lambda_c/(4n_b)$, alternating throughout one dimension as schematically shown in Fig. 1.9 (a). For normally incident light with a wavelength in the vicinity of λ_c the structure's reflectivity is close to unity. It is the positive interference of waves, reflected from all interfaces between the layers, that is responsible for such a good reflectivity. The use of DBRs is ubiquitous in mesoscopic scale devices operating with

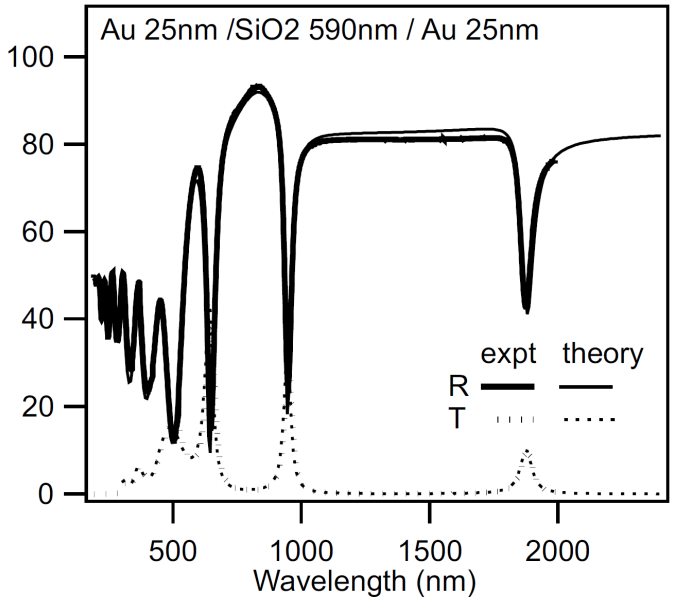

Figure 1.8: Reflection and transmission (experiment and theory) of a planar microcavity consisting of a gold-coated 590 nm glass spacer, taken from [19].

light. The microresonators based on DBRs are relatively easy to fabricate and are characterized by a very large Q-factor in the optical region of the spectrum.

To calculate the properties of DBRs we employ the transfer matrix approach. Let us consider a plane wave propagating along the structure growth direction z. The electric field's component (say $E_x(z) = E(z)$) is represented as

$$E(z) = E_{\rightarrow}(z)e^{ikn(z)z-i\omega t} + E_{\leftarrow}(z)e^{-ikn(z)z-i\omega t}, \tag{1.119}$$

where ω and $\lambda = 2\pi/k$ are the wave frequency and length in a vacuum. The electric field is represented as a sum of the wave propagating along the growth direction z with the envelope amplitude $E_{\rightarrow}$ and the wave propagating opposite to the z-axis with the envelope amplitude $E_{\leftarrow}$. These two envelope amplitudes can be cast into a 2 by 1 vector

$$\mathbf{A}(z) = \begin{bmatrix} E_{\rightarrow}(z) \\ E_{\leftarrow}(z) \end{bmatrix}. \tag{1.120}$$

To relate the amplitudes on the opposite ends of a corresponding layer (A or B), we introduce 2 by 2 matrices T_a and T_b. These objects $T_{a(b)}$ are called transfer matrices and they relate the vectors $\mathbf{A}_t$ and $\mathbf{A}_b$ on the opposite ends of a layer, so that $\mathbf{A}_b = T_{a(b)}\mathbf{A}_t$.

For an incident plane wave with the wave vector $k = 2\pi/\lambda$ each individual layer's

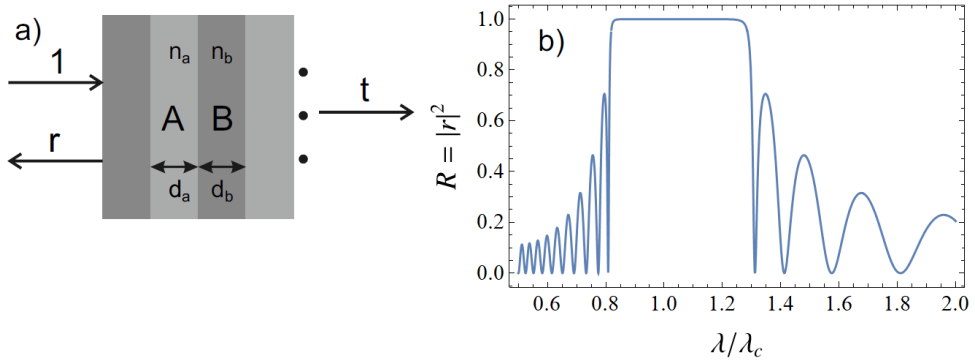

Figure 1.9: (a) A sketch of the DBR (b) Dependence of the reflectivity (abs. val. squared) on the wavelength for a DBR consisting of 10 periods of layers with refraction indices $n_a = 1$ and $n_b = 2$.

transfer matrix is constructed by noting that the wave acquires the phase $\varphi_{a(b)} = kn_{a(b)}d_{a(b)}$ while propagating, and thus:

$$T_{a(b)} = \begin{pmatrix} \exp\left(i\varphi_{a(b)}\right) & 0 \\ 0 & \exp\left(-i\varphi_{a(b)}\right) \end{pmatrix} \tag{1.121}$$

The transfer matrices for the interfaces (AB and BA) between the two media are constructed by means of Fresnel's equations:

$$T_{ab} = \begin{pmatrix} 1 & \tilde{n} \\ \tilde{n} & 1 \end{pmatrix}, \tag{1.122}$$

$$T_{ba} = \begin{pmatrix} 1 & -\tilde{n} \\ -\tilde{n} & 1 \end{pmatrix}, \tag{1.123}$$

where

$$\tilde{n} = \frac{n_a - n_b}{n_a + n_b}. \tag{1.124}$$

It is clear, that the transfer matrix of one structure period (AB) is $T = T_a T_{ab} T_b T_{ba}$. If we focus on a semi-infinite structure the reflectivity is obtained by calculating the eigenvectors of the period transfer matrix. Since eigenvectors are defined up to normalization, one can always recast the corresponding eigenvector to the following form $(1, r)$, such that its upper element is unity, which matches the case of an incident plane wave with unit amplitude. Then the lower element would correspond to the reflectivity. After performing this simple calculation for the perfectly tuned wavelength $\lambda = \lambda_c$, one gets $r = 1$ (perfect reflection). If the light frequency is slightly detuned from λ_c, then we have

$$r = \exp\left[i\frac{L_{\mathrm{DBR}}}{n_0 c}\left(\omega - \omega_c\right)\right], \tag{1.125}$$

where the coefficient L_{DBR}, frequently called the effective length of a Bragg mirror, is defined as

$$L_{\mathrm{DBR}} = \frac{n_a n_b \lambda_c}{2\,(n_a - n_b)}. \tag{1.126}$$

Here n_0 is the refractive index of the medium outside of the DBR. For finite DBRs the structure's transfer matrix is $T_{\mathrm{full}} = T^N$, where N is the number of periods (for example, if $N = 2$ we have ABAB). Knowing the full transfer matrix T_{full}, the (complex) reflectivity coefficient is extracted as $r = -T_{\mathrm{full}21}/T_{\mathrm{full}22}$. We performed this procedure for $n_a = 1$, $n_b = 2$ and the result for the reflectivity $R = |r|^2$ as a function of the incident wavelength is shown in Fig. 1.9 (b). If we considered an infinite structure, it would be characterized by allowed and forbidden (stop) bands analogously to the case of a quantum particle in a periodic potential. If we take an infinite DBR structure and introduce a defect layer, then it is possible for the light to be localized in the vicinity of the defect layer. Such excitation would lay within the stopband.

1.3.2 Cavity-embedded quantum wells

For the finite system, sketched in Fig. 1.10, where one has two DBR mirrors of finite width surrounding a "defect" (a semiconductor layer that differs from A and B) the light cannot be trapped in such a resonator for an infinitely long time even if we completely neglect absorption in the material. The reason for this is that light can leave the cavity through its boundaries. Thus, the cavity optical mode has a linewidth Γ, defined as the frequency width at half maximum (FWHM). The inverse quantity Γ^{-1} has the meaning of the cavity photon lifetime. Clearly, accounting for absorption diminishes the lifetime.

To characterize the quality of trapping the light in the presence of losses, the quality factor of a cavity Q is introduced. It describes the average number of oscillations made by the trapped electric field before it leaves the cavity. A quality factor is defined as

$$Q = \frac{\omega_c}{2\pi\Gamma}, \tag{1.127}$$

Another important characteristic of microcavities is the finesse of the cavity, which is defined as

$$F = \frac{\Delta\omega}{2\pi\Gamma}. \tag{1.128}$$

If the cavity hosts more than one modes, then to ensure that the spectral lines of the cavity are well-resolved one has to provide that the condition $F \gg 1$ is fulfilled. In this case, if we are tuned to a specific mode, the microcavity can be effectively treated as a single-mode resonator. This can be provided by diminishing the size of cavities, whereas the achievement of a high Q-factor is more challenging.

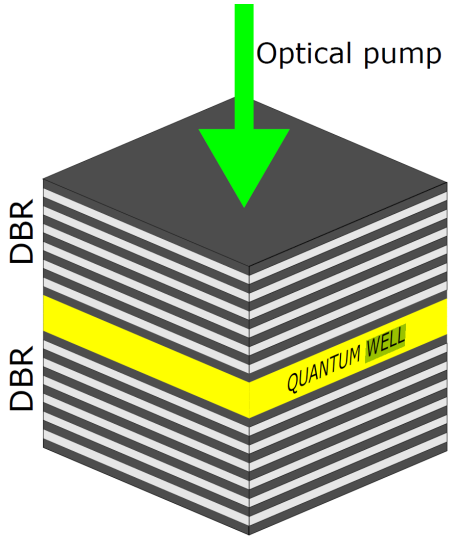

Figure 1.10: A planar microcavity: a quantum well sandwiched between two DBRs.

We note, that the electromagnetic field can propagate freely in the plane of the well while being confined in the growth direction. This circumstance allows one to introduce an effective mass of photons in such structures by means of the following procedure. We focus on a single cavity mode and neglect losses for a moment than its dispersion for small in-plane momentum $\mathbf{k} = (k_x, k_y)$ can be written as follows

$$E_C(k) = \frac{\hbar c}{n_{\text{eff}}} \sqrt{\left(\frac{2\pi}{\lambda}\right)^2 + k^2} \approx E_C(0) + \frac{\hbar^2 k^2}{2m_C}, \tag{1.129}$$

where $k = \sqrt{k_x^2 + k_y^2}$ denotes the absolute value of the in-plane wave vector $\mathbf{k}$ and

$$n_{\text{eff}} = \frac{\int_0^L n(z) E^2(z) \mathrm{d}z}{\int_0^L E^2(z) \mathrm{d}z} \tag{1.130}$$

is the effective refractive index, with $E(z)$ being the amplitude of the mode's electric field. The first term in Eq. (1.130) is nothing but the cavity mode frequency (energy), while the second term describes the in-plane propagation of waveguide modes.

The abovementioned set-ups based on DBR microcavities are of vast interest for theoretical studies since they allow for achieving the regime of strong-light matter coupling which is one of the central aspects of cavity quantum electrodynamics (CQED).

As for the practical applications of optical microcavities, it is worth mentioning a Vertical Cavity Surface Emitting Laser (VCSEL), which is a type of semiconductor laser diode. Contrary to conventional edge-emitting semiconductor lasers, a VCSEL emits a light beam perpendicular from the top surface. A VCSEL is now a commercialized product and is used for making computer mouses, fiber optic communications, laser printers, Face ID, and smartglasses. VCSELs typically operate in the weak coupling regime, where the decay rates of the light and matter components overcome the light-matter coupling strength.

1.4 Excitons

In the previous section, we discussed how to trap light in a microcavity in order to couple the trapped photons to the matter excitation of a nano-structure, placed in the microcavity. In this section, we will discuss the special type of matter excitations (excitons). The results, presented in this section, are relevant for *Chapters* 3, 4, 6, and 7 of the current thesis.

1.4.1 Bulk excitons

An exciton is a composite bosonic quasi-particle, that consists of a conduction band electron and a valence band hole. It may be understood as an excitation quantum over the ground state semiconductor (or insulator) electron subsystem. The two types of excitons are distinguished, depending on their characteristic size: Frenkel and Wannier-Mott excitons. The first ones correspond to the situation where the average electron-hole distance is of the order of the lattice constant. The second one corresponds to the opposite limit, where the distance between the electron and the hole greatly exceeds the size of a unit cell. In the present thesis, we deal with Wannier-Mott excitons, whereas Frenkel excitons are mostly relevant to organic molecular crystals.

In the effective mass approximation, a Wannier-Mott exciton in a bulk crystal can be described as a two-body bound state with the Coulombic attraction between the electron and the hole, and therefore the Hamiltonian of the exciton is analogous to that of the Hydrogen atom

$$\hat{H} = -\frac{\hbar^2}{2m_c}\nabla_e^2 - \frac{\hbar^2}{2m_v}\nabla_h^2 - \frac{e^2}{4\pi\varepsilon_0\varepsilon|\mathbf{r}_e - \mathbf{r}_h|} \tag{1.131}$$

where the first two terms describe the kinetic energies of the conduction band electron with the effective mass m_c and the valence band hole with the effective mass m_v, and ε is the effective dielectric permittivity of the crystal (this description only applicable on the scales larger than the lattice constant).

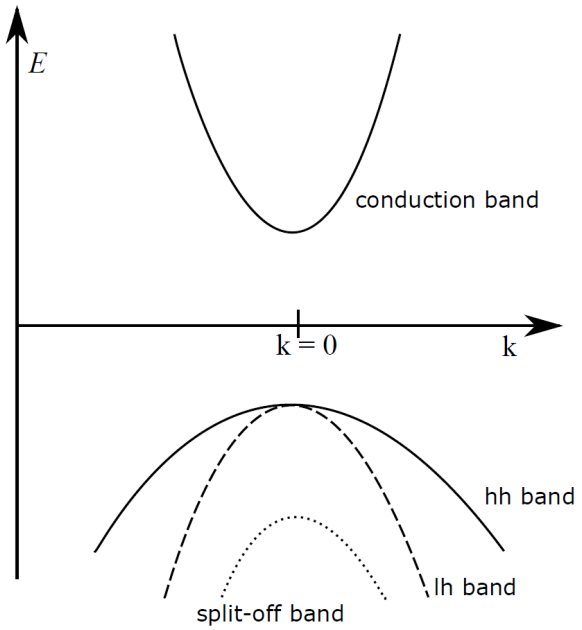

Figure 1.11: The bandstructure of a typical direct-gap semiconductor with a Zincblende crystal lattice.

An important role in the current thesis is played by GaAs-based materials. They have the Zincblende structure, which is characterized by a direct energy gap in the Γ-point of the Brillouin zone. Valence band energy dispersion splits into the heavy hole and light hole branches, see Fig. 1.11.

When one shines on a semiconductor sample with the appropriate frequency, the sample absorbs light. If we neglect excitons for a moment then the process goes as follows: the photons cause the transitions of electrons from the valence band to the conduction band (dashed blue line in Fig. 1.12) and the absorption is proportional to the density of electronic states in the conduction band and no absorption occurs unless the frequency of the light is greater or equal than the bandgap with since there are no states within the bandgap for the electrons to transfer to. If one takes the excitons into account, they manifest themselves as peaks below the single-particle continuum since their energy levels are located in the bandgap (red line Fig. 1.12).

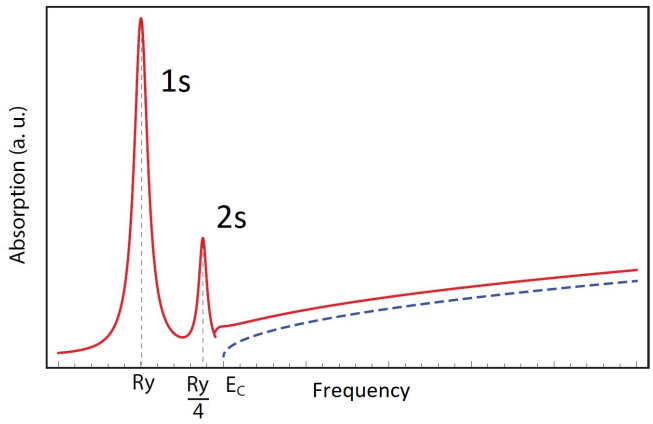

Figure 1.12: Absorption spectrum of a direct-gap bulk semiconductor as a function of frequency (photon energy). The peaks correspond to the excitonic states that are located in the bandgap.

1.4.2 2D excitons

In confined Zincblende systems, such as quantum wells or wires, the size quantization effects remove the degeneracy between the heavy and light holes at the Γ-point. That leads to the fact, that the heavy hole exciton is the lowest energy state of an electron-hole pair. Since the electron's spin projection is $\pm 1/2$ and the heavy holes total momentum projection is $\pm 3/2$, then the spin structure of the exciton consists of four possible total momentum projections -2, -1, $+1$ and $+2$. The optically active (i.e. may decay with photon emission) bright states are those with total momentum projections ± 1, whereas states with ± 2 are called dark, see Fig. 1.13. The frequency of the emitted photon is defined by the exciton transition energy, $E_g + E_e + E_h - E_B$, where E_B is the exciton binding energy, $E_{e(h)}$ is the electron (hole) energy originating from size quantization, and E_g is the bulk bandgap width.

Below we give a mathematical description of two-dimensional excitons, which starts with the following Hamiltonian

$$\hat{H}_{2D} = \frac{\hbar^2(\hat{k}_{e||}^2 + \hat{k}_{ez}^2)}{2m_e} + \frac{\hbar^2(\hat{k}_{h||}^2 + \hat{k}_{hz}^2)}{2m_h} - \frac{e^2}{4\pi\varepsilon_0\varepsilon|\mathbf{r}_e - \mathbf{r}_h|} + U(z_e) + U(z_h), \quad (1.132)$$

where the first two terms correspond to the kinetic energies of the electron and the hole, the third term describes the Coulomb interaction, and the last two terms stand for the confinement potential in the z-direction that restricts the motion of the electron and the hole. In the limit of narrow quantum well the motions of the electron and the hole the problem can be projected on the lowest size quantization subband and thus now regard $\mathbf{r}_{e(h)}$ as the in-plane coordinates of the particles. Switching to the

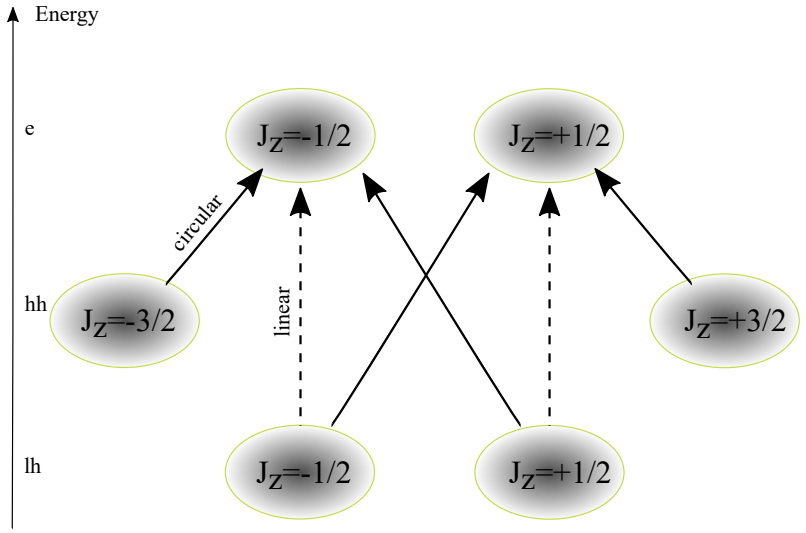

Figure 1.13: Light with certain polarization can induce an interband optical transition between the energy-split hole subbands and the electron band, depending on the indicated projection of the total angular momentum on the chosen axis (usually the growth axis). For example, when a circularly polarized light (photon) causes the transition from the heavy-hole branch with $J_z = -3/2$ to the conduction band with $J_z = -1/2$, the z-projection of the total angular momentum of the system becomes equal to $-(-3/2) + (-1/2) = +1$. One may understand it as either considering the state of a hole as the time-reversal state of the corresponding electron state or by noting that when one deletes an electron with some value of J_z from the system, the total J_z of the system changes by the value of $-J_z$. Interband optical transition matrix elements are proportional to J_z, thus the hh to CB optical transition is 3 times stronger than the lh to CB transition.

center-of-mass and relative coordinates $\mathbf{r} = \mathbf{r}_e - \mathbf{r}_h$, $\mathbf{R} = (m_e\mathbf{r}_e + m_h\mathbf{r}_h)/(m_e + m_h)$, and decoupling all the degrees of freedom from the relative motion we get

$$\hat{H}_{2D\text{exc}} = -\frac{\hbar^2 \Delta_{\mathbf{r}}}{2\mu} - \frac{e^2}{4\pi\varepsilon_0\varepsilon|\mathbf{r}|}, \tag{1.133}$$

which is nothing but the 2D analog of the Schrödinger equation for the hydrogen atom in the medium, having dielectric permittivity ε. By μ we denoted the reduced mass $\mu = m_e m_h/(m_e + m_h)$. The eigenfunctions and eingenvalues of this system can be found using the same approach as in the 3D case [8]. The corresponding energy spectrum reads

$$E_n = -\frac{1}{(4\pi\varepsilon_0\varepsilon)^2}\frac{\mu e^4}{2\hbar^2(n-1/2)^2} = -\frac{1}{4\pi\varepsilon_0\varepsilon}\frac{e^2}{4a_{2D}(n-1/2)^2}, \tag{1.134}$$

where $a_{2D} = 4\pi\varepsilon_0\varepsilon\hbar^2/(2\mu e^2)$ is the two-dimensional Bohr radius (2 times smaller

compared to 3D) and $n = 1, 2, 3, \ldots$. The above-described formalism is physically correct only in the case of low concentrations of excited electron-hole pairs, which should be below the critical value, called the Mott density. Thus the validity of the application of exciton formalism is the condition

$$n_{\text{exc}} a_{2D}^2 \ll 1, \tag{1.135}$$

where n_{exc} denotes the exciton concentration.

When an exciton gas is formed, its properties strongly depend on the interactions between the excitons. There are four possible processes, contributing to the exciton-exciton-interaction [154]: direct Coulomb interaction between electrons and holes, exchange of electrons (holes) between excitons, and simultaneous exchange of the electron and the hole. The interaction between excitons is short-range. It was shown that the contribution to the interaction coming from electron and hole exchange significantly outweighs the direct interaction between excitons. The main contribution governed by the exchange terms can be accurately estimated as [155]:

$$V_{XX} \approx \frac{6 E_b a_{2D}^2}{A}, \tag{1.136}$$

where A is the normalization area that is not present in any observables. In the current thesis, we will apply this formalism to study exciton-exciton interactions for both the ground and excited states in transition-metal dichalcogenide monolayers (TMD), where excitonic properties are especially well pronounced even at room temperature.

1.5 Strong light-matter coupling in microcavities

In the section, we discuss different aspects of the coupling between the microcavity photons (quanta of an electromagnetic field) and the matter excitations (excitons) of low-dimensional nanostructures, embedded in microcavities. The results, presented in this section, are relevant for *Chapters* 3, 4, 6, and 7 of the current thesis.

1.5.1 Quantization of an electromagnetic field

We start our discussion with the quantization of an electromagnetic field since for our future considerations the quantum nature of an electromagnetic field will be crucial. We choose the Coulomb gauge (non-relativistic), for which $\nabla \cdot \mathbf{A} = 0$, makes $\mathbf{A}$ transverse. The Fourier expansion of the vector potential in a finite box of volume $V = L^3$ is then

$$\mathbf{A}(\mathbf{r}, t) = \sum_{\mathbf{k}} \sum_{\mu = \pm 1} \left(\mathbf{e}^{(\mu)}(\mathbf{k}) a_{\mathbf{k}}^{(\mu)}(t) e^{i\mathbf{k}\cdot\mathbf{r}} + \overline{\mathbf{e}}^{(\mu)}(\mathbf{k}) \bar{a}_{\mathbf{k}}^{(\mu)}(t) e^{-i\mathbf{k}\cdot\mathbf{r}} \right) \tag{1.137}$$

where $\bar{a}$ stands for the complex conjugate of a. The wave vector $\mathbf{k}$ shows the propagation direction of the corresponding polarized monochromatic wave (a Fourier component) of $\mathbf{A}(\mathbf{r},t)$; the length of the wave vector is

$$|\mathbf{k}| = \frac{\omega}{c} \tag{1.138}$$

with ω the frequency of the mode. In this summation $\mathbf{k}$ runs over quarter-space.

Two $\mathbf{e}^{(\mu)}$ polarization vectors are unit vectors for left and right hand circular polarized (LCP and RCP) electromagnetic waves and they are perpendicular to $\mathbf{k}$:

$$\mathbf{e}^{(\pm 1)} \equiv \frac{\mp 1}{\sqrt{2}} \left(\mathbf{e}_x \pm i\mathbf{e}_y\right) \qquad \text{with} \qquad \mathbf{e}_x \cdot \mathbf{k} = \mathbf{e}_y \cdot \mathbf{k} = 0 \tag{1.139}$$

From the field equations of $\mathbf{B}$ and $\mathbf{E}$ in terms of $\mathbf{A}$ above, electric and magnetic fields read

$$\begin{aligned}
\mathbf{E}(\mathbf{r},t) &= i\sum_{\mathbf{k}}\sum_{\mu=\pm 1} \omega \left(\mathbf{e}^{(\mu)}(\mathbf{k}) a_{\mathbf{k}}^{(\mu)}(t) e^{i\mathbf{k}\cdot\mathbf{r}} - \overline{\mathbf{e}}^{(\mu)}(\mathbf{k}) \bar{a}_{\mathbf{k}}^{(\mu)}(t) e^{-i\mathbf{k}\cdot\mathbf{r}}\right) \\
\mathbf{B}(\mathbf{r},t) &= i\sum_{\mathbf{k}}\sum_{\mu=\pm 1} \left\{ \left(\mathbf{k}\times\mathbf{e}^{(\mu)}(\mathbf{k})\right) a_{\mathbf{k}}^{(\mu)}(t) e^{i\mathbf{k}\cdot\mathbf{r}} - \left(\mathbf{k}\times\overline{\mathbf{e}}^{(\mu)}(\mathbf{k})\right) \bar{a}_{\mathbf{k}}^{(\mu)}(t) e^{-i\mathbf{k}\cdot\mathbf{r}} \right\},
\end{aligned} \tag{1.140}$$

where we absorbed the trivial time dependence in the coefficients $a_{\mathbf{k}}^{(\mu)}(t) = a_{\mathbf{k}}^{(\mu)} e^{-iwt}$. Now we quantize the field be means of the quantization rules are:

$$\begin{aligned}
a_{\mathbf{k}}^{(\mu)}(t) &\to \sqrt{\tfrac{\hbar}{2\omega V\epsilon_0}}\, \hat{a}^{(\mu)}(\mathbf{k}) \\
\bar{a}_{\mathbf{k}}^{(\mu)}(t) &\to \sqrt{\tfrac{\hbar}{2\omega V\epsilon_0}}\, \hat{a}^{\dagger(\mu)}(\mathbf{k})
\end{aligned} \tag{1.141}$$

satisfying to the bosonic commutation relations

$$\left[\hat{a}^{(\mu)}(\mathbf{k}), \hat{a}^{(\mu')}(\mathbf{k}')\right] = 0 \tag{1.142}$$

$$\left[\hat{a}^{\dagger(\mu)}(\mathbf{k}), \hat{a}^{\dagger(\mu')}(\mathbf{k}')\right] = 0 \tag{1.143}$$

$\left[\hat{a}^{(\mu)}(\mathbf{k}), \hat{a}^{\dagger(\mu')}(\mathbf{k}')\right] = \delta_{\mathbf{k},\mathbf{k}'}\delta_{\mu,\mu'}$. The square brackets indicate a commutator.

Thus, the quantized fields (operator fields) have the following form

$$\begin{aligned}
\hat{\mathbf{A}}(\mathbf{r}) &= \sum_{\mathbf{k},\mu} \sqrt{\tfrac{\hbar}{2\omega V\epsilon_0}} \left\{ \mathbf{e}^{(\mu)} \hat{a}^{(\mu)}(\mathbf{k}) e^{i\mathbf{k}\cdot\mathbf{r}} + \overline{\mathbf{e}}^{(\mu)} \hat{a}^{\dagger(\mu)}(\mathbf{k}) e^{-i\mathbf{k}\cdot\mathbf{r}} \right\} \\
\hat{\mathbf{E}}(\mathbf{r}) &= i\sum_{\mathbf{k},\mu} \sqrt{\tfrac{\hbar\omega}{2V\epsilon_0}} \left\{ \mathbf{e}^{(\mu)} \hat{a}^{(\mu)}(\mathbf{k}) e^{i\mathbf{k}\cdot\mathbf{r}} - \overline{\mathbf{e}}^{(\mu)} \hat{a}^{\dagger(\mu)}(\mathbf{k}) e^{-i\mathbf{k}\cdot\mathbf{r}} \right\} \\
\hat{\mathbf{B}}(\mathbf{r}) &= i\sum_{\mathbf{k},\mu} \sqrt{\tfrac{\hbar}{2\omega V\epsilon_0}} \left\{ \left(\mathbf{k}\times\mathbf{e}^{(\mu)}\right) \hat{a}^{(\mu)}(\mathbf{k}) e^{i\mathbf{k}\cdot\mathbf{r}} - \left(\mathbf{k}\times\overline{\mathbf{e}}^{(\mu)}\right) \hat{a}^{\dagger(\mu)}(\mathbf{k}) e^{-i\mathbf{k}\cdot\mathbf{r}} \right\}.
\end{aligned} \tag{1.144}$$

1.5.2 Cavity exciton-polaritons

In the previous sections, we discussed how to trap matter excitation and how to trap light. In this subsection, we will discuss the interaction between the microcavity mode and the excitons in the quantum well. It turns out that if one has two sufficiently narrow interacting modes then the regime of strong coupling may appear under conditions discussed below. Thus, the excitons and the microcavity mode, are good candidates for achieving the regime of strong light-matter coupling contrary to the electron-hole continuum.

Early theoretical predictions of the strong exciton-photon coupling regime were done in the mid-fifties [14–16], however experimentally this was implemented several decades later – in 1992 in a 2D semiconductor nanostructure, consisting of two DBRs and quantum wells sandwiched between the mirrors [17].

The two-dimensional excitons interact with trapped cavity photons. By adjusting the parameters of the system one can tune the cavity mode to be in resonance with the excitonic transition energy. By doing this, one makes it possible to achieve a strong exciton-photon coupling regime. In the language of quantum mechanics, this leads to the emergence of a hybrid quasiparticle, called exciton-polariton (or polariton for brevity). In this regime, the spectrum of the system gets modified (the anticrossing appears) as shown in Fig. 1.14, which manifests itself in photoluminescence experiments. An analogous process takes place in classical mechanics when one considers the behavior of two coupled oscillators: if the modes of the oscillators coincide (or close to each other) then the normal modes of the joint system are different ("repel" each other) by the quantity which is proportional to the coupling strength.

We proceed with giving the overview of the quantum theory for exciton-polaritons, where we neglect spins for brevity. The second-quantized Hamiltonian of a semiconductor reads

$$\hat{H} = \int \hat{\Psi}(\mathbf{r})^\dagger \left(-\frac{\hbar^2}{2m}\nabla^2 + V(\mathbf{r}) \right) \hat{\Psi}(\mathbf{r}) d\mathbf{r} \tag{1.145}$$

$$+ \frac{1}{2} \iint \hat{\Psi}(\mathbf{r})^\dagger \hat{\Psi}\left(\mathbf{r}'\right)^\dagger \frac{e^2}{4\pi\varepsilon_0 |\mathbf{r} - \mathbf{r}'|} \hat{\Psi}\left(\mathbf{r}'\right) \hat{\Psi}(\mathbf{r}) d^2\mathbf{r} d^2\mathbf{r}' \tag{1.146}$$

where $\hat{\Psi}(\mathbf{r})$ is the electron annihilation field operator and $V(\mathbf{r})$ is the periodic lattice potential. We restict our consideration by only two bands, labeled below as $i = c$ (conduction) and $i = v$ (valence). The operator $\hat{\Psi}$ can be expanded in terms of single-particle wavefunctions $\varphi_{i,\mathbf{k}}(\mathbf{r}) = S^{-1/2} e^{i\mathbf{k}\mathbf{r}} u_{i,\mathbf{k}}(\mathbf{r})$, labelled by momentum k and by the band index $i = c, v$:

$$\hat{\Psi}(\mathbf{r}) = \sum_{i \in \{c,v\}} \sum_{\mathbf{k}} \varphi_{i,\mathbf{k}}(\mathbf{r}) \hat{c}_{i,\mathbf{k}} \tag{1.147}$$

After applying Bloch's theorem and switching to the momentum space, one may intro-

duce hole annihilation operators $\hat{h}_{\mathbf{k}} = \hat{c}^{\dagger}_{v,-\mathbf{k}}$ (spin is also reversed if present). Then, in the low-density limit, one may perform the bosonization procedure by rewriting (with several assumptions) the initial Hamiltonian in terms of the exciton creation operators,

$$\hat{X}^{\dagger}_{\nu,\mathbf{k}} \equiv \sum_{\mathbf{k}_1,\mathbf{k}_2} \langle \mathbf{k}_2, \mathbf{k}_1 | \nu, \mathbf{k} \rangle \, \hat{c}^{\dagger}_{\mathbf{k}_1} \hat{h}^{\dagger}_{\mathbf{k}_2} = \sum_{\mathbf{p}} \varphi_{\nu}(\mathbf{p}) \hat{c}^{\dagger}_{\mathbf{k}/2+\mathbf{p}} \hat{h}^{\dagger}_{\mathbf{k}/2-\mathbf{p}} \tag{1.148}$$

with

$$\langle \mathbf{k}_2, \mathbf{k}_1 | \nu, \mathbf{k} \rangle = \langle \underbrace{\frac{\mathbf{k}_1 - \mathbf{k}_2}{2}}_{\text{rel. momentum}} | \nu \rangle \langle \underbrace{\mathbf{k}_1 + \mathbf{k}_2}_{\text{C.M. momentum}} | \mathbf{k} \rangle =$$

$$\langle \frac{\mathbf{k}_1 - \mathbf{k}_2}{2} | \nu \rangle \delta_{\mathbf{k},\mathbf{k}_1+\mathbf{k}_2} \equiv \varphi_{\nu}(\frac{\mathbf{k}_1 - \mathbf{k}_2}{2}) \delta_{\mathbf{k},\mathbf{k}_1+\mathbf{k}_2}, \tag{1.149}$$

where $\varphi_{\nu}(\mathbf{p}) = \langle \mathbf{p} | \nu \rangle$ is the exciton wave function, written in the momentum space, and $\hat{c}_{\mathbf{k}} \equiv \hat{c}_{c,\mathbf{k}}$. The exciton moves as a whole with momentum $\hbar\mathbf{k}$, carrying energy $E_{\nu}(\mathbf{k})$, here ν is the quantum number, describing the internal exciton state. The reversed transformation is given by $\hat{c}^{\dagger}_{\mathbf{k}_1} \hat{h}^{\dagger}_{\mathbf{k}_2} = \sum_{\nu,\mathbf{k}} \langle \nu, \mathbf{k} | \mathbf{k}_2, \mathbf{k}_1 \rangle \, \hat{X}^{\dagger}_{\nu,\mathbf{k}}$. We note, that for the sake of simplicity the formulas above were written with the assumption that the electron and the hole have the same effective mass, allowing us to write the relative momentum as $(\mathbf{k}_1 - \mathbf{k}_2)/2$. In general, the relative momentum of a two-body system is given by $(m_2\mathbf{k}_1 - m_1\mathbf{k}_2)/(m_1 + m_2)$, however, this simplification doesn't affect any of the results, presented in this section. Thus, using the bosonization procedure, one may extract the exciton Hamiltonian:

$$\hat{H}_X = \sum_{\nu,\mathbf{k}} E^{\nu}_X(\mathbf{k}) \hat{X}^{\dagger}_{\nu,\mathbf{k}} \hat{X}_{\nu,\mathbf{k}}. \tag{1.150}$$

This Hamiltonian is quadratic, however, it only looks simple, because actually excitons are not true bosons, which can be seen direct calculation of the commutator of their creation/annihilation operators:

$$\left[\hat{X}_{\nu,\mathbf{k}}, \hat{X}^{\dagger}_{\mu,\mathbf{q}} \right] = \delta_{\nu,\mu} \delta_{\mathbf{k},\mathbf{q}} - \hat{D}_{\nu,\mu,\mathbf{k},\mathbf{q}}, \tag{1.151}$$

where an operator $\hat{D}_{\nu,\mu,\mathbf{k},\mathbf{q}}$ describes the deviation from bosonicity due to the composite nature of excitons. For example, $\hat{D}_{\nu,\nu,\mathbf{0},\mathbf{0}} = \sum_{\mathbf{p}} |\varphi_{\nu}(\mathbf{p})|^2 \left(\hat{c}^{\dagger}_{\mathbf{p}} \hat{c}_{\mathbf{p}} + \hat{h}^{\dagger}_{\mathbf{p}} \hat{h}_{\mathbf{p}} \right)$. Fortunately, at low densities we have $\langle \left[\hat{X}_{\nu,\mathbf{0}}, \hat{X}^{\dagger}_{\nu,\mathbf{0}} \right] \rangle = 1 - \mathcal{O}\left(n_X a_{\mathrm{B}}^2 \right)$, where n_X is the density of excitons. Thus, excitons can be treated as bosons when the condition $n_X a_{\mathrm{B}}^2 \ll 1$ is fulfilled, as was discussed in the previous sections.

Now let us switch to the description of exciton-photon interaction. In the dipole approximation, the dipole moment of the electron-hole pair couples to the light field, described by the electric field operator $\hat{\mathbf{E}}$, which results in the following interaction

term in the full many-body Hamiltonian

$$\hat{H}_{CX\ \mathrm{int}} = \int \hat{\Psi}^{\dagger}(\mathbf{r})[-e\mathbf{r}\cdot\hat{\mathbf{E}}(\mathbf{r})]\hat{\Psi}(\mathbf{r})d\mathbf{r} \tag{1.152}$$

Applying the bosonization procedure, outlined above, and using the rotating wave approximation together with the assumption that only 1s-excitons are relevant for the processes we consider, we arrive at the following Hamiltonian, describing the exciton-photon interaction

$$\begin{aligned}&\hat{H}_{CX} = \hat{H}_C + \hat{H}_X + \hat{H}_{CX\ \mathrm{int}} \approx \\ &\sum_{\mathbf{k}} E_C(\mathbf{k})\hat{C}^{\dagger}_{\mathbf{k}}\hat{C}_{\mathbf{k}} + \sum_{\mathbf{k}} E_X(\mathbf{k})\hat{X}^{\dagger}_{\mathbf{k}}\hat{X}_{\mathbf{k}} + \sum_{\mathbf{k}} \hbar g(\mathbf{k})\left(\hat{C}^{\dagger}_{\mathbf{k}}\hat{X}_{\mathbf{k}} + \hat{X}^{\dagger}_{\mathbf{k}}\hat{C}_{\mathbf{k}}\right)\end{aligned} \tag{1.153}$$

with $\hbar g(\mathbf{k}) = d_{cv}(\mathbf{k})\varphi_{1s}(0)\sqrt{E_C(\mathbf{k})/\left(2\epsilon_0\epsilon L\right)}$, and $d_{cv}(\mathbf{k})$ being the dipole matrix element for the transition between the valence and conduction bands states, labeled by $\mathbf{k}$, $\hat{C}_{\mathbf{k}}$ is the cavity photon annihilation operator. We note, that the coupling constant $\hbar g(\mathbf{k})$ may be regarded as constant in the regime under consideration. The Hamiltonian (1.153) can be diagonalized, using the Bogoliubov canonical transformation

$$\hat{a}^{\mathrm{L}}_{\mathrm{k}} \equiv \mathcal{X}_{\mathrm{k}}\hat{X}_{\mathrm{k}} - \mathcal{C}_{\mathrm{k}}\hat{C}_{\mathrm{k}} \tag{1.154}$$

$$\hat{a}^{\mathrm{U}}_{\mathrm{k}} \equiv \mathcal{C}_{\mathrm{k}}\hat{X}_{\mathrm{k}} + \mathcal{X}_{\mathrm{k}}\hat{C}_{\mathrm{k}} \tag{1.155}$$

where the so-called Hopfield coefficients $\mathcal{C}_{\mathrm{k}}$ and $\mathcal{X}_{\mathrm{k}}$ satisfy $|\mathcal{C}_{\mathrm{k}}|^2 + |\mathcal{X}_{\mathrm{k}}|^2 = 1$, so that the new operators $\hat{a}^{\mathrm{L,U}}_{\mathbf{k}}$ operators follow the bosonic commutation relations as well. After the transformation, the Hamiltonian(1.153) reduces to quadratic form:

$$\hat{H}_{CX} = \sum_{\mathbf{k}} E_{\mathrm{U}}(\mathbf{k})\hat{a}^{\mathrm{U}\dagger}_{\mathbf{k}}\hat{a}^{\mathrm{U}}_{\mathbf{k}} + \sum_{\mathbf{k}} E_{\mathrm{L}}(\mathbf{k})\hat{a}^{\mathrm{L}\dagger}_{\mathbf{k}}\hat{a}^{\mathrm{L}}_{\mathbf{k}}, \tag{1.156}$$

with annihilation operators a^{U} and a^{L} that are responsible for the excitations of upper and lower-polariton branches, respectively. The spectrum of the resulting Hamiltonian consist of two abovementioned branches, and is

$$E_{\mathrm{U(L)}}(\mathbf{k}) = \frac{1}{2}\left(E_X(\mathbf{k}) + E_C(\mathbf{k})\right) \pm \sqrt{\hbar^2 g(\mathbf{k})^2 + \left(\Delta_{\mathbf{k}}/2\right)^2}, \tag{1.157}$$

where E_C is the cavity mode dispersion and E_X is the exciton dispersion, usually approximated by a parabola with a large effective mass. The detuning Δ_{k} between the cavity mode and excitonic transition energy is defined as

$$\Delta_{\mathbf{k}} \equiv E_C(\mathbf{k}) - E_X(\mathbf{k}). \tag{1.158}$$

The squares of the Hopfield coefficients correspond to the photon/exciton fraction of the polariton and their analytical form is presented below:

$$|\mathcal{C}_{\mathbf{k}}|^2 = \frac{E_{\mathrm{U}}(\mathbf{k})E_X(\mathbf{k}) - E_{\mathrm{L}}(\mathbf{k})E_C(\mathbf{k})}{\left(E_C(\mathbf{k}) + E_X(\mathbf{k})\right)\sqrt{\Delta^2_{\mathbf{k}} + 4\hbar^2 g(\mathbf{k})^2}} \tag{1.159}$$

$$|\mathcal{X}_{\mathbf{k}}|^2 = \frac{E_{\mathrm{U}}(\mathbf{k})E_C(\mathbf{k}) - E_{\mathrm{L}}(\mathbf{k})E_X(\mathbf{k})}{\left(E_C(\mathbf{k}) + E_X(\mathbf{k})\right)\sqrt{\Delta^2_{\mathbf{k}} + 4\hbar^2 g(\mathbf{k})^2}} \tag{1.160}$$

In order to account for finite lifetimes of excitons and photons one should supply

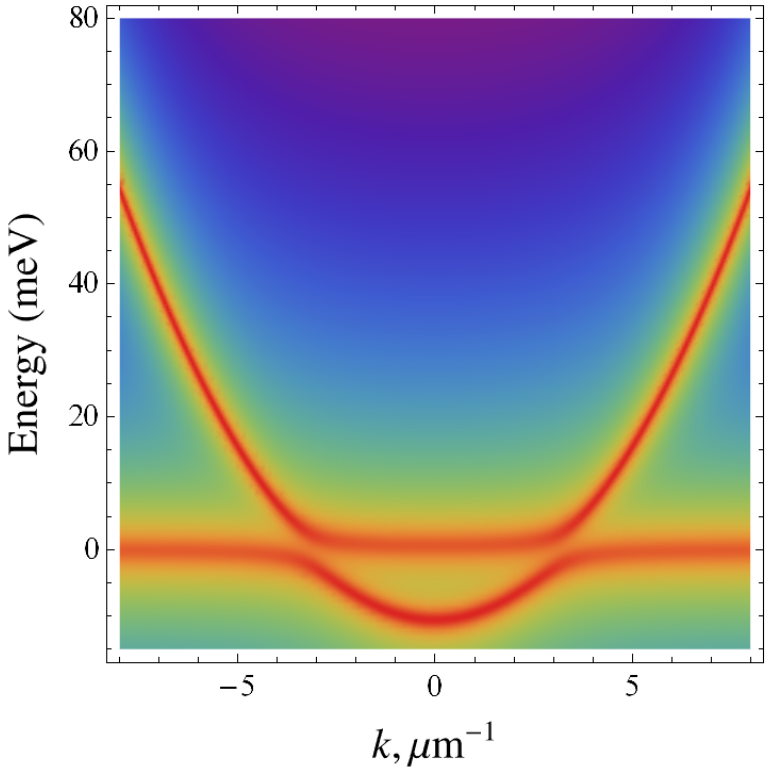

Figure 1.14: The dispersion (the spectral function) of upper and lower polariton branches plotted for the detuning value $\Delta_{\mathbf{k}} = 10$ meV. The interaction constant is set to $2g(\mathbf{k}) = 10$ meV. The thickness of the lines is determined by the broadenings $\gamma_{C,X}$.

the corresponding dispersion relations by additional imaginary terms $-i\gamma_{X,C}$, respectively. In this case, the polariton spectrum becomes complex, and its real part yields the dispersion of polariton modes, while the imaginary part describes the spectral broadenings with a Lorentzian shape. In this case, the Rabi frequency, i.e. the distance between the real parts of the polariton branches at in the point of avoided crossing, is equal to

$$\hbar\Omega_R = \begin{cases} \sqrt{4g(\mathbf{k})^2 - (\gamma_X - \gamma_C)^2}, & 4g(\mathbf{k})^2 > (\gamma_X - \gamma_C)^2 \\ 0, & 4g(\mathbf{k})^2 < (\gamma_X - \gamma_C)^2 \end{cases} \tag{1.161}$$

Thus, the strong coupling regime appears when (a) the difference between exciton and photon damping rates is lower than the coupling strength and (b) when the Rabi frequency is greater than the sum of the broadenings $\hbar\Omega_R > \gamma_X + \gamma_C$ (i.e. the spectral

lines at the anticrossing point are well-resolved). The polariton spectral function, accounting for the losses is shown in Fig. 1.14.

Planar microcavities with embedded quantum wells operating in strong coupling regimes recommended themselves as a platform for experimental testing of various collective quantum phenomena. At the same time, the microcavities are used for novel generation optoelectronic devices [20]. Also, as we discuss in the next section, the bosonic nature of exciton-polaritons paves the way to Bose-Einstein condensation of polaritons [243, 271] and superfluidity [21, 22]. Indeed, provided the extremely small polariton mass and strong interparticle interactions, stemming from the excitonic fraction results in the possibility for the particles to condense in the ground state at moderate temperatures. Moreover, the wide gap semiconductor materials such as GaN allowed achieving the condensation even at room temperature, where the polariton lasing was observed [25, 85].

1.5.3 Pseudospin of exciton-polaritons

An exciton is a bound state of an electron and a hole, i.e., of two fermions. If the electron is taken from the conduction band formed by s-electrons, then its projection of total angular momentum on an arbitrary axis (say, the z-axis) is equal to $J_z^e = \pm 1/2$. Correspondingly, the hole in the valence band formed by p-electrons has a projection of total angular momentum equal to $J_z^h = \pm 1/2, \pm 3/2$, where the states with $J_z^h = \pm 1/2$ correspond to the light hole-branch, and $J_z^h = \pm 3/2$ to the heavy-hole branch. Here we do not account for various splitting that naturally presents in quantum wells, such as the splitting caused by the features of the crystal structure for the sake of simplicity. As we discussed previously, in the bulk samples the light and heavy hole branches are degenerate at Γ-point. However, due to the difference in their effective masses the degeneracy is lifted in the quantum wells due to quantum confinement. The top of the heavy-hole branch at $\mathbf{k} = 0$ is closer to the bottom of the conduction band the top of the light-hole branch, therefore, the total angular momentum of a 2D exciton J_z^{ex} has four possible projections: ± 1, ± 2. We note, that the presence of electron-hole exchange interaction, which we ignored in our considerations, may split the states $J_z^{\text{ex}} = \pm 1$ and $J_z^{\text{ex}} = \pm 2$.

Now, let us discuss the influence of angular momentum on the exciton-exciton interactions. As we described previously, the exciton-exciton interaction mainly stems from the Coulomb exchange terms, which dominates over the direct interaction terms. The direct interaction is angular-momentum-independent, while the exchange one is sensitive to the angular momentum orientation of the excitons. To understand this sensitivity, let us consider two interacting bright excitons. For excitons with the same angular momentum projection, $J_{1z}^{\text{ex}} = J_{2z}^{\text{ex}}$, the exchange of electrons or holes between the excitons leaves the individual angular momenta unaltered. If the angular momentum projections of the excitons are opposite $J_{1z}^{\text{ex}} = -J_{2z}^{\text{ex}}$, then the exchange of

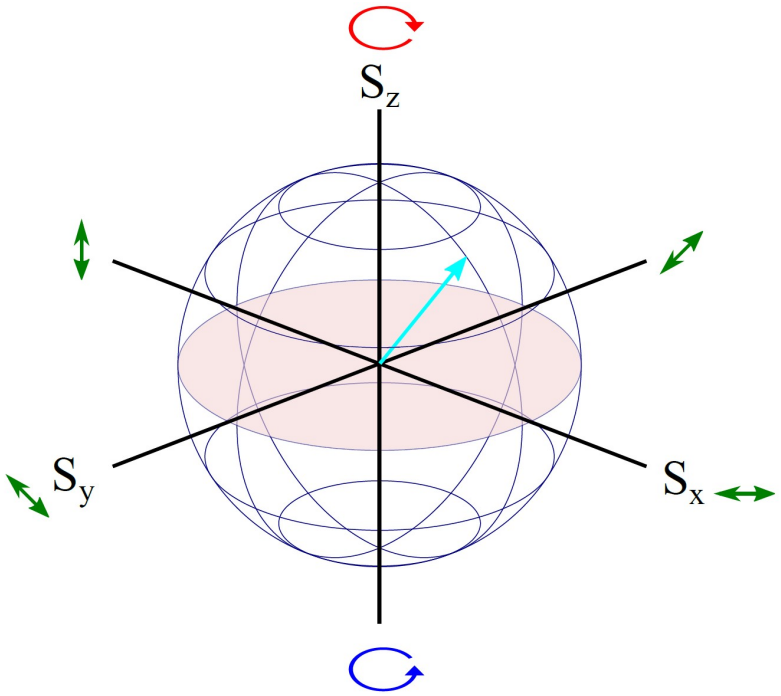

Figure 1.15: The Bloch sphere showing the relation between the vector $\mathbf{s_k}$ *and the polarization of the light.*

electrons or holes turns the bright excitons into a pair of dark excitons ($J_{1z}^{\mathrm{ex}} = \pm 2$, $J_{2z}^{\mathrm{ex}} = \pm 2$).

A photon is a spin-1 particle (boson), thus its spin projection on the direction of propagation may take only two values $J_z^{\mathrm{ph}} = \pm 1$, corresponding to the two circular polarizations, left and right. Thus, the process of single-photon creation of excitons with $J_z^{\mathrm{ex}} = \pm 2$ is prohibited by the conservation of the total angular momentum. Due to this reason, the states exciton $J_z^{\mathrm{ex}} = \pm 2$ are referred to as *dark*, opposite to the states $J_z^{\mathrm{ex}} = \pm 1$ that are called *bright*. In the regime of strong light-matter coupling in microcavities, bright exciton states form exciton-polaritons and their energy becomes detuned from the exciton states by the value of the Rabi splitting, which significantly reduces the efficiency of transitions between bright and dark states. Thus, the angular momentum part of the exciton-polariton wave function (will be referred to as pseudospin) can be effectively treated as a two-level system.

The polarization dynamics of a polaritonic system are closely related to the polariton pseudospin. Since pseudospin can take only two values, it is convenient to introduce a 2 by 2 polariton density matrix in the momentum space, which can be written in

terms of the three Pauli matrices σ_j and an identity 2 by 2 matrix $\mathbf{I}$:

$$\rho_{\mathbf{k}} = \frac{n_{\mathbf{k}}}{2}\mathbf{I} + \sum_{i=x,y,z} s_{i\mathbf{k}}\sigma_i, \tag{1.162}$$

where the vector $\mathbf{s_k}$ shows the directions of the pseudospin of polaritons, having wavevector $\mathbf{k}$ and $n_{\mathbf{k}}$ is the occupation number of the corresponding mode. This density matrix may be used to calculate the Stokes parameters of the light emitted by the polaritons. It is convenient to depict the vector $\mathbf{s_k}$ on the so-called Bloch sphere as shown in Fig. 1.15. If the length of the vector $\mathbf{s_k}$ equals $n_{\mathbf{k}}/2$ then the vector is on the Bloch sphere and the light is completely polarized. The opposite limit $|\mathbf{s_k}| = 0$ corresponds to unpolarized light.

1.6 Bose-Einstein condensation and dynamics of bosonic quasi-particles

In the previous sections we discussed the physics of excitons and exciton-polaritons, which are bosonic quasi-particles, and thus one may wonder if they are able to form a Bose-Einstein condensate. This section is aimed to properly address this question. The results presented in this section are relevant for *Chapters* 3, 4, and 6 of the current thesis.

1.6.1 Condensation in 3D

Bosons are particles with integer spin. For a given temperature T obey Bose-Einstein statistics, which has the following form in case of a non-interacting boson gas with parabolic dispersion $\epsilon_{\mathbf{k}} = \hbar^2 k^2/(2m)$

$$n_{\mathbf{k}}(\mu, T) = \frac{1}{\exp\beta\left(\epsilon_{\mathbf{k}} - \mu\right) - 1} \tag{1.163}$$

where $n_{\mathbf{k}}$ denotes the occupation number of a given state with energy ϵ_i. The factor $\beta = 1/k_B T$. The chemical potential is found from the normalization condition which fixes the average total number of particles

$$N = \sum_{\mathbf{k}} n_{\mathbf{k}}(\mu, T). \tag{1.164}$$

After taking the thermodynamic limit by dividing both parts by volume $V = L^3$ and sending V and N to infinity, while keeping the concentration $n = N/V$ constant, we get

$$n\lambda^3 = g_{3/2}(z) \tag{1.165}$$

where $\lambda = h/\sqrt{2\pi m k_B T}$ is the thermal de Broglie wavelength and $z = \exp(\beta\mu)$ is fugacity. We replaced the summation in the RHS of Eq. (1.164) by integration as

$$\frac{1}{V}\sum_{\mathbf{k}} \to \int \frac{d^n k}{(2\pi)^n} \tag{1.166}$$

In the RHS of Eq. (1.165), we have the Bose function

$$g_s(z) = \sum_{l=1}^{\infty} \frac{z^l}{l^s} \tag{1.167}$$

This series converges for $z \leq 1$ and is bounded from above by $g_{3/2}(z = 1)$

$$g_{3/2}(1) = \sum_{l=1}^{\infty} \frac{1}{l^{3/2}} = \zeta(3/2) = 2.61237\ldots, \tag{1.168}$$

where $\zeta(z)$ is the Riemann zeta function. The equation (1.165) has a solution if

$$n\lambda^3 \leq \zeta(3/2) \tag{1.169}$$

However, it is clear that either by sufficiently increasing n or by sufficiently decreasing T one may violate this inequality. This happens because we have to consider the state $\mathbf{k} = 0$ separately. We make a step back in our derivation, before we have taken the thermodynamic limit, and rewrite the whole sum (integral), isolating the state $\mathbf{k}$ from all the other states $k > 0$:

$$\begin{aligned} \frac{N}{V} &= \frac{1}{V}\frac{z}{1-z} + \frac{1}{V}\sum_{|\mathbf{k}|>0} \frac{1}{z^{-1}\exp\left(\beta\frac{\hbar^2 k^2}{2m}\right) - 1} \approx \\ &\frac{1}{V}\frac{z}{1-z} + \int \frac{d^3\mathbf{k}}{(2\pi)^3} \frac{1}{z^{-1}\exp\left(\beta\frac{\hbar^2 k^2}{2m}\right) - 1} \end{aligned} \tag{1.170}$$

We see, that if $z = 1$ then in the limit $V \to \infty$ the first term of the equation above, representing the condensate density $n_{\mathbf{k}=\mathbf{0}}/V$ in the ground state, does not vanish, contrary to the case $z \neq 1$ when it is equal to zero. After passing this critical point, the value of z remains unchanged (equal to one). Substituting $z = 1$ in Eq. (1.165) we get the critical temperature T_c of Bose-Einstein condensation (BEC) at a given density n:

$$k_B T_c = \frac{2\pi\hbar^2}{m}\left(\frac{n}{\zeta(3/2)}\right)^{2/3} \approx 3.31\frac{\hbar^2 n^{2/3}}{m} \tag{1.171}$$

Thus, for a 3D Bose gas the condensation occurs if we sufficiently lower the temperature. Alternatively, the onset of condensation may be achieved by increasing the particle density at given temperature above the critical value n_c:

$$n_c = \zeta(3/2)\left(\frac{m k_B T}{2\pi\hbar^2}\right)^{2/3} \tag{1.172}$$

1.6.2 Condensation in 2D

When we consider a Bose gas in two spatial dimensions, the situation drastically changes. To see this, let us rewrite Eq. (1.170) in 2D:

$$\frac{N}{L^2} = \frac{1}{L^2}\frac{z}{1-z} + \frac{1}{L^2}\sum_{|\mathbf{k}|>0}\frac{1}{z^{-1}\exp\left(\beta\frac{\hbar^2k^2}{2m}\right)-1} \approx \frac{1}{L^2}\frac{z}{1-z} + \int\frac{d^2\mathbf{k}}{(2\pi)^2}\frac{1}{z^{-1}\exp\left(\beta\frac{\hbar^2k^2}{2m}\right)-1}. \tag{1.173}$$

Now let us calculate the total concentration of particles with $k > 0$ in the thermodynamic limit:

$$n_{\mathbf{k}>0} = \int\frac{d^2\mathbf{k}}{(2\pi)^2}\frac{1}{z^{-1}\exp\left(\beta\frac{\hbar^2k^2}{2m}\right)-1} = -\frac{m\ln(1-z)}{2\pi\beta\hbar^2}. \tag{1.174}$$

We see that the amount of particles that can be accommodated in the states $k > 0$ is not restricted from above is contrary to the 3D case. Thus the Bose-Einstein condensation does not take place in two dimensions in the thermodynamic limit. This

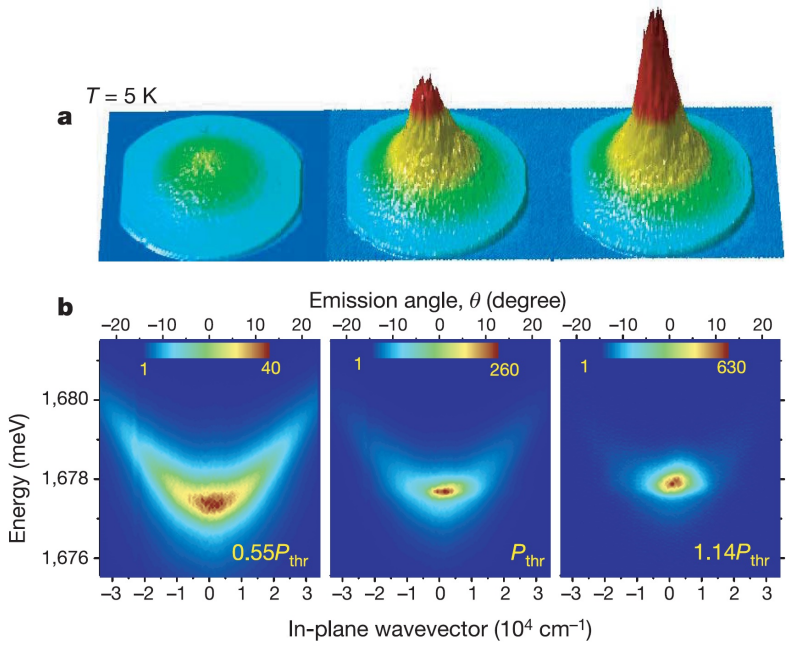

Figure 1.16: Far field emission profiles of an incoherently pumped planar microcavity, which show the formation of a macroscopically occupied coherent state, from [243].

is the consequence of a "no-go" theorem by Mermin, Wagner, Bogoliubov, Berezinskii,

and Hohenberg. It forbids continuous symmetry to become spontaneously broken at finite temperature in systems with sufficiently short-range interactions if the number of dimensions is less than three. The spontaneous symmetry breaking manifests itself in the appearance of the order parameter – i.e. some physical observable which is becomes non-zero after the phase transition takes place. Bose-Einstein condensation in 3D has most of the properties of a second-order phase transition. The Hamiltonian of a non-interacting (or weakly interacting) Bose gas has $U(1)$ symmetry, which implies that if the ground state has the same symmetry as the Hamiltonian, then the average occupancy in the ground state must be zero. However, as we have seen above after the onset of condensation, the ground state becomes populated. It means, that the $U(1)$ symmetry gets spontaneously broken, but this only takes place in 3D. Does it mean, that it is impossible to observe BEC in 2D? Let us take a look at it.

It turns out that the absence of spontaneous symmetry breaking for a bunch of non-interacting bosons can be circumvented by introducing a confinement potential of a special form [51]. Let us we consider a two-dimensional Bose gas confined by a generic power-law potential $U(x,y) = U_1(x/b)^{\eta_1} + U_2(y/c)^{\eta_2}$. Since the Hamilton is not translation-invariant, a wavevector is no longer a good quantum number. For these potentials, the energy level spacing is such that $k_B T \gg \epsilon_{i+1} - \epsilon_i$, the variable i numbers the eigenstates. Therefore, the system can be effectively described by a continuum of states, however, the discrete ground state must be explicitly retained. For simplicity we will focus on the isotropic shape of the potential: $U(r) = U_0(r/a)^{\eta}$.

In this case a 2D system with $U(r) = U_0(r/a)^{\eta}$ the generalized density of states, calculated in the semiclassical approximation, where it is assumed that each region $d^2\mathbf{r}d^2\mathbf{p}$ of the phase space contains $d^2\mathbf{r}d^2\mathbf{p}/h^2$ states, is given by

$$\rho(\epsilon) = \frac{d(\#\text{ of states with energy} \leq \epsilon)}{d\epsilon} = \frac{d}{d\epsilon}\int_{S^*(\epsilon)}\int_{\mathbf{p}\in\{\mathbf{p}:\epsilon\geq\mathbf{p}^2/(2m)+U(r)\}}\frac{d^2\mathbf{r}d^2\mathbf{p}}{h^2} =$$
$$\frac{m}{2\pi\hbar^2}\int_{S^*(\epsilon)} d^2\mathbf{r} = \frac{2\pi m}{h^2}\int_0^{r^*(\epsilon)} 2\pi r dr = \frac{2\pi^2 m a^2}{h^2}\left(\frac{\epsilon}{U_0}\right)^{2/\eta}, \tag{1.175}$$

where $r^*(\epsilon)/a = (\epsilon/U_0)^{1/\eta}$ and $S^*(\epsilon) = \pi r^*(\epsilon)^2$ is the available area for particles with energy $\leq \epsilon$. We note, that in the absence of a trapping potential the semiclassical calculation above restores the correct answer $m/(2\pi\hbar^2)L^2$ for the 2D density of states of free bosons with a parabolic dispersion in a square box (here L is the system size).

Consequently, the total number of particles can be expressed as

$$N = N_0 + \int_0^{\infty} n(\epsilon,\mu,T)\rho(\varepsilon)d\varepsilon =$$
$$N_0 + \frac{2\pi^2 m a^2}{h^2\,(U_0)^{2/\eta}}(k_B T)^{2/\eta+1}\Gamma(2/\eta+1)g_{2/\eta+1}\left(\exp\frac{\mu}{k_B T}\right), \tag{1.176}$$

here N_0 is the occupation of the ground state, $n(\epsilon,\mu,T) = (\exp\beta\,(\epsilon-\mu)-1)^{-1}$, and

the integral representation of the Bose function $g_s(z)$ (or $\mathrm{PolyLog}_s(z)$) is given by

$$g_s(z) = \frac{1}{\Gamma(s)} \int_0^\infty \frac{y^{s-1}}{e^y/z - 1} dy. \tag{1.177}$$

For $\mu = 0$, we obtain

$$\Gamma(2/\eta + 1) g_{2/\eta+1}(1) = \Gamma(2/\eta + 1)\zeta(2/\eta + 1), \tag{1.178}$$

which remains finite for all positive values of η. Therefore, in an ideal two-dimensional gas confined by a power-law trap, BEC always occurs at finite temperature. It is instructive to notice that in case of a rigid box which corresponds to $\eta \to \infty$ the quantity $g_1(1)$ diverges, and BEC does not occur, in agreement with the no-go theorem. If the system of non-interacting particles is subjected to a non-isotropic 2D potential, the requirement for BEC to occur at finite temperature is that $\eta_1^{-1} + \eta_2^{-1} < \infty$. By setting $N_0 = 0$ and $\mu = 0$ we immediately find the critical temperature in 2D trap from the equation above:

$$k_B T_c^{\mathrm{2D}} = \left(\frac{N h^2 U_0^{2/\eta}}{2\pi^2 m a^2 \Gamma(2/\eta + 1)\zeta(2/\eta + 1)} \right)^{\eta/(2+\eta)}. \tag{1.179}$$

Since in real systems one must have some trap in order to confine the bosons to form a (quasi-)2D system, it implies that BEC may occur at finite temperature despite the Mermin–Wagner–Bogoliubov-Berezinskii-Hohenberg theorem, which prohibits spontaneous breaking of continuous symmetries in systems with sufficiently short-range interactions in dimensions $d \leq 2$. However, the form of the trap significantly affects the value of the critical temperature.

In 2006, Bose-Einstein condensation of exciton-polaritons was achieved at the temperature of 20K [243], which highly exceeds the critical temperature for cold-atom condensates. They demonstrated a large occupation of the lowest momentum state after passing the threshold, see Fig. 1.16.

However, we have to comment on the difference between the conventional cold atom BEC and polariton BEC. Polaritons have a finite lifetime and thus in order to achieve the stationary state one has to facilitate an external pump to compensate for the radiative decay of the particles.

1.6.3 Gross-Pitaevskii equation

We know that at low temperatures the system experiences a phase transition (BEC) and a macroscopic fraction of particles gets accumulated in the ground state, even though, strictly speaking, the critical temperature $T_c = 0$ in 1D or 2D, see details

in the previous sections. The phase transition is accompanied by the $U(1)$ symmetry breaking which can be understood with the help of a symmetry-breaking field as shown in [45, 46]. The basic idea can be demonstrated as follows, we start with many-body Hamiltonian describing a set of interacting bosons without internal degrees of freedom

$$\hat{H} = \int d^2r\hat{\psi}^\dagger(\mathbf{r})(\frac{-\hbar^2}{2m})\Delta\hat{\psi}(\mathbf{r}) + \frac{1}{2}\iint d^2rd^2r'\hat{\psi}^\dagger(\mathbf{r})\hat{\psi}^\dagger(\mathbf{r}')\hat{V}(\mathbf{r},\mathbf{r}')\hat{\psi}(\mathbf{r}')\hat{\psi}(\mathbf{r}), \quad (1.180)$$

where as usual

$$\hat{\psi}(\mathbf{r}) = \sum_{\mathbf{k}} \psi_{\mathbf{k}}(\mathbf{r})\hat{a}_{\mathbf{k}}, \quad (1.181)$$

and

$$\left[\hat{\psi}(\mathbf{r}), \hat{\psi}^\dagger(\mathbf{r}')\right] = \delta(\mathbf{r}-\mathbf{r}'). \quad (1.182)$$

The low energy scattering properties of a realistic interaction potential can be reproduced by an effective contact repulsive potential $\hat{V}(\mathbf{r},\mathbf{r}') = \alpha\delta(\mathbf{r}-\mathbf{r}')$ if the corresponding macroscopic wavefunction (will be introduced below) varies slowly on the distances of the order of the range of the realistic interaction potential. The chemical potential is set to zero. If one adds a symmetry breaking of the form $-\nu\sqrt{V}\left(e^{-i\phi}\hat{a}_0 + e^{i\phi}\hat{a}_0^\dagger\right)$, where V is the volume (area) of the system, then the following statement holds [45, 46]

$$\lim_{\nu\to 0}\lim_{V\to\infty}\frac{1}{\sqrt{V}}\langle\hat{a}_0\rangle \neq 0, \quad (1.183)$$

which shows that the ground state spontaneously breaks the $U(1)$ symmetry and the ground state occurs a non-zero expectation value of the operator $\hat{a}_0$, which hints us that the ground state is a coherent state. Let's now use the following trial many-body state that is parameterized by a complex-valued "macroscopic wave function" $\phi(\mathbf{r})$:

$$\hat{D}(\hat{\psi},\phi) = e^{\int d^2r\left[\phi(\mathbf{r})\hat{\psi}^\dagger(\mathbf{r}) - \phi^*(\mathbf{r})\hat{\psi}(\mathbf{r})\right]} \quad (1.184)$$

$$|\phi\rangle = \hat{D}|0\rangle \quad (1.185)$$

where $|0\rangle$ is the vacuum state. *This is equivalent to demanding that each mode in the reciprocal space is in the coherent state.* For this trial wave function, the following relation holds

$$\hat{\psi}(\mathbf{r})|\phi\rangle = \phi(\mathbf{r})|\phi\rangle. \quad (1.186)$$

We note that this ansatz for the many-body state cannot describe all correlations present in the true ground state, it captures the leading term in the energy for dilute systems. Using this state as an initial state of the system we write down the Heisenberg equation of motion for the field operator $\hat{\psi}(\mathbf{r},t)$:

$$\mathrm{i}\partial_t\phi(\mathbf{r},t) = -\frac{\hbar^2}{2m}\Delta\phi(\mathbf{r},t) + \alpha|\phi(\mathbf{r},t)|^2\phi(\mathbf{r},t) \quad (1.187)$$

which is called the Gross-Pitaevskii equation and is suitable for describing the propagation of coherent polariton wave packets in microcavities.

Now we recall that actually polaritons possess an internal degree of freedom – pseudospin and thus the macroscopic wavefunction has two components. In real space, it has the following form in the basis of circularly polarized states

$$\Phi(\mathbf{r}) = \begin{pmatrix} \phi_\uparrow(\mathbf{r}) \\ \phi_\downarrow(\mathbf{r}) \end{pmatrix}. \tag{1.188}$$

This wavefunction allows to calculate the Stokes parameters:

$$n(\mathbf{r}) = |\phi_\uparrow(\mathbf{r})|^2 + |\phi_\downarrow(\mathbf{r})|^2, \tag{1.189}$$

$$s_x(\mathbf{r}) = \mathrm{Re}\left[\phi_\downarrow^*(\mathbf{r})\phi_\uparrow(\mathbf{r})\right], \tag{1.190}$$

$$s_y(\mathbf{r}) = \mathrm{Im}\left[\phi_\downarrow^*(\mathbf{r})\phi_\uparrow(\mathbf{r})\right], \tag{1.191}$$

$$s_z(\mathbf{r}) = \frac{1}{2}\left[|\phi_\uparrow(\mathbf{r})|^2 - |\phi_\downarrow(\mathbf{r})|^2\right], \tag{1.192}$$

and how they vary in space and time.

Now let us discuss the spin anisotropy of the polariton interaction. Polaritons interact due to their excitonic component. As we have shown previously the interaction of excitons is dominated by the exchange interaction and the direct interaction can be disregarded. In the case of two bright polaritons with the same pseudospin projection, the exchange interaction leaves them bright. On the contrary, for two bright excitons with opposite pseudospin projections the exchange interaction turns them into a pair of dark excitons. The later process is suppressed for polaritons as compared to the former. This leads to a spin anisotropy of the interaction, i.e. the absolute value of the interaction strength α_1 of the excitons with the same pseudospin projections are typically much larger than the interaction strength α_2 of excitons with opposite pseudospin projections [43], which is negative ($\alpha_2 < 0$).

1.6.4 Semiclassical Boltzmann equation

The opposite regime to the one, considered in the previous section where we introduced the Gross-Pitaevskii equation, corresponds to relatively high temperatures. This regime ignores any coherent processes occurring in the system and is governed by the rate equations (Semiclassical Boltzmann equations) for the occupation numbers $n_{\mathbf{k}}$. The corresponding rate equations are obtained from the Lindblad equation for the density matrix. This approach is sketched below. We start the Liouville-von Neumann equation for the density matrix ρ of exciton-polaritons (or excitons) and phonons, written in the interaction picture

$$i\hbar\frac{d\rho}{dt} = [\hat{H}_{\mathrm{int}}(t), \rho], \tag{1.193}$$

where the Hamiltonian $\hat{H}_{\rm int}(t)$ in the second-quantization form reads

$$\hat{H}_{\rm int}(t) = \sum_{\mathbf{k},\mathbf{k}'} V_{\mathbf{k},\mathbf{k}'} e^{i\left(\Omega_{\mathbf{k}'} - \Omega_{\mathbf{k}} - \omega_{\mathbf{k}'-\mathbf{k}}\right)t} b_{\mathbf{k}'-\mathbf{k}} a_{\mathbf{k}} a^{\dagger}_{\mathbf{k}'} + h.c. \tag{1.194}$$

Here a $\left(a^{\dagger}\right)$ are the polariton annihilation (creation) operators and b $\left(b^{\dagger}\right)$ are the phonon annihilation (creation) operators. $\Omega_{\mathbf{k}}$ and $\omega_{\mathbf{k}}$ are the dispersions of the polaritons and phonons, respectively, and $V_{\mathbf{k},\mathbf{k}'}$ are the corresponding scattering matrix elements.

Now we assume that initially the bath and the system are not correlated $\rho(t=0) = \rho_{\rm ph} \otimes \rho_{\rm pol}(t=0)$. Usually, as the next step in many textbooks, it is assumed there are no correlations between the polariton subsystem and its environment (phonons) at any future moment of time such that the total density matrix can be written as a tensor product for any $t > 0$. Even though this assumption is not correct as shown in [47], since the bath gets entangled with the system, it leads to the right master equation. The correct (weakened) assumption is

$$\mathrm{Tr}_{ph}[\Lambda\rho(t)] = \mathrm{Tr}_{ph}\left[\Lambda\rho_{ph}(t)\right]\rho_{pol}(t), \tag{1.195}$$

where Λ is an arbitrary operator defined in the bath (phonons) Hilbert space. This is the Born approximation that requires: (a) that bath-related observables can be calculated from the bath density matrix solely and the state of the system doesn't significantly affect them; (b) this property holds throughout the evolution. These assumptions are justified if the interaction is weak, and if the environment is much larger than the system. The next step is the Markov approximation, which states the system has negligibly short phase memory (it requires that environmental (phonon) correlation functions decay on a time-scale fast compared to those of the system) and $d\rho_{\rm pol}(t)/dt$ depends only on the density matrix of the total system $\rho(t)$ at the same moment of time and not on $\rho(\tau)$ for $\tau < t$. After tracing out the phonon degrees of freedom we arrive at the following equation for the polariton density matrix

$$\begin{aligned}\frac{d\rho_{\rm pol}}{dt} = &\frac{1}{2}\sum_{\mathbf{k}}\sum_{\mathbf{k}\neq\mathbf{k}'} W_{\mathbf{k}'\to\mathbf{k}}\left(2a^{\dagger}_{\mathbf{k}}a_{\mathbf{k}'}\rho_{\rm pol}a^{\dagger}_{\mathbf{k}'}a_{\mathbf{k}} - a_{\mathbf{k}}a^{\dagger}_{\mathbf{k}}a^{\dagger}_{\mathbf{k}'}a_{\mathbf{k}'}\rho_{\rm pol} - \rho_{\rm pol}a_{\mathbf{k}}a^{\dagger}_{\mathbf{k}}a^{\dagger}_{\mathbf{k}'}a_{\mathbf{k}'}\right)\\ &+\frac{1}{2}\sum_{\mathbf{k}}\sum_{\mathbf{k}\neq\mathbf{k}'} W_{\mathbf{k}\to\mathbf{k}'}\left(2a^{\dagger}_{\mathbf{k}'}a_{\mathbf{k}}\rho_{\rm pol}a_{\mathbf{k}'}a^{\dagger}_{\mathbf{k}} - a_{\mathbf{k}'}a^{\dagger}_{\mathbf{k}'}a^{\dagger}_{\mathbf{k}}a_{\mathbf{k}}\rho_{\rm pol} - \rho_{\rm pol}a_{\mathbf{k}'}a^{\dagger}_{\mathbf{k}'}a^{\dagger}_{\mathbf{k}}a_{\mathbf{k}}\right)\end{aligned} \tag{1.196}$$

where from Fermi's golden rule the scattering rate is given by [19]

$$W_{\mathbf{k}\to\mathbf{k}'} = \frac{2\pi}{\hbar}\sum_{\mathbf{k}-\mathbf{k}'} |V_{\mathbf{k},\mathbf{k}'}|^2 \left(\theta_{\mp} + N_{\mathbf{k}-\mathbf{k}'}\right)\delta\left(E\left(\mathbf{k}'\right) - E(\mathbf{k}) \mp \hbar\omega_{\mathbf{k}-\mathbf{k}'}\right), \tag{1.197}$$

where $N_{\mathbf{q}}$ is the phonon distribution which in equilibrium follows the Bose distribution, and $\theta_{\pm} = 1, 0$ is a quantity whose sign fits the one in the delta function corresponding to

phonon emission/absorption. As the next step we neglect quantum entanglement and correlations between different $\mathbf{k}$-states which is reasonable in the absence of polariton-polariton interactions, by writing the polariton density matrix in the following form

$$\rho_{\text{pol}} = \prod_{\mathbf{k}} \rho_{\mathbf{k}} \tag{1.198}$$

The populations of the polariton states with wavevector $\mathbf{k}$ are given by $n_{\mathbf{k}} = \text{Tr}\left(a^{\dagger}_{\mathbf{k}} a_{\mathbf{k}} \rho_{\mathbf{k}}\right)$, from where one obtains

$$\frac{dn_{\mathbf{k}}}{dt} = -n_{\mathbf{k}} \sum_{\mathbf{k}'} W_{\mathbf{k}\to\mathbf{k}'} \left(1 + n_{\mathbf{k}'}\right) + \left(1 + n_{\mathbf{k}}\right) \sum_{\mathbf{k}'} W_{\mathbf{k}'\to\mathbf{k}} n_{\mathbf{k}'} \tag{1.199}$$

To include pump and decay one may rewrite the equation above as

$$\frac{dn_{\mathbf{k}}}{dt} = P_{\mathbf{k}} - \Gamma_{\mathbf{k}} n_{\mathbf{k}} - n_{\mathbf{k}} \sum_{\mathbf{k}'} W_{\mathbf{k}\to\mathbf{k}'} \left(1 + n_{\mathbf{k}'}\right) + \left(1 + n_{\mathbf{k}}\right) \sum_{\mathbf{k}'} W_{\mathbf{k}'\to\mathbf{k}} n_{\mathbf{k}'} \tag{1.200}$$

where $P_{\mathbf{k}}$ is the (incoherent) pump term, $\Gamma_{\mathbf{k}}$ is the particle decay rate.

1.7 Quantum Rabi Model

In the previous sections, we discussed the regime of strong light-matter coupling in planar microcavities, where both the matter excitations and photons could freely propagate in the plane. In this section we discuss the Quantum Rabi Model, which describes the interaction between a zero-dimensional two-level system and a single photonic (bosonic) mode, being the full quantum generalization of the simple model of light-matter interaction, introduced in *Subsection* 1.2.3. The results, presented in this section, are relevant for *Chapter* 5 of the current thesis.

The Quantum Rabi Model describes the interaction between a two-level system (for example, a trapped atom or quantum dot) and a cavity mode, in which this two-level system is placed. Its Hamiltonian has the following from

$$\hat{H}_{\text{Rabi}} = \omega_0 \hat{a}^{\dagger}\hat{a} + \frac{\Omega}{2}\sigma_z - \hat{\mathbf{d}} \cdot \hat{\mathbf{E}}(\mathbf{r}_0) = \omega_0 \hat{a}^{\dagger}\hat{a} + \frac{\Omega}{2}\sigma_z - \lambda\sigma_x \left(\hat{a} + \hat{a}^{\dagger}\right) \tag{1.201}$$

where $\sigma_{x,z}$ are Pauli matrices for a two-level system and $\hat{a}\left(\hat{a}^{\dagger}\right)$ is an annihilation (creation) operator for a cavity field. The cavity field frequency is ω_0, the transition frequency Ω, and the coupling strength λ. We denote $|\uparrow(\downarrow)\rangle$ as eigenstates of σ_z, and $|m\rangle$ the eigenstate of $\hat{a}^{\dagger}\hat{a}$. The first term describes the energy of the cavity mode, the second term describes the energy of the two-level system, and the third describes the energy of their interaction. The interaction term $-\hat{\mathbf{d}} \cdot \hat{\mathbf{E}}(\mathbf{r}_0)$ is written in the dipole

approximation (i.e. it is assumed that the size of the two-level system, located at $\mathbf{r}_0$, is much smaller than the wavelength of the cavity mode). The dipole moment operator of the two-level system has the form $\hat{\mathbf{d}} = \mathbf{d}_{eg}\sigma_x$, and the electric field operator of the quantized cavity mode is

$$\hat{\mathbf{E}}(\mathbf{r}_0) = i\sqrt{\frac{\hbar\omega_0}{2V\epsilon\epsilon_0}}\left(\hat{a} - \hat{a}^\dagger\right)\mathbf{U}(\mathbf{r}_0), \tag{1.202}$$

where $\mathbf{U}(\mathbf{r}_0)$ is the cavity eigenmode, taken at the point $\mathbf{r} = \mathbf{r}_0$. If we replace $\hat{a} \to i\hat{a}$ (this transformation preserves the canonical commutation relation $[\hat{a}, \hat{a}^\dagger] = 1$), we get the following interaction term

$$-\hat{\mathbf{d}} \cdot \hat{\mathbf{E}}(\mathbf{r}_0) = \sqrt{\frac{\hbar\omega_0}{2V\epsilon\epsilon_0}}\mathbf{d}_{eg} \cdot \mathbf{U}(\mathbf{r}_0)\sigma_x\left(\hat{a} + \hat{a}^\dagger\right) \equiv -\lambda\sigma_x\left(\hat{a} + \hat{a}^\dagger\right). \tag{1.203}$$

This model is relevant for many experimental set-ups, including a quantum dot in a microcavity, circuit-QED and trapped cold atom systems. In the ultrastrong coupling regime between the two-level system and the cavity mode, its ground state is characterized by a nonzero average number of photons, which is quite surprising. It is known that in the ultra-strong and deep-strong coupling regime ($\lambda > \omega_0$) of the Rabi model the system is characterized by the non-vacuum ground state $|\Psi_G\rangle$ which can be approximated by $|\Psi_G\rangle \approx \frac{1}{\sqrt{2}}(|+\rangle \otimes |\alpha\rangle + |-\rangle \otimes |-\alpha\rangle)$ [314], where $|\pm\alpha\rangle$ are the bosonic coherent states, and $|\pm\rangle = \frac{1}{\sqrt{2}}(|\uparrow\rangle \pm |\downarrow\rangle)$ are the superpositions of the ground and excited qubit states. Thus, in this regime, the ground state is a superposition of two different classical states of light, which is why it is called the Schrödinger cat.

It turns out that the Quantum Rabi Model has some symmetry - all its non-degenerate eigenstates, including the ground state, are eigenvectors of the parity operator, $\hat{\Pi} = e^{i\pi\left(\hat{a}^\dagger\hat{a} + \frac{1}{2}(1+\sigma_z)\right)}$, which measures an even-odd parity of total excitation number and commutes with H_{Rabi}. The parity operator squared yield the identity operator, thus the parity symmetry, together with the identity operator, form the cyclic group of order 2 $\mathbb{Z}_2$.

1.7.1 Jaynes-Cummings model

When the coupling strength is much less than the energy scales set by the atomic transition frequency and the bosonic mode frequency, i.e. $\lambda \ll \omega_0, \Omega$ and when the detuning is small ($|\omega - \Omega| \ll |\omega + \Omega|$), the quantum Rabi model can be effectively reduced to the Jaynes-Cummings model, described by the following Hamiltonian

$$\hat{H}_{\text{JC}} = \omega_0\hat{a}^\dagger\hat{a} + \frac{\Omega}{2}\sigma_z - \lambda\left(\sigma_+\hat{a} + \sigma_-\hat{a}^\dagger\right), \tag{1.204}$$

where the raising and lowering atomic operators are defined as $\sigma_\pm = (\sigma_x \pm i\sigma_y)/2$ (it must be tensor-multiplied with an identity operator, acting in the bosonic subspace).

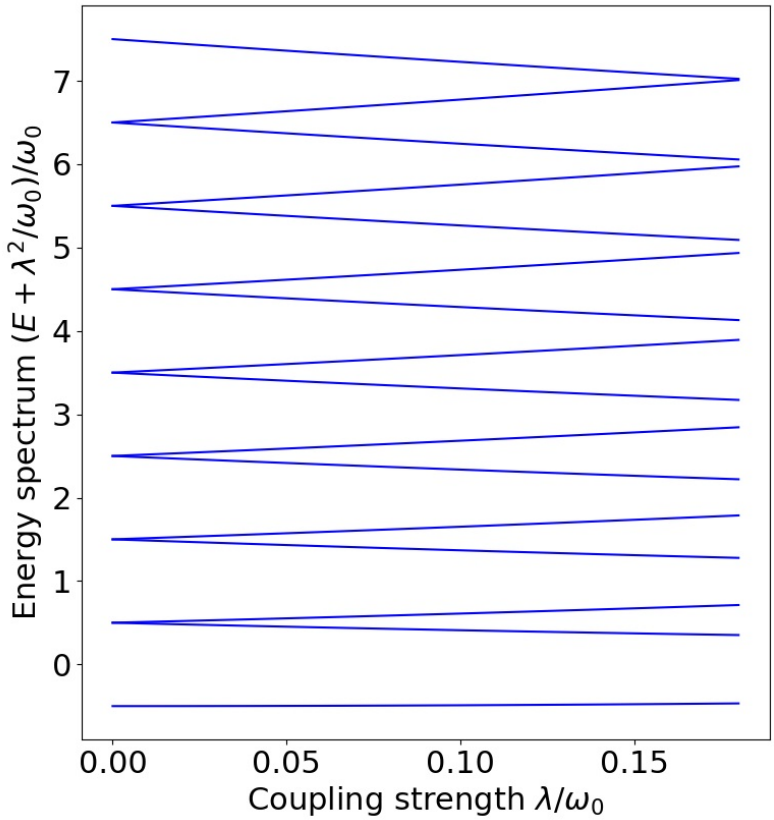

Figure 1.17: Jaynes-Cummings ladder: the energy spectrum (first 16 levels) of the Jaynes-Cummings model at zero detuning between the cavity mode and the two level system $\Omega = \omega_0$

The Jaynes-Cummings Hamiltonian is obtained in the rotating wave approximation, discussed earlier, by noting that in the aforementioned regime the two out of four terms of the interaction term in the full Hamiltonian can be omitted $\lambda\sigma_x(\hat{a} + \hat{a}^\dagger) = \lambda(\sigma_+ + \sigma_-)(\hat{a} + \hat{a}^\dagger) \rightarrow \lambda(\sigma_+\hat{a} + \sigma_-\hat{a}^\dagger)$. This is an exactly solvable model and its spectrum (the so-called Jaynes-Cummings ladder) is shown in Fig. 1.17. We note that the Jaynes-Cummnigs ladder corresponds with the exact spectrum of the quantum Rabi model at small coupling strength, as seen in Fig. 1.18.

In the mean-field approximation, when the bosonic is assumed to be in the coherent state one may replace the bosonic creation and annihilation operators $\hat{a}(\hat{a}^\dagger)$ by numbers $\alpha(\alpha^*)$, which yields the following Hamiltonian

$$\hat{H}_{\mathrm{JC}}^{\mathrm{MF}} = \frac{\Omega}{2}\sigma_z - \lambda\left(\sigma_+\alpha + \sigma_-\alpha^*\right). \tag{1.205}$$

This mean-field Hamiltonian corresponds to the case when the photonic mode is described by a classical light field and it was discussed earlier (it coincides with the Hamiltonian (1.55)), and the parameter α has the meaning of the square root of the average photon number in the cavity mode ($|\alpha|^2 = \langle \hat{n} \rangle = \langle \hat{a}^\dagger \hat{a} \rangle$).

1.7.2 Quantum phase transitions and spontaneous symmetry breaking

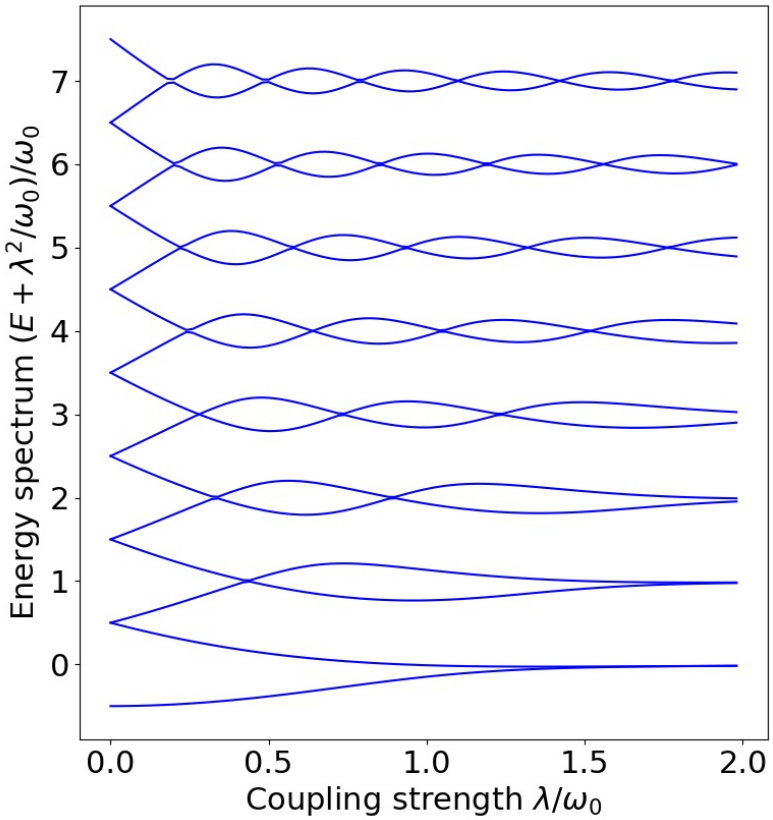

Figure 1.18: The energy spectrum (first 16 levels) of the Quantum Rabi Model at zero detuning between the cavity mode and the two level system $\Omega = \omega_0$

Quantum phase transitions that arise in the Quantum Rabi Model in the strong coupling regime. However, increasing the coupling strength, the energy distance between the ground state and the first excited state decreases and tends to zero in the limit of the infinitely strong coupling, which means that in this limit the ground state becomes

degenerate (see Fig. 1.18). Any linear combination of the states from the degenerate subspace is also an eigenstate. But linear combinations of distinct eigenstates are no longer obliged to respect the symmetry of the Hamiltonian. This situation, when the ground state of the system does not possesses the symmetry of the Hamiltonian, is called spontaneous symmetry breaking. Can spontaneous symmetry breaking occur with a finite coupling strength? We will address this question in the next paragraph.

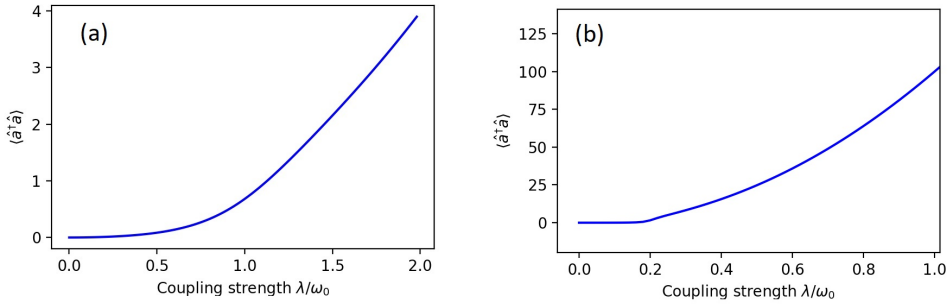

Figure 1.19: Expectation value of the photon occupation $\langle \hat{a}^\dagger \hat{a} \rangle$ in the ground state for the case when (a) $\Omega = \omega_0$ and (b) $\Omega = 10\omega_0$. We clearly see that when approaching the limit $\Omega/\omega_0 \to \infty$, the average number of photons in the ground state is zero before the threshold and nonzero after the threshold. These plots are obtained numerically by exact diagonalization, the photon Hilbert space was truncated at 300 photons. One should note, that when performing numerical calculations the results are valid only when the corresponding occupation numbers involved in the simulation are less than the truncation value.

Spontaneous symmetry breaking is inextricably linked with phase transitions. Let us recall the second-order phase transition ferromagnet-paramagnet from classical statistical mechanics: when the temperature drops below the Curie temperature, the material becomes spontaneously magnetized, i.e. a preferred direction of magnetization appears in it, although the system itself (its Hamiltonian function) is invariant under rotations - an example of spontaneous symmetry breaking. However, this happens only in the thermodynamic limit, i.e. when the number of particles and the volume of the system tends to infinity while maintaining their ratio (concentration). Such a transition has an order parameter (a value equal to zero before the transition and having a finite value after the transition) - the average magnetization. Can one find an analog of the thermodynamic limit in the Rabi quantum model? It is possible [319], due to the fact that the Hilbert space of the bosonic mode is infinite: one needs to consider the following limit $\Omega/\omega_0 \to \infty$. In this limit, a spontaneous breaking of $\mathbb{Z}_2$ symmetry occurs at a finite coupling strength, and the order parameter of this phase transition is $\langle \hat{a} \rangle$, i.e. the average value of the photon annihilation operator in the ground state ($\mathbb{Z}_2$ symmetry forbids such an average to be nonzero). Also, for this quantum phase transition the average number of photons in the ground state $\langle \hat{a}^\dagger \hat{a} \rangle$

is equal to zero before the transition (when the coupling strength is less than critical value) and become nonzero after the transition as shown in Fig. 1.19(b) ($\mathbb{Z}_2$ symmetry does not forbid this quantity to be nonzero, in contrast to $\langle \hat{a} \rangle$).

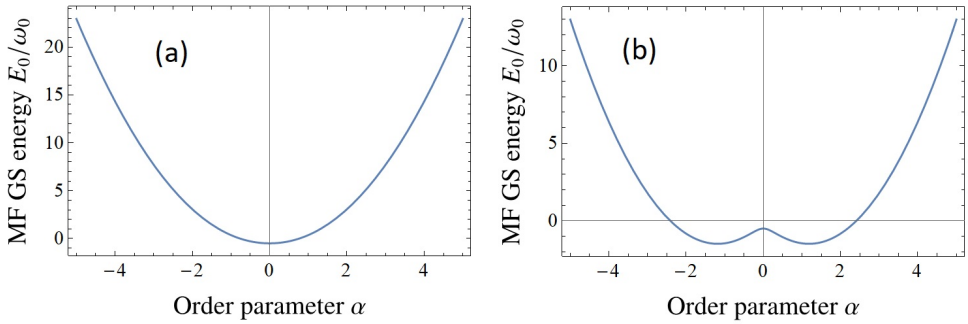

Figure 1.20: Mean-field ground state energy $E_0/\omega_0 = |\alpha|^2 - \sqrt{(\Omega/\omega_0)^2 + 16(\lambda/\omega_0)^2\,\mathrm{Re}(\alpha)}/2$ *as the function of the order parameter* α *(assumed to be real). The subplot (a) corresponds to* $\lambda = 0.2 < \lambda_c^{MF}$ *where there is only a single minimum, the subplot (b) corresponds to* $\lambda = 1.2 > \lambda_c^{MF}$ *where there are two different minima. Here we set* $\omega_0 = \Omega = 1$.

Few notes about the quantum phase transition (QPT) in the Quantum Rabi Model. First, this phase transition is quantum, since occurs at zero temperature. Second, this QPT is second-order because its order parameter $\langle \hat{a} \rangle$ is a continuous function of the coupling strength λ, but its derivative is not (the same holds for $\langle \hat{a}^\dagger \hat{a} \rangle$ as shown in Fig. 1.19(b)). Third, the QPT in the Quantum Rabi Model can be understood from the mean-field theory, by assuming that the photonic component of the total wavefunction is described by the coherent state (classical light), which corresponds to replacing the photon annihilation operator by a number $\hat{a} \to \alpha$. Then one may find the ground state of the resulting Hamiltonian, which is plotted as a function of α in Fig. 1.20 (a) and (b) for two different values of the coupling strength. It is clearly seen, that when the coupling strength λ is less than some critical value λ_c^{MF} predicted by the mean-field approach then the single minimum at $\alpha = 0$ is replaced by two minima that are symmetric with respect to zero ($\pm\alpha$), which is reminiscent of the superradiant phase transition in the Dicke model. The mean-field approximation does not respect the $\mathbb{Z}_2$ symmetry of the initial Hamiltonian, forbidding the eigenstates to have a non-zero expectation value of the photon annihilation operator $\hat{a}$, thus the real ground state turns out to be a linear combination of the two mean-field minima solutions in the deep-strong coupling regime as discussed in one of the previous paragraphs. This can be interpreted as the quantum tunneling between the classical mean-field solutions, leading to their mixing. In the thermodynamic limit $\Omega/\omega_0 \to \infty$ the height of the barrier between the valleys where the minima are located becomes infinite, and thus after the phase transition, the real ground state spontaneously breaks the $\mathbb{Z}_2$ symmetry and becomes equal to one of the classical mean-field solutions with a non zero expectation value $\langle \hat{a} \rangle$.

The quantum Rabi model is a paradigm for (strongly) interacting quantum systems in general, and for the light-matter interaction in particular. It exhibits rich and complex behavior while being at the same time remarkably simple and exactly solvable [57]. Since the quantum Rabi model describes the interaction between a two-level system and a single bosonic mode, it is relevant far beyond the domain of light-matter coupling, and, in particular, in *Chapter* 5 of the current thesis, the quantum Rabi model and its generalizations will appear in the context of strongly coupled quantum optomechanical systems.

2 Quantum rings in the regime of strong light-matter coupling

We demonstrate theoretically that a strong high-frequency circularly polarized electromagnetic field can turn a two-dimensional periodic array of interconnected quantum rings into a topological insulator. The elaborated approach is applicable to calculate and analyze the electron energy spectrum of the array, the energy spectrum of the edge states and the corresponding electronic densities. As a result, the present theory paves the way to optical control of the topological phases in ring-based mesoscopic structures.

2.1 A 2D array of dressed quantum rings as a topological insulator

2.1.1 Introduction

Symmetries play a crucial role in modern science since they determine physical properties of various systems. Particularly, the translational and inversion symmetries together with the time-reversal symmetry defines the electronic structure of solids. If one of the symmetries is broken, the electron energy spectrum complicates and the electron system can reach topologically nontrivial phases [90]. So, the breaking of inversion symmetry in semiconductor structures can lead to the transition from the normal semiconducting state to the topological insulator — the matter that behaves as an insulator in its interior but whose edges contain conducting electronic states [91, 92, 256]. The breaking of time-reversal symmetry — for instance, by application of a magnetic field — radically changes the electron energy spectrum as well, resulting in the discrete set of Landau levels within the bulk and the chiral edge states at the boundaries. In turn, the Coulomb interaction can further complicate the physical picture leading to the incompressible Laughlin states and other exotic phases of matter [93].

It has been recently shown that topologically nontrivial phases may arise not only in the condensed-matter electronic systems but also in photonic structures [94, 95]

or in the strongly coupled light-matter systems based on cavity polaritons [96–99]. Moreover, in ring-like nanostructures (particularly, in mesoscopic ballistic rings) the coherent coupling of electrons to a circularly polarized electromagnetic field leads to the appearance of an effective $U(1)$ gauge field which breaks the time-reversal symmetry. Particularly, this field results in the physical nonequivalence of clockwise and counterclockwise electron rotations in an irradiated QR similarly to a stationary magnetic field [100–102]. The field-controlled interference of the electron waves corresponding to these rotations opens a way to an optical tuning of QR arrays [103]. Currently, QRs are actively studied both experimentally and theoretically as a basis for various nanoelectronic applications [104]. Developing this the scientific trend in the present chapter, we demonstrate theoretically that a circularly polarized field can turn a two-dimensional (2D) array of interconnected QRs into a topological insulator.

The chapter is organized as follows. In Sec. 2.1.2, we elaborate the theory describing the stationary electronic properties of an irradiated array of QRs. In Sec. 2.1.3, we derive the electron energy spectrum of the array, calculate the spectrum of electronic edge states and the corresponding electronic densities, and analyze the found edge states within the formalism based on the Chern numbers.

2.1.2 Model

Let us consider the 2D periodic array of interconnected QRs which are irradiated by a high-frequency circularly polarized electromagnetic wave with the electric field amplitude, $\widetilde{E}_0$, and the frequency, ω, assumed to be far from resonant frequencies of electrons (see Fig. 2.1). Since the wave is both off-resonant and high-frequency ("dressing field" within the conventional terminology of quantum optics), it cannot be absorbed by conduction electrons (see, e.g., the discussion in Refs. [105, 106]). Correspondingly, the effects caused by the dressing field substantially differ from the effects induced in QRs by absorption of light (see, e.g., Refs. [107–110]). Physically, the circularly polarized dressing field breaks the time-reversal symmetry and, therefore, effects on the electron system in the QR similarly to a stationary magnetic field [100]. In particular, the electronic properties of a dressed QR can be described by the effective stationary Hamiltonian,

$$H_{\text{eff}} = \frac{(\hat{p}_\phi - eA_{\text{eff}})^2}{2m_e}, \tag{2.1}$$

where $\hat{p}_\phi$ is the operator of electron momentum in the QR, and

$$A_{\text{eff}} = \frac{eE_0^2}{2Rm_e\omega^3} \tag{2.2}$$

is the artificial $U(1)$ gauge potential produced by the interaction between electrons in the QR and circularly polarized photons of the dressing field [101]. It follows from Eqs. (2.1)–(2.2) that the effective vector potential, A_{eff}, is responsible for the optically

induced Aharonov-Bohm effect [101, 102] and results in the phase incursion of an electron wave traveling between nearest quantum point contacts (QPCs),

$$\phi_0 = \frac{e\pi R A_{\text{eff}}}{2\hbar} = \frac{\pi e^2 \widetilde{E}_0^2}{4 m_e \hbar \omega^3}. \tag{2.3}$$

Within the conventional scattering matrix approach [111, 112], the amplitudes of electronic waves propagating in the array, $A_\pm$, $B_\pm$, $C_\pm$, $D_\pm$, $F_\pm$, $G_\pm$, $H_\pm$, $I_\pm$, satisfy the following set of equations,

$$\begin{pmatrix} A_- e^{-iqd/2} \\ F_+ \\ I_+ \end{pmatrix} = S \begin{pmatrix} A_+ e^{iqd/2} \\ F_- e^{i(\pi qR/2-\phi_0)} \\ I_- e^{i(\pi qR/2+\phi_0)} \end{pmatrix}, \tag{2.4}$$

$$\begin{pmatrix} B_+ e^{-iqd/2} \\ F_- \\ G_- \end{pmatrix} = S \begin{pmatrix} B_- e^{iqd/2} \\ F_+ e^{i(\pi qR/2+\phi_0)} \\ G_+ e^{i(\pi qR/2-\phi_0)} \end{pmatrix}, \tag{2.5}$$

$$\begin{pmatrix} C_- e^{-iqd/2} \\ G_+ \\ H_+ \end{pmatrix} = S \begin{pmatrix} C_+ e^{iqd/2} \\ G_- e^{i(\pi qR/2+\phi_0)} \\ H_- e^{i(\pi qR/2-\phi_0)} \end{pmatrix}, \tag{2.6}$$

$$\begin{pmatrix} D_+ e^{-iqd/2} \\ H_- \\ I_- \end{pmatrix} = S \begin{pmatrix} D_- e^{iqd/2} \\ H_+ e^{i(\pi qR/2+\phi_0)} \\ I_+ e^{i(\pi qR/2-\phi_0)} \end{pmatrix}, \tag{2.7}$$

where the scattering matrix is

$$S = \begin{pmatrix} \sqrt{1-2\varepsilon^2} & \varepsilon & \varepsilon \\ \varepsilon & \frac{-(1+\sqrt{1-2\varepsilon^2})}{2} & \frac{(1-\sqrt{1-2\varepsilon^2})}{2} \\ \varepsilon & \frac{(1-\sqrt{1-2\varepsilon^2})}{2} & \frac{-(1+\sqrt{1-2\varepsilon^2})}{2} \end{pmatrix}, \tag{2.8}$$

ε is the electron transmission amplitude through QPCs ($0 \le \varepsilon \le 1/\sqrt{2}$), $\hbar q = \sqrt{2 m_e E}$ is the electron momentum, m_e is the electron effective mass, E is the electron energy, and ϕ_0 is the field-induced phase incursion (2.3). Applying the Bloch theorem to the considered periodic array of QRs, we arrive at the equations

$$\begin{pmatrix} C_- \\ C_+ \end{pmatrix} = e^{ik_x T} \begin{pmatrix} A_+ \\ A_- \end{pmatrix}, \tag{2.9}$$

$$\begin{pmatrix} B_+ \\ B_- \end{pmatrix} = e^{ik_y T} \begin{pmatrix} D_- \\ D_+ \end{pmatrix}, \tag{2.10}$$

where $\mathbf{k} = (k_x, k_y)$ is the electron wave vector originated from the periodicity of the array and $T = d + 2R$ is the period of the array. Mathematically, Eqs. (2.4)-(2.7) and Eqs. (2.9)-(2.10) form the homogeneous system of sixteen linear algebraic equations for the sixteen amplitudes $A_\pm$, $B_\pm$, $C_\pm$, $D_\pm$, $F_\pm$, $G_\pm$, $H_\pm$, $I_\pm$. Solving the secular equation of this algebraic system numerically, we arrive at the sought electron energy spectrum of the irradiated array, $E(\mathbf{k})$, which is discussed below.

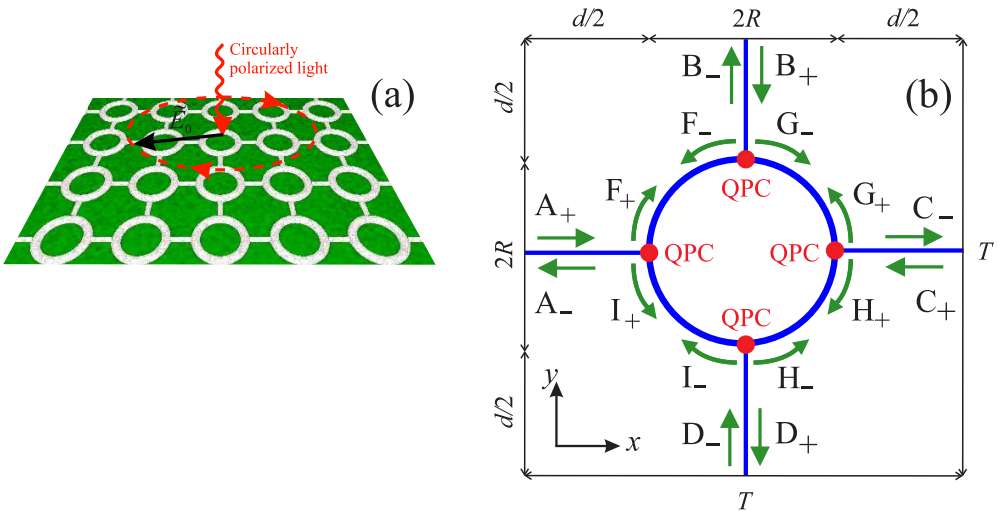

Figure 2.1: Sketch of the system under consideration: (a) The 2D periodic array of quantum rings (QRs) irradiated by a circularly polarized electromagnetic wave with the electric field amplitude $\widetilde{\mathbf{E}}_0$; (b) The elementary cell of the 2D array with the period T, which consists of a QR with the radius R, four leads with the length $d/2$ and four quantum point contacts (QPC). The green arrows correspond to electron waves traveling in different ways with the amplitudes $A_\pm$, $B_\pm$, $C_\pm$, $D_\pm$, $F_\pm$, $G_\pm$, $H_\pm$, $I_\pm$.

2.1.3 Results and discussion

The first six energy bands, $E(\mathbf{k})$, of the 2D infinite periodic array of QRs with transparent QPCs ($\varepsilon = 1/\sqrt{2}$) are plotted in Figs. 2.2a–2.2c for various directions Γ-X-M-Γ in the Brillouin zone of the array (see Fig. 2.2d) and various phase incursions, ϕ_0. In the absence of the dressing field ($\phi_0 = 0$), the electron energy spectrum plotted in Fig 2a has no gaps in the density of electronic states and consists of two flat bands (1 and 6), which correspond to electron states localized within QRs, and four bands (2–5) corresponding to delocalized electron states propagating along the array. The dressing field ($\phi_0 \neq 0$), firstly, results in coupling between localized and delocalized electron states (see the dispersions of the 6-th band in Figs. 2.2a and 2.2b) and, secondly, induces the energy gaps between different bands (see the green strips in Figs. 2.2b–2.2c). In what follows, the gaps between the bands with the numbers i and j are denoted as Δ_{ij}. It should be noted that the values of the field-induced gaps depend periodically on the dressing field as it is shown in Fig. 2.2e. Let us demonstrate that edge states — both topologically protected and unprotected — appear within these field-induced band gaps.

Following the conventional theory of topological insulators [256], we have to fold the

Brillouin zone pictured in Fig. 2.2d as a torus T^2. Then the Chern number corresponding to the n-th band of the considered periodic array is defined as

$$C_n = \frac{1}{2\pi i} \int_{T^2} d^2k F_{xy}(\mathbf{k}), \tag{2.11}$$

where $F_{xy}(\mathbf{k}) = \partial A_y/\partial k_x - \partial A_x/\partial k_y$ is the field strength associated with the Berry connection, $A_j(\mathbf{k}) = \langle n(\mathbf{k})|\frac{\partial}{\partial k_j}|n(\mathbf{k})\rangle$ is the vector potential of the field, and $|n(\mathbf{k})\rangle$ is the normalized Bloch wave function of the n-th band [256]. Applying Eq. (2.11) to the Bloch functions found from Eqs. (2.4)–(2.10), we arrive at the Chern numbers of the considered bands: $C_1 = 0$, $C_2 = -1$, $C_3 = 1$, $C_4 = 1$ and $C_5 = -1$. According to the bulk-boundary correspondence [256], the sum of the Chern numbers of the bands below a certain gap is equal to the number of topologically protected edge modes in the gap (per each boundary):

$$N = \Big|\sum_i C_i\Big|. \tag{2.12}$$

It follows from Eq. (2.12) that two branches of the topologically protected edge states must exist within each of the two band gaps, Δ_{23} and Δ_{45}, if the array of QRs is of finite size along one dimension. To find the energy spectrum of the branches, let us restrict the consideration by the array which is infinite along the x axis and includes only five QRs along the y axis (see Fig. 2.3a). The energy spectrum of electrons in this array can be easily calculated within the approach developed in Sec. 2.1.2 with the only difference: The elementary cell of the finite array pictured in Fig. 2.3a consists of five QRs, where the edge rings (with the numbers 1 and 5) have three QPCs unlike the others. The energy spectrum of the lowest bands of delocalized electrons in this array, $E(\mathbf{k})$, is plotted in Fig. 2.3b. As a first consequence of the finite size of the array along the y axis, each delocalized band of the 2D infinite array (see the branches 2–5 pictured in Figs. 2.2a–2.2c) is split into five subbands in Fig. 2.3b. As a second consequence, the branches of edge states within the band gaps appear (see the red, blue, and green curves in Fig. 2.3b). The edge character of these branches follows clearly from the calculated electron density, $\mathcal{R}$, which has its maximum at edge QRs with the numbers 1 and 5 (see Figs. 2.3c–2.3e). It follows from the aforesaid that the branches of edge states plotted in red and blue — which connects two adjacent bands — are topologically protected since their numbers satisfy the condition (2.12). On the contrary, the edge states plotted in green are not topologically protected since they correspond to the zero number (2.12).

It should be noted that the bandgap, Δ_{34}, can also be opened by varying the electron transmission amplitude through QPCs, ε. Namely, $\Delta_{34} \neq 0$, if the transmission amplitude is $\varepsilon < 1/\sqrt{2}$. However, this gap opening does not result in topological edge states since the corresponding number (2.12) is zero. As a consequence, only field-induced band gaps can turn the periodic array of QRs into topological insulator and, therefore, the strong electron coupling to a circularly polarized dressing field is crucial for the effect under consideration. Physically, this follows from the fact that the circularly polarized dressing field effects on electron system in a QR similarly

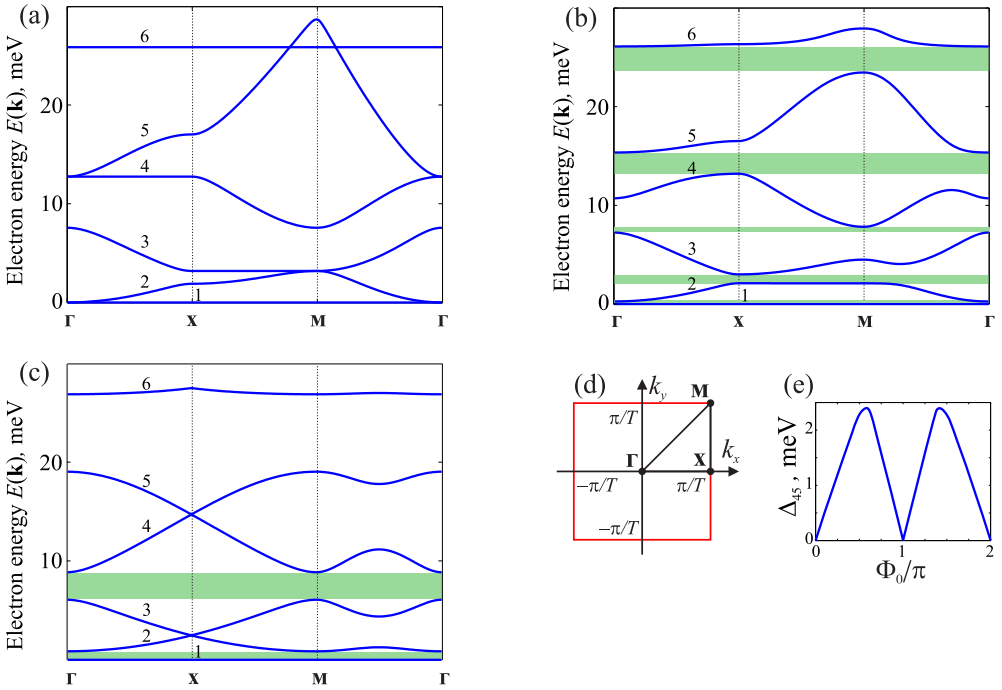

Figure 2.2: Electron energy spectrum, $E(\mathbf{k})$, of the first six bands (1–6) in the 2D infinite periodic array of GaAs-based QRs with the radius $R = 30$ nm, the period $T = 100$ nm and the electron transmission amplitude, $\varepsilon = 1/\sqrt{2}$, in the presence of a circularly polarized electromagnetic field with the different phase incursions, ϕ_0: (a) $\phi_0 = 0$; (b) $\phi_0 = \pi/9$; (c) $\phi_0 = \pi/4$. The green strips depict the field-induced band gaps, the plot (d) shows the first Brillouin zone of the 2D periodic array of QRs and the plot (e) presents the dependence of the bandgap, Δ_{45}, on the field-induced phase incursion along a whole QR, $\Phi_0 = 4\phi_0$.

to a stationary magnetic field (see Eqs. (2.1)–(2.3) and the detailed discussion in Refs. [100–102]). As a consequence, formation of the edge electron states similar to those appearing in the quantum Hall effect takes place in the considered periodic array of irradiated QRs.

Finalizing the discussion, we have to formulate the conditions of observability of the predicted effects. From this viewpoint, there are the two fundamental restrictions: (i) the mean free path of electron for inelastic scattering processes should be much greater then the array period T; (ii) the time of electron traveling through a ring should be much less than the field period, $2\pi/\omega$. In the considered case of GaAs-based QRs with the Fermi energy of meV scale and the array period $T \sim 10^{-5}$cm, the both conditions can be satisfied for a dressing field near the THz frequency range. Since the calculated field-induced band gaps are of meV scale for such a dressing field with the intensity

$I \sim$ kW/cm^2, the discussed topological edge states can be detected in state-of-the-art experiments.

In conclusion, we developed the theory of electronic properties of the 2D periodic array of interconnected ballistic quantum rings (QRs) interacting with an off-resonant circularly polarized high-frequency electromagnetic wave (dressing field). It was demonstrated that the Aharonov-Bohm effect induced by the dressing field substantially modifies the electron energy spectrum of the array, opening band gaps, and producing edge states — both topologically protected and unprotected — within the field-induced gaps. As a result, the light-induced topological insulator appears. The present theory paves the way to optical control of the electronic properties of QR-based mesoscopic structures.

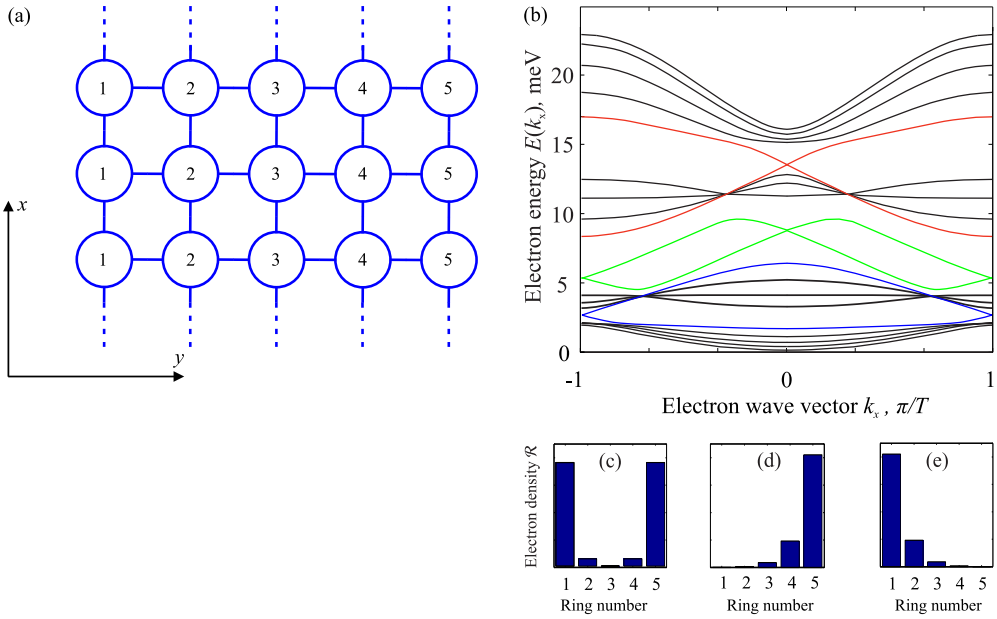

Figure 2.3: Electronic properties of the finite array of QRs: (a) Sketch of the finite array of QRs which is infinite along the x axis and consists of five QRs along the y axis; (b) The energy bands, $E(\mathbf{k})$, of the finite array consisting of GaAs-based QRs with the radius $R = 30$ nm, the period $T = 100$ nm and the electron transmission amplitude, $\varepsilon = 1/\sqrt{2}$, in the presence of a circularly polarized electromagnetic field with the phase incursions, $\phi_0 = \pi/9$. The red and blue lines correspond to the topologically protected edge states, whereas the green lines correspond to unprotected ones; (c)–(e) distribution of the electron density, $\mathcal{R}$, in QRs with the different numbers for the state corresponding to the intersection of the red branches at $k = 0$ in the plot (c), the state corresponding to the upper red branch at $k_x T/\pi = -0.007$ in the plot (d), and the state corresponding to the upper red branch at $k_x T/\pi = 0.007$ in the plot (d).

2.2 Dressed quantum ring with the Rashba spin-orbit interaction

In the section, we developed the theory of electronic properties of a semiconductor quantum ring with the Rashba spin-orbit interaction irradiated by a high-frequency linearly-polarized electromagnetic field (dressing field). Within the Floquet theory of periodically driven quantum systems, it is demonstrated that the dressing field drastically modifies electronic characteristics of the rings and leads to light-induced spin-orbit coupling.

2.2.1 Model

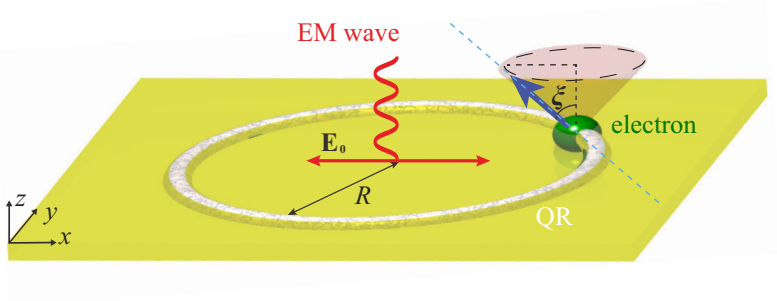

Figure 2.4: Sketch of the system under consideration: The quantum ring (QR) with the radius R irradiated by a linearly polarized electromagnetic (EM) wave with the electric field amplitude E_0. The electron spin (the dark blue arrow) is directed along the local quantization axis (the dashed blue line) with the spin angle ξ.

To describe an irradiated QR (see Fig. 2.4), we have to start from the Hamiltonian describing an irradiated two-dimensional (2D) electron system with the Rashba spin-orbit interaction

$$\hat{\mathcal{H}}_{2\mathrm{D}} = \frac{(\hat{\mathbf{p}} - e\mathbf{A})^2}{2m} + \alpha[\sigma_x(\hat{p}_y - eA_y) - \sigma_y(\hat{p}_x - eA_x)], \tag{2.13}$$

where $\hat{\mathbf{p}} = (\hat{p}_x, \hat{p}_y)$ is the operator of electron momentum, m is the effective electron mass, e is the electron charge, α is the Rashba spin-orbit coupling constant, $\sigma_{x,y,z}$ are the Pauli matrices, $\mathbf{A} = (A_x, A_y) = ([E_0/\omega]\cos\omega t, 0)$ is the vector potential of a linearly polarized electromagnetic wave (dressing field) in the 2D plane, E_0 is the electric field amplitude of the wave, and ω is the wave frequency which is assumed to be far from resonant electron frequencies. Applying the standard approach [253] to transform the 2D electron system into the one-dimensional (1D) ring-shaped one, we

arrive from the 2D Hamiltonian (2.13) at the Hamiltonian of irradiated QR,

$$\hat{\mathcal{H}}_{\rm QR} = \hat{\mathcal{H}}' + \left[\sum_{n=1}^{2} \hat{V}_n e^{in\omega t} + \text{H.c.}\right], \tag{2.14}$$

where the stationary part,

$$\hat{\mathcal{H}}' = \frac{\hat{l}_z^2}{2mR^2} + \frac{\alpha}{R}\left[\sigma_\rho \hat{l}_z - i\hbar\frac{\sigma_\varphi}{2}\right] + \frac{e^2E_0^2}{4m\omega^2}, \tag{2.15}$$

is the Hamiltonian of the unperturbed QR up to a field-induced constant shift of energy,

$$\hat{V}_1 = \frac{eE_0}{2mR\omega}\left(\sin\varphi\,\hat{l}_z - i\hbar\frac{\cos\varphi}{2}\right) + \frac{\alpha eE_0}{2\omega}\sigma_y, \tag{2.16}$$

$$\hat{V}_2 = \frac{e^2E_0^2}{8m\omega^2}, \tag{2.17}$$

is the periodical part with the two harmonics originated from the irradiation, R is the QR radius, $\hat{l}_z = -i\hbar\,\partial/\partial\varphi$ is the operator of angular momentum along the z-axis, φ is the polar angle of an electron in the QR, $\sigma_\rho = \cos\varphi\,\sigma_x + \sin\varphi\,\sigma_y$ and $\sigma_\varphi = -\sin\varphi\,\sigma_x + \cos\varphi\,\sigma_y$ are the Pauli matrices written in the polar coordinates. Applying the conventional Floquet-Magnus approach to renormalize the Hamiltonian of irradiated QR and restricting the consideration by the leading terms in the high-frequency limit, we can reduce the time-dependent Hamiltonian (2.14) to the effective time-independent one,

$$\hat{\mathcal{H}} = \hat{\mathcal{H}}' + \sum_{n=1}^{2}\frac{\left[\hat{V}_n, \hat{V}_n^\dagger\right]}{\hbar n\omega} + \sum_{n=1}^{2}\frac{\left[\left[\hat{V}_n, \hat{\mathcal{H}}'\right], \hat{V}_n^\dagger\right] + \text{H.c.}}{2(\hbar n\omega)^2}. \tag{2.18}$$

Substituting Eqs. (2.15)–(2.17) into Eq. (2.18), one can rewrite the effective Hamiltonian (2.18) as

$$\hat{\mathcal{H}} = \hat{\mathcal{H}}_0 + \hat{V}, \tag{2.19}$$

where

$$\begin{aligned}\hat{\mathcal{H}}_0 &= \frac{\hat{l}_z^2}{2m^*R^2} + \frac{\alpha}{R}\left[\sigma_\rho\hat{l}_z - i\hbar\frac{\sigma_\varphi}{2}\right] - \left(\frac{eE_0\alpha}{R\omega^2}\right)^2\frac{\hat{l}_z\sigma_z}{m\hbar} \\ &+ \frac{e^2E_0^2}{4m\omega^2} + \frac{1}{2m}\left(\frac{\hbar eE_0}{4mR^2\omega^2}\right)^2,\end{aligned} \tag{2.20}$$

$$\begin{aligned}\hat{V} &= \left[\frac{3}{16}\gamma_1^2\cos 2\varphi - \gamma_1^2\gamma_2\left(\gamma_2^2 - \frac{1}{4}\right)i\sigma_x\sin\varphi\right]\frac{\hbar^2}{2mR^2} \\ &+ \left[\frac{i\gamma_1^2\sin 2\varphi}{2} - 2\gamma_1^2\gamma_2\left(\gamma_2^2 - \frac{1}{4}\right)\sigma_x\cos\varphi\right]\frac{\hbar\,\hat{l}_z}{2mR^2} \\ &+ \frac{\gamma_1^2\cos 2\varphi}{8mR^2}\,\hat{l}_z^2,\end{aligned} \tag{2.21}$$

where

$$m^* = \frac{m}{1 + 3\left(eE_0/2mR\omega^2\right)^2} \tag{2.22}$$

is the effective electron mass renormalized by the irradiation, $\gamma_1 = |e|E_0/(mR\omega^2)$ is the dimensionless parameter describing the strength of electron-field coupling, and $\gamma_2 = mR\alpha/\hbar$ is the dimensionless parameter describing the strength of Rashba spin-orbit coupling. As expected, the Hamiltonian (2.19) exactly coincides with the Hamiltonian of unirradiated QR [253] in the absence of the field ($E_0 = 0$).

It should be noted that all effects originated from the direct spin interaction with the magnetic component of the dressing field (particularly, the Zeeman effect and the Aharonov-Bohm effect) are relativistically negligible since the amplitude of magnetic induction of the field, $B_0 = E_0/c$, is very small for reasonable field intensities. Therefore, they are omitted in the developed theory. We also neglected effects arisen from overlying electronic modes, assuming the typical distance between transverse electronic minibands (tens meV for state-of-the-art QRs [113]) to be sufficiently large than the photon and electron energies under consideration.

2.2.2 Reuslts and discussion

To consider the Schrödinger problem with the effective Hamiltonian (2.19), let us start from its part (2.20). Two exact eigenstates of the Hamiltonian (2.20) can be written as

$$\Psi_1(\varphi) = e^{ij_z\varphi}\begin{pmatrix} \cos(\xi/2)e^{-i\varphi/2} \\ -\sin(\xi/2)e^{i\varphi/2} \end{pmatrix} \tag{2.23}$$

and

$$\Psi_2(\varphi) = e^{ij_z\varphi}\begin{pmatrix} \sin(\xi/2)e^{-i\varphi/2} \\ \cos(\xi/2)e^{i\varphi/2} \end{pmatrix}, \tag{2.24}$$

where

$$\xi = \arctan\left[\frac{2m^*R\alpha/\hbar}{2(m^*/m)\left(eE_0\alpha/\omega^2\hbar\right)^2 + 1}\right] \tag{2.25}$$

is the angle between the local spin quantization axis and the z-axis (see Fig. 2.4). It follows from single-valuedness of the eigenstates, $\Psi_{1,2}(\varphi) = \Psi_{1,2}(\varphi + 2\pi)$, that the z-component of total angular momentum of the electron, j_z, must satisfy the condition, $j_z = \lambda n + 1/2$, where $n = 0, 1, 2, ...$ is the orbital quantum number corresponding to the electron rotation in QR and the sign $\lambda = \pm$ describes the direction of the rotation (counterclockwise/clockwise). Omitting constant terms which only shift the zero energy, one can write the electron energy spectrum of the eigenstates (2.23)-(2.24)

as

$$\varepsilon^s_{\lambda n} = \frac{\hbar^2}{2m^*R^2}\left(\lambda n + \frac{1}{2}\right)^2 + \frac{\hbar^2}{2m^*R^2}\left|\lambda n + \frac{1}{2}\right| s \times \sqrt{\left[2\left(\frac{m^*}{m}\right)\left(\frac{eE_0\alpha}{\hbar\omega^2}\right)^2 + 1\right]^2 + \left[\frac{2\alpha m^* R}{\hbar}\right]^2}, \tag{2.26}$$

where $s = \pm 1$ is the quantum number describing the spin direction along the local quantization axis (see Fig. 2.4) and the spin $s = +1$ corresponds to the greater energy (2.26). Within the conventional notation [114] based on the three quantum numbers, $|n, \lambda, s\rangle$, the eigenstates (2.23)-(2.24) can be written as

$$|n, +, -1\rangle = e^{in\varphi}\begin{pmatrix} \cos(\xi/2) \\ -\sin(\xi/2)e^{i\varphi} \end{pmatrix}, \tag{2.27}$$

$$|n, +, +1\rangle = e^{in\varphi}\begin{pmatrix} \sin(\xi/2) \\ \cos(\xi/2)e^{i\varphi} \end{pmatrix}, \tag{2.28}$$

$$|n, -, +1\rangle = e^{-in\varphi}\begin{pmatrix} \cos(\xi/2) \\ -\sin(\xi/2)e^{i\varphi} \end{pmatrix}, \tag{2.29}$$

$$|n, -, -1\rangle = e^{-in\varphi}\begin{pmatrix} \sin(\xi/2) \\ \cos(\xi/2)e^{i\varphi} \end{pmatrix}, \tag{2.30}$$

for $n = 1, 2, 3...$ and

$$|0, +, -1\rangle = \begin{pmatrix} \cos(\xi/2) \\ -\sin(\xi/2)e^{i\varphi} \end{pmatrix}, \tag{2.31}$$

$$|0, +, +1\rangle = \begin{pmatrix} \sin(\xi/2) \\ \cos(\xi/2)e^{i\varphi} \end{pmatrix} \tag{2.32}$$

for $n = 0$. It follows from Eq. (2.26), particularly, that $\varepsilon^s_{-n} = \varepsilon^s_{n-1}$. This means that the states $|n, -, s\rangle$ and $|n-1, +, s\rangle$ are degenerated.

The eigenstates and eigenenergies (2.23)–(2.32) can be easily verified by direct substitution into the Schrödinger equation with the Hamiltonian (2.20). However, the total effective Hamiltonian (2.19) consists of the two parts, including both the discussed Hamiltonian $\hat{\mathcal{H}}_0$ and the term $\hat{V}$. Therefore, we have to analyze the effect of the term $\hat{V}$ on the found solutions of the Schrödinger problem with the Hamiltonian $\hat{\mathcal{H}}_0$. It follows from Eqs. (2.21) and (2.27)–(2.32) that $\langle n', \lambda', s'|\hat{V}|n, \lambda, s\rangle \sim \delta_{\lambda'\lambda}$ for $n, n' \geq 1$. Thus, the term $\hat{V}$ does not split the degenerate states $|n, -, s\rangle$ and $|n-1, +, s\rangle$. It should be noted also that the discussed regime of strong light-matter coupling is conventionally defined as a light-induced renormalization of electronic properties without the light absorption by electrons (see, e.g., the discussion in Ref. [120]). Particularly, the main absorption mechanism for semiconductor structures dressed by an off-resonant electromagnetic field — the collisional absorption of the field by conduction electrons — can be neglected if $\omega\tau \gg 1$, where τ is the electron relaxation time [115]. Therefore,

we have to consider the case of high-frequencies, ω, when the condition $\gamma_1 \ll 1$ can take place. It follows from this that the discussed term $\hat{V} \sim \gamma_1^2$ can be considered as a weak perturbation for a broad range of QR parameters. Particularly, the conventional criterion of perturbation theory,

$$\left| \frac{\langle n', \lambda', s' | \hat{V} | n, \lambda, s \rangle}{\varepsilon^{s'}_{\lambda' n'} - \varepsilon^{s}_{\lambda n}} \right| \ll 1, \tag{2.33}$$

can be satisfied for the first tens of energy levels (2.26) in the typical case of InGaAs-based QRs with the effective mass $m = 0.045 m_e$, radius $R \approx 200$ nm and the Rashba coupling constant $\alpha \approx 10^4$ m/s. As a consequence, the effective Hamiltonian (2.19) can be reduced to the simplified Hamiltonian (2.20). Correspondingly, the found eigenstates and eigenenergies (2.23)–(2.32) can be applied to describe electronic properties of the irradiated QR.

It follows from the Hamiltonian (2.20) that the irradiation of QR results in the two main effects: First, it renormalizes the electron effective mass (2.22) and, second, it leads to the unusual spin-orbit coupling $\sim l_z \sigma_z$ described by the third term of the Hamiltonian (2.20). In turn, these effects lead to the dependencies of the spin angle (2.25) and the energy levels (2.26) on the irradiation intensity. Namely, the relatively weak irradiation can decrease the angle to tens percents of its initial value in the unirradiated QR, $\xi_0 = \arctan(2\alpha m R/\hbar)$. Since the modulation of spin orientation by various external actions lies in the core of modern spintronics [116–119], the found strong dependence of the spin polarization on the irradiation can be used, particularly, in prospective ring-shaped spintronic devices operated by light. The irradiation also strongly affects the energy of the electron levels in the QR and their spin splitting. Such a light-induced modification of the energy spectrum (2.26) can manifest itself, particularly, in optical measurements.

2.3 Conclusions

We considered the 2D periodic array of interconnected ballistic quantum rings, dressed by an off-resonant circularly polarized high-frequency electromagnetic wave. It was shown that the light-induced Aharonov-Bohm effect opens topological band gaps in the band structure of the array. As a result, the light-induced Floquet topological phase appears.

Also, we demonstrated that the key electronic characteristics of QRs with the Rashba spin-orbit interaction — the structure of electron energy levels and the spin polarization of electrons — strongly depend on off-resonant irradiation. Particularly, the modification of both electron effective mass and the spin-orbit coupling appears. It is shown that the irradiation-induced renormalization of the electron energy spectrum can be observed in state-of-the-art optical experiments, whereas the light sensitivity

of the spin orientation can be exploited in prospective spintronic devices operated by light.

3 Topological metamaterials based on polariton rings

Chern insulator phase is shown to emerge in two-dimensional arrays of polariton rings where time-reversal symmetry is broken due to the application of an out-of-plane magnetic field. The interplay of Zeeman splitting with the photonic analog of spin-orbit coupling (TE-TM splitting) inherently present in this system leads to the appearance of synthetic U(1) gauge field and the opening of topologically nontrivial spectral gaps. This results in the onset of topologically protected chiral edge states similar to those forming in the quantum Hall effect. In one dimensional zigzag arrays of polariton rings edge states similar to those appearing in the Su-Schrieffer–Heeger (SSH) model are formed.

3.1 Introduction

Since the discovery of the quantum Hall effect [233] and its interpretation in terms of topological invariance [270], there were several breakthroughs in the field of topological condensed matter physics. Fractional quantum Hall effect [234, 269] was interpreted in terms of composite fermion theory by Jain [236] and non-Abelian anyon statistics by Xiao-Gang Wen [237]. Later on, ideas of the topological protection of the quantum Hall phase edge states were generalized to the concept of the bulk-boundary correspondence [235]. Finally, the introduction of the hierarchy of topological invariants [258] drastically increased the range of available topologically nontrivial electronic configurations and corresponding edge states [251].

The recent decade has seen the rise of topological photonics, following the prediction of topologically protected optical crystal edge states similar to the conducting electronic edge states [259]. Existing proposals for topological photonics exploit symmetry breaking with synthetic magnetic fields in arrays of coupled waveguides [260], a spatial analog of Floquet modulation [261], and magneto-optic metamaterials [262]. Recently, strong light-matter interaction in coupled microcavities was predicted to yield topological polaritonic edge states [263–265].

In contrast to topological photonics, the topological states of polaritonic systems can

be controlled with a real magnetic field or via strong particle-particle interactions [266]. The latter gives an additional twist to polariton-based systems, which can demonstrate nonlinear topological effects related to optical bistability [267]. Moreover, bosonic stimulation of polariton-polariton scattering allows spontaneous coherent emission from topologically nontrivial states [268]. Overall, the nonlinearity stemming from polariton-polariton interactions, responsible for the crossover from polariton lasing to polariton Bose-Einstein condensation, provides a unique opportunity of studying new interacting bosonic topological phases.

Polaritons are neutral particles, so the application of an external magnetic field affects only their spin but not orbital motion. However, as it was shown in the Ref.[247] in non-simply connected geometry such as polariton ring, the interplay of Zeeman splitting with the photonic analog of spin-orbit coupling (TE-TM splitting) inherently present in this system leads to the appearance of synthetic U(1) gauge field affecting orbital motion. The effect is due to the appearance of the non-zero geometric Berry phase during one round of the rotation along the ring [248]. In this chapter, we extend the idea of synthetic U(1) field for polariton system to the case of periodic arrays of microcavity rings. We demonstrate that in a 2D array of polariton rings the presence of synthetic U(1) field leads to the nontrivial band topology, characterized by nonzero Chern numbers, and induces topologically protected unidirectional edge states, similar to those appearing in QHE. In a 1D zigzag array of the rings edge states similar to those appearing in the Su-Schrieffer-Heeger (SSH) model are formed.

The work is organized as follows. In Section II we construct and diagonalize the Hamiltonian of a single polariton ring accounting for both TE-TM and Zeeman splitting. The results are then used for the topological analysis of two-dimensional cavity ring arrays presented in Section III and zigzag chains of annular cavities presented in Section IV. Conclusions summarize the results of the work.

3.2 Single polariton ring

In this section, we derive formally the effective 1D Hamiltonian describing a single polariton ring (see Fig. 3.1) with the TE-TM splitting in the presence of a magnetic field. We start with from the Hamiltonian of 2D polariton inside a planar microcavity [291]

$$\widehat{H}_{2D} = \begin{pmatrix} \widehat{H}_0(\hat{\mathbf{k}}) + \Delta_z/2 & \widehat{H}_{\text{TE-TM}}(\hat{\mathbf{k}}) \\ \widehat{H}^{\dagger}_{\text{TE-TM}}(\hat{\mathbf{k}}) & \widehat{H}_0(\hat{\mathbf{k}}) - \Delta_z/2 \end{pmatrix}, \tag{3.1}$$

where the diagonal terms $\hat{H}_0$ describe the kinetic energy of lower cavity polaritons, and the off-diagonal terms $\widehat{H}_{\text{TE-TM}}$ correspond to the longitudinal-transverse splitting.

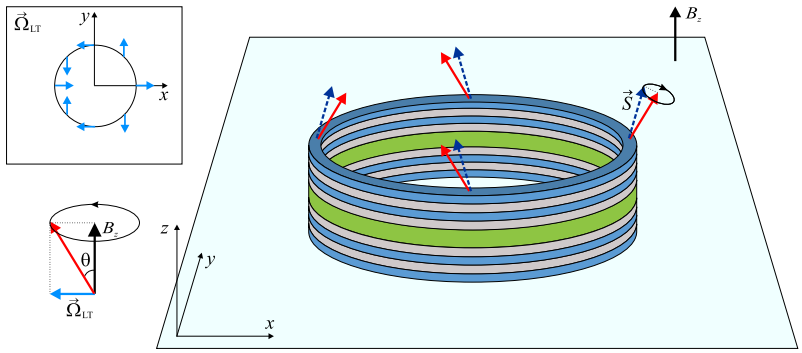

Figure 3.1: Schematic of the considered geometry. The cavity (polariton ring) is constituted by two Distributed Bragg Reflectors sandwiching a cavity with embedded Quantum Well. The polariton ring is placed into an external magnetic field B_z perpendicular to its interface. The total effective magnetic field acting on the polariton's spin is a combination of the real magnetic field and the field provided by TE-TM splitting. The direction of the total effective magnetic field changes along the ring as is shown by the red solid arrows. If one moves along the ring it twice covers a cone characterized by angle θ. The dashed arrow shows the direction of the Stokes vector $\vec{S}$. In adiabatic approximation, the direction of the Stokes vector coincides with the direction of the total effective magnetic field, while they become different for the exact solution of the Schrodinger equation.

We further employ the effective mass approximation

$$\widehat{H}_0(\hat{\mathbf{k}}) = \frac{\hbar^2 \hat{\mathbf{k}}^2}{2m_{\text{eff}}}. \tag{3.2}$$

The TE-TM part is given by

$$\widehat{H}_{\text{TE-TM}}(\hat{\mathbf{k}}) = \beta \left(\frac{\partial}{\partial y} + i \frac{\partial}{\partial x} \right)^2, \tag{3.3}$$

where β is a constant, characterizing the strength of the TE-TM splitting which can be expressed via the longitudinal and transverse polariton effective masses m_l and m_t as $\beta = (\hbar^2/4)(m_l^{-1} - m_t^{-1})$. In order to proceed with the derivation of the correct 1D Hamiltonian let us pass to the cylindrical coordinates and add the confining potential $V(r)$, which forces the polariton wave functions to be localized on the ring in the radial direction to $\widehat{H}_{2D}$. The terms associated with the TE-TM splitting rewritten in polar coordinates read

$$\begin{aligned} &\left(\frac{\partial}{\partial y} \pm i \frac{\partial}{\partial x} \right)^2 = e^{\mp 2i\varphi} \times \\ &\left(-\frac{\partial^2}{\partial r^2} \pm \frac{2i}{r} \frac{\partial^2}{\partial r \partial \varphi} \mp \frac{2i}{r^2} \frac{\partial}{\partial \varphi} + \frac{1}{r} \frac{\partial}{\partial r} + \frac{1}{r^2} \frac{\partial^2}{\partial \varphi^2} \right). \end{aligned} \tag{3.4}$$

We decompose the Hamiltonian Eq. (3.1) into two parts $\widehat{H}_{2D} = \widehat{H}_0(r) + \widehat{H}_1(r,\varphi)$ where

$$\widehat{H}_0(r) = -\frac{\hbar^2}{2m_{\text{eff}}}\left(\frac{\partial^2}{\partial r^2} + \frac{1}{r}\frac{\partial}{\partial r}\right) + V(r). \tag{3.5}$$

Following the conventional procedure [253], the Hamiltonian of 1D ring is given by

$$\widehat{H} = \langle R_0(r)|\widehat{H}_1(r,\varphi)|R_0(r)\rangle, \tag{3.6}$$

where $R_0(r)$ is a the lowest radial mode of the Hamiltonian (3.5). For the confining potential $V(r) = A(r-R)^2/2$ from Ref. [253] we have

$$R_0(r) = \left(\frac{\gamma}{R\sqrt{\pi}}\right)^{1/2} e^{-\gamma^2(r-R)^2/2}, \tag{3.7}$$

where $\gamma^4 = m_{\text{eff}}A/\hbar^2$ and the 1D limit is putting ationγ to infinity. The desirable Hamiltonian $\widehat{H} = \langle R_0(r)|\widehat{H}_1(r,\varphi)|R_0(r)\rangle$ contains three types of terms. Namely, the first type is $\langle R_0(r)|r^{-2}|R_0(r)\rangle$, arising from the kinetic and TE-TM parts of $\widehat{H}_1(r,\varphi)$. The other two terms $\langle R_0(r)|\partial^2/\partial r^2|R_0(r)\rangle$ and $\langle R_0(r)|r^{-1}\partial/\partial r|R_0(r)\rangle$ in turn stem only from the TE-TM part. Due to the fact that $R_0^2(r) = \gamma/(R\sqrt{\pi})e^{-\gamma^2(r-R)^2}$ converges to $\delta(r-R)/R$ as $\gamma\to\infty$, the first term yields $\lim\limits_{\gamma\to\infty}\langle R_0(r)|r^{-2}|R_0(r)\rangle = R^{-2}$. The second term can be calculated straightforwardly $\langle R_0(r)|r^{-1}\partial/\partial r|R_0(r)\rangle = 1/2R_0^2(r)|_0^\infty = 0$.

The direct calculation of the third term yields $\langle R_0(r)|\partial^2/\partial r^2|R_0(r)\rangle \sim -\gamma^2/2$ when $\gamma\to\infty$, so this term dominates over the others in $\langle R_0(r)|\widehat{H}_{\text{TE-TM}}(r,\varphi)|R_0(r)\rangle$ and we can neglect them. Thus, we arrive at the correct Hamiltonian (3.8) of a polariton ring with $\Delta_{\text{LT}} = \gamma^2\beta/2$ which, in turn, is inversely proportional to the characteristic width of the microcavity.

After averaging all the terms in Eq. (3.4) we arrive at

$$\widehat{H} = \frac{\hbar^2}{2m_{\text{eff}}R^2}\begin{pmatrix}\hat{\tilde{k}}^2 + \Delta_2/2 & \Delta_1 e^{-2i\varphi}\\ \Delta_1 e^{2i\varphi} & \hat{\tilde{k}}^2 - \Delta_2/2\end{pmatrix}, \tag{3.8}$$

where $\hat{\tilde{k}} = -i(d/d\varphi)$, R is the radius of the ring. For the sake of simplicity we introduced dimensionless parameters $\Delta_{1,2}$ corresponding to the LT and Zeeman splittings as $\Delta_{\text{LT}(z)} = \Delta_{1(2)}\hbar^2/(2m_{\text{eff}}R^2)$ and $\Delta_{LT} \approx \beta/2a^2$ with a being lateral width of the ring. The Hamiltonian (3.8) was proposed earlier basing on symmetry considerations [248]. The approach developed here allows establishing correspondence between the parameters of the Hamiltonian and the geometrical dimensions of the structure.

In general, solutions of the stationary Schrodinger equation with Hamiltonian (3.8) can be represented in the following form:

$$\widetilde{\psi}(\varphi) = \widetilde{\chi}(\varphi,\tilde{k})e^{i\tilde{k}\varphi}, \tag{3.9}$$

where $\widetilde{\chi}(\varphi, \tilde{k})$ is a corresponding spinor

$$\widetilde{\chi}(\varphi, \tilde{k}) = \frac{1}{\sqrt{\xi(\tilde{k})^2 + 1}} \begin{pmatrix} e^{-i\varphi} \\ \xi(\tilde{k}) e^{i\varphi} \end{pmatrix}, \tag{3.10}$$

and $\xi(\tilde{k}) = \Delta_1/((E + \Delta_2/2) - (1 + \tilde{k})^2)$. The energy of the state Eq. (3.9) (measured in units of $\hbar^2/2m_{\text{eff}}R^2$) is given by:

$$E = (\tilde{k}^2 + 1) \pm \sqrt{\Delta_1^2 + (\Delta_2/2 - 2\tilde{k})^2}, \tag{3.11}$$

For a given energy Eq. (3.11) has four solutions for $\tilde{k}_{\mathrm{i}}$, $\mathrm{i} = 1 \ldots 4$ two positive and two negative, corresponding to clockwise and anti-clockwise propagation and two opposite spin orientations. Analytical expressions for them are listed below. For this purpose, we introduce the auxiliary variables $a_{1,2}$ and b given by

$$a_1 = \Bigg(-72\Delta_1^2 + 36\Delta_2^2 + 64E^3 - 96E^2 - 72\Delta_1^2 E - 18\Delta_2^2 E - 96E + 64 + \tag{3.12}$$

$$\Big(4\left(4(E+1)\left(-9\Delta_1^2 + 4E(2E-5) + 8\right) - 9\Delta_2^2(E-2)\right)^2 -$$

$$\left(4\left(-3\Delta_1^2 + 4(E-1)E + 4\right) - 3\Delta_2^2\right)^3\Big)^{1/2}\Bigg)^{1/3}, \tag{3.13}$$

$$a_2 = 16 - 16E + 16E^2 - 12\Delta_1^2 - 3\Delta_2^2, \tag{3.14}$$

$$b = (4(E+1) + a_2/a_1 + a_1)/12. \tag{3.15}$$

As a result, the equations on the dispersion relations for a single polariton ring (Eq. (3.11)) can be conveniently expressed in these variables:

$$\tilde{k}_{1,2} = \sqrt{b} \mp \sqrt{E + 1 - b - \Delta_2/(2\sqrt{b})}, \tag{3.16}$$

$$\tilde{k}_{3,4} = -\sqrt{b} \mp \sqrt{E + 1 - b + \Delta_2/(2\sqrt{b})}. \tag{3.17}$$

It should be noted that if the Zeeman splitting is present, $E(\tilde{k}) \neq E(-\tilde{k})$ which corresponds to the breaking of the time-reversal symmetry in the system leading to non-equivalence of clockwise and anti-clockwise propagation directions. In the arrays of interconnected rings, this will lead to the appearance of the topologically protected edge states as we will demonstrate later on.

The general solution corresponding to a given energy thus reads:

$$\widetilde{\Psi}(\varphi) = \sum_{\mathrm{i}} \widetilde{C}^{(\mathrm{i})} \widetilde{\psi}_{\mathrm{i}}(\varphi), \tag{3.18}$$

where the summation is performed over all real roots of Eq. (3.11) and $\widetilde{\psi}_{\rm i}(\varphi)$ is an eigenfunction (Eq. (3.9)) at $\tilde{k} = \tilde{k}_{\rm i}$. The Stokes vector given by

$$\vec{S} = \widetilde{\psi}^{\dagger}\vec{\sigma}\widetilde{\psi} = \begin{pmatrix} \sin\theta\cos 2\varphi \\ \sin\theta\sin 2\varphi \\ \cos\theta \end{pmatrix}. \tag{3.19}$$

characterizes the distribution of the spin projection along the ring and defines the profile of the polarization of the emission along the ring, and $\tan\theta/2 = \xi(\tilde{k})$. Note, that the direction of the Stokes vector is not exactly the same as the direction of the total effective magnetic field as in the case of adiabatic approximation [248].

As we consider only bright excitons with spin ± 1 as a two-level system, the z-projection of the operator of total angular momentum is $\hat{J}_z = \hbar\hat{\tilde{k}} + \hbar\sigma_z$. One can check that $\hat{J}_z\widetilde{\psi}(\varphi) = \hbar\tilde{k}\widetilde{\psi}(\varphi)$ which clarifies the physical meaning of $\tilde{k}$. If there is only a single isolated ring, one should impose periodic boundary condition $\widetilde{\psi}(\varphi) = \widetilde{\psi}(\varphi + 2\pi)$, so that $\tilde{k}$ is integer and corresponds to the orbital quantized angular momentum and according to Eq. (3.11) energy becomes quantized as well.

3.3 Two-dimensional array of rings

We consider a two-dimensional array of polariton rings, as shown in Figs. 3.2 (a) and (b). Each ring can be considered as a plaquette in a square lattice where the wave propagates via leads connecting neighboring cavity rings. Every ring has four leads attached to it. There is an applied magnetic field B_z in addition to the effective magnetic field $\vec{\Omega}_{\rm LT}$ that stems from the TE-TM splitting and lies in the plane of the array. The splitting values $\Delta_z = g\mu_{\rm B}B_z$, $\Delta_{\rm LT} = g\mu_{\rm B}|\vec{\Omega}_{\rm LT}|$, where g is the effective Lande g-factor for the 2D exciton and $\mu_{\rm B}$ is the Bohr magneton. In the unit cell presented in Fig. 3.2(b) the wave function is piecewise-defined.

For the lead (polariton wire), the wave function can be obtained similarly to the case for a ring by noticing that the polariton wire Hamiltonian is the ring Hamiltonian (Eq. (3.8)) at the limit $R \to \infty$. For example, two branches (upper and lower, due to the TE-TM and Zeeman splittings) of the dispersion are given by

$$E = (kR)^2 \pm \sqrt{\Delta_1^2 + (\Delta_2/2)^2}, \tag{3.20}$$

where again E is measured in $\hbar^2/(2m_{\rm eff}R^2)$ units. When $E \geq \sqrt{\Delta_1^2 + (\Delta_2/2)^2}$ we have four eigenfunctions of a lead

$$\psi_{1,2}(x) = \frac{1}{\sqrt{\xi_0^2+1}}\begin{pmatrix} -\xi_0 \\ 1 \end{pmatrix} e^{\pm ik_l x}, \tag{3.21}$$

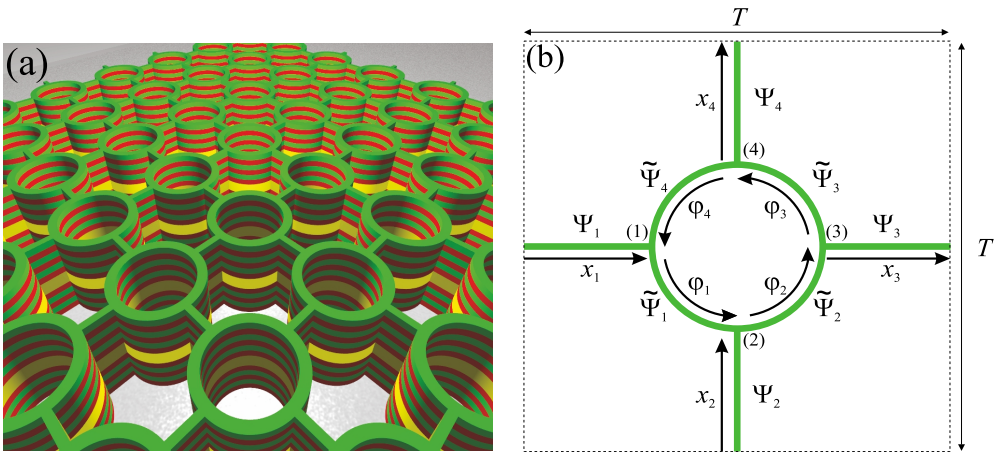

Figure 3.2: (a) Geometry of the structure: two-dimensional square lattice of the exciton-polariton ring resonators connected via leads. (b) A unit cell of the structure: a polariton ring of radius R with four attached leads of length $d/2$. The period of the structure is $T = d + 2R$, and the corresponding variables are defined as $x_{1,2} \in [0, d/2]$, $x_{3,4} \in [-d/2, 0]$ and $\varphi_{1,\ldots,4} \in [0, \pi/2]$. The ring-lead junctions are labeled as (1)-(4).

$$\psi_{3,4}(x) = \frac{1}{\sqrt{\xi_0^2 + 1}} \begin{pmatrix} 1 \\ \xi_0 \end{pmatrix} e^{\pm i k_u x}, \tag{3.22}$$

where $k_{u,l} = R^{-1}\sqrt{E \mp \sqrt{\Delta_1^2 + (\Delta_2/2)^2}}$ and

$$\xi_0 = \frac{\Delta_1}{\Delta_2/2 + \sqrt{\Delta_1^2 + (\Delta_2/2)^2}}. \tag{3.23}$$

In the case $E < \sqrt{\Delta_1^2 + (\Delta_2/2)^2}$ only $\psi_{1,2}(x)$ are relevant. Hence, the general solution for the m-th lead ($\mathrm{m} = 1 \ldots 4$, see Fig. 3.2(a)) read

$$\Psi_{\mathrm{m}}(x) = \sum_{\mathrm{i}} C_{\mathrm{m}}^{(\mathrm{i})} \psi_{\mathrm{i}}(x), \tag{3.24}$$

where the summation is performed over all real roots of Eq. (3.20) for a given energy. Similarly, for the $\widetilde{\mathrm{m}}$-th arc ($\widetilde{\mathrm{m}} = 1 \ldots 4$), in obedience to Eq. (3.18), we have

$$\widetilde{\Psi}_{\widetilde{\mathrm{m}}}(\varphi) = \sum_{\mathrm{i}} \widetilde{C}_{\widetilde{\mathrm{m}}}^{(\mathrm{i})} \widetilde{\psi}_{\mathrm{i}}(\varphi), \tag{3.25}$$

where the summation is performed over all real roots of Eq. (3.11).

To define the behavior of the polariton waves at the junctions connecting the rings and the leads we use Griffith's boundary conditions [255] stating that the wave functions

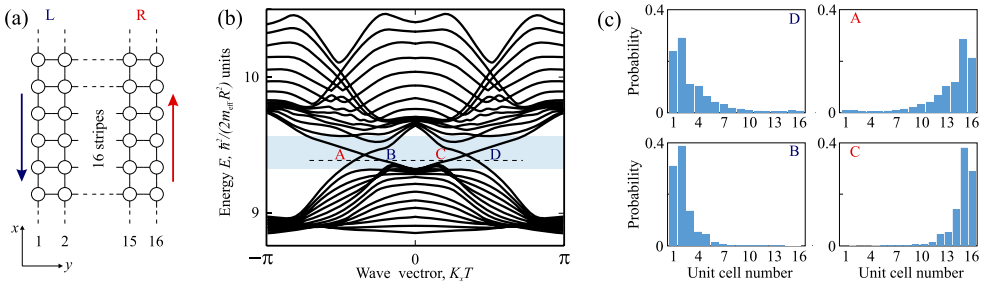

Figure 3.3: Topologically protected edge states for $\Delta_1 = 5$, $\Delta_2 = 2$ and $h = d/R = 1.2$. The corresponding Chern number $C = 2$ is a sum of all C_n below the energy level (denoted by the dashed black line). (a) The geometry of the structure: a two-dimensional square lattice of the exciton-polariton ring resonators that is infinite in the x-direction and finite in the y-direction. Blue and red arrows indicate the directions of the propagation along left and right edges. (b) Band structure of the stripe consisting of 16 periods in the y-direction. The rectangle marks the bandgap of the bulk system. For a given energy marked by the dashed line there are two edge states labeled as A and C corresponding to the right boundary, and two states B and D corresponding to the left boundary. Note, that the sign of the group velocity is the same for the states propagating along the same edge. This means that these states are chiral and topologically protected with respect to backscattering. (c) Probability distribution profiles of the edge states marked at the band diagram. Direction of their propagation is set by the sign of the product $B_z g$.

have to be continuous and the input probability currents must be exactly compensated by the output. Together with the Bloch periodic boundary condition, this gives the closed set of linear algebraic equations allowing to define the band structure of the system.

The scattering equations for the junctions (1) through (4) in Fig. 3.2(b) are given by

Griffith's conditions [255] and read as follows

$$\begin{aligned} &\Psi_1(d/2) = \widetilde{\Psi}_4(\pi/2) = \widetilde{\Psi}_1(0) \\ &R\Psi_1'(d/2) + \widetilde{\Psi}_4'(\pi/2) = \widetilde{\Psi}_1'(0), \end{aligned} \tag{3.26}$$

$$\begin{aligned} &\Psi_2(d/2) = \widetilde{\Psi}_1(\pi/2) = \widetilde{\Psi}_2(0) \\ &R\Psi_2'(d/2) + \widetilde{\Psi}_1'(\pi/2) = \widetilde{\Psi}_2'(0), \end{aligned} \tag{3.27}$$

$$\begin{aligned} &\Psi_3(-d/2) = \widetilde{\Psi}_2(\pi/2) = \widetilde{\Psi}_3(0) \\ &R\Psi_3'(-d/2) + \widetilde{\Psi}_3'(0) = \widetilde{\Psi}_2'(\pi/2), \end{aligned} \tag{3.28}$$

$$\begin{aligned} &\Psi_4(-d/2) = \widetilde{\Psi}_3(\pi/2) = \widetilde{\Psi}_4(0) \\ &R\Psi_4'(-d/2) + \widetilde{\Psi}_4'(0) = \widetilde{\Psi}_3'(\pi/2), \end{aligned} \tag{3.29}$$

Due to the lattice periodicity, the Bloch boundary condition read

$$\begin{aligned} C_3^{(\mathrm{i})} &= e^{iK_xT} C_1^{(\mathrm{i})} \\ C_4^{(\mathrm{i})} &= e^{iK_yT} C_2^{(\mathrm{i})} \end{aligned} \tag{3.30}$$

where $\mathbf{K} = (K_x, K_y)$ is the polariton envelope wave vector originating from the periodicity of the array and $T = d + 2R$ is the period of the array. Eqs. (3.26)-(3.30) form a set of linear equations for the variables $\{C_{\mathrm{m}}^{(\mathrm{i})}\} \cup \{\widetilde{C}_{\widetilde{\mathrm{m}}}^{(\mathrm{i})}\}$. The secular equation in obtained by equating the determinant to zero.

It should be noted that one may use the S-matrix approach instead of imposing Griffith's conditions.

Once the spectrum of the bulk system is obtained from the secular equation, the Chern numbers can be calculated. The Chern number corresponding to the n-th band of the considered periodic array is defined as

$$C_n = \frac{1}{2\pi i} \int\limits_{1\mathrm{BZ}} d^2K F_{xy}(\mathbf{K}), \tag{3.31}$$

where $F_{xy}(\mathbf{K}) = \partial A_y/\partial K_x - \partial A_x/\partial K_y$ is the field strength associated with the Berry connection, $A_j(\mathbf{K}) = \langle n(\mathbf{K})|\frac{\partial}{\partial K_j}|n(\mathbf{K})\rangle$ is the vector potential of the field, and $|n(\mathbf{K})\rangle$ is the normalized Bloch wave function of the n-th band [256]. The integration is performed over the first Brillouin zone (1BZ).

Topological gaps open in the case of non-zero both TE-TM and Zeeman splittings. The Chern numbers are calculated for the gapped system (see the caption of Fig. 3.3). Since there are gaps with non-zero Chern invariant, the bulk-boundary correspondence

suggests the existence of topologically protected edge states for a finite lattice. To explore the properties of the edge states, one should add the boundaries to the system. Let us consider the system depicted in Fig. 3.3(a): a strip composed of 16 rings in the y-direction and infinite in the x-direction. The spectrum of the strip can be obtained by writing down Eqs. (3.26)-(3.29) for the rings $2 \dots 15$ supplemented by a slightly modified version of these equations for the outer rings (number 1 and 16 in Fig. 3.3(a)) as they are deprived of the first and fourth leads respectively. Also, one should add the Bloch condition only for the x-direction as the periodicity is broken in the y-direction. Finally, we obtain a linear system for the variables $\{C^{(\mathrm{i})}_{\aleph,\mathrm{m}}\} \cup \{\widetilde{C}^{(\mathrm{i})}_{\aleph,\widetilde{\mathrm{m}}}\}$ (where $\aleph = 1 \dots 16$ numbers the unit cells along an arbitrarily chosen row in Fig. 3.3(a)), with the secular equation yielding the spectrum, presented in Fig 3.3(b).

As can be seen from Fig. 3.3(b), there exist topological edge states at the bulk gap. For a given energy level, plotted with the dashed black line in Fig. 3.3(b), there exist two edge states per boundary. The wave function density at the unit cell scale, corresponding to the edge states, is shown in Fig. 3.3(c). Similar to the case of QHE, edge states are chiral and topologically protected: the direction of the propagation is linked to the edge, so backscattering is possible only if it is accompanied by hopping from one edge to another.

3.4 Zigzag chain of polariton rings

We now proceed to the analysis of zigzag arrays of polariton rings. Let us consider a system of rings connected into a zigzag chain as shown in Fig. 3.4. It is reminiscent of the Su-Schrieffer-Heeger model [251], where each carbon atom of polyacetylene is replaced with a polariton ring and the role of the 'relative-bond-strength' (for polyacetylene) is played by the 'bond angle α (see Fig. 3.4(a)). In this section, we focus on the effects that arise in the absence of an external magnetic field ($B_z = 0 \Rightarrow \Delta_2 = 0$). The application of the external magnetic field in the case of the 1D chain of the rings does not change significantly the results.

As shown in Fig. 3.4(a), there are two rings per unit cell and within each unit cell, there are different effective magnetic fields in the leads that are not parallel to each other. The directions of these effective magnetic fields depend on the angle α.

In a similar manner as in the previous section, we immediately derive the scattering equations given by Griffith's and Bloch's boundary conditions. For the junctions from

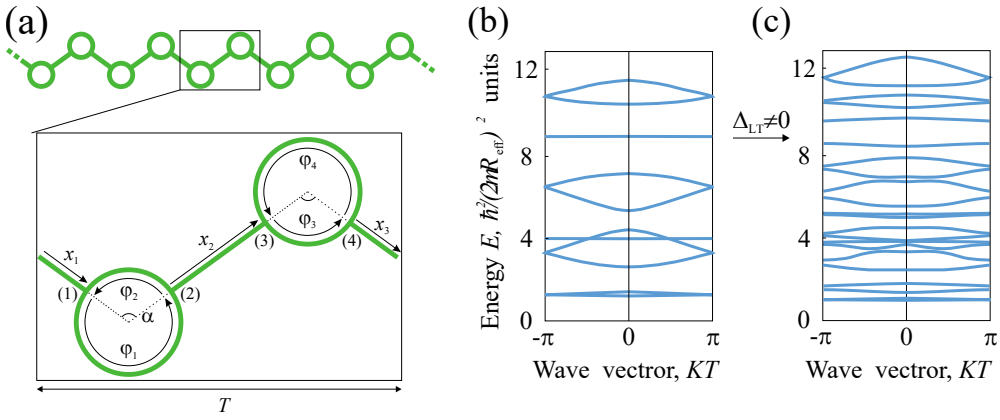

Figure 3.4: (a) Sketch of a zigzag array of polariton rings and a unit cell of the structure. Each ring is of radius R and each lead is of length d. The period of the structure is $T = 2(d + 2R)\sin\alpha/2$. The corresponding variables are defined as $\varphi_{1,4} \in [0, 2\pi - \alpha]$, $\varphi_{2,3} \in [0, \alpha]$ and $x_1 \in [0, d/2]$, $x_2 \in [-d/2, d/2]$, $x_3 \in [-d/2, 0]$. The band diagram for an infinite zigzag chain (with $\alpha = \pi/2$) in the absence of LT-splitting ($\Delta_1 = 0$) (b) and at $\Delta_1 = 2$ (c).

(1) to (4) in Fig. 3.4(a) they read as follows

$$\begin{aligned} &\Psi_1(d/2) = \widetilde{\Psi}_2(\alpha) = \widetilde{\Psi}_1(0) \\ &R\Psi_1'(d/2) + \widetilde{\Psi}_2'(\alpha) = \widetilde{\Psi}_1'(0), \end{aligned} \tag{3.32}$$

$$\begin{aligned} &\Psi_2(-d/2) = \widetilde{\Psi}_1(2\pi - \alpha) = \widetilde{\Psi}_2(0) \\ &R\Psi_2'(-d/2) + \widetilde{\Psi}_2'(0) = \widetilde{\Psi}_1'(2\pi - \alpha), \end{aligned} \tag{3.33}$$

$$\begin{aligned} &\Psi_2(d/2) = \widetilde{\Psi}_4(2\pi - \alpha) = \widetilde{\Psi}_3(0) \\ &R\Psi_2'(d/2) + \widetilde{\Psi}_4'(2\pi - \alpha) = \widetilde{\Psi}_3'(0), \end{aligned} \tag{3.34}$$

$$\begin{aligned} &\Psi_3(-d/2) = \widetilde{\Psi}_3(\alpha) = \widetilde{\Psi}_4(0) \\ &R\Psi_3'(-d/2) + \widetilde{\Psi}_4'(0) = \widetilde{\Psi}_3'(\alpha). \end{aligned} \tag{3.35}$$

Due to the chain periodicity, the Bloch boundary condition read

$$C_3^{(i)} = e^{iKT} C_1^{(i)}. \tag{3.36}$$

The secular equation is found by setting the determinant to zero.

For $\alpha = \pi/2$ and zero effective magnetic field, the corresponding band diagram (see

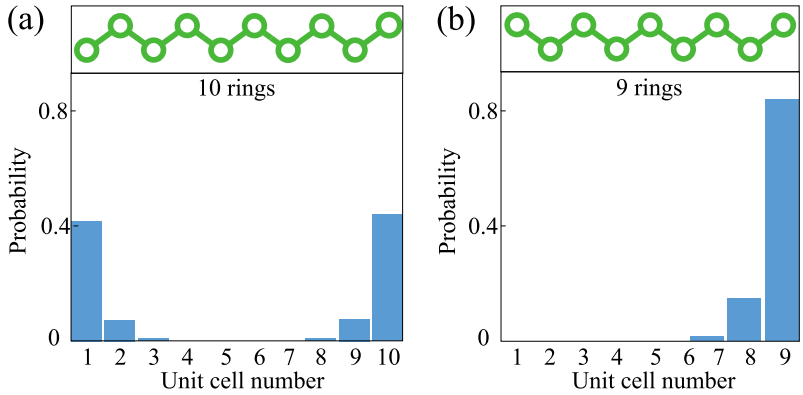

Figure 3.5: Probability distribution of the edge states in polariton ring zigzag chains with $\alpha = \pi/2$ and $h = d/R = 1.2$ for even (a) and odd (b) number of rings. In the odd number case (b) there also exists a symmetric edge state that is localized on the left side of the chain. The profiles are shown for $\Delta_1 = 2$, $E = 8.985$ (in $\hbar^2/(2m_{eff}R^2)$ units). The energy value is chosen to lay within the bulk bandgap.

Fig. 3.4(b)), exhibits flat bands that are reminiscent of Landau levels related to the states localized within the ring. As we introduce a non-zero LT-splitting, new gaps open (see Fig. 3.4(c)). As one introduces boundaries to the system the edge states appear (see Fig. 3.5(a) and (b)). In both cases in Fig. 3.5 (the even and the odd number of the rings), the edge states are twice degenerate. Thus, by taking their linear combination one can prepare a state localized either at both sides of the chain or at one side. We note that in the case of the chain, no external magnetic field is required for the emergence of the edge-states since the angle α not equal to π breaks the equivalence of the clockwise and counter-clockwise propagating modes in the separate rings. As the angle, α gets closer to π, the localization length of the edge states increases.

3.5 Conclusions and Outlook

To conclude, we have shown that a two-dimensional array of the polariton rings is characterized by the non-trivial Chern invariants and supports topologically protected chiral edge states analogously to the case of Quantum Hall insulator. Also, the edge states are shown to emerge in a zigzag chain of polariton rings. The existence of topologically protected states can find their applications in spintronics.

4 Dynamics of spin polarization in tilted polariton rings

We have observed the effect of a pseudo magnetic field originating from the polaritonic analog of spin-orbit coupling (TE−TM splitting) on a polariton condensate in a ring-shaped microcavity. The effect gives rise to a stable four-leaf pattern around the ring as seen from the linear polarization measurements of the condensate photoluminescence. This pattern is found to originate from the interplay of the cavity potential, energy relaxation, and TE-TM splitting in the ring. Our observations are compared to the dissipative one-dimensional spinor Gross-Pitaevskii equation with the TE-TM splitting energy which shows good qualitative agreement.

4.1 Introduction

Over a decade has passed since the first demonstration of Bose-Einstein condensation of exciton-polaritons in a semiconductor microcavity [243, 271]. It stands out as a unique platform for exploring physics of out of equilibrium systems. Recent reports on the observation of thermal equilibration [272, 273] on one hand has triggered interest in studying equilibrium physics in non-hermitian systems, while on the other have shown promise for making devices based on polariton condensates that operate near equilibrium. Such a feat has been achieved in microcavities with $Q > 10^5$, allowing several collision events between polaritons to distribute energy and thermalize in their lifetime [272–275].

These systems also naturally offer a way for describing a pseudo-spin 1/2 Bose gas [276]. The order parameter of a polariton condensate is described by a two-component complex valued spinor, which is connected to the electric polarization of the polaritons in the microcavity [277]. In the presence of a non-aligned magnetic field the spin of the polaritons is precessing similarly to the spin of an electron in a magnetic field. It turns out that for a quantum well embedded inside a semiconductor microcavity, a small but non-negligible momentum dependent effective magnetic field is present which lies in the plane of the quantum well. This has been used to realize a polaritonic analog of extrinsic [278] as well as intrinsic [279] spin Hall effect. In contrast to the electronic systems where the spin Hall effect gives rise to a spin current and no mass transport,

the optical spin Hall effect is realized by actual transport of polaritons while the spin of the polaritons precess as they move.

In this chapter, we address how the two spinor components of a gas of highly excited trapped polaritons evolve following a quench in a long lifetime ($\approx$ 200 ps) microcavity. The trapping potential is created by patterning the top mirror of the GaAs microcavity in the shape of a ring. The polaritons in the ring maintain the same long lifetime ($\approx$ 200 ps), high quality ($Q > 10^5$), and low disorder as in the two-dimensional planar microcavity used previously [272, 274, 280–282]. With the presence of a unidirectional gradient in the energy of the polaritons, the circular symmetry of the ring is broken, giving rise to a rigid rotor potential. Combined with a momentum-dependent effective magnetic field in the trap, this results in an intrinsic optical spin Hall effect as the polaritons are transported to the region with the lowest energy in the trap. We map the spin of the condensed polaritons in the ring using space- and time-resolved spin-polarized spectroscopy.

The rings are fabricated by etching the top distributed Bragg reflector (DBR) of this microcavity in the shape of rings of width (the difference of the outer and the inner radii) 15 μm and radius (average of outer and inner radii) 50 μm. Further details may be found in the previous papers [282–284]. Across the typical dimensions of the ring, the thickness of the microcavity varies which leads to a cavity energy gradient ($\approx 7-9$ meV/mm). The cavity gradient effect is similar to artificial gravity for the polaritons making the rings look tilted on the potential energy plane. Due to the analogy to gravity, here we will refer to the point of highest potential energy as the "top" of the ring, and the point of lower potential energy, on the opposite side of the ring, as the "bottom". The effect of artificial gravity on the spin-polarized polaritons has been theoretically studied in Ref. [285].

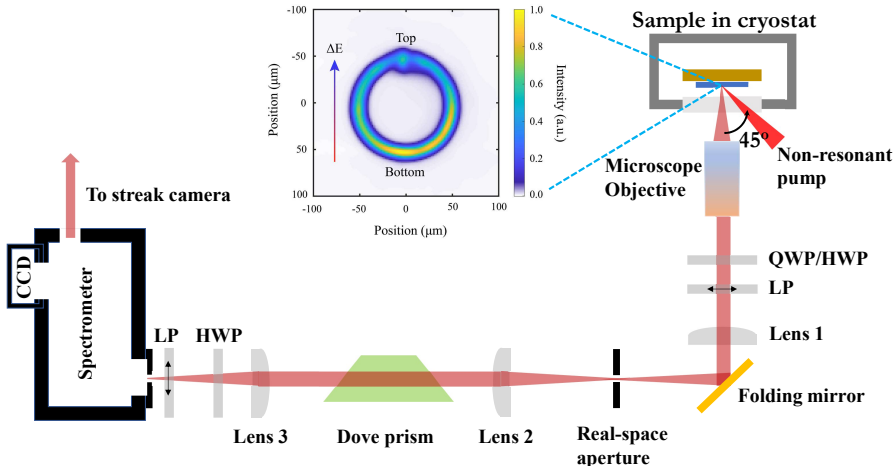

Figure 4.1: Schematic of the experimental setup. Inset shows a time integrated image of the photoluminiscence from the ring microcavity also showing the direction of the cavity gradient ΔE. QWP: quarter waveplate, HWP: half waveplate, LP: linear polarizer.

4.2 Experiment

The top of the rings is non-resonantly pumped ($E_{\text{pump}} \approx 1710$ meV which is at least 100 meV higher than the energy of the lower branch polaritons at the point of excitation) with a mode-locked Ti:sapphire laser with a pulse repetition rate of 76 MHz, a pulse width of ≈ 2 ps, a spot size of ≈ 15 μm on the sample and incident at an angle of $\approx 45°$ from the plane of the sample with more than 90% linear polarization. Due to the high angle injection, the pump spot is not circular on the plane of the sample and creates asymmetry in the direction of the polaritons streaming from the pump spot. Photoluminescence (PL) from the rings was collected using a microscope objective with a numerical aperture (NA) of 0.40 and imaged onto the entrance slit of a spectrometer. The image was then sent through the spectrometer either to a standard charged coupled device (CCD) chip located at one of the exit ports of the spectrometer for time-integrated imaging or onto a Hamamatsu streak camera located at the other exit port for time-resolved imaging. All measurements were performed by cooling the microcavity to low temperature (below 10 K) in a continuous-flow cold-finger cryostat. A sketch of the experimental setup is shown in Fig. 4.1.

The non-resonant optical pulse excites a population of free electrons and holes at the top of the ring which undergoes rapid thermalization, turning into excitons. Excitons further relax down in energy and reach the anti-crossing spectral region of the photonic and excitonic dispersion branches, forming a dense polariton gas (see, for example, Tassone et al. [286]), which above a critical density undergoes non-equilibrium Bose-

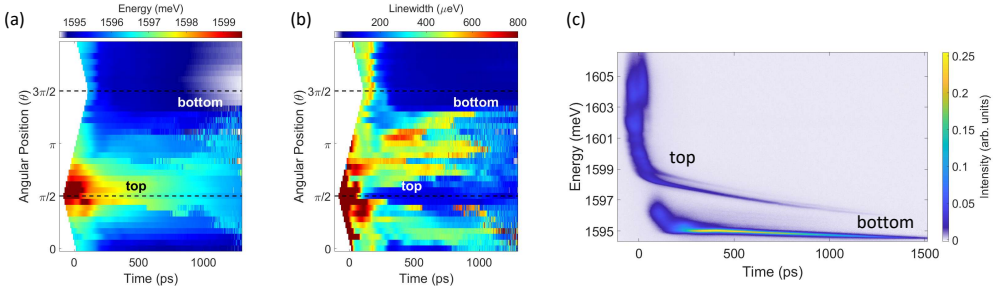

Figure 4.2: Example of condensate energy (a) and linewidth (b) as a function of time from different locations on the ring. $3\pi/2$ corresponds to the bottom of the ring. The zero of the time axis corresponds to the time of excitation at the top of the ring. The condensate energy is obtained at each spatial location by fitting a lorentzian function to the energy- and time- resolved image captured by the streak camera. (c) shows a spectral comparison between the PL emission from the top and bottom of the ring as a function of time.

Einstein condensation. This non-equilibrium condensate streams out ballistically from the excitation spot and fills the entire ring, while also dropping in energy as it moves in the ring. As shown in Fig. 4.2 (c) the polaritons are initially formed with large blue-shifted energy at the pump spot which rapidly redshifts with time. This is followed by a spectrally narrow emission which slowly drops in energy, asymptotically approaching the $k_{||} = 0$ lower polariton energy at this location. The initial blue shift seen at the pump spot is due to the interaction of polaritons with the exciton cloud. The rate of energy drop of the polaritons measures the rate at which the exciton cloud decays. By the time the polaritons arrive at the bottom of the ring trap, it has already undergone considerable energy relaxation ($\approx$ 2 meV). The energy- and time-resolved image from the bottom in Fig. 4.2 (c) shows that as the occupation density of the polaritons increases, the spectral linewidth of the emission narrows indicating a build-up of coherence in the bottom of the trap. We have combined the streak images from the top and bottom of the ring for comparison in Fig. 4.2 (c). In Fig. 4.2 (a) and (b) we show spatially and temporally resolved energy and linewidth of the emission from the full ring. From these plots, we infer that the spatial coherence extends at most to one-third of the ring circumference at any given point in time, which is signaled by the energy locking of the emission. At late times the energy of the emission approaches the local, low density $k_{||} = 0$ lower polariton energy.

We resolved the polarization of the PL from the ring by performing a full Stokes vector measurement (S_0, S_1, S_2, S_3) using combinations of half or quarter waveplate and a linear polarizer. The measurement was done on the collimated signal just after the microscope objective. The transmission axis of the polarizer was chosen to be vertical in the lab frame and was kept fixed throughout the experiment. This was done to remove the polarization sensitivity of the optics downstream in the setup. We used

another half waveplate and a polarizer before the entrance slit of the spectrometer to collect all the signal which didn't get reflected, scattered or absorbed after passing through the optics. For all the measurements the orientation of the transmission axis of the final polarizer was also kept fixed, which removed the polarization sensitivity of all the optics inside the spectrometer as the light that entered the spectrometer was always at a fixed linear polarization. Two images were taken for each individual measurement, one with the half waveplate fast axis (placed just before the final polarizer) at 0° and one with it at 45°. By adding these two images together, the total contribution of both polarizations (both parallel and orthogonal to the final polarizer) was taken into account.

Time-resolved Stokes vector measurements were done using the streak camera. A diametric slice of the image of the ring was aligned with the horizontal time slit of the streak camera. To collect the PL from a different location on the ring, the image was rotated using a dove prism. The dove prism was placed in a nearly collimated region of the optical path, as shown in Fig. 4.1. Before the experiment, the dove prism was carefully aligned to minimize the image walk-off when the prism was rotated by adjusting the tilt screws on the mount. Small adjustments were made during data collection by moving the final imaging lens, Lens 3, in the transverse plane to ensure consistent overlap of the diametric slice of the ring with the time slit. We note that the intensity collected by the streak camera after a pulsed excitation of the ring is the sum of the intensity of millions of such realizations. The density of polaritons created by each pulse was above the critical density of polaritons required for undergoing Bose-Einstein condensation (BEC) at the given temperature. If the realization of each instance of the BEC picks up a random polarization state in the ring, then by averaging we should obtain a strong component of unpolarized light in the emission. However, from previous time-resolved studies on spontaneously formed polariton BEC, it is known that the polarization of the BEC is not random and is sensitive to underlying crystal symmetries and other symmetries or imperfections of the microcavity. Therefore, the degree of polarization is an important parameter distinguishing between emission from condensed and uncondensed or excited polaritons.

We compare the time-resolved polarization of the PL emission from the point of excitation (top) and the diametrically opposite point (bottom) on the ring in Fig. 4.3. We find a rapid build-up of the degree of polarization (DOP) of the emission at the pump spot following the arrival of the pump pulse. This is correlated with a decrease in the PL emission intensity at the pump spot. This signal is post hot thermalization and indicates the appearance of a local non-equilibrium condensate that undergoes further energy relaxation. As the condensate streams and fills the ring, the DOP plateaus. At the same time, there is a slow build-up of the polarized emission from the bottom of the ring which persists as long as the polaritons leak from the microcavity. In contrast, the DOP drops at the pump location after plateauing because the condensate drifts away from this location towards the bottom of the ring. The oscillations in the intensity of the PL emission from the bottom of the ring is due to the pendulum-like oscillations about the ring trap minimum [284].

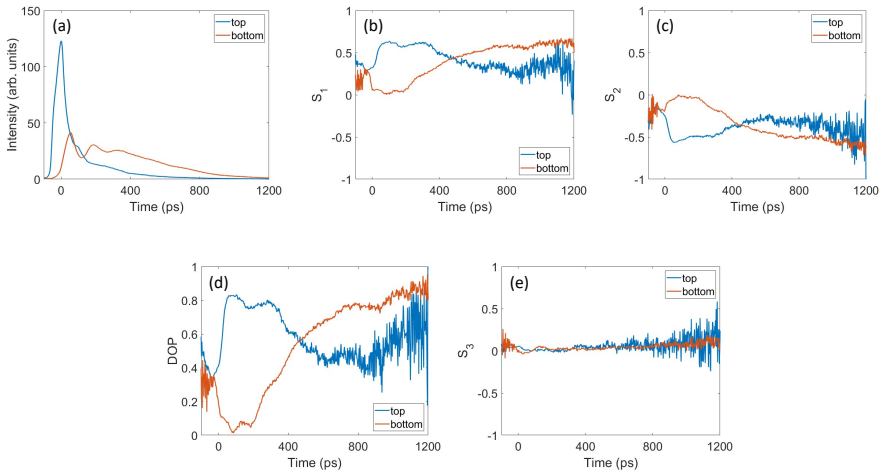

Figure 4.3: Comparison of the polarization between the top and bottom of the ring as a function of time. Degree of polarization (DOP) is given by $\sqrt{S_1^2 + S_2^2 + S_3^2}$.

Measurement of the time-resolved components of the Stokes vector from different angular positions on the ring are shown in Fig. 4.6 and a Bloch vector visualization at different time instances are shown in Fig. 4.4. The circular polarization component S_3 in these measurements reveal that before the appearance of condensate in the ring, highly excited non-thermal polaritons moving out from the pump spot show spin imbalance polarity depending on whether they are moving in the clockwise or anti-clockwise direction. This is due to the polariton pseudo-spins experiencing the effect of the in-plane magnetic field arising due to the splitting of the transverse electric (TE) and transverse magnetic (TM) mode in the cavity and depending on the polariton wave-vector. It is easily verified in a simulation showing the time evolution of a linearly polarized wavepacket under the TE-TM splitting Hamiltonian.

The linear polarization components S_1 and S_2 show a spontaneous emergence of four-leaf angular pattern as shown in Fig. 4.6 (b) and (c). This pattern persists in the ring until the polaritons fully leak from the microcavity. Manifestation of this pattern could be visualized by representing the Stokes vector on the Bloch sphere and tracing it around the ring. The projection of the Stokes vector on the equatorial plane of the Bloch sphere gives the component of linear polarization of the emission. This is shown in black arrows in Fig. 4.4 at different time instances. We see in these figures and in Fig. 4.5 that after t = 265 ps, the linear polarization component appears to wrap around the ring by 4π radians, which corresponds to a rotation by 2π radians for the major axis of the elliptically polarized emission from the ring. In Fig. 4.5 we compare the direction of the linear polarization of the Stokes vector from different angular positions in the ring at two different time instances. The wrapping of the linear polarization component by 4π radians is found at t = 265 ps, while it only wraps by

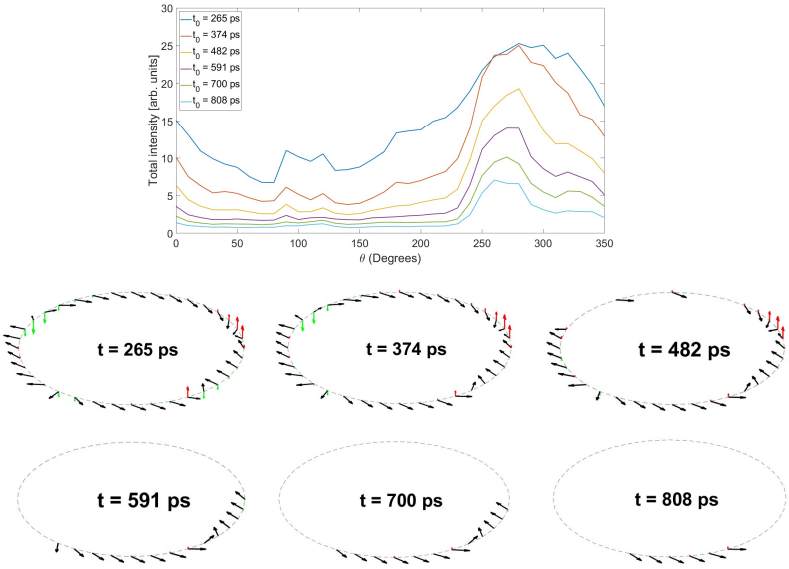

Figure 4.4: PL intensity from the ring at different time instances t_0 and the corresponding polarized emission shown with the Bloch sphere representation of the Stokes vectors at different angular positions on the ring. Black arrows depict the projection of the Stokes vector on the equatorial plane of the Bloch sphere. The length of the arrow is a measure of the degree of linear polarization within the polarized sector of emission and half of the angle w.r.t. the positive x-axis measures the direction of the linear polarized light. The red and green arrows depict the spin up and spin down projection of the polariton spinor respectively. The length of these arrows indicate the degree of circular polarization (or spin polarization) of the polaritons. Stokes vectors for intensity below a cut-off level ($I_{cut} = 3$) is not plotted due to poor signal to noise ratio. The linear polarization pattern in the time range shown is quasi-stationary.

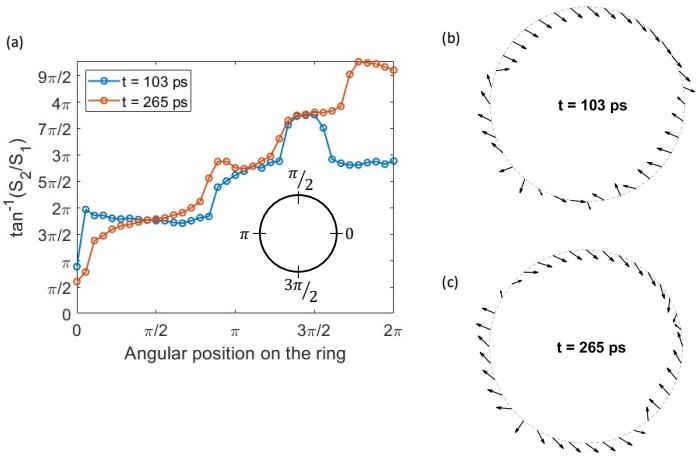

Figure 4.5: (a) The direction pointed by the linearly polarized Stokes vector $S_1\hat{x} + S_2\hat{y}$ around the ring at two-time instances. The angle $tan^{-1}(S_2/S_1)$ has been unwrapped in the range $[0, 6\pi]$. (b) and (c) show the linearly polarized Stokes vector in the ring at $t = 103$ ps and $t = 265$ ps respectively.

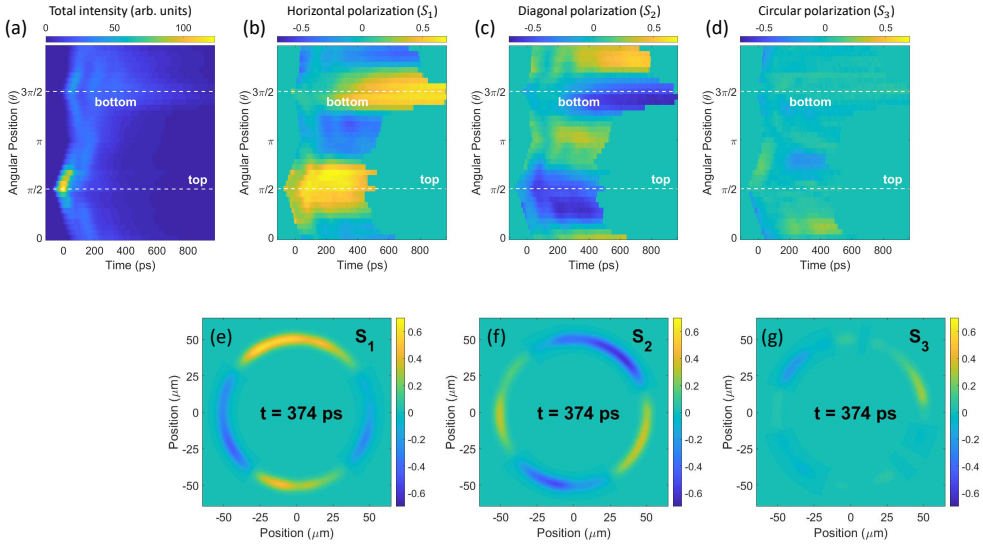

Figure 4.6: Example of time and polarization resolved PL from tilted ring. Components of the Stokes vector S_0, S_1, S_2 and S_3 measured at an angular resolution of 10° as a function of time. We integrated the polarization resolved PL over the radial width of the ring to process the Stokes components at any given angular position on the ring. The intensity collected by the streak camera after a pulsed excitation of the ring is the sum of the intensity of millions of such realizations. Bottom row shows the four-leaf pattern in the components S_1 and S_2 at $t = 374$ ps.

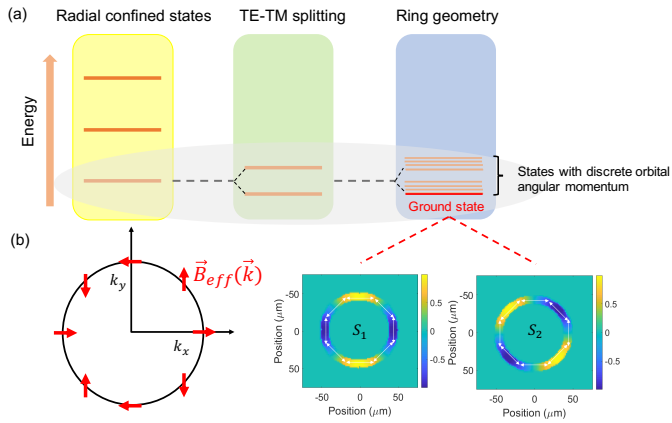

Figure 4.7: (a) A schematic showing the effect of the radial confinement, TE-TM splitting and the ring geometry on the quantum states in the ring. Visualization of the expectation value of the Stokes components in the ground state of the ring without the tilt is also shown. In the ground state $S_z = 0$ while S_1 and S_2 components are phase shifted by $\pi/4$ w.r.t. each other. The white arrows depict the polarization plane direction, corresponding to the local Stokes parameters. In the ground state the polarization wraps in the azimuthal direction in the ring. (b) Direction of the effective magnetic field due to TE-TM splitting shown with red arrows in the momentum space.

2π radians at t = 103 ps. The linear polarization component forms domains in the ring where the direction changes slowly within a domain while across a domain there is a change in the direction by $\pm\pi/2$ or more. The direction of the linear polarization component from the lower half of the ring remains nearly stationary in time after t = 265 ps as shown in Fig. 4.4. This is despite the fact that there is a noticeable angular variation of the intensity of emission from this region with time as shown in S_0 component in Fig. 4.6 (a) as well as in Figure 4.4. Both spatial and temporal dependence of the PL intensity from the ring indicates a variation of the density of the polaritons in the ring. The overall polarization component of the emission does not show a strong dependence on the polariton density which could be deduced from plots of the Stokes vector around the ring in Fig. 4.4. We can thus conclude that the interactions between the polaritons do not play a dominant role in determining the polarization direction of the emission. At late times, the non-equilibrium state shows very little spin imbalance as shown in Fig. 4.6 (d) which is due to good spatial overlap of nearly identical density profiles of the two spin components.

In the following section, we develop a minimal model capturing the qualitative features discussed above highlighting the essential physics needed to interpret our observations. We derive an effective one-dimensional Hamiltonian by projecting the two-dimensional Hamiltonian onto the ground state of the radially confining potential due to the finite

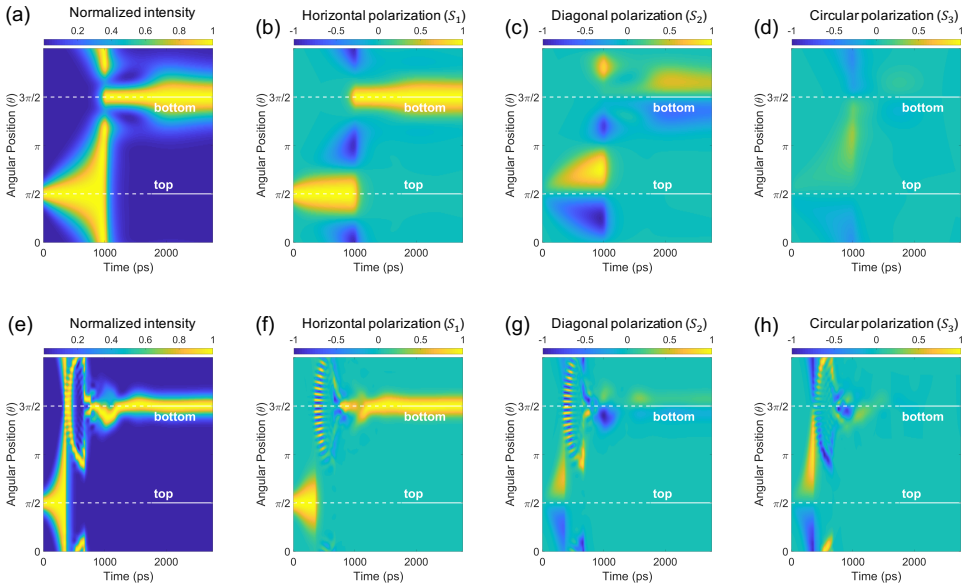

Figure 4.8: Time evolution of the horizontally polarized condensate spinor. Parameters for both rows are $m_{eff} = 6.14 \times 10^{-5} m_0$, $B = 0.05$, $\tau = 200$ ps, and $\Delta = 250$, where m_0 is the rest mass of an electron in vacuum. Top row (a-d): $V_0 = 16$, $\Lambda = 1$; Bottom row (e-h): $V_0 = 335$, $\Lambda = 0.3$; A larger energy damping rate is chosen for smaller tilt case (top row) because the initial state has a lower potential energy than the larger tilt case (bottom row), so energy relaxation is slower for the same value of Λ in the smaller tilt case.

width of the ring channel. The periodicity of the wavefunction in the azimuthal direction results in discrete orbital angular momentum states in the ring. We assume that the polaritons occupy only a small part of the lower polariton dispersion near $k_{||} = 0$, allowing us to make an effective mass approximation for the polaritons. The cavity gradient in the ring reduces the circular symmetry to left-right mirror symmetry in the ring. It also creates a small spatial anisotropy in the TE-TM splitting energy which is ignored in the present model. A schematic of the quantum states in the ring in absence of a cavity gradient is shown in Fig. 4.7 (a). We also neglect the spin-dependent interactions for reasons discussed previously.

4.3 Theoretical model

Here we present the theoretical model of a single polariton ring of radius R and width a with a cavity gradient along the vertical axis (see the inset in Fig. 4.1), where only

the lowest radial mode is occupied.

We start with the Hamiltonian of 2D polaritons inside a planar microcavity neglecting the cavity width gradient [291]

$$\widehat{H}_{2D} = \begin{pmatrix} \widehat{H}_0(\hat{\mathbf{k}}) & \widehat{H}_{\text{TE-TM}}(\hat{\mathbf{k}}) \\ \widehat{H}^{\dagger}_{\text{TE-TM}}(\hat{\mathbf{k}}) & \widehat{H}_0(\hat{\mathbf{k}}) \end{pmatrix}, \tag{4.1}$$

where the diagonal terms $\hat{H}_0$ describe the kinetic energy of lower cavity polaritons, and the off-diagonal terms $\widehat{H}_{\text{TE-TM}}$ correspond to the TE-TM splitting. We further employ the effective mass approximation

$$\widehat{H}_0(\hat{\mathbf{k}}) = \frac{\hbar^2 \hat{\mathbf{k}}^2}{2m_{\text{eff}}}. \tag{4.2}$$

The TE-TM part is given by

$$\widehat{H}_{\text{TE-TM}}(\hat{\mathbf{k}}) = \beta \left(\frac{\partial}{\partial y} + i \frac{\partial}{\partial x} \right)^2, \tag{4.3}$$

where β governs the strength of the TE-TM splitting and may be expressed in the longitudinal and transverse polariton effective masses m_l and m_t as $\beta = (\hbar^2/4)(m_l^{-1} - m_t^{-1})$. In order to proceed with the derivation of the correct 1D Hamiltonian let us pass to the polar coordinates and add the confining potential $V(r)$ confining the polariton wave functions on the ring in the radial direction to the planar cavity Hamiltonian $\widehat{H}_{2D}$. The confining potential is taken as an infinite square well in the radial direction. The terms associated with the TE-TM splitting in polar coordinates read

$$\begin{aligned} &\left(\frac{\partial}{\partial y} \pm i \frac{\partial}{\partial x} \right)^2 = e^{\mp 2i\varphi} \times \\ &\left(-\frac{\partial^2}{\partial r^2} \pm \frac{2i}{r} \frac{\partial^2}{\partial r \partial \varphi} \mp \frac{2i}{r^2} \frac{\partial}{\partial \varphi} + \frac{1}{r} \frac{\partial}{\partial r} + \frac{1}{r^2} \frac{\partial^2}{\partial \varphi^2} \right). \end{aligned} \tag{4.4}$$

We decompose the Hamiltonian Eq. (4.1) into two parts $\widehat{H}_{2D} = \widehat{H}_0(r) + \widehat{H}_1(r, \varphi)$, where

$$\widehat{H}_0(r) = -\frac{\hbar^2}{2m_{\text{eff}}} \left(\frac{\partial^2}{\partial r^2} + \frac{1}{r} \frac{\partial}{\partial r} \right) + V(r). \tag{4.5}$$

Since we can now separate the variables assuming only the lowest radial mode occupation $\widetilde{\Psi}(r, \varphi) = R_0(r)\Psi(\varphi)$, the effective Hamiltonian [253] for $\Psi(\varphi)$ reads

$$\widehat{H} = \langle R_0(r) | \widehat{H}_1(r, \varphi) | R_0(r) \rangle, \tag{4.6}$$

where $R_0(r)$ is the lowest radial mode of the Hamiltonian (4.5). For an infinite square well potential of width a centered at R in the radial direction, the radial modes, which

are non-zero only in $[R-a/2, R+a/2]$, are given by

$$R_n(r) = \tag{4.7}$$
$$A_n\left(Y_0(\frac{\epsilon_n r}{R}) - \frac{Y_0(\epsilon_n(1-\frac{a}{2R})))_0F_1(1;-(\frac{\epsilon_n r}{2R})^2)}{{}_0F_1(1;-(\epsilon_n(1-\frac{a}{2R}))^2/4)}\right),$$

where we introduced the dimensionless energy eigenvalues $\epsilon_n = \frac{\sqrt{2mE_n}R}{\hbar}$ and ${}_0F_1(a;z)$ is the confluent hypergeometric function and A_n is the normalization constant. The eigenvalues ϵ_n satisfy the following equation

$$\frac{Y_0(\epsilon_n(1+\frac{a}{2R}))_0F_1(1;-(\epsilon_n(1-\frac{a}{2R}))^2/4)}{Y_0(\epsilon_n(1-\frac{a}{2R}))_0F_1(1;-(\epsilon_n(1+\frac{a}{2R}))^2/4)} = 1. \tag{4.8}$$

Now we perform the averaging over the lowest radial mode $R_0(r)$ corresponding to the lowest eigenvalue ϵ_0. First we observe $\langle R_0(r)|\frac{1}{r}\frac{\partial}{\partial r}|R_0(r)\rangle = \int_0^\infty R_0(r)R'(r)dr = R_0^2(r)/2|_0^\infty = 0$ for any $R_0(r)$ such that $R_0(0) = R_0(+\infty) = 0$. Then, we calculate $\langle R_0(r)|\frac{\partial^2}{\partial r^2}|R_0(r)\rangle = -C_0/a^2$, where we used that $R_0'' + r^{-1}R_0' = -(2m_{\text{eff}}/\hbar^2)E_0R_0$ and the fact that from dimensional analysis it follows that $E_0 = \hbar^2 C_0/(2ma^2)$, where C_0 is dimensionless. Finally, we have

$$\begin{aligned}
&\langle R_0(r)|\frac{\partial^2}{\partial r^2}|R_0(r)\rangle = -C_0/a^2,\\
&\langle R_0(r)|\frac{1}{r}\frac{\partial}{\partial r}|R_0(r)\rangle = 0,\\
&\langle R_0(r)|\frac{1}{r^2}|R_0(r)\rangle = \mathcal{F}(a/R)/R^2,
\end{aligned} \tag{4.9}$$

where the equation in the last line is obtained from dimensional analysis and $\mathcal{F}(x)$ is a dimensionless function. We approximate $R_0(r)$ by its first Fourier harmonic, which is reasonable as long as only the lowest radial mode is occupied $R_0(r) \approx \sqrt{\frac{2}{aR}}\sin(\frac{\pi(r-(R-a/2)}{a})$. This function is properly normalized $\int_0^\infty R_0^2(r)rdr = 1$ and satisfy the boundary conditions $R_0(R-a/2) = R_0(R+a/2) = 0$. Then, we have $C_0 = \pi^2$ and for $0 < x < 1$ it follows $\mathcal{F}(x) \approx 1$ to two decimal places. Thus, we finally arrive at the following hamiltonian

$$\widehat{H} = \frac{\hbar^2}{2m_{\text{eff}}R^2}\cdot$$
$$\begin{pmatrix} \hat{\hat{k}}^2 & Be^{-2i\varphi}(-\hat{\hat{k}}^2 + 2\hat{\hat{k}} + \Delta) \\ Be^{2i\varphi}(-\hat{\hat{k}}^2 - 2\hat{\hat{k}} + \Delta) & \hat{\hat{k}}^2 \end{pmatrix} \tag{4.10}$$

where $\hat{\hat{k}} = -i(d/d\varphi)$ and the energy levels are now shifted by a constant as compared to the Hamiltonian (4.1). For the sake of simplicity, we introduced a dimensionless parameter B corresponding to the TE-TM splitting as $B = 2\beta m_{\text{eff}}/\hbar^2$ and a dimensionless parameter $\Delta = (\pi R/a)^2$ corresponding to the LT-splitting, stemming from

the confinement in the radial direction. In the case where the ring is infinitely thin, the model reduces to the one described in [288].

In general, solutions of the stationary Schrodinger equation with the Hamiltonian (4.10) can be represented in the following form

$$\Psi_{k,\alpha}(\varphi) = \widetilde{\chi}_\alpha(\varphi, k) e^{ikR\varphi}, \tag{4.11}$$

where $\widetilde{\chi}_\alpha(\varphi, k)$ is the corresponding spinor

$$\widetilde{\chi}_\alpha(\varphi, k) = \frac{1}{\sqrt{\xi_\alpha(k)^2 + 1}} \begin{pmatrix} e^{-i\varphi} \\ \xi_\alpha(k) e^{i\varphi} \end{pmatrix}, \tag{4.12}$$

and

$$\xi_\alpha(k) = -\frac{a^2 B(kR-1)(kR-3) + 8\pi^2 R^2}{a^2((kR+1)^2 - E_k^\alpha)}. \tag{4.13}$$

The energy spectrum of the Hamiltonian can be found analytically, the energy levels are given by

$$E_k^{L,U} = 1 + k^2 R^2 \mp \frac{\sqrt{B^2\pi^4 + 2a^2B^2\pi^2(3 + k^2R^2)R^{-2} + a^4(4k^2R^2 + B^2(9 - 10k^2R^2 + k^4R^4))R^{-4}}}{(a/R)^2} \tag{4.14}$$

in $\hbar^2/(2m_{\text{eff}}R^2)$ units. As we consider polaritons with spin ± 1 as a two-level system, the z-projection of the operator of total angular momentum is $\hat{J}_z = \hbar\hat{\tilde{k}} + \hbar\sigma_z$. One can check that $\hat{J}_z\Psi(\varphi) = \hbar\tilde{k}\Psi(\varphi)$ which clarifies the physical meaning of $\tilde{k} = kR$. The periodic boundary condition imposes the condition $\Psi(\varphi) = \Psi(\varphi + 2\pi)$, which yields integer $\tilde{k}$ corresponding to the quantized orbital angular momentum. According to Eq. (4.14) the energy becomes quantized as well.

To account for the tilt of the well one needs to replace B in the Hamiltonian (4.10) by $B + V_1 \sin\varphi$ and add $V_0 \sin\varphi$ to the diagonal elements, where we assume that the value of the TE-TM splitting, as well as the shift of the energy levels, linearly depends on the width of the well. Having done that, we arrive at the Hamiltonian (4.22), where an additional splitting between linear polarizations is added (see the text) below Eqs. (4.22).

The dependence of the TE-TM splitting on the local width of the ring can be calculated as follows. Introducing the coefficient

$$L_{\text{DBR}} = \frac{n_a n_b \bar{\lambda}}{2(n_b - n_a)}, \tag{4.15}$$

which is frequently called the effective length of a Bragg mirror, where $n_{a,b}$ are the refractive indexes of the layers comprising the DBRs and $\bar{\lambda}$ is the wavelength, corresponding to the central frequency of the stop-band $\bar{\lambda} = 2\pi c/\bar{\omega}$. Next, introducing

$$\delta = \omega_c - \bar{\omega} \tag{4.16}$$

where ω_c is the real part of the cavity complex eigenfrequency, the TE-TM splitting thus reads [276]

$$\omega^{\mathrm{TE}}(L_c, \omega_c, \phi_0) - \omega^{\mathrm{TM}}(L_c, \omega_c, \phi_0) \approx \frac{L_c L_{\mathrm{DBR}}}{(L_c + L_{\mathrm{DBR}})^2} \frac{2\cos\phi_{\mathrm{eff}} \sin^2\phi_{\mathrm{eff}}}{1 - 2\sin^2\phi_{\mathrm{eff}}} \delta, \tag{4.17}$$

where $\phi_{\mathrm{eff}} \approx \arcsin\left((n_0/n_c)\sin\phi_0\right)$, the coefficients and L_c is the width of the cavity, n_0 and n_c are the refractive indexes of the surrounding media and the cavity respectively. Now, one can relate the parameters $B = \beta m_{\mathrm{eff}}/\hbar^2$ and V_1 introduced in Eq. (4.22) as

$$\begin{aligned} \beta = & \\ & \lim_{k_{||}\to 0} \frac{\hbar(\omega^{\mathrm{TE}}(L_{c,0}, \omega_c, \phi_0) - \omega^{\mathrm{TM}}(L_{c,0}, \omega_c, \phi_0))}{k_{||}^2} = \\ & = \frac{2\hbar L_{c,0} L_{\mathrm{DBR}} (\omega_{c,0} - \bar{\omega}) c^2 n_0}{(L_{c,0} + L_{\mathrm{DBR}})^2 n_c^2 \omega_{c,0}^2}, \end{aligned} \tag{4.18}$$

and

$$\begin{aligned} & \beta + \frac{\hbar^2 V_1}{m_{\mathrm{eff}}} = \\ & \lim_{k_{||}\to 0} \frac{\hbar(\omega^{\mathrm{TE}}(L_{c,\pi/2}, \omega_c, \phi_0) - \omega^{\mathrm{TM}}(L_{c,\pi/2}, \omega_c, \phi_0))}{k_{||}^2} = \\ & = \frac{2\hbar L_{c,\pi/2} L_{\mathrm{DBR}} (\omega_{c,0} - \bar{\omega}) c^2 n_0}{(L_{c,\pi/2} + L_{\mathrm{DBR}})^2 n_c^2 \omega_{c,0}^2}, \end{aligned} \tag{4.19}$$

where $k_{||} = (\omega_c/c)\sin\phi_0$ and $L_{c,0}$, $L_{c,\pi/2}$ are the widths of the cavity at the points of the ring defined by $\varphi = 0, \pi$, respectively and $\omega_{c,0}$ is a cavity eigenfrequency at $k_{||} = 0$, which also depends on the local width of the cavity.

Let us investigate the ground state of a flat ring (no tilt) and in the absence of birefringence. For the experimentally relevant values $B = 0.052$ and $\Delta = 61.36$, the ground state $\Psi_{0,L}$ is non-degenerate and corresponds to $\tilde{k} = 0$ of the lower branch (minus sign in Eq. (4.14)), the expression for it reads

$$\psi_{0,L} = \frac{1}{\sqrt{2}} \begin{pmatrix} e^{-i\varphi} \\ e^{i\varphi} \end{pmatrix}. \tag{4.20}$$

The Stokes vector for this state is given by

$$\vec{S} = \Psi_{0,L}^{\dagger} \vec{\sigma} \Psi_{0,L} = \begin{pmatrix} -\cos 2\varphi \\ -\sin 2\varphi \\ 0 \end{pmatrix}, \tag{4.21}$$

thus, the ground state of a flat ring with no birefringence is completely linearly polarized with the polarization direction remaining tangential to the ring. It should be noted, that the Stokes vector in the ground state (4.20) repeats the pattern of the effective magnetic field produced by the TE-TM splitting (shown in Fig. 4.7 (b)), but in the XY-plane. We observed a large degree of linear polarization and a small degree of circular polarization in the ring as seen in Fig. 4.6 and Fig. 4.8; the TE-TM splitting term in the Hamiltonian mixes the left and right circular components of the pseudo spinor creating a large component of linear polarized state with a small circular component. Although, the four-leaf angular pattern in S_1 and S_2 are not phase-shifted by $\pi/2$ as predicted from the theory the 2φ angular dependence of both the patterns point towards the 2φ angular dependence of the pseudo magnetic field originating from the TE-TM splitting in the ring microcavity.

In the absence of the polariton-polariton and polariton-reservoir interaction, the ring is described by the following matrix Hamiltonian $\widehat{H}$, whose elements are given by

$$\begin{aligned}
&\widehat{H}_{11} = \widehat{H}_{22} = \frac{\hbar^2}{2m_{\text{eff}}R^2}(\hat{\tilde{k}}^2 + V_0 \sin\varphi), \\
&\widehat{H}_{12} = \widehat{H}_{21}^{\dagger} = \frac{\hbar^2}{2m_{\text{eff}}R^2}\cdot \\
&\left((B + V_1 \sin\varphi)e^{-2i\varphi}(-\hat{\tilde{k}}^2 + 2\hat{\tilde{k}} + \Delta) + \alpha e^{-i\varphi_0}\right),
\end{aligned} \tag{4.22}$$

where $\hat{\tilde{k}} = -i(d/d\varphi)$. φ is measured from the positive direction of the x-axis in anticlockwise sense. For the sake of simplicity we introduced the dimensionless quantity $B + V_1 \sin\varphi$ which corresponds to the TE-TM splitting, inherited from the plane microcavity, here $B = 2\beta m_{\text{eff}}/\hbar^2$ (β defines the TE-TM splitting of the plane microcavity without tilt) and V_1 accounts for the dependence of the TE-TM splitting on the changing width of the quantum well. V_0 describes the position-dependent shift of the energy levels due to the cavity gradient. The dimensionless parameter $\Delta = (\pi R/a)^2$ corresponds to the LT-splitting, stemming from the confinement in the radial direction. We also consider an additional splitting between linear polarizations which acts as a static in-plane field, and described by α and φ_0. This field is usually linked with the crystallographic axes and appears because of the anisotropy of the quantum well.

The time evolution of the polariton condensate spinor Ψ in presence of energy relaxation and finite lifetime τ reads:

$$i\hbar\frac{\partial\Psi}{\partial t} = (1 - i\Lambda)\,\hat{H}\Psi - \frac{i\hbar}{2\tau}\Psi \tag{4.23}$$

Energy relaxation is phenomenologically included in the model by multiplying the

Hamiltonian (4.22) by the complex coefficient $1 - i\Lambda$, where Λ is the dimensionless energy relaxation parameter. This is an energy diminishing scheme, where the higher energy eigenstates relax more quickly than the lower energy eigenstates. For longer temporal evolution only the ground state survives. This form of energy relaxation was first suggested by Pitaevskii and applied in the context of damped atomic condensates. Since the rate of energy dissipation and the rate of particle loss are not equal, we accounted for the leakage rate with the parameter τ. While numerically integrating the term proportional to Λ we preserve the norm of the wave function by adding back the particles that are lost during the energy relaxation step. To account for the finite lifetime of the polaritons we added another imaginary term proportional to Ψ, which describes the loss of particles from the microcavity with time. Thus, the number of polaritons in the simulation exponentially decays with time at a rate $1/\tau$. An order of magnitude estimate for Λ is obtained from the damping of the oscillations at the bottom of the ring as shown in Fig. 4.6 (a), which gives Λ of the order of 0.1, an order of magnitude higher than previous studies.

We evolve an initial state which is close to the state observed in the experiment after hot thermalization at the pump spot. As shown in Figs. 4.3 and 4.6, the Stokes parameters are $S_1 \sim 0.5$ and $S_2 \sim -0.5$ when the degree of polarization is maximum at the top of the ring. This implies that the linear polarization makes an angle of about -22.5° with the horizontal axis. Any spatially extended state with this uniform polarization is not a polarization eigenstate of the ring because it lacks the left-right mirror symmetry of the ring. In the simulations, we preferred to use an initial state which respects the mirror symmetry of the ring to show that the observed experimental signatures like the four-leaf pattern (in S_1 and S_2) and the spin flips (in S_3) arise in the course of dynamics and do not sensitively depend on the choice of the initial conditions. Since the initial condensate is over 80% horizontally polarized, the initial condensate order parameter in the simulations was chosen to be completely horizontally polarized and localized at the top of the ring,

$$\Psi(\varphi, t = 0) = \exp\left[-\frac{(\varphi - \pi/2)^2}{2d^2}\right][1, 1]^{\mathrm{T}}. \tag{4.24}$$

This initial polarized state has a left-right mirror symmetry with $S_2(\varphi, t = 0) = 0$ as well as spin balanced $S_3(\varphi, t = 0) = 0$. Such an initial state would clarify the dynamical signature of the pseudo magnetic field on the propagating polariton condensate when S_2 and S_3 become non-zero during evolution. The angular width ($d = \pi/10$) of the gaussian wavepacket in the simulations was chosen comparable to the spot size of the pump $\approx 15\mu m$. The numerical solution of Equation (4.23) is shown in Fig. 4.8 for two different choices of cavity tilt and different energy relaxation rates to elucidate the role of the cavity gradient and the energy damping in the polarization pattern formation in the ring. The simulation captures the coherent evolution of the polariton spinor after excitation by a single pulse.

As the initial spin balanced state diffuses from the top, the two components of the spinor are pushed in opposite directions creating a spin imbalanced state. This is shown

at early times in the circular polarization components S_3 in Fig. 4.8 (d) and (h). In the first 100 ps we observed a similar spin imbalance near the top of the ring in the S_3 component as shown in Fig. 4.6. This imbalance is manifested by the appearance of opposite polarity of the S_3 component for the clockwise and counterclockwise flow of the polariton condensate. From Fig. 4.6 (c) we also see that after 200 ps, the top half of the ring shows a spin-flip, i.e. the region where $S_3 > 0$ in the first 100 ps becomes $S_3 < 0$ and vice-versa. From our simulations, we see this when the condensate motion is not strongly damped in Fig. 4.8 (h). The opposite spin components do not immediately come to rest on reaching the bottom from the top and continue onward motion converting back the gained kinetic energy into potential energy. It is during this course of motion that we observe spin-flip in the ring. In Fig. 4.8 (d) we do not see this feature because the condensate motion is overdamped, dissipating the kinetic energy very quickly and bringing the condensate to rest in the bottom of the ring. In the linear polarization sector, which is a measure of the relative phase between the two spinor components, we find a rotation of the polarization as the condensate flows out from the point of generation. This is shown by the appearance of the non-zero S_2 component shortly after the evolution of the initial state in Fig. 4.8 (b) and (f). As the condensate fills the entire ring, we see the emergence of the four-leaf pattern in S_1 and S_2. This is clearly seen in Fig. 4.8 (b) and (c) while obfuscated in Fig. 4.8 (f) and (g) due to interference between clockwise and anti-clockwise moving waves. Similar observation made in Fig. 4.6 (b-c) and the four-leaf pattern is shown in Fig. 4.6 (e-f). As the condensate settles to the minimum of the trap potential, this pattern is seen at the bottom of the ring in Fig. 4.8 (b), (c), (f), and (g). In this state the circular polarization is nearly absent as the ground state of the ring is not circularly polarized. The S_3 component at late times in Fig. 4.6 (d) is also absent in the bottom half of the ring. It should be noted that the model neglects the evolution of the excitonic reservoir in the ring, which dynamically reshapes the effective potential for polaritons. Evidence of long transport of the reservoir was shown in these rings in Ref. [284]. Also, the contribution of the higher radial modes is not included which are found to be occupied only at early times after the quench since we address a much slower spin precession dynamics. We found that these are not crucial for understanding the generic polarization patterns in the ring but will be important when addressing details regarding the transport and energy relaxation of the nonequilibrium polariton condensate in the ring. The model introduced in this section captures all the qualitative aspects of the linear and circular polarization precession following a quench, which emphasizes the role of the TE-TM splitting on the condensate dynamics. Finally, we note that the polarization of the condensate observed in the experiment at late times doesn't correspond to an eigenstate of the tilted ring and requires further theoretical investigation into the details of energy relaxation and thermalization processes which could lead to such a pre-thermal state.

4.4 Conclusion

Ring shaped polariton waveguides is attracting a great deal of attention for exploring various topological effects [287–290] due to the TE-TM splitting in these structures. We present in this direction the first experiments on etched polariton rings. We studied the polarization dynamics of a non-equilibrium polariton condensate formed after a pulsed excitation. Through time resolved measurements we were able to observe the temporal signature of intrinsic optical Hall effect shortly after quench. We provide a qualitative estimate of the length scale over which the spatial coherence builds up in the ring by observing spatial energy locking and linewidth narrowing of the emission. We also present a theoretical model which captures qualitatively the formation of a four-leaf pattern in the S_1 and S_2 components of the Stokes vector, the relative angular phase offset between S_1 and S_2 and finally the contrasting ratio between the degree of linear and circular polarization in the ring thus elucidating the role of the anisotropic pseudo magnetic field originating from the TE-TM splitting and the tilt in the microcavity structure.

Future work will explore making the rings radially thinner pushing further apart the radially confined states in energy while also diminishing the cavity tilt. These rings could then serve as an ideal platform for studying one-dimensional macroscopic quantum phenomena similar to superconducting rings. Already with these long lifetime samples we could address interesting questions in nonequilibrium physics, such as generation of long lived non thermal states, which could be observed and studied in this system.

5 Chiral waveguide optomechanics: quantum phase transitions in the ultrastrong coupling regime

We present a direct mapping between the quantum optomechanical problem of the atoms harmonically trapped in the vicinity of a chiral waveguide and a generalized quantum Rabi model and discuss the analogy between the self-organization of atomic chains in photonic structures and Dicke-like quantum phase transitions in the ultrastrong coupling regime. We extend the class of the superradiant phase transitions for the systems possessing $\mathbb{Z}_3$ rather than parity $\mathbb{Z}_2$ symmetry and demonstrate the emergence of the multicomponent Schrodinger cat ground states in these systems.

5.1 Introduction

The arrays of quantum emitters coupled to a common one-dimensional photonic reservoir are the main object studied by the emerging field of waveguide quantum electrodynamics (WQED) [292, 293]. The field currently experiences rapid progress due to developments in quantum technologies allowing realizations of this type of system based on a variety of platforms including superconducting qubits [294, 295], cold-atoms [296] or semiconductor quantum dots [297]. The key features of waveguide quantum optical set-ups are the emergent long-range correlations between the qubits harnessed through the exchange of the propagating waveguide photons and the inherent open nature of these systems provided by the leakage of the photons. Recently, the set-ups comprising the ring-shaped topological waveguides have been suggested [298, 299] which combine the long-range inter-qubit correlations and quasi-hermiticity. These set-ups could be particularly useful for the emulation of the strongly correlated quantum models since the latter are usually Hermitian ones.

One of the factors limiting the diversity of the quantum many-body phenomena supported by the WQED set-ups is the relatively small radiative coupling of the individual qubits to the photonic mode as compared to the transition frequencies. This leaves us in the weak coupling region of the light-matter interaction. At the same time, reaching the regime of the ultrastrong coupling [300, 301] at which the coupling strength be-

comes comparable with the transition frequencies would enable the access to a plethora of fascinating quantum phenomena such as non-vacuum and correlated ground states, and possible application in quantum memory [302] and quantum metrology [303, 304]. Also, it turns out that superradiant phases are a general property of the ultrastrong coupling limit [305].

In this chapter, we show that the consideration of the atomic mechanical degree of freedom opens the route towards the realization of the ultrastrong coupling regime in the WQED structures. While the joint dynamics of mechanical and internal degrees of freedom have been considered previously, the analysis relied on the approximations of either classical dynamics of both positions and polarization of atoms [306] or the truncated Hilbert space for the phonons [307]. In this chapter, we provide a rigorous mapping from the optomechanical problem to the quantum Rabi model and show that the self-organization of atoms predicted in the classical picture corresponds to the Rabi-like phase transition known to appear in the ultrastrong coupling regime. Since there has recently been tremendous progress in finding analytical solutions to the Rabi model [308] we believe that the presented mapping is of substantial importance for the further developments of the quantum optomechanics in the regime of strong optomechanical coupling.

5.2 Model

We consider a system depicted in Fig.1: N qubits are placed in the laser harmonic traps on top of the chiral ring resonator. The qubit can absorb or emit a waveguide photon, and the radiative relaxation to the far-field is suppressed. The Hamiltonian of the system reads

$$\hat{H} = \sum_k \omega_k \hat{c}_k^\dagger \hat{c}_k + \sum_{j=1}^{N} \omega_x \sigma_j^+ \sigma_j + \sum_{j=1}^{N} \Omega \hat{a}_j^\dagger \hat{a}_j + \hat{H}_{\text{int}}, \tag{5.1}$$

where $\omega_k = vk$ is the dispersion of the chiral waveguide modes which is assumed to be linear, v is the speed of light in the waveguide, ω_x is the qubit resonance frequency, and Ω is the optical trap phonon energy, $\hat{a}_j, \hat{a}_j^\dagger$ are annihilation and creation phonon operators respectively. The interaction Hamiltonian reads

$$\hat{H}_{\text{int}} = g \sum_{k,j} \left[\sigma_j^\dagger \hat{c}_k e^{\mathrm{i}k[R\phi_j + x_j]} + \text{H.c.} \right], \tag{5.2}$$

where g is the Rabi splitting, R is the radius of the ring, x_j corresponds to the deviation of the j-th atom from its equilibrium position which is equal to $u_0(\hat{a}_j + \hat{a}_j^\dagger)$, $u_0 = \sqrt{\hbar/(2M\Omega)}$ is the quantum of the mechanical motion, where M is the mass of the qubit. Actually, the optical spectrum of the ring is discrete rather than continuous

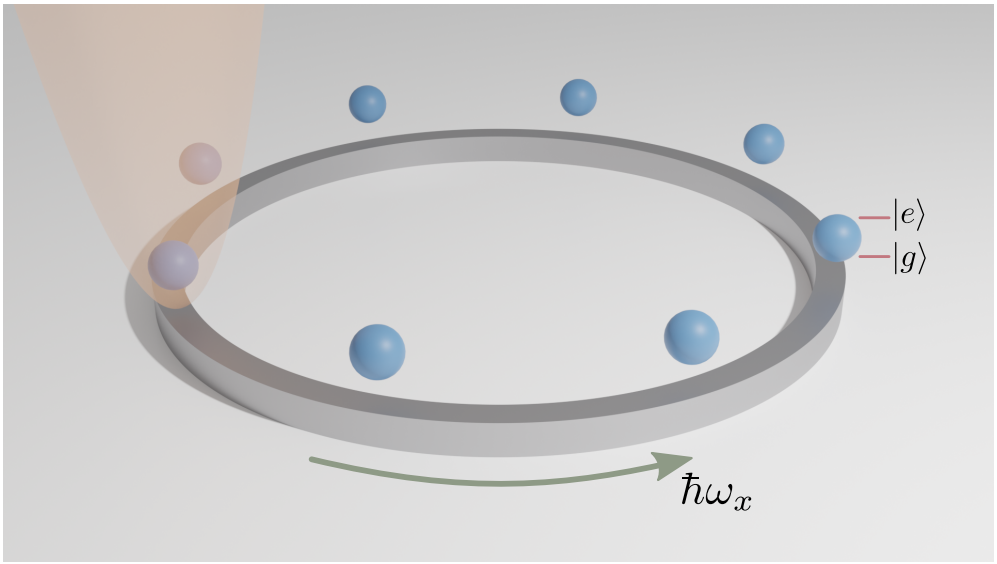

Figure 5.1: Geometry of the structure: an array of two-level atoms placed in the vicinity of the chiral ring resonator. The parabolic trapping potential is shown with a shaded region only for one atom.

with the frequency difference between the modes given by $\delta\omega = v/R$. However, for a large resonator when $v/R \ll \omega_x$ the limit of the continuous spectrum can be employed.

We then integrate out the waveguide degrees of freedom by performing the Schrieffer-Wolff transform [309] to obtain the effective Hamiltonian up to the second order of the qubit-photon coupling g:

$$\hat{H}_{\text{eff}} = \sum_j \omega_x \sigma_j^+ \sigma_j + \sum_j \Omega \hat{a}_j^\dagger \hat{a}_j$$
$$-\frac{\Gamma_0}{2} \sum_{i<j} \left[\mathrm{i}\sigma_i^+ \sigma_j e^{\mathrm{i}qR\phi_{ij}} e^{\mathrm{i}\eta(\hat{a}_i + \hat{a}_i^\dagger - \hat{a}_j - \hat{a}_j^\dagger)} + \text{H.c.} \right], \tag{5.3}$$

where $q = \omega_x/v$, $\Gamma_0 = g^2/v$ is the radiative decay rate of a single qubit, and $\eta = qu_0$ is the dimensionless optomechanical interaction. In deriving Eq. (5.3) we used the Markov approximation neglecting the frequency dispersion in the phase factor ($k \approx q$). The Markov approximation holds for $R\Gamma_0/v \ll 1$. In stark contrast to the WQED case the resulting Hamiltonian is Hermitian. This is both due to the fact that unlike the case of an infinite waveguide our system is a closed one, and because the radiation to the far field has been neglected. The latter approximation can be adopted when the radiative coupling to the waveguide mode Γ_0 is much stronger than that to the far-field continuum Γ'. This can be achieved in the photonic crystal waveguide geometries, where $\Gamma_0/\Gamma' > 9$ has been experimentally reported [310].

The qubit excitation energy ω_x is the largest energy scale of the problem. Since the Hamiltonian commutes with the excitation number operator, we can safely project the Hamiltonian to the subspace with a single excitation. In this case, the qubit subspace is spanned by N states corresponding to excitation localized at each of N qubits. We assume the equidistant spacing of the harmonic traps, i.e. $\phi_{i+1,i} = \phi$.

The third term in Eq. (5.3) contains the exponent of the bosonic operators making it highly nonlinear in the region $\eta \approx 1$. It is instructive to estimate the experimentally relevant range of parameters of the model. Parameter η is defined by the ratio of the length scale of the atomic motion, u_0 and the wavelength of the photon in the waveguide, λ, $\eta = 4\pi u_0/\lambda$. The coherence of the atomic motion is preserved at the scale of the atomic de Broglie wavelength $\lambda = \hbar/p_{\rm th}$, where the thermal momentum $p_{\rm th} = \sqrt{3Mk_BT}$. Thus, the condition of the coherent atomic motion implies that $u_0 < \hbar/p_{\rm th}$. For the lithium atoms and the resonant wavelength of approximately 700 nm the value of $\eta = 1$ is achieved at $T = 640$ nK, which is a temperature that has been achieved in recent cold atom experiments (see the review [311] and references within). The corresponding phonon energy is then approximately 2.4 kHz. The radiative decay rate Γ_0 can be tuned in a wide range of frequencies from zero to GHz. Therefore, the range of $\Gamma_0/\Omega, \eta \sim 1$ can be achieved in the state of the art cold atom experiments. Thus, it is relevant to explore the properties of Hamiltonian (5.3) outside the small η regime.

5.3 Mapping to the N-state quantum Rabi model

We start with the Hamiltonian, given by Eq. (3) in the main text, and project it on the subspace of a single qubit excitation

$$\hat{H}_{\rm eff} = \hat{H}_{phon} + \hat{H}_c = \sum_{j=1}^{N} \Omega \hat{a}_j^\dagger \hat{a}_j - \frac{\Gamma_0}{2} \sum_{(i<j)}^{N} \left[\mathrm{i}|i\rangle\langle j| e^{\mathrm{i}qR\phi(i-j)} e^{\mathrm{i}qu_0(\hat{a}_i + \hat{a}_i^\dagger - \hat{a}_j - \hat{a}_j^\dagger)} + \mathrm{H.c.} \right], \tag{5.4}$$

where $|i\rangle$ are the basis vectors in the N-dimensional space, corresponding to the excitation, localized at the i-th qubit. We then introduce the unitary operator $\hat{T} = \hat{S} \times \hat{\Phi}$, where

$$\hat{\Phi}_{ij} = \delta_{ij} e^{-\mathrm{i}qR\phi(i-1)} e^{-\mathrm{i}qu_0(\hat{a}_i + \hat{a}_i^\dagger)}, \quad i, j = 1 \dots N, \tag{5.5}$$

and $\hat{S}$ is the matrix, which lines are the normalized eigenvectors of the matrix $\sum_{j>i} [-\mathrm{i}|j\rangle\langle i|] + H.c.$ The unitary transformation $\hat{T}$ diagonalizes $\hat{H}_c$. The resulting diagonal matrix has non-degenerate eigenvalues, located symmetrically with respect to zero. For $N = 2$, the eigenvalues are $\pm\Gamma_0/2$.

The transformation $\hat{\Phi}\hat{H}_{phon}\hat{\Phi}^\dagger$ results in

$$\hat{\Phi}\hat{H}_{phon}\hat{\Phi}^\dagger = \sum_{j=1}^{N} \Omega\hat{a}_j^\dagger\hat{a}_j + \Omega\eta^2 + \Omega\eta \times \mathrm{diag}[\mathrm{i}(\hat{a}_i^\dagger - \hat{a}_i)], \tag{5.6}$$

where $\eta = qu_0$. We then can introduce the phonon *center-of-mass* creation operator $\hat{a}_{CM} = \frac{1}{\sqrt{N}}\sum_i \hat{a}_i$. Namely, for $N = 2$ the resulting Hamiltonian reads

$$\Omega\hat{a}_{CM}^\dagger\hat{a}_{CM} + \Omega a_d^\dagger a_d - \Omega\mathrm{i}\frac{\eta}{\sqrt{2}}(\hat{a}_{CM} - \hat{a}_{CM}^\dagger) + \Omega\eta^2 + \sigma_x\Omega\frac{\eta}{\sqrt{2}}(\mathrm{i}\hat{a}_d - \mathrm{i}\hat{a}_d^\dagger) - \frac{\Gamma_0}{2}\sigma_z, \tag{5.7}$$

where $\hat{a}_d = (\hat{a}_1 - \hat{a}_2)/\sqrt{2}$ corresponds to the relative motion of the two qubits. As can be seen this Hamiltonian is exactly the one describing the Quantum Rabi model plus the decoupled bosonic mode, corresponding to the center-of-mass motion. Now we introduce the new variables

$$\hat{a} = \hat{a}_{CM} + \mathrm{i}\frac{\eta}{\sqrt{2}}, \quad \hat{a}^\dagger = \hat{a}_{CM}^\dagger - \mathrm{i}\frac{\eta}{\sqrt{2}}, \tag{5.8}$$

for which we have

$$\Omega\hat{a}_{CM}^\dagger\hat{a}_{CM} - \Omega i\frac{\eta}{\sqrt{2}}(\hat{a}_{CM} - \hat{a}_{CM}^\dagger) = \Omega\hat{a}^\dagger\hat{a} - \frac{\Omega\eta^2}{2} \tag{5.9}$$

thus finally we arrive at

$$\hat{\tilde{H}}_{\mathrm{eff}} = T\hat{H}_{eff}T^\dagger = \Omega\hat{a}^\dagger\hat{a} + \Omega\hat{a}_d^\dagger\hat{a}_d + \frac{\Omega\eta^2}{2} + \sigma_x\Omega\frac{\eta}{\sqrt{2}}(\mathrm{i}\hat{a}_d - \mathrm{i}\hat{a}_d^\dagger) - \frac{\Gamma_0}{2}\sigma_z, \tag{5.10}$$

For $N = 3$ qubits the Hamiltonian is given by

$$\hat{\tilde{H}}_{\mathrm{eff}} = T\hat{H}_{\mathrm{eff}}T^\dagger = \Omega\hat{a}_{CM}^\dagger\hat{a}_{CM} - \Omega\mathrm{i}\frac{\eta}{\sqrt{3}}(\hat{a}_{CM} - \hat{a}_{CM}^\dagger) + \Omega(\hat{a}_x^\dagger\hat{a}_x + \hat{a}_y^\dagger\hat{a}_y) + \Omega\eta^2 -$$
$$\frac{\sqrt{3}\Gamma_0}{2}\begin{pmatrix}1 & 0 & 0\\ 0 & -1 & 0\\ 0 & 0 & 0\end{pmatrix} - \Omega\frac{\eta}{\sqrt{6}}(\mathrm{i}\hat{a}_x - \mathrm{i}\hat{a}_x^\dagger)\begin{pmatrix}0 & 1 & 1\\ 1 & 0 & 1\\ 1 & 1 & 0\end{pmatrix} + \Omega\frac{\eta}{\sqrt{6}}(\hat{a}_y - \hat{a}_y^\dagger)\begin{pmatrix}0 & 1 & -1\\ -1 & 0 & 1\\ 1 & -1 & 0\end{pmatrix}, \tag{5.11}$$

where $\hat{a}_x = \frac{1}{\sqrt{6}}(-\hat{a}_1 - \hat{a}_2 + 2a_3)$, $\quad \hat{a}_y = \frac{1}{\sqrt{2}}(\hat{a}_1 - \hat{a}_2)$. Now we introduce new variables

$$\hat{a} = \hat{a}_{CM} + \mathrm{i}\frac{\eta}{\sqrt{3}}, \quad \hat{a}^\dagger = \hat{a}_{CM}^\dagger - \mathrm{i}\frac{\eta}{\sqrt{3}}, \tag{5.12}$$

for which we have

$$\Omega\hat{a}_{CM}^\dagger\hat{a}_{CM} - \Omega\mathrm{i}\frac{\eta}{\sqrt{3}}(\hat{a}_{CM} - \hat{a}_{CM}^\dagger) = \Omega\hat{a}^\dagger\hat{a} - \frac{\Omega\eta^2}{3} \tag{5.13}$$

thus finally we arrive at

$$\hat{\tilde{H}}_{\text{eff}} = T\hat{H}_{\text{eff}}T^{\dagger} = \Omega\hat{a}^{\dagger}\hat{a} + \Omega(\hat{a}_x^{\dagger}\hat{a}_x + \hat{a}_y^{\dagger}\hat{a}_y) + \Omega\frac{2\eta^2}{3} - \frac{\sqrt{3}\Gamma_0}{2}\begin{pmatrix}1 & 0 & 0\\ 0 & -1 & 0\\ 0 & 0 & 0\end{pmatrix} - \Omega\frac{\eta}{\sqrt{6}}(\mathrm{i}\hat{a}_x - \mathrm{i}\hat{a}_x^{\dagger})\begin{pmatrix}0 & 1 & 1\\ 1 & 0 & 1\\ 1 & 1 & 0\end{pmatrix} + \Omega\frac{\eta}{\sqrt{6}}(\hat{a}_y - \hat{a}_y^{\dagger})\begin{pmatrix}0 & 1 & -1\\ -1 & 0 & 1\\ 1 & -1 & 0\end{pmatrix}. \tag{5.14}$$

In general, we have a generalized Rabi model with N-dimensional matrices.

For the case of two qubits, T_2 reads $\hat{T}\hat{H}_{\text{eff}}\hat{T}^{\dagger}$, where

$$T = \frac{1}{\sqrt{2}}\begin{pmatrix}\mathrm{i}e^{-\mathrm{i}\eta\hat{x}_1} & e^{-\mathrm{i}\eta\hat{x}_2 - \mathrm{i}qR\phi}\\ -\mathrm{i}e^{\mathrm{i}\eta\hat{x}_1} & e^{-\mathrm{i}\eta\hat{x}_2 - \mathrm{i}qR\phi}\end{pmatrix}, \tag{5.15}$$

where $\hat{x}_i = \hat{a}_i + \hat{a}_i^{\dagger}$, and the transformed Hamiltonian

$$\hat{T}_2\hat{H}_{\text{eff}}\hat{T}_2{}^{\dagger} = \Omega\left[\hat{a}_{CM}^{\dagger}\hat{a}_{CM} + \hat{a}_d^{\dagger}\hat{a}_d + \frac{\eta^2}{2} + \sigma_x\frac{\eta}{\sqrt{2}}(\mathrm{i}\hat{a}_d - \mathrm{i}\hat{a}_d^{\dagger}) - \frac{\Gamma_0}{2\Omega}\sigma_z\right], \tag{5.16}$$

$\hat{a}_{CM} = \frac{1}{\sqrt{2}}(\hat{a}_1 + \hat{a}_2 + i\eta)$ corresponds to the center-of-mass qubit motion and $\hat{a}_d = \frac{1}{\sqrt{2}}(\hat{a}_1 - \hat{a}_2)$ corresponds to the relative motion of two qubits. The center-of-mass momentum operator is shifted from the equilibrium position on η. This is due to the unidirectional propagation of the chiral waveguide photon which *pushes* the qubits as whole in one direction. Then, we see that the spectrum of the problem does not depend on the static phase difference ϕ which is typical for the chiral waveguide quantum optical set-ups [312, 313]. Finally, we see that up-to the center-of-mass kinetic energy term which decouples from the rest of the system, the effective Hamiltonian is exactly the one corresponding to the quantum Rabi model. The radiative decay Γ_0 plays the role of the resonant transition energy and the η defines the effective coupling strength. The case of strong optomechanical interaction $\eta > 0.1\sqrt{2}$ thus directly maps to the ultrastrong coupling regime (USC). It is known that in the USC and deep-strong coupling regime ($\eta > \sqrt{2}$) of the Rabi model the system is characterized by the non-vacuum ground state $|\Psi_G\rangle$ which can be roughly approximated by the superposition of the coherent states $|\Psi_G\rangle \approx \frac{1}{\sqrt{2}}(|+\rangle \otimes |\alpha\rangle + |-\rangle \otimes |-\alpha\rangle)$ [314], where $|\pm\alpha\rangle$ are the bosonic coherent states, and $|\pm\rangle = \frac{1}{\sqrt{2}}(|\uparrow\rangle \pm |\downarrow\rangle)$ - are the superpositions of the ground and excited qubit states. Also, the direct mapping to the Rabi model is valid only in the purely chiral case. However, as we show in Section 5.6, the numerically obtained spectrum for the non-perfectly chiral waveguide qualitatively is very similar to the perfectly chiral case.

For three qubits the unitary transformation T_3 results in the Hamiltonian [315]):

$$\hat{T}_3\hat{H}_{\text{eff}}\hat{T}_3{}^{\dagger} = \hat{\tilde{H}}_{\text{eff}} = \hat{H}_{ph} + \hat{H}_q + \hat{H}_c, \tag{5.17}$$

where $\hat{H}_{ph}$ is the phonon kinetic energy given by

$$\hat{H}_{ph} = \Omega(\hat{a}^\dagger\hat{a} + \hat{a}_x^\dagger\hat{a}_x + \hat{a}_y^\dagger\hat{a}_y + \frac{2\eta^2}{3}), \tag{5.18}$$

where $\hat{a}$ corresponds to the shifted operator of center-of-mass motion, $\hat{a} = \frac{1}{\sqrt{3}}(\hat{a}_1 + \hat{a}_2 + \hat{a}_3 + \mathrm{i}\eta)$, and $\hat{a}_x = \frac{1}{\sqrt{6}}(-\hat{a}_1 - \hat{a}_2 + 2\hat{a}_3)$, $\hat{a}_y = \frac{1}{\sqrt{2}}(\hat{a}_1 - \hat{a}_2)$ are operators of normal modes. The qubit Hamiltonian $\hat{H}_q$ reads

$$\hat{H}_q = -\frac{\sqrt{3}\Gamma_0}{2}\hat{\lambda}_3, \tag{5.19}$$

where $\hat{\lambda}_i$ is the 3×3 Gell-Mann matrix. Finally, the coupling term $\hat{H}_c$ reads

$$\hat{H}_c = -\frac{\Omega\eta}{\sqrt{3}}\left[\hat{p}_x(\hat{\lambda}_1 + \hat{\lambda}_4 + \hat{\lambda}_6) + \hat{p}_y(-\hat{\lambda}_2 + \hat{\lambda}_5 - \hat{\lambda}_7)\right], \tag{5.20}$$

where $\hat{p}_i = \frac{\mathrm{i}}{\sqrt{2}}(\hat{a}_i - \hat{a}_i^\dagger)$. The Hamiltonian $\hat{\tilde{H}}_{\text{eff}}$ (up to the decoupled center-of-mass motion) describes the two-dimensional Bose-Einstein condensate (BEC) of spin 1 particles localized in a harmonic trap (given by $\hat{H}_{ph}$) and in perpendicular magnetic field ($\hat{H}_q$). The term $\hat{H}_c$ describes the spin-orbit coupling (SOC) for spin 1 particles. This type SOC has been introduced for the BECs of spin particles previously [316, 317]. Thus, we highlight a link between the waveguide optomechanical systems and BEC physics.

Despite seeming similarity, the Hamiltonian in Eq. (5.17) is qualitatively different from the Dicke model Hamiltonian. Namely, the qubit operators do not obey the angular momentum commutation relations. Moreover, the Hamiltonian (5.17) possesses global $\mathbb{Z}_3$ symmetry. Consider the unitary operator

$$\hat{R} = e^{-\mathrm{i}\hat{L}_z\frac{2\pi}{3}} \otimes \begin{pmatrix} 1 & 0 & 0 \\ 0 & e^{\mathrm{i}4\pi/3} & 0 \\ 0 & 0 & e^{\mathrm{i}2\pi/3} \end{pmatrix}, \tag{5.21}$$

where $\hat{L}_z = \hat{x}\hat{p}_y - \hat{y}\hat{p}_x$ is the angular momentum operator. Operator $\hat{R}$ obeys $\hat{R}^2 = \hat{R}^\dagger$ and thus $\left[\mathbb{1}, \hat{R}, \hat{R}^2\right]$ form a group. We note that $\hat{R}\hat{\tilde{H}}_{\text{eff}}\hat{R}^\dagger = \hat{\tilde{H}}_{\text{eff}}$ and thus $[\hat{R}, \hat{\tilde{H}}_{\text{eff}}] = 0$. Therefore, the eigenstates of $\hat{R}$ are also eigenstates of $\hat{\tilde{H}}_{\text{eff}}$. The three distinct eigenvalues of $\hat{R}$ are $\left[1, e^{\mathrm{i}2\pi/3}, e^{\mathrm{i}4\pi/3}\right]$.

5.4 Quantum phase transition

We then assume the limit of the classical motion of the qubits by assuming $\hat{p}_x, \hat{p}_y$ to be classical variables and find the eigenvalues of the corresponding matrix Hamiltonian obtained from Eq. (5.17). We find the ground state energy by minimizing the smallest eigenvalue with respect to p_x, p_y. Moving to the polar coordinates

$(p_x, p_y) = (p\cos\theta, p\sin\theta)$ we find that the minimum energy is obtained for $\cos 3\theta = 1$. With this condition fulfilled, the expression for the ground state energy as a function of p reads

$$\epsilon_G = \frac{2\eta^2\Omega}{3} + \frac{\sqrt{3}\Gamma_0}{2}\left[\frac{\tilde{p}^2}{2\mu} - 2(\tilde{p}^2 + \frac{1}{3})^{\frac{1}{2}}\cos\left(\frac{\gamma}{3}\right)\right], \tag{5.22}$$

where $\mu = \sqrt{4/27}\eta^2\Omega/\Gamma_0$, $\tilde{p} = 2\eta\Omega/(3\Gamma_0)p$, and $\gamma = \arctan\left((81\tilde{p}^4 + 27\tilde{p}^2 + 3)^{\frac{1}{2}}/9\tilde{p}^3\right)$. For small $\tilde{p}$ we can write

$$\epsilon_G \approx \frac{2\eta^2\Omega}{3} + \frac{\sqrt{3}\Gamma_0}{2}\left[-1 - \tilde{p}^3 + \frac{9\tilde{p}^4}{8} + \frac{\mu - 3}{2\mu}\tilde{p}^2\right] \tag{5.23}$$

For $\eta \ll 1$ Eq. (5.23) has a single local minimum at $\tilde{p} = 0$. For $\eta > \eta_c = \sqrt{3\sqrt{3}\Gamma_0/(7\Omega)}$ it has an additional minimum at $\tilde{p}_c$ which for $\eta \approx \eta_c$ can by approximated by $\tilde{p}_c \approx \frac{1}{3}(1 + \sqrt{7 - 2/\mu})$. Then, for $\eta > \sqrt{\sqrt{3}\Gamma_0/(2\Omega)}$, there is only a single minimum at $\tilde{p}_c$. At $\eta = \eta_c$ the first derivative of ϵ_G is discontinuous which is a hallmark of the first order quantum phase transition [318].

We plot dependence of ϵ_G given by Eq. (5.22) in Fig. 5.2(a). We can see that indeed there exists a range of parameters where there are two local minima signifying the phase co-existence regime. Thus, the quantum phase transition (QPT) in the classical limit is indeed of the first order. This is in stark contrast to the classical limit of the quantum Rabi model, where the phase transition is of the second order [319].

The map of the ϵ_G in (p_x, p_y) space is shown in Fig. 5.2(b). For the case $\eta < \eta_c$ shown in left panel, there is a single minimum corresponding to $\tilde{p} = 0$. For $\eta > \eta_c$ (right) panel three degenerate minima emerge.

Since the QPTs can occur only in the thermodynamic limit we shall refine our analysis of the ground state energy. For that, we first consider that the actual quantum states corresponding to the minimal energy in the classical limit are the direct products of the spin states and the coherent states of the qubit motion at small p_c

$$|l\rangle \approx \mathcal{N}_c \begin{pmatrix} \tilde{p}_c/2 \\ -[1 - \frac{5}{8}\tilde{p}_c^2]e^{2\mathrm{i}\theta_l} \\ \tilde{p}_c e^{\mathrm{i}\theta_l} \end{pmatrix} \otimes |\tilde{p}_c\cos\theta_l, \tilde{p}_c\sin\theta_l\rangle\,, \tag{5.24}$$

where $l = 0, 1, 2$, $\theta_l = 2\pi l/3$, and $\mathcal{N}_c$ is the normalization factor. It is evident that $\langle l|\hat{\tilde{H}}_{\mathrm{eff}}|l\rangle$ yields the classical mean-field ground state energy. However, these states can not be the eigenstates of Hamiltonian $\hat{\tilde{H}}_{\mathrm{eff}}$ since they are not eigenstates of operator $\hat{R}$. Namely, $\hat{R}|l\rangle = |[(l+1)\mathrm{mod}3]\rangle$. Moreover, due to nonorthogonality of the coherent states $\langle l'|\hat{\tilde{H}}_{\mathrm{eff}}|l\rangle \neq E\delta_{l',l}$ and $\langle l'|l\rangle \neq \delta_{l',l}$. We thus can solve the characteristic equation for the eigenvalues $\det[\langle l'|\hat{\tilde{H}}_{\mathrm{eff}}|l\rangle - E\langle l'|l\rangle] = 0$. The explicit form of the characteristic

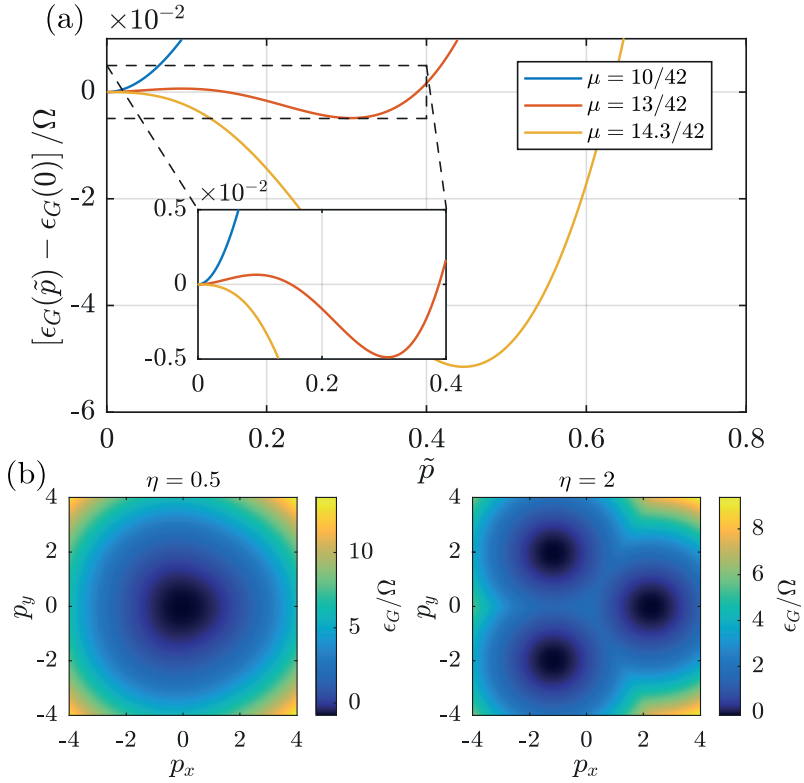

Figure 5.2: (a) Dependency of the ground state energy on $\tilde{p}$ for different values of the parameter μ; $\Gamma_0/\Omega = 2.5$. (b) Dispersion of the lowest energy surface in the classical approximation for qubit motion in the two cases: $\eta = 0.5$ and $\eta = 2.0$; $\Gamma_0/\Omega = 2.5$, $\eta_c \approx 1.36$.

equation is cumbersome and presented in Section 5.5. However, the non-diagonal elements of the matrix representation of the Hamiltonian are proportional to the overlap of the coherent states which is proportional to $\exp[-3\tilde{p}_c^2]$. The explicit form of the eigenstates can be found from the symmetry considerations. Namely, the eigenstates should also be the eigenstates of the operator $\hat{R}$. We then can easily find the mutually orthogonal linear superpositions of states $|l\rangle$ which satisfy this condition. Namely, the ground and two excited states are given by:

$$
\begin{aligned}
|\Psi_G\rangle &= \frac{1}{\sqrt{3}}\left[|0\rangle + |1\rangle + |2\rangle\right], \\
|\Psi_{E1}\rangle &= \frac{1}{\sqrt{3}}\left[|0\rangle + e^{4i\pi/3}|1\rangle + e^{2i\pi/3}|2\rangle\right], \\
|\Psi_{E2}\rangle &= \frac{1}{\sqrt{3}}\left[|0\rangle + e^{2i\pi/3}|1\rangle + e^{4i\pi/3}|2\rangle\right].
\end{aligned}
\tag{5.25}
$$

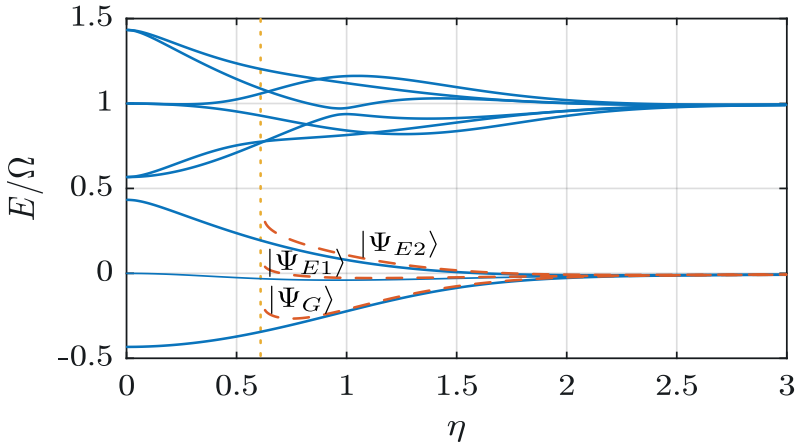

Figure 5.3: Eigenenergies of first nine eigenstates of $\hat{\tilde{H}}_{eff}$ vs optomechanical coupling η with $\Gamma_0/\Omega = 0.5$. Red dashed lines show the dispersions of states in Eq. (5.25) and the blue solid lines show the results of the numerical diagonalization. The vertical dotted line corresponds to critical optomechanical coupling $\eta_c \approx 0.61$. For the numerical diagonalization, the phonon sub-space was truncated with maximal phonon occupation number - 100.

The spectrum of $\hat{\tilde{H}}_{\text{eff}}$ as a function of the coupling strength η is shown in Fig. 5.3 for the case of the ground state of the center-of-mass degree of freedom $\hat{n}_{CM} = 0$. The spectrum has been obtained via direct numerical diagonalization by truncating the phonon subspace. We can see that at large η the ground state becomes quasi-degenerate. We also plot the analytically obtained dispersions of states $|\Psi_G\rangle, |\Psi_{E1}\rangle, |\Psi_{E2}\rangle$. The first three low energy states given by Eq. (5.25) are the analog of the triangular Schrodinger cat states [320]. While the Schrodinger cat states are generally regarded as extremely fragile with respect to decoherence, it has been recently revealed that the two-component cat states appearing in the USC of the conventional Rabi model appear two be robust to decoherence and can be used to realize protected quantum gates with high fidelity [321, 322]. Thus, the states $|\Psi_{[G,E1,E2]}\rangle$ as the three-component generalizations of the cat states originating in the USC are likely to remain sufficiently stable and can be used for quantum information processing.

We have shown that the phase transition occurs in the classical limit. The classical limit can be regarded as a thermodynamic limit of the vanishing harmonic oscillator energy Ω [319, 323–325]. To explore this limit, we redefine the energy constants in $\hat{\tilde{H}}_{\text{eff}}$ in the following way: we set $\eta\Omega \to \eta'$ as an independent variable and redefine $\Gamma_0 = \xi\omega$, $\Omega = \omega/\xi$. The thermodynamic limit is then achieved for $\xi \to \infty$.

In Fig. 5.4 we plot the first derivative of the ground state energy as a function of η' for $\omega = 1$ and for different ξ. As ξ increases this function steepens in the vicinity

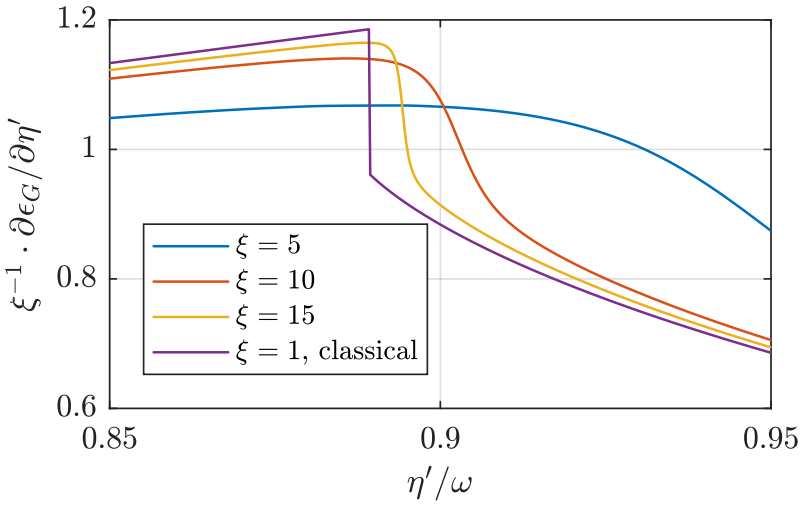

Figure 5.4: First derivative of the ground state energy $\partial\epsilon_G/\partial\eta'$ for different values of scaling parameter ξ. $\omega = 1$.

of η'_c. In the limit of infinite ξ we would observe the discontinuity of the $\partial\epsilon_G/\partial\eta'$ just as in the classical limit and the establishment of the QPT with $\mathbb{Z}_3$ symmetry breaking. The $\Omega \to 0$ limit can be regarded as the classical limit of the atomic motion. Thus, the predicted phase transition corresponds to the appearance of non-zero phonon occupation in the ground state and self-organization of atomic motion due to the photon-mediated inter-atomic interactions. The self-organization of atoms has been predicted within the classical approach in WQED systems [306]. We thus reveal the direct connection of the self-organization phenomena and quantum phase transitions similar to that occurring in the Rabi model.

5.5 Hamiltonian, projected on the three lowest energy states

In this subsection we calculate the 3 by 3 matrix ($l, l' = 0, 1, 2$) $\langle l'|\hat{\tilde{H}}_{\text{eff}}|l\rangle$ – i.e. the projection of our Hamiltonian $\hat{\tilde{H}}_{\text{eff}}$ on the three lowest energy states. The states $|l\rangle$ are given by Eq. (13) from the main text, but it is important to note that in this equation one has to interpret the phonon state $|\tilde{p}_c \cos\theta_l, \tilde{p}_c \sin\theta_l\rangle$ (with $\theta_l = 2\pi l/3$) as a product of coherent states of x- and y-phonons, namely, $|\tilde{p}_c \cos\theta_l, \tilde{p}_c \sin\theta_l\rangle = |\alpha^{(l)}_{c;x}\rangle \otimes |\alpha^{(l)}_{c;y}\rangle$. The coherent states satisfy $\hat{a}_x|\alpha^{(l)}_{c;x}\rangle = \alpha^{(l)}_{c;x}|\alpha^{(l)}_{c;x}\rangle$ and $\hat{a}_y|\alpha^{(l)}_{c;y}\rangle = \alpha^{(l)}_{c;y}|\alpha^{(l)}_{c;y}\rangle$. How are the parameters $\alpha^{(l)}_{c;x}$ and $\alpha^{(l)}_{c;y}$ of the coherent states related to the pair of numbers

$(\tilde{p}_c\cos\theta_l, \tilde{p}_c\sin\theta_l)$? We remind, that $\hat{p}_i = \frac{\mathrm{i}}{\sqrt{2}}(\hat{a}_i - \hat{a}_i^\dagger)$ and $\hat{x}_i = \frac{1}{\sqrt{2}}(\hat{a}_i + \hat{a}_i^\dagger)$, here $i = x, y$. Now, by definition $\langle\alpha_{c;x}^{(l)}|\hat{p}_x|\alpha_{c;x}^{(l)}\rangle = p_x = p_c\cos\theta_l$, $\langle\alpha_{c;y}^{(l)}|\hat{p}_y|\alpha_{c;y}^{(l)}\rangle = p_y = p_c\sin\theta_l$ and we remind that $\tilde{p}_c = 2\eta\Omega/(3\Gamma_0)p_c$. On the other hand, $p_x = \langle\alpha_{c;x}^{(l)}|\hat{p}_x|\alpha_{c;x}^{(l)}\rangle = \frac{\mathrm{i}}{\sqrt{2}}(\alpha_{c;x}^{(l)} - \alpha_{c;x}^{(l)*})$ and $p_y = \langle\alpha_{c;y}^{(l)}|\hat{p}_y|\alpha_{c;y}^{(l)}\rangle = \frac{\mathrm{i}}{\sqrt{2}}(\alpha_{c;y}^{(l)} - \alpha_{c;y}^{(l)*})$. Also, we can introduce x_c and y_c as $x_c = \langle\alpha_{c;x}^{(l)}|\hat{x}|\alpha_{c;x}^{(l)}\rangle = \frac{1}{\sqrt{2}}(\alpha_{c;x}^{(l)} + \alpha_{c;x}^{(l)*})$ and $y_c = \langle\alpha_{c;y}^{(l)}|\hat{y}|\alpha_{c;y}^{(l)}\rangle = \frac{1}{\sqrt{2}}(\alpha_{c;y}^{(l)} + \alpha_{c;y}^{(l)*})$, and thus we now have a simple linear one-to-one map $\alpha_{c;x}^{(l)} = (-\mathrm{i}p_c\cos\theta_l + x_c)/\sqrt{2}$ and $\alpha_{c;y}^{(l)} = (-\mathrm{i}p_c\sin\theta_l + y_c)/\sqrt{2}$, which, in other words, means that to fully characterize a coherent state we need to know the average position and the average momentum in this coherent state. However, in the states $|l\rangle$ the coherent parameters $\alpha_{c;x}^{(l)}$ and $\alpha_{c;y}^{(l)}$ are pure imaginary, and thus $x_c = y_c = 0$. We now proceed with calculating the matrix elements, assuming that $|l\rangle = A_c^{(l)} \otimes |\alpha_{c;x}^{(l)}\rangle \otimes |\alpha_{c;y}^{(l)}\rangle = A_c^{(l)} \otimes |-\mathrm{i}p_c\cos\theta_l/\sqrt{2}\rangle \otimes |-\mathrm{i}p_c\sin\theta_l/\sqrt{2}\rangle$, where $A_c^{(l)}$ is the corresponding column-vector in Eq. 13 (from the main text) with the normalization factor $\mathcal{N}_c$. In our derivation below we use that the overlap of coherent states is given by $\langle\beta|\alpha\rangle = e^{-(|\beta|^2+|\alpha|^2-2\beta^*\alpha)/2}$. And we use the fact, that our Hamiltonian is written in the normal-ordered form $\hat{\tilde{H}}_{\mathrm{eff}}[\hat{a}_x, \hat{a}_x^\dagger, \hat{a}_y, \hat{a}_y^\dagger] =: \hat{\tilde{H}}_{\mathrm{eff}}[\hat{a}_x, \hat{a}_x^\dagger, \hat{a}_y, \hat{a}_y^\dagger] :$, i.e. in each term, each creation operator is to the left of each annihilation operator, which greatly simplifies "sandwiching" the Hamiltonian between coherent states. We arrive at the following result (we omit the center-of-mass term)

$$
\begin{aligned}
&\langle l'|\hat{\tilde{H}}_{\mathrm{eff}}|l\rangle = \\
&A_c^{(l')\dagger} \otimes \langle\frac{-\mathrm{i}p_c\cos\theta_{l'}}{\sqrt{2}}| \otimes \langle\frac{-\mathrm{i}p_c\sin\theta_{l'}}{\sqrt{2}}|\hat{\tilde{H}}_{\mathrm{eff}} A_c^{(l)} \otimes |\frac{-\mathrm{i}p_c\cos\theta_l}{\sqrt{2}}\rangle \otimes |\frac{-\mathrm{i}p_c\sin\theta_l}{\sqrt{2}}\rangle = \\
&A_c^{(l')\dagger}\hat{\tilde{H}}_{\mathrm{eff}}[\hat{a}_x \to \alpha_{c;x}^{(l)}, \hat{a}_x^\dagger \to \alpha_{c;x}^{(l')*}, \hat{a}_y \to \alpha_{c;y}^{(l)}, \hat{a}_y^\dagger \to \alpha_{c;y}^{(l')*}]A_c^{(l)} = \\
&\begin{pmatrix} \tilde{H}_{\mathrm{eff},00} & \tilde{H}_{\mathrm{eff},01} & \tilde{H}_{\mathrm{eff},01}^* \\ \tilde{H}_{\mathrm{eff},01}^* & \tilde{H}_{\mathrm{eff},00} & \tilde{H}_{\mathrm{eff},01} \\ \tilde{H}_{\mathrm{eff},01} & \tilde{H}_{\mathrm{eff},01}^* & \tilde{H}_{\mathrm{eff},00} \end{pmatrix},
\end{aligned}
\tag{5.26}
$$

and we remind that $\alpha_{c;x}^{(l)} = -\mathrm{i}p_c\cos\theta_l/\sqrt{2}$ and $\alpha_{c;y}^{(l)} = -\mathrm{i}p_c\sin\theta_l/\sqrt{2}$. Since $\tilde{H}_{\mathrm{eff},00} = \tilde{H}_{\mathrm{eff},11} = \tilde{H}_{\mathrm{eff},22}$ and $\tilde{H}_{\mathrm{eff},01} = \tilde{H}_{\mathrm{eff},12} = \tilde{H}_{\mathrm{eff},02}^*$, thus due to hermiticity we have to list only two matrix elements:

$$
\begin{aligned}
&\tilde{H}_{\mathrm{eff},00} = \langle 0|\hat{\tilde{H}}_{\mathrm{eff}}|0\rangle = \\
&\frac{1}{30}\left(-57\sqrt{3}\Gamma_0 + \frac{72\sqrt{3}\Gamma_0^2\left(324\Gamma_0^3 + 45\Gamma_0\eta^2p_c^2\Omega^2 - 20\eta^3p_c^3\Omega^3\right)}{324\Gamma_0^4 + 25\eta^4p_c^4\Omega^4} + 5\Omega\left(4\eta^2 + 3p_c^2\right)\right),
\end{aligned}
\tag{5.27}
$$

$$\tilde{H}_{\text{eff},01} = \langle 0|\hat{\tilde{H}}_{\text{eff}}|1\rangle = \frac{e^{-\frac{3p_c^2}{4}}}{24\left(324\Gamma_0^4 + 25\eta^4 p_c^4 \Omega^4\right)}\cdot$$
$$[-1944\left(\sqrt{3}+3\mathrm{i}\right)\Gamma_0^5 - 648\left(\sqrt{3}-3\mathrm{i}\right)\Gamma_0^3\eta^2 p_c^2\Omega^2 +$$
$$36\Gamma_0^2\eta^2 p_c^2\Omega^3\left(24\left(1+3\mathrm{i}\sqrt{3}\right)\eta^2 + \left(-9-27\mathrm{i}\sqrt{3}\right)p_c^2 - 8\left(\sqrt{3}+3\mathrm{i}\right)\eta p_c\right) +$$
$$324\left(1+\mathrm{i}\sqrt{3}\right)\Gamma_0^4\Omega\left(3p_c^2 - 8\eta^2\right) + 30\left(7\sqrt{3}-3\mathrm{i}\right)\Gamma_0\eta^4 p_c^4\Omega^4 +$$
$$25\left(1+\mathrm{i}\sqrt{3}\right)\eta^4 p_c^4\Omega^5\left(3p_c^2 - 8\eta^2\right)] \tag{5.28}$$

Diagonalizing this matrix $\langle l'|\hat{\tilde{H}}_{\text{eff}}|l\rangle$ for $\eta > \eta_c$, we get as eigenstates exactly the states, described by Eq. (14) from the main text.

5.6 Non-chiral waveguide

Let us consider the case when the waveguide is non-chiral. Here we focus on the case when there are 2 qubits suspended above the waveguide. Then the effective Hamiltonian up to the second-order of the qubit-photon couplings $g_{1,2}$ reads

$$\hat{H}_{\text{eff}} = \sum_j \omega_x \sigma_j^+\sigma_j + \sum_j \Omega \hat{a}_j^\dagger \hat{a}_j$$
$$-\frac{\Gamma_0}{2}\sum_{i<j}\left[\mathrm{i}\sigma_i^+\sigma_j e^{\mathrm{i}qR\phi_{ij}} e^{\mathrm{i}\eta(\hat{a}_i+\hat{a}_i^\dagger-\hat{a}_j-\hat{a}_j^\dagger)} + \text{H.c.}\right]$$
$$-\frac{\Gamma_1}{2}\sum_{i<j}\left[\mathrm{i}\sigma_i^+\sigma_j e^{-\mathrm{i}qR\phi_{ij}} e^{-\mathrm{i}\eta(\hat{a}_i+\hat{a}_i^\dagger-\hat{a}_j-\hat{a}_j^\dagger)} + \text{H.c.}\right], \tag{5.29}$$

where $q = \omega_x/v$, $\Gamma_{0,1} = g_{1,2}^2/v$ are the radiative decay rate of a single qubit into modes with opposite chirality, and $\eta = qu_0$ is the dimensionless optomechanical interaction. Below we present a plot of the comparison between the two cases: a perfect chiral waveguide with $\Gamma_0 = 0.5\Omega$, $\Gamma_1 = 0$ and a non-chiral waveguide with $\Gamma_0 = \Gamma_1 = 0.5\Omega$. We clearly see, that the corresponding spectrum resembles the one of a perfectly chiral waveguide. If the waveguide is nearly chiral (i.e. $\Gamma_1 \ll \Gamma_0$) then the gaps between different groups of the dispersion branches $E(\eta)$ are smaller, than for a perfectly chiral waveguide (Fig. 5.5a). For a non-chiral waveguide (i.e. $\Gamma_0 = \Gamma_1$) these gaps completely vanish, as shown on the lower panel of the figure below (Fig. 5.5b). The figure below obtained by numerical diagonalization of the Hamiltonian above, after projecting on the subspace with a single photon in the system.

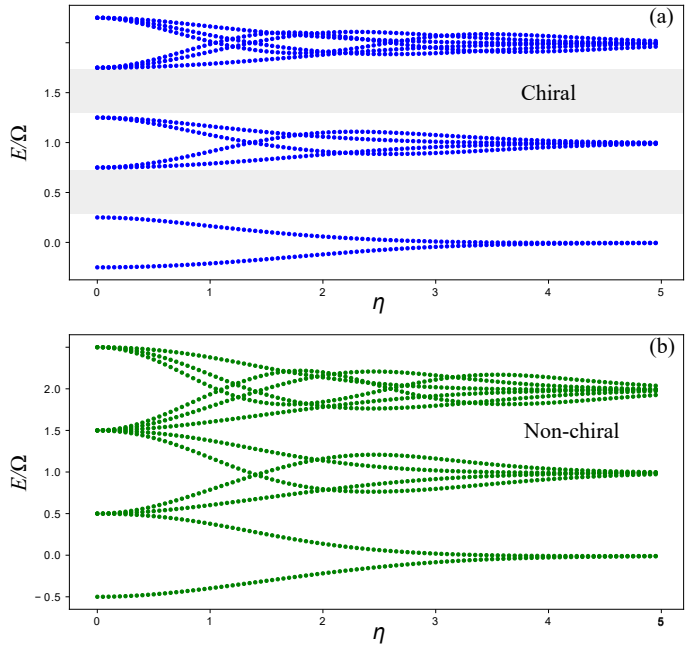

Figure 5.5: Comparison of the energy spectra $E(\eta)$ between (a) the perfect chiral waveguide (top panel) and (b) the non-chiral waveguide (lower panel) for the system with 2 qubits and a single photon in the system. The gaps between different groups on the dispersion branches are marked with grey rectangles in the top panel. For a non-chiral waveguide these gaps disappear. Here we assumed $\phi = \pi/(qR)$.

5.7 Conclusion

To conclude, we have established a direct mapping between the quantum optomechanical set-up in the chiral waveguide and the generalization of the quantum Rabi-model. While for two qubits the system directly maps to the quantum Rabi model, already for the case of three qubits the system possesses unconventional $\mathbb{Z}_3$ symmetry, exhibiting multi-component Schrodinger-cat ground states as well as $\mathbb{Z}_3$ symmetry breaking first order phase transitions in the thermodynamic limit. The work establishes solid connections between the self-organization of atoms in photonic structures which has been previously treated and quantum phase transitions. It also poses an interesting question on the structure of the ground state in the limit of a large number of qubits N. While it can demonstrated that the $\mathbb{Z}_N$ symmetry holds for the case of N qubits,

the nature of the phase transition and the structure of the ground state is yet to be explored.

The results of the work can be applied to a more general class of systems of moving atoms in the photonic structures since it reveals that the apparatus developed in the studies of USC can be directly applied to explore both fundamental aspects of quantized spin-motion coupling and perspective applications in quantum information processing.

6 Anomalous exciton Hall effect

It is well known that electrically neutral excitons can still be affected by crossed electric and magnetic fields that make them move in a direction perpendicular to both fields. This effect is at the origin of the magnetic Stark effect for excitons and is described in terms of a synthetic gauge field. We show that a similar effect appears in the absence of external electric fields, in the case of scattering of an exciton flow by charged impurities in the presence of the external magnetic field. As a result, the exciton flow changes the direction of its propagation that may be described in terms of the Hall conductivity for excitons. We develop a theory of this effect, which we refer to as the anomalous exciton Hall effect, to distinguish it from the exciton Hall effect that arises due to the valley selective exciton transport in transition metal dichalcogenides. According to our estimations, the effect is relatively weak for optically active or bright excitons in conventional GaAs quantum wells, but it becomes significant for optically inactive or dark excitons, because of the difference in the lifetimes. This makes the proposed effect a convenient tool for spatial separation of dark and bright excitons.

6.1 Introduction

Thomas and Hopfield [58] were the first to point out that excitons propagating in the presence of an external magnetic field orthogonal to their velocity acquire stationary dipole polarisation perpendicular to both the magnetic field and their propagation direction. This is the manifestation of the magnetic Stark effect for excitons that was experimentally evidenced in a variety of semiconductor systems [59–61]. This effect is caused by the Lorentz force that pulls an electron and a hole apart if an exciton as a whole particle moves in the presence of a magnetic field. Imamoglu [62, 63] pointed out that once an exciton is placed in crossed electric and magnetic fields, it starts moving as a whole in the direction perpendicular to the directions of both fields, that leads to the renormalization of the excitonic dispersion in quantum wells or two-dimensional semiconductor crystals. The dynamics of electrically neutral quantum liquids in the presence of crossed electric and magnetic fields were studied by Shevchenko [80–82]. Onga *et al.* [64] have recently reported the experimental observation of an exciton Hall effect in atomically thin layers of MoS_2 that manifests itself in the appearance of an off-diagonal exciton conductivity in the presence of a magnetic field. The effect is caused by the strong spin-valley locking in monolayer transition metal dichalcogenides

(TMDs).

Here we predict an anomalous exciton Hall effect that is independent of the exciton spin structure. We show that in conventional GaAs quantum wells containing charged impurities, an exciton flow may be reoriented in the real space due to the combined effect of the local electrostatic potential created by charged impurities and the orbital effect of a magnetic field applied in normal to the plane direction. Conceptually, this effect is similar to the cross-field effect proposed by Imamoglu [62, 63] and it manifests itself in a very similar phenomenology to the exciton Hall effect studied by Onga *et al.* [64], however, it is different from both above-mentioned effects as neither external electric field nor spin-valley locking is required in our case. To distinguish from the previous studies and emphasize the similarity with the anomalous Hall effect (AHE), we refer to the effect we study as an anomalous exciton Hall effect.

We argue that the effect may have a significant magnitude in fluids of optically inactive, dark excitons due to their long lifetimes, and it is much weaker for short-living bright excitons in conventional GaAs-based quantum wells. This makes the anomalous exciton Hall effect a powerful tool for spatial separation of dark and bright excitons.

6.2 Synthetic gauge fields

In condensed matter physics, gauge fields are ubiquitous. The best-known example is a magnetic field $\mathbf{B}$, which can be introduced into a single particle Hamiltonian by substitution $\hat{p}_i \to \hat{p}_i - qA_i$, with q being the electric charge of the particle, A_i being components of the vector potential, $\mathbf{B} = \nabla \times \mathbf{A}$. The presence of a magnetic field dramatically modifies the properties of the system and leads to such fundamental phenomena as the quantum Hall and Aharonov-Bohm effects. For neutral particles with $q = 0$, a magnetic field does not affect the orbital degree of freedom directly, and thus can not be considered as a real gauge field. However, if a particle possesses internal degrees of freedom, such as spin, polarization, or an internal set of energy levels, the creation of so-called synthetic gauge fields becomes feasible. In particular, for cold atoms both Abelian and non-Abelian gauge potentials can be engineered by a resonant drive of the system with spatially inhomogeneous laser beams [65]. For photons, the methods to create synthetic gauge fields include dynamic modulation [66], use of coupled optical resonators [260], engineering lattices with strain [261], or reciprocal metamaterials [67].

In condensed matter physics, the typical example of an electrically neutral quasiparticle is an exciton. Excitons govern the optical response of semiconductor materials at low and, in many cases, at high temperatures [172]. The recent study of the electric field effect on the gauge fields for exciton strongly coupled to light (exciton-polaritons) [63] showed the high potentiality of the gauge field approach to the description of ex-

citon and polariton dynamics in the presence of a magnetic field. In this chapter, we demonstrate how the combination of the magnetic Stark effect [58] with excitonic scattering by an impurity potential leads to the anomalous exciton Hall effect link to the appearance of an effective U(1) gauge field acting on the motion of the exciton center-of-mass.

6.3 Phenomenological model

To reveal the nature of the proposed effect, we start with a simplified phenomenological model, assuming that the motion of the exciton center of mass is decoupled from the relative motion of the electron-hole pair. We consider a 2D exciton confined in the xy-plane and subject to the external magnetic field directed along the z-axis. If the exciton center of mass is characterised by a non-zero momentum $\mathbf{k} \neq 0$, the magnetic field acting on the electron and hole would dipole-polarize the exciton in the direction perpendicular to $\mathbf{k}$, so that the electric dipole moment of the exciton reads $\langle \hat{\mathbf{d}} \rangle = f(B)[\mathbf{e}_z \times \mathbf{k}]$, where $f(B)$ is a function of the magnetic field, which depends linearly on B at weak fields, but becomes inversely proportional to B at the large fields in the magneto-exciton regime [68–70]. At small magnetic fields one can find $f(B)$ by passing to the center-of-mass reference frame, where the magnetic field is absent, but an electric field $\mathbf{E}' = [\hbar\mathbf{k} \times \mathbf{B}]/M$ appears, here M is the exciton mass. If this electric field is weak, then $\langle \hat{\mathbf{d}} \rangle = -e\langle \mathbf{r} \rangle = \alpha \mathbf{E}' = \alpha[\hbar\mathbf{k} \times \mathbf{B}]/M$, where $\alpha = 21 a_{\mathrm{B}}^3 4\pi\varepsilon_0\varepsilon/128$ is the 2D exciton polarizability [79], thus $f(B) = -\alpha\hbar B/M$. At strong magnetic fields, in the magneto-exciton regime, the dipole moment is given by [70] $\langle \hat{\mathbf{d}} \rangle = -e\langle \mathbf{r} \rangle = -e[\mathbf{e}_z \times \mathbf{k}] l_B^2$, where $l_B = \sqrt{\hbar/(eB)}$ is the magnetic length, thus $f(B) = -\hbar/B$.

The presence of impurities and fluctuations of the doped quantum well width leads to the appearance of the scattering potential $U_{\mathrm{sc}}(\mathbf{R})$ for excitons, here $\mathbf{R}$ denotes the position of the exciton center-of-mass. Moreover, it generates some non-zero in-plane distribution of the electric field $\mathbf{E}(\mathbf{R})$, which can affect the exciton dipole moment (see Fig. 6.1 (a)). Using these assumptions we write down the model Hamiltonian of the system as:

$$\hat{H}^{\mathrm{dip}} = \frac{\hat{\mathbf{p}}^2}{2M} + \hat{V}^{\mathrm{dip}} = \frac{\hat{\mathbf{p}}^2}{2M} + U_{sc}(\mathbf{R}) - \frac{1}{2}(\hat{\mathbf{d}} \cdot \mathbf{E} + \mathbf{E} \cdot \hat{\mathbf{d}}), \tag{6.1}$$

where $\hat{\mathbf{d}} = f(B)[\mathbf{e}_z \times \hat{\mathbf{k}}]$, M is the exciton mass, and $\hat{\mathbf{p}} = \hbar\hat{\mathbf{k}}$ is the exciton center-of-mass momentum operator. Note, that as an exciton is a composite particle, there is no simple straightforward relation between the scattering potential and the electric field $\mathbf{E} = \mathbf{E}(\mathbf{R})$, produced by the scatterer. After some algebra this can be cast in form $\hat{H}^{\mathrm{dip}} = \left(\hat{\mathbf{p}} - e\mathbf{A}_{\mathrm{eff}}(\mathbf{R})\right)^2/(2M) + U_{\mathrm{eff}}(\mathbf{R})$, where
$\mathbf{A}_{\mathrm{eff}}(\mathbf{R}) = Mf(B)(\hbar e)^{-1}\left(\mathbf{e}_x E_y(\mathbf{R}) - \mathbf{e}_y E_x(\mathbf{R})\right)$ is a synthetic vector potential, corresponding to the magnetic field $\mathbf{B}_{\mathrm{eff}}(\mathbf{R}) = -\mathbf{e}_z M f(B)(\hbar e)^{-1} \operatorname{div} \mathbf{E}(\mathbf{R})$. $U_{\mathrm{eff}}(\mathbf{R}) =$

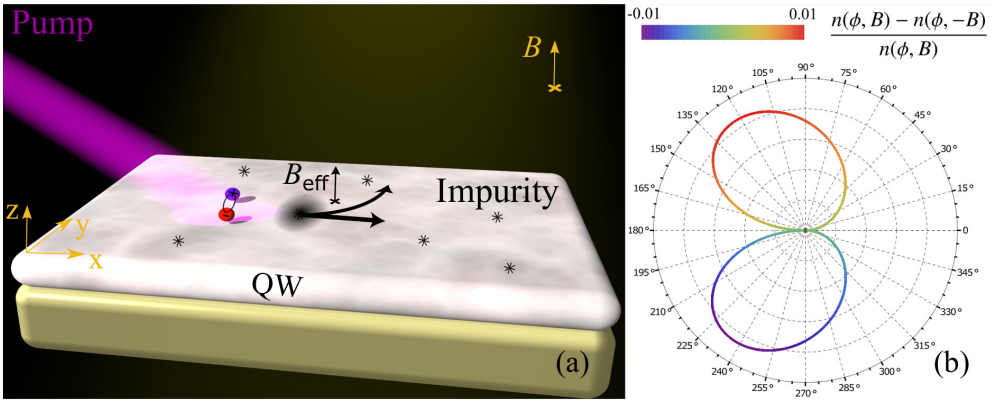

Figure 6.1: (a) The sketch of the system under consideration. Excitons created by the optical pump travel in the plane of a disordered quantum well in the presence of a uniform orthogonal magnetic field $\mathbf{B}$*. The magnetic field induces an in-plane dipole moment of excitons which leads to the asymmetric scattering of excitons by impurities. This problem can be mapped to the scattering of a charged particle by an impurity in the presence of the position-dependent synthetic magnetic field* $\mathbf{B}_{eff}(\mathbf{R})$*, depicted by the grey domain around the scatterer in the figure. (b) Polar plot of* $(n(\varphi, B) - n(\varphi, -B))/n(\varphi, B)$*, where* $n(\varphi, B)$ *is the concentration of excitons, propagating in the direction given by the in-plane polar angle* φ*, plotted at* $B = 1$ *T.*

$U_{\rm sc}(\mathbf{R}) - Mf^2(B)(2\hbar^2)^{-1}\mathbf{E}^2(\mathbf{R})$ is the effective scalar potential. One can see that for the appearance of a non-trivial synthetic gauge field, two conditions need to be fulfilled: (a) $B \neq 0$ and (b) the presence of an inhomogeneous electric field.

We consider now the scattering of an exciton by a single radially symmetrical impurity with $U_{sc}(\mathbf{R}) = U_{sc}(R)$ and $\mathbf{E}(\mathbf{R}) = E(R)\mathbf{R}/R$. We obtain the following elastic scattering matrix elements between the exciton states with the center-of-mass momenta $\mathbf{k}$ and $\mathbf{k}'$ ($|\mathbf{k}| = |\mathbf{k}'|$)

$$V^{\rm dip}_{\mathbf{k},\mathbf{k}'} = U_{\rm sc}(\Delta\mathbf{k}) + \frac{i\hbar f[\mathbf{k}' \times \mathbf{k}]_z}{4\pi|\Delta\mathbf{k}|}\int\limits_0^\infty \mathrm{d}R^2 E J_1(|\Delta\mathbf{k}|R). \tag{6.2}$$

Here we performed the integration over the polar angle, which yielded the Bessel functions, $\Delta\mathbf{k} = \mathbf{k}' - \mathbf{k}$ is the transferred momentum, the arguments of $f(B)$ and $E(R)$ are omitted for brevity. The first term $U_{\rm sc}(\Delta\mathbf{k}) \equiv (2\pi)^{-1}\int\limits_0^\infty R\mathrm{d}RU_{sc}(R)J_0(|\Delta\mathbf{k}|R)$ is real and it describes the normal symmetric scattering of an exciton by an impurity, while the second imaginary term accounts for the breaking of the time reversal symmetry by the magnetic field (as $V^{\rm dip}_{\mathbf{k},\mathbf{k}'} \neq V^{\rm dip}_{-\mathbf{k}',-\mathbf{k}}$). This term gives rise to the asymmetric scattering (analogous to skew scattering) of excitons by the impurities and thus leads to the excitonic analog of the anomalous Hall effect. Thus, the physical mechanism of

the proposed effect is similar to the AHE [87], where the role of spin-orbit coupling is replaced by momentum-dependent exciton dipole polarization.

6.4 Microscopic theory

Now we proceed with a full microscopic model of exciton-impurity scattering in the presence of a magnetic field that accounts for the coupling of electron-hole relative motion and the exciton center-of-mass motion.

The Hamiltonian $\hat{H}_{\rm rel}$ of the relative motion of an $e-h$ pair characterized by the center-of-mass momentum $\hbar\mathbf{k}$ in the presence of a perpendicular magnetic field $\mathbf{B}=(0,0,B)$ has the form [68, 72, 83]

$$\begin{aligned}\hat{H}_{\rm rel} = &-\frac{\hbar^2}{2\mu}\nabla_{\mathbf{r}}^2 - \frac{i\hbar e}{2}\left(\frac{1}{m_e}-\frac{1}{m_h}\right)\mathbf{B}\cdot[\mathbf{r}\times\nabla_{\mathbf{r}}] + \\ &\frac{e^2B^2}{8\mu}r^2 + \frac{e\hbar}{M}\mathbf{B}\cdot[\mathbf{r}\times\mathbf{k}] - \frac{e^2}{4\pi\varepsilon_0\varepsilon|\mathbf{r}|} + \frac{\hbar^2\mathbf{k}^2}{2M},\end{aligned} \tag{6.3}$$

where $\mathbf{r}=\mathbf{r}_e-\mathbf{r}_h$ is the relative $e-h$ coordinate, and $\mu^{-1}=m_e^{-1}+m_h^{-1}$. Deriving this expression we have taken advantage of the existence of an exact integral of motion, namely the magnetic center-of-mass momentum [72], defined by the operator $\hbar\hat{\mathbf{k}} = -i\hbar\nabla_{\mathbf{R}} - e\mathbf{A}(\mathbf{r})$, where $\mathbf{R}=\left(m_e\mathbf{r}_e+m_h\mathbf{r}_h\right)/M$ is the center-of-mass coordinate, $M=m_e+m_h$, and the vector potential is taken in the symmetrical gauge $\mathbf{A}(\mathbf{r})=\mathbf{B}\times\mathbf{r}/2$. The exciton wave function has the form $\Psi_{\mathbf{k}}(\mathbf{R},\mathbf{r})=\exp\left\{i\frac{\mathbf{R}}{\hbar}\left[\hbar\mathbf{k}+e\mathbf{A}(\mathbf{r})\right]\right\}\Phi_{\mathbf{k}}(\mathbf{r})$, where $\Phi_{\mathbf{k}}(\mathbf{r})$ is the corresponding eigenstate of the Hamiltonian above. An important point is that the wave function $\Phi_{\mathbf{k}}$ of the relative motion depends on the center-of-mass momentum $\hbar\mathbf{k}$ [72] i.e., the relative motion and the center-of-mass motion are coupled. The scattering matrix elements $V_{\mathbf{k},\mathbf{k}'}=\langle\Psi_{\mathbf{k}}|\hat{V}|\Psi_{\mathbf{k}'}\rangle$ between the exciton states with the center-of-mass momenta $\mathbf{k}$ and $\mathbf{k}'$ in the external potential $\hat{V}=V_e(\mathbf{r}_e)+V_h(\mathbf{r}_h)$ are given below.

6.5 Weak magnetic fields

In the weak-field limit, $l_B \gg a_{\rm B}$, the scattering matrix elements can be found analytically, here $a_{\rm B}=4\pi\varepsilon_0\varepsilon\hbar^2/(\mu e^2)$ is the Bohr radius (the $1s$ exciton radius is $a_{\rm B}/2$). We shall neglect excitonic transitions to the excited states of internal $e-h$ motion, i.e. the center-of-mass momentum $|\mathbf{k}|\ll a_{\rm B}^{-1}$. The ground-state wave function $\Phi_{\mathbf{k}}(\mathbf{r})$ is calculated in a magnetic field using the perturbation theory. The corresponding

scattering matrix elements $V_{\mathbf{k},\mathbf{k}'}$ are obtained in Ref. [71] and read as follows

$$V_{\mathbf{k},\mathbf{k}'} = \tilde{V}_e(\Delta\mathbf{k})\mathcal{F}_e(\Delta\mathbf{k}) + \tilde{V}_h(\Delta\mathbf{k})\mathcal{F}_h(\Delta\mathbf{k}) + i[\mathbf{k}' \times \mathbf{k}]_z a_{\mathrm{B}}^2 \left(\frac{a_{\mathrm{B}}}{l_B}\right)^2 \left(\tilde{V}_e(\Delta\mathbf{k})\alpha_e - \tilde{V}_h(\Delta\mathbf{k})\alpha_h\right). \tag{6.4}$$

Here $\tilde{V}_j(\mathbf{k})$ is the two-dimensional Fourier transform of the potentials $V_j(\mathbf{r})$ $(j = e, h)$, $\mathcal{F}_{e(h)}(\Delta\mathbf{k}) = \left[1 - 3a_{\mathrm{B}}^2 m_{h(e)}^2(\Delta\mathbf{k})^2/(32M^2) + \beta_{e(h)}(\Delta\mathbf{k})^2 a_{\mathrm{B}}^2 \left(a_{\mathrm{B}}/\ell_B\right)^4\right]$, and $\Delta\mathbf{k} = \mathbf{k}' - \mathbf{k}$ is the transferred momentum. In the derivation above only the terms of up to the second order in B and the lowest order in $|\mathbf{k}|a_{\mathrm{B}}$ are taken into account. The expressions for the dimensionless constants $\alpha_{e(h)}$ and $\beta_{e(h)}$ for a 2D Wannier-Mott exciton can be found in [71] (we corrected typos in the original formulas): $\beta_{e(h)} = 4^{-6}M^{-2}\left(105m_{h(e)}^2 - 159\mu^2/2\right)$ and $\alpha_{e(h)} = -2m_{h(e)}\kappa/M$, $\kappa = -21\mu/(16^2 M)$. Note that $\beta_e, \beta_h > 0$ are positive, therefore, the exciton scattering cross-section increases with B when $l_B \gg a_{\mathrm{B}}$. An important point is that the time-reversal symmetry is broken $V_{\mathbf{k},\mathbf{k}_1} \neq V_{-\mathbf{k}_1,-\mathbf{k}}$, and the structure of $V_{\mathbf{k},\mathbf{k}'}$ resembles its counterpart (6.2) from the simplified phenomenological model. The ground-state exciton energy spectrum is given by

$$\epsilon(\mathbf{k}) = \frac{\hbar^2\mathbf{k}^2}{2M}\left[1 - 2|\kappa|\left(\frac{a_{\mathrm{B}}}{l_B}\right)^4\right] - \epsilon_0\left[1 - \left(\frac{l_2}{l_B}\right)^4\right], \tag{6.5}$$

where the parameter $l_2 = (3/128)^{1/4}a_{\mathrm{B}}$ determines the diamagnetic shift. The first term stands for the center-of-mass kinetic energy, whereas the second term represents the binding energy.

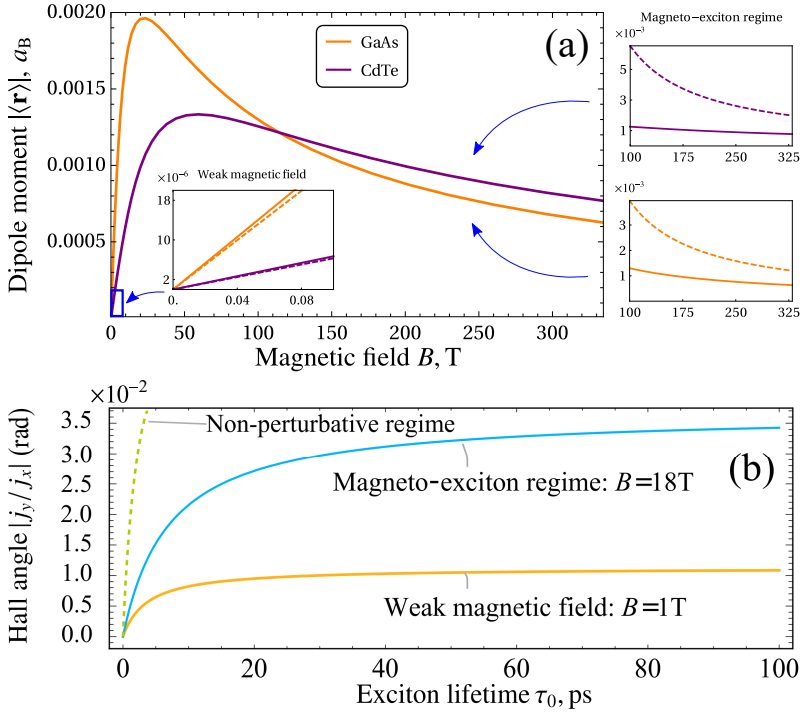

Figure 6.2: (a) The dependence of the dipole moment (absolute value $|\langle \mathbf{r} \rangle|$) on the magnetic field strength for GaAs and CdTe quantum wells. The solid lines are obtained from the numerically found eigenstates of Eq. (6.3), whereas the dashed lines are obtained, using the perturbation theory. The parameters of the plot are typical of GaAs quantum wells: the effective electron and hole masses $m_e = 0.067 m_{e0}$, $m_h = 0.5\, m_{e0}$, the dielectric constant of the quantum well $\varepsilon = 12.5$ (average dielectric constant of the surroundings). The exciton momentum corresponds to the wavelength of the absorbed photon $\lambda = 860$ nm as $|\mathbf{k}| = 2\pi \sin(\pi/2 - \pi/8)/\lambda$, where the angle of incidence is set to $\pi/2 - \pi/8$. The linear part of the curve describes the weak magnetic field limit, whereas the decaying tail corresponds to the magneto-exciton regime. (b) The Hall angle in a GaAs quantum well as a function of the exciton lifetime in two regimes: weak fields $a_B/l_B \ll 1$ and the magneto-exciton regime $a_B/l_B \gg 1$. The expected behavior in the non-perturbative regime $a_B/l_B \sim 1$, where the Hall angle is expected to be the largest, is shown with the dashed curve.

6.6 Magneto-exciton regime

In the opposite regime, where the magnetic field is strong (i.e. $a_\mathrm{B} \gg l_B$), one can neglect the Coulomb interaction term in the Hamiltonian (6.3) and the exciton dynamics is governed by the magnetic field solely. In this regime, which is often referred to as

the magneto-exciton regime, one can calculate the dispersion of the ground state of the system, treating the $e-h$ Coulomb potential as a perturbation [77, 78]

$$\epsilon(\mathbf{k}) = \frac{1}{2}\hbar\omega_{\mathrm{C}} - \sqrt{\frac{\pi}{2}}\frac{e^2}{4\pi\varepsilon_0\varepsilon l_B}e^{-\frac{k^2 l_B^2}{4}} I_0\left(\frac{k^2 l_B^2}{4}\right), \tag{6.6}$$

where I_0 is the modified Bessel function. The corresponding impurity scattering matrix elements are given by

$$\begin{aligned} V_{\mathbf{k},\mathbf{k}'} =& \tilde{V}_e(\Delta\mathbf{k}) \exp\left(-\frac{i}{2}\left[\mathbf{k}'\times\mathbf{k}\right]_z l_B^2 - \frac{\Delta\mathbf{k}^2 l_B^2}{4}\right) + \\ & \tilde{V}_h(\Delta\mathbf{k}) \exp\left(+\frac{i}{2}\left[\mathbf{k}'\times\mathbf{k}\right]_z l_B^2 - \frac{\Delta\mathbf{k}^2 l_B^2}{4}\right), \end{aligned} \tag{6.7}$$

here $\omega_{\mathrm{C}} = eB/\mu$ is the cyclotron frequency.

6.7 Scattering rates

The impurity scattering matrix elements, discussed above for the two regimes, is the starting point for calculating the scattering T-matrix can be defined as $T_{\mathbf{k},\mathbf{k}'} = \langle\Psi_{\mathbf{k}}|\hat{V}|\tilde{\Psi}_{\mathbf{k}'}\rangle$, where $\hat{V} = V_e(\mathbf{r}_e) + V_h(\mathbf{r}_h)$ is the impurity potential operator, $|\Psi_{\mathbf{k}}\rangle$ is the eigenstate of the free Hamiltonian $\hat{H}_0$, describing a 2D exciton in a magnetic field, and $|\tilde{\Psi}_{\mathbf{k}'}\rangle$ is the eigenstate of the full Hamiltonian $\hat{H} = \hat{H}_0 + \hat{V}$. The T-matrix satisfies the Lippmann-Schwinger equation

$$T_{\mathbf{k},\mathbf{k}'} = V_{\mathbf{k},\mathbf{k}'} + \int \frac{d^2\mathbf{g}}{(2\pi)^2}\frac{V_{\mathbf{k},\mathbf{g}}T_{\mathbf{g},\mathbf{k}'}}{E-\epsilon(\mathbf{g})+i0}, \tag{6.8}$$

where $\epsilon(\mathbf{g})$ is the dispersion of the bare Hamiltonian $\hat{H}_0$ and it is given by Eq. (6.5) and Eq. (6.6) for the two regimes under consideration, respectively, and E is the energy eigenvalue corresponding to $|\tilde{\Psi}_{\mathbf{k}'}\rangle$. Two contributions can be distinguished in the square modulus of the T-matrix: $\nu_0^2\left|T_{\mathbf{k},\mathbf{k}'}\right|^2 = \mathcal{G}_{\mathbf{k},\mathbf{k}'} + \mathcal{J}_{\mathbf{k},\mathbf{k}'}$, here $\mathcal{G}_{\mathbf{k},\mathbf{k}'} \equiv \mathcal{G}(\theta) = \mathcal{G}(-\theta)$, $\mathcal{J}_{\mathbf{k},\mathbf{k}'} \equiv \mathcal{J}(\theta) = -\mathcal{J}(-\theta)$ are dimensionless symmetric and asymmetric contributions to the scattering rate, respectively, $\theta = \varphi - \varphi'$ is the scattering angle, φ, φ' are the polar angles of $\boldsymbol{k}, \boldsymbol{k}'$, and $\nu_0 = M/(2\pi\hbar^2)$ is the 2D density of states of free particles with parabolic dispersion, which is introduced here to write the scattering matrices in dimensionless form. The density of states is defined as $\nu(\mathbf{k}) = \left|\partial\epsilon(\mathbf{k})/\partial k\right|^{-1} k/(2\pi)$. Here we restrict ourselves to the case of elastic scattering $|\mathbf{k}| = |\mathbf{k}'|$. It is the asymmetric part $\mathcal{J}_{\mathbf{k},\mathbf{k}'}$ of exciton scattering by impurities that give rise to the Hall current. The properties of $\mathcal{J}_{\mathbf{k},\mathbf{k}'}$ are discussed in details in Ref. [73–75].

The elastic scattering rate $W_{\mathbf{k},\mathbf{k}'}$ from $\mathbf{k}'$ to $\mathbf{k}$ state is expressed with use of the Fermi golden rule $W_{\mathbf{k},\mathbf{k}'} = 2\pi\hbar^{-1} n_{\mathrm{imp}}\left|T_{\mathbf{k},\mathbf{k}'}\right|^2 \delta\left(\epsilon_{\mathbf{k}} - \epsilon_{\mathbf{k}'}\right)$, where n_{imp} is the surface density

of impurities. The presence of the magnetic field breaks the time inversion symmetry in the problem and leads to the disbalance of scattering rates $W_{\mathbf{k},\mathbf{k}'}$ and $W_{\mathbf{k}',\mathbf{k}}$, which is why a non-zero Hall contribution $\mathcal{J}_{\mathbf{k},\mathbf{k}'}$ emerges.

Let us assume that the impurity potential is described by the Coulomb potential [76] $V_e(r) = -V_h(r) = -eq_{\text{imp}}/(4\pi\varepsilon_0\varepsilon r)$. The Lippmann-Schwinger equation can not be treated perturbatively for such a potential in our system, which is why we solve this integral equation (6.8) numerically.

The developed formalism allows us to predict the anisotropy of an angular distribution of the exciton emission that would appear if a flow of excitons propagates in a plane of a doped quantum well in the presence of a magnetic field normal to the plane of the well (as Fig. 6.1 (a) shows schematically). The angular distribution of the exciton emission may be found as $n(\phi) = \int\limits_0^\infty n_{\mathbf{k}} \, \dfrac{kdk}{(2\pi)^2}$, where $n_{\mathbf{k}}$ is the occupation numbers of exciton states having wave vectors $\mathbf{k}$. The normalized variation of this quantity due to the inversion of the orientation of the applied field is shown in Fig. 6.1 (b). The observation of a predicted variation of the angular distribution of the excitonic emission can be considered as a smoking gun for the anomalous exciton Hall effect. We note, that dark excitons contribute very little to the intensity of photoluminescence, while they strongly contribute to its blue shift [88, 89]. Experimental measurement of the angular resolved blue-shift of the bright exciton photoluminescence peak might certify the presence of a flow of dark excitons.

Having solved the Lippmann-Schwinger equation numerically in the two regimes under consideration, one may proceed with calculating the Hall current appearing in the system. To obtain the Hall angle, we study the classical transport regime $|\mathbf{k}|l \gg 1$, where l is the exciton mean free path. We use the semiclassical Boltzmann equation

$$\frac{dn_{\mathbf{k}}}{dt} = P_{\mathbf{k}} - \Gamma n_{\mathbf{k}} + \int \frac{d^2\mathbf{k}'}{(2\pi)^2}(W_{\mathbf{k},\mathbf{k}'}n_{\mathbf{k}'} - W_{\mathbf{k}',\mathbf{k}}n_{\mathbf{k}}), \tag{6.9}$$

here $P_{\mathbf{k}}$ is the pump term, $\Gamma = 1/\tau_0$ is the particle decay rate. Once the equilibrium is reached, $n_{\mathbf{k}}$ doesn't depend on time, and thus the time derivative term can be omitted. Then, performing the integration over the absolute value of $\mathbf{k}'$, the Boltzmann kinetic equation can be rewritten as

$$0 = P_{\mathbf{k}} - \Gamma n_{\mathbf{k}} + \int d\varphi' \left(w_{\mathbf{k},\mathbf{k}'}n_{\mathbf{k}'} - w_{\mathbf{k}',\mathbf{k}}n_{\mathbf{k}}\right), \tag{6.10}$$

where $w_{\mathbf{k},\mathbf{k}'} = n_{\text{imp}}\nu_0/(\hbar\nu(\mathbf{k})^2)\,(\mathcal{G}_{\mathbf{k},\mathbf{k}'} + \mathcal{J}_{\mathbf{k},\mathbf{k}'})$ and the exciton density of states $\nu(\mathbf{k}) = |\partial\epsilon(\mathbf{k})/\partial k|^{-1}\, k/(2\pi)$. Let us assume the in-plane wave vector $\mathbf{k}_0$ of the pump is pointing along the x-axis, i.e. $\mathbf{k}_0 = (k_0, 0)^T$, which implies $P_{\mathbf{k}} = P_0\delta(\mathbf{k} - \mathbf{k}_0) = (P_0/k)\delta(k - k_0)\delta(\varphi)$ and we note that this function is even with respect to φ. Since $w_{\mathbf{k},\mathbf{k}'}$ depends on the difference between the momentum angles, to perform the integration over φ' in the collision integral, the particle density $n_{\mathbf{k}}$ and the scattering rate $w_{\mathbf{k},\mathbf{k}'}$ should be expanded in cylindrical harmonics $\cos m\varphi$, $\sin m\varphi$, where

$m \geq 0$ is integer. Assuming that only the dipole type of anisotropy of the momentum-space distribution function is significant, we represent $n_{\mathbf{k}} = n_0(k) + \delta n(\mathbf{k})$, where $\delta n(\mathbf{k}) = n_+(k)\cos\varphi + n_-(k)\sin\varphi$, $n_0(k)$ is the isotropic part of the distribution function which depends only on energy. The coefficients $n_\pm(k)$ are to be found. Substituting this decomposition into the kinetic equation (6.10) and integrating over φ' in the collision term, we obtain

$$0 = \frac{P_0}{k}\delta(k-k_0)\delta(\varphi) + \cos\varphi\left(\Omega(k)n_-(k) - \frac{n_+(k)}{\tau(k)}\right) - \sin\varphi\left(\Omega(k)n_+(k) + \frac{n_-(k)}{\tau(k)}\right) - \frac{n_{\mathbf{k}}}{\tau_0}, \tag{6.11}$$

where $\tau(k)$ is given by the symmetric scattering term $\tau(k)^{-1} = n_{\text{imp}}\nu_0/(\hbar\nu(\mathbf{k})^2)\int_0^{2\pi}\mathcal{G}_{\mathbf{k},\mathbf{k}'}(1-\cos\theta)d\theta$, here $\theta = \varphi - \varphi'$ is the scattering angle. The factor $\Omega(k)$ is governed by the asymmetric scattering term $\Omega(k) = -n_{\text{imp}}\nu_0/(\hbar\nu(\mathbf{k})^2)\int_0^{2\pi}\mathcal{J}_{\mathbf{k},\mathbf{k}'}\sin\theta d\theta$, and it mixes the even $n_+(k)$ and odd $n_-(k)$ contributions to the density distribution, yielding a Hall current in the transverse y-direction. Using the orthogonality of $\sin\varphi$ and $\cos\varphi$, the kinetic equation is readily solved, yielding $n_-(k) = -\Omega(k)\tau_{\text{tot}}(k)n_+(k)$. Here we introduced the total relaxation time $\tau_{\text{tot}}(k) = (\tau_0^{-1} + \tau(k)^{-1})^{-1}$. The Hall angle [84], is defined as the ratio of the Hall current j_y and the longitudinal current j_x, is $j_y/j_x = -\Omega(k_0)\tau_{\text{tot}}(k_0)$, where $j_{x,y} = \int \hbar k_{x,y}\delta n(\mathbf{k})d^2\mathbf{k}/(2\pi)^2$. Note that Onga et al. [64] use a different definition. We estimate the Hall angle for the typical parameters of doped GaAs quantum wells $n_{\text{imp}} \approx 10^{11}$ cm^{-2}, $k_0 \approx 7\cdot 10^6$ m^{-1} (see the caption of Fig. 6.2), $\varepsilon = 12.5$, $q_{\text{imp}} = e$, and $\tau_0 \approx 10$ ps (for bright excitons). At a weak magnetic field $B = 1$ T the numerical solution of the Lippmann-Schwinger equation with the kernel (6.4), yields $\tau(k_0) \approx 3.8$ ps and $j_y/j_x = -\Omega(k_0)\tau_{\text{tot}}(k_0) \approx 0.8\%$. At increased concentration and a strong magnetic field $B = 18$ T we solve the Lippmann-Schwinger integral equation numerically with the magneto-exciton kernel (6.7), which yields $j_y/j_x = -\Omega(k_0)\tau_{\text{tot}}(k_0) \approx 1.8\%$. One may expect, by looking at Fig. 6.2(a), that at intermediate magnetic field strengths (about $B \approx 10$ T) the Hall angle would be significantly larger, as the exciton dipole moment reaches its largest value in this non-perturbative regime, while still not switching to the magneto-exciton regime. We also note, that the range of magnetic fields corresponding to the largest dipole moment is easily achievable experimentally, which makes the observation of the predicted phenomenon realistic. The dependence of the Hall angle on the exciton lifetime is shown in Fig. 6.2(b). Clearly, for dark excitons whose lifetime is significantly larger than the lifetime of bright excitons, the Hall angle is notably larger. This shows that the anomalous exciton Hall effect may be used as a tool for spatial separation of dark and bright excitons.

6.8 Conclusions

In conclusion, we demonstrated that the magnetic Stark effect for 2D excitons may lead to the emergence of an effective U(1) gauge field. This field can result in the excitonic analog of the anomalous Hall effects. For the latter we presented a detailed microscopic description of the scattering mechanism and analyzed the transport properties, showing that the effect can be observed experimentally in conventional GaAs quantum wells and that it is much stronger for dark than bright excitons.

7 Tunable optical nonlinearity for TMD polaritons dressed by a Fermi sea

We study a system of a transition metal dichalcogenide (TMD) monolayer placed in an optical resonator, where the strong light-matter coupling between excitons and photons is achieved. We present quantitative theory of the nonlinear optical response for exciton-polaritons for the case of a doped TMD monolayer, and analyze in detail two sources of nonlinearity. The first nonlinear response contribution stems from the Coulomb exchange interaction between excitons. The second contribution comes from the reduction of Rabi splitting that originates from phase space filling at increased exciton concentration and the composite nature of excitons. We demonstrate that both nonlinear contributions are enhanced in the presence of free electrons. As free electron concentration can be routinely controlled by an externally applied gate voltage, this opens a way of electrical tuning of the nonlinear optical response.

7.1 Introduction

Planar microcavities in the regime of strong light-matter coupling represent a robust platform for nonlinear optics. The hybridization of excitons with optical cavity photons leads to the formation of ultralight interacting quasiparticles—polaritons—that enable polariton lasing [85, 86, 243, 271] and emergent polariton fluid behavior [121–124]. For conventional quantum well (QW) nanostructures in III-V and II-VI semiconductors in this regime various nonlinear effects were studied, including formation of solitons [125–128], vortices [129–133], polarization multistability [134–139], and nontrivial polariton lattice dynamics [140–146]. These unique properties can be used for experimental realization of ultra fast polariton-based nonlinear optical integrated devices [147–153].

In these systems the nonlinear response mainly originates from the Coulomb-based exciton-exciton scattering [154–160], typically observed at macroscopic mode occupations. For high quality samples prerequisite signatures of a quantum nonlinear behavior were recently observed [161, 162], thanks to outstanding fabrication advances. The limitations for QW-based platform come from low operation temperatures, relatively

small light-matter coupling (~ 4 meV per QW), and complex growth techniques [163].

Recent advances in the field of optically-active two-dimensional (2D) materials have largely increased capabilities of polaritonics [164, 165]. In this case excitons are hosted by monolayers of transition metal dichalcogenide (TMD) materials—atom-thick nanostructures with a direct optical bandgap [166–171] and excellent optical properties [172, 173]. To date light-matter coupling for TMD excitons was observed in various configurations, including optical microcavities [174–178], Tamm plasmon structures [179], photonic crystals [180, 181], surface plasmons [182–184] and nanoantennas [185, 186]. Due to the relatively large electron/hole masses and reduced screening, TMD exciton binding energy ranges in hundreds of meVs, and multicharge bound complexes (trions [187–191], biexcitons [192]) can be observed. Importantly, small exciton volume leads to large Rabi frequency, and excitonic optical response dominates already at room temperature [172]. Further list of exceptional properties of TMD monolayers includes strong spin-orbit interaction and valley-dependent physics [193–195], peculiar exciton transport properties [196, 197], and strong dependence on dielectric properties for observed physical effects [198–200]. For doped and gated TMD samples bandgap renormalization was shown [201–204], which opens the way to engineering of material properties. Finally, studies of trapped excitons and strain-induced lattices revealed efficient defect-based single photon emission from two-dimensional materials [205–208].

The natural next step in TMD polaritons is exploring of the nonlinear response. This so far has proven to be a nontrivial task, as the very same large binding leads to reduction of the exciton-exciton scattering cross-section evidenced theoretically [209] and experimentally [210]. However, the situation changes drastically once large light-matter coupling is achieved and a TMD monolayer is doped with free carriers. First, the deviation of excitonic statistics from ideal bosons [211, 212] leads to the nonlinear Rabi splitting behavior[158, 213–215]—optical saturation—that in the case of strongly-coupled TMD polaritons was shown to give significant contribution [178]. Second, the presence of free electron gas (Fermi sea) strongly modifies the optical response of TMD monolayers. It depends on the density of the electrons, and leads to several characteristic regimes [216, 217]. At low free electron concentrations sharp additional peak appears that is typically attributed to charged exciton complexes (trions), being bound states of two electrons and one hole [178, 187, 190]. At high electron concentrations the broad spectral peak was observed and attributed to an exciton polaron-polariton—correlated state of an exciton dressed by the Fermi sea [177, 218–220]. In each case the enhancement of the nonlinear response was reported [178, 220, 221].

One should note, however, that besides formation of the additional peak, corresponding to the appearance of new quasiparticles, the presence of free electrons shall modify substantially the optical response of the exciton mode itself. This is especially pronounced in the case of intermediate electron densities, where excitons are spectrally separated from the other modes. Differently from the cases of very low and high electron densities, this region remains unexplored so far. In the current chapter we

aim to bride the gap between the regimes of low and high electron densities, focusing on nonlinear optical properties of the system. In particular, we demonstrate that Fermi sea strongly contributes to the screening of Coulomb potential and the onset of additional correlations stemming from the Pauli exclusion principle. These effects change both light matter coupling and exciton-exciton interactions, thus resulting in renormalization of the strength of nonlinearity. Our theory shows that the change of the free electron density, which can be routinely realized in gated TMD samples, gives a powerful tool for controlling the optical nonlinearity.

The chapter is organized as follows. In Section 7.2 we present the theory describing the behavior of an exciton in a TMD monolayer in the presence of Fermi sea. It accounts for both screening (S) of the Coulomb potential and the Pauli blocking (PB) effect. We study the modification of the excitonic wavefunctions, excitonic binding energy and Bohr radius. In Section 7.3 we calculate exciton-exciton interaction potentials in the presence of an electron gas. We demonstrate that the screening and the Pauli blocking play opposite roles, the former increasing and the latter decreasing effective exciton-exciton interaction constant. We find that this counterintuitive effect of the Pauli blocking comes from the mixing of exciton ground and excited states. As a result of the competition of these two mechanisms we report an overall increase of the interaction constant with electron density. In Section 7.4 we analyze the impact of free electrons on nonlinear reduction of the Rabi splitting in the system, and show that nonlinearity increases with electron density. In Sections 7.5, 7.6, 7.7, and 7.8 we present the detailed analysis of the saturation effects and the impact of trion state on the exciton-polariton spectra. Section 7.9 summarizes our findings.

7.2 2D excitons in the presence of a Fermi sea

We study a transition metal dichalcogenide monolayer where optical response is strongly dominated by tightly-bound neutral Wannier excitons. Considering a doped monolayer, we account for the presence of the Fermi sea formed by the excessive charge. This can lead to the modification of an optical response in several different ways, and dominant contributions depend on the free electron density n and correspondingly the location of the Fermi level E_F. At low electron concentrations charged excitons—trions—are formed. In TMD monolayers these three-particle bound states have binding energy E_b^T being much smaller than an exciton binding energy E_b^X. Therefore, in the low-density regime $E_F \ll E_b^T$ trion- and exciton-based response is spectrally well-separated. However, properties of excitons in doped monolayers are modified by an electron gas through screening and Pauli blocking (Fig. 7.1). In the high density regime where $E_F \sim E_b^T$ strong many-body correlations between excitons and electrons become important, and the system is described in terms of exciton-polarons [218] (dressed exciton-electron quasiparticles). For instance, in MoS_2 monolayer with $E_b^T = 18$ meV this corresponds to the concentration of excess carriers $n \sim 10^{12}..10^{13}$ cm^{-2}.

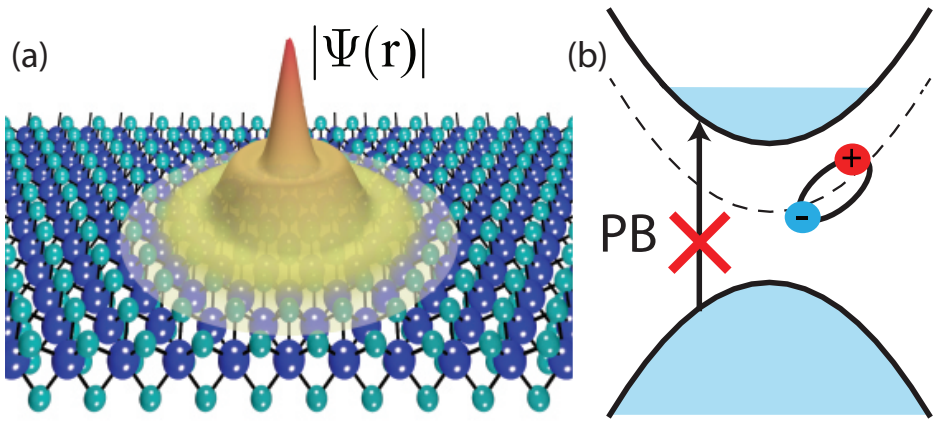

Figure 7.1: Sketch of the system. (a) Absolute value of an excitonic wavefunction in a TMD monolayer that is strongly modified by the free electron gas in the conduction band. (b) Sketch of the excitation process where the Pauli principle excludes occupied states in the conduction band preventing the exciton formation.

In the present work we focus on the low- and intermediate-density regime, where the exciton-based optical response is modified by the Fermi sea through the exciton wavefunction and energy renormalization. To account for electrons we solve the Wannier equation for the eigenenergy E_{X} and the momentum-space exciton wavefunction $C_{\mathbf{p}}$ that reads[218]

$$\left(\frac{\hbar^2 k^2}{2\mu} + \Sigma_g\right) C_{\mathbf{k}} - \sum_{\mathbf{k}'} B_{\mathbf{k}} V_{\mathbf{k}-\mathbf{k}'} B_{\mathbf{k}'} C_{\mathbf{k}'} = E_{\mathrm{X}} C_{\mathbf{k}}, \tag{7.1}$$

where the exciton binding energy $E_b^X = |E_{\mathrm{X}} - \Sigma_g|$ accounts for the band gap renormalization Σ_g caused by excessive charge carriers. In Eq. (7.1) $\mu = mm_v/(m+m_v)$ is an exciton reduced mass, and m and m_v stand for the conduction and valence band effective mass, respectively. $B_{\mathbf{k}} = [1 - n_F(E_{\mathbf{k}}^c)]^{1/2}$ is the Pauli blocking factor that excludes filled electronic states from the space available for exciton formation, $E_{\mathbf{k}}^c$ denotes an energy dispersion for the conduction band, and n_F is a Fermi-Dirac distribution. To account for the effects of screening caused by the excess charge carriers [222, 223] and the atomic thickness of the material [224], we consider the screened interaction potential

$$V_{\mathbf{k}} = \frac{2\pi e^2}{(4\pi\varepsilon_0\kappa)[k + \rho_0 k^2 + k_{sc}(k)]}, \tag{7.2}$$

where ε_0 is the vacuum permittivity, ρ_0 is a screening parameter associated to the intrinsic polarizability of the two-dimensional layer, $k_{sc}(k) = -2\pi e^2 \Pi(k)/(4\pi\varepsilon_0\kappa)$

is the screening momentum, and κ denotes a dielectric constant of the surrounding media. We use the static polarization operator of two-dimensional electron gas [222] $\Pi(k) = -m/(\pi\hbar^2)[1 - \Theta(k - 2k_F)(1 - 4k_F^2/k^2)^{1/2}]$, where the Fermi wavevector is $k_F = \sqrt{2mE_F}/\hbar$. Σ_g accounts for the bandgap renormalization by carriers due to screening and phase space filling effects, and reads

$$\Sigma_g = -\sum_{\mathbf{k}} V_{\mathbf{k}} n_F(E^c_{\mathbf{k}}) - \sum_{\mathbf{k}} (V^0_{\mathbf{k}} - V_{\mathbf{k}}) n_F(E^v_{\mathbf{k}}), \tag{7.3}$$

where $E^c_{\mathbf{k}} = \hbar^2\mathbf{k}^2/2m - E_F$ and $E^v_{\mathbf{k}} = \hbar^2\mathbf{k}^2/2m_v - E_g - E_F$ denote the energies of conduction and valence bands, E_g is the non-screened bandgap width and $V^0_{\mathbf{k}} = 2\pi e^2/[4\pi\varepsilon_0\kappa(k + \rho_0 k^2)]$. For the sake of simplicity we neglect the renormalization of electron masses in conduction and valence bands, and retain only the bandgap renormalization Σ_g.

The rotational symmetry of the potential $V_{\mathbf{k}}$ allows one to write the wavefunction in the form

$$C_{\mathbf{k}} = C^{n,m_z}(k)\frac{e^{im_z\theta}}{\sqrt{2\pi}} \tag{7.4}$$

where we use polar coordinates $\mathbf{k} = (k, \theta)$. Then the Wannier equation (7.1) for $C^{n,m_z}(k)$ reads

$$E_{\mathrm{X}} C^{n,m_z}(k) = \left(\frac{\hbar^2 k^2}{2\mu} + \Sigma_g\right) C^{n,m_z}(k) + \int_0^\infty \frac{k'dk'}{(2\pi)^2} B(k) V_1(k,k') B(k') C^{n,m_z}(k') \tag{7.5}$$

where $V_1(k, k')$ is

$$V_1(k,k') = -\int_0^{2\pi} d\theta V(\sqrt{k^2 + k'^2 - 2kk'\cos\theta}) e^{im_z\theta}. \tag{7.6}$$

We solve Eq. (7.5) numerically for a monolayer of transition metal dichalcogenide. The structure parameters vary a lot throughout the literature and depend on the choice of both TMD monolayer material and its surrounding. Here we set the screening length to $r_0 = 4$ nm and the bandgap to $E_g = 2.6$ eV, which are typical for MoS_2 layer [167, 225, 226]. We also fix equal effective masses, $m_v = m$. As a reference, we choose the case of freestanding monolayer ($\kappa = 1$), and set $m = 0.35m_0$ (m_0 is a free electron mass), being typically the case for TMD monolayers [227]. We consider only the exciton ground-state, so that we set $m_z = 0$. The results of calculations are shown in Fig. 7.2. In Fig. 7.2(a) we present the momentum space distribution for the excitonic wavefunction. We observe that the increase of free electron gas density leads to the strong modification of the wavefunction as compared to standard two-dimensional

hydrogen-like wavefunction that has a form $\propto \left[1 + (\lambda k)^2\right]^{-3/2}$. The quenching of low-momenta region stems from the Pauli blocking effect. In order to extract the relative contributions of Pauli blocking factor and the screening of interaction induced by electron gas, we simulate Eq. (7.5) in the regimes when one of the factors is effectively turned off. At low density the impact of both effects is small, and the wavefunctions plotted for this two cases nearly coincide (not shown). At relatively high density of the free electron gas the momentum space wavefunction is shown in Fig. 7.2(c) (thick blue curve). We see that the additional screening leads to re-scaling of wavefunction [Fig. 7.2(c), green curve], while the Pauli blocking is responsible for the suppression of low momenta region [Fig. 7.2(c), red curve].

Plots in Fig. 7.2(b, d) illustrate the electron density dependence of the exciton binding energy and Bohr radius. The latter is defined as an average electron-hole separation $a_B(n) = \langle \psi_n(r)|r|\psi_n(r)\rangle$, where $\psi_n(r)$ is the exciton wavefunction in the real space, and we highlight that it depends on the free electron gas density n. The growth of the electron concentration leads to stronger interaction screening, which results in weaker binding of excitons. In the absence of screening the Pauli blocking factor becomes essential for larger values of electron density, leading to reduction of binding energy and corresponding increase for the exciton Bohr radius.

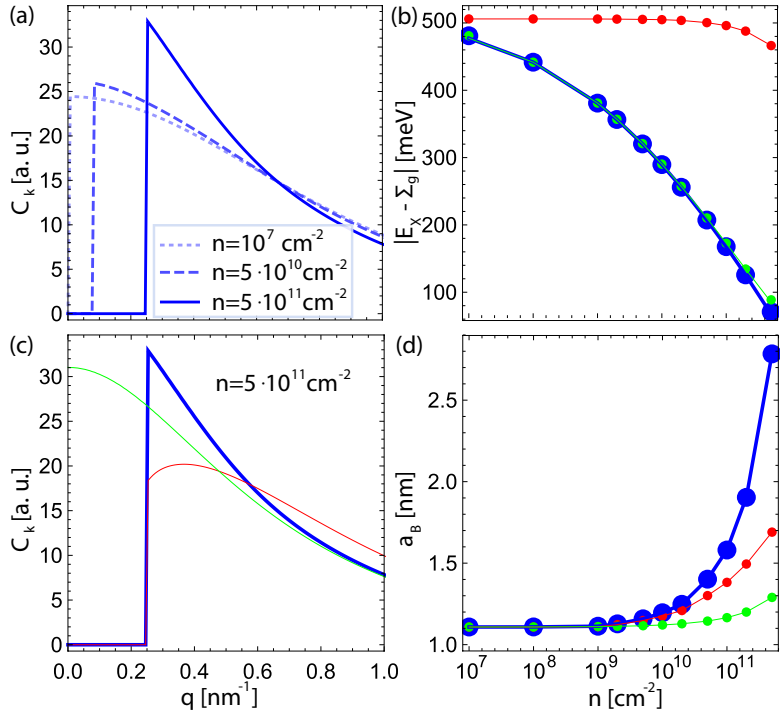

Figure 7.2: (a) Exciton wavefunction in the momentum space shown for different electron gas density. The shift of wavefunction maximum is caused by the increase of Fermi energy and the corresponding wavevector. (b) Exciton binding energy as a function of free electron concentration. Here the green curve corresponds to the absence of Pauli blocking, the red curve corresponds to the absence of interaction screening by electron gas, and the blue solid curve accounts both effects. (c) The impact of screening and Pauli blocking factors on exciton wavefunction at high density of free electron gas. Colors are the same as in panels (b). Notably, screening by the free electron gas leads to rescaling of hydrogen-like wave function (green curve), whereas the Pauli blocking determines the modified shape of the wavefunction (red curve). (d) Bohr radius shown as a function of free electron concentration. Labelling is the same as in (b).

7.3 Exciton-exciton interaction

Next, we study the exciton-exciton interaction processes for TMD monolayers that originate from Coulomb interaction of electrons and holes. We use the standard scattering theory approach [154–156] and exploit the calculated exciton wavefunction to account for the presence of the electron gas. First, we note that the direct interaction is suppressed due to the electron-hole equal effective masses, $m_v = m$ [154]. Hence, the total interaction constant g_{tot} is determined by the electron and hole exchange terms, which are identical due to equal effective masses. Thus, $g_{\text{tot}} = 2g^e_{\text{exch}}$, with g^e_{exch} denoting the electron exchange interaction constant. The latter reads [156]

$$g^e_{\text{exch}}(Q) = \frac{2}{A}\sum_{\mathbf{k},\mathbf{q}} V_{\mathbf{q}} C_{\mathbf{k}-\mathbf{q}/2} C_{\mathbf{k}-(\mathbf{Q}-\mathbf{q})/2} C_{\mathbf{k}+\mathbf{q}/2} \left[C_{\mathbf{k}+(\mathbf{Q}-\mathbf{q})/2} - C_{\mathbf{k}+(\mathbf{Q}+\mathbf{q})/2}\right], \tag{7.7}$$

where $\mathbf{Q}$ is an exchanged momentum, and A is the normalization area.

In Fig. 7.3(a) we present the dependence of the electron exchange interaction constant as a function of exchange momenta. The maximum of interaction constant demonstrates a moderate increase with increasing n, and the shape of exchange momenta dependence is generally unchanged. Fig. 7.3(b) presents the dependence of interaction maxima on the electron density. Particularly one can see that the dependence is non-monotonous, with the local minima appearing at moderate electron densities. The latter stems from complex interplay between multiple factors, discussed below.

In order to understand the origin of this non-trivial dependence of interaction on the electron gas density, we perform calculations (i) in the absence of Pauli blocking factor, and (ii) in the effective absence of screening. The corresponding dependence on exchange momenta is shown in Fig. 7.3(c) for $n = 5 \cdot 10^{11}$ cm^{-2} density of free electrons. We observe that the interaction has its highest value when both effects are accounted (blue thick curve). In the absence of Pauli blocking the screening leads to the slight decrease of interaction maxima [case (i), green curve]. In turn the Pauli blocking leads to significant reduction [case (ii), red curve]. In Fig. 7.3(d) we plot the maxima of interaction versus the density of the electron gas. We observe that screening leads to the monotonous enhancement of interaction [case (i), green curve], and the Pauli blocking leads to its monotonous reduction [case (ii), red curve].

The enhancement of the interaction coefficient due to the interaction screening [case (i)] is caused by the enhancement of exciton Bohr radius that dominates the weakening of interaction potential. The origin of reduction due to the Pauli blocking [case (ii)] stems from the fact that the Pauli blocking leads to mixing of exciton ground and excited states. In its turn, it was shown earlier, that the interaction between excited exciton states is of attractive nature [209, 228], explaining the overall decrease of repulsive interaction between excitons. Here we find that the exciton wave function in

the presence of Pauli blocking can be expanded in terms of $1s$, $2s$, $3s$ exciton states, and the calculation of exciton-exciton interaction in terms of such functions agrees well with the one calculated in the presence of Pauli blocking (see Fig. 7.6). The details of the calculation are shown in Section 7.5. The presence of both Pauli blocking and screening leads to a complicated dependence on the density of free electron gas, with regions dominated by the reduction stemming from Pauli blocking and the enhancement arising from screening, as depicted in Fig. 7.3(d)].

We further analyze the dependence of exciton-exciton interaction on material and substrate parameters. The results are shown in Fig. 7.4. We observe that the interaction constant demonstrates non-monotonous dependence with local minima at intermediate density regardless the structure parameters. The latter means that the observed effect is of general character and does not depend qualitatively on the material choice. It is remarkable that the growth of Bohr radius due to increase of dielectric constant is nearly compensated by the corresponding reduction of interaction potential, leading to overall weak dependence of exciton-exciton constant on the dielectric properties of surrounding media [cf. blue and black curves in Fig. 7.4(a)]. On the other hand, the smaller effective mass of electrons leads to larger Bohr radius, resulting in enhancement of exchange interaction, as the increase of Bohr radius here is not compensated by corresponding reduction of interaction potential [cf. blue and green curves in Fig. 7.4(a)]. It should be mentioned, that all the characteristic peculiarities of the free electron gas impact on the exciton Coulomb nonlinearity remain unaltered in the case of unequal effective masses of conduction and valence bands (see Section 7.6 for the details).

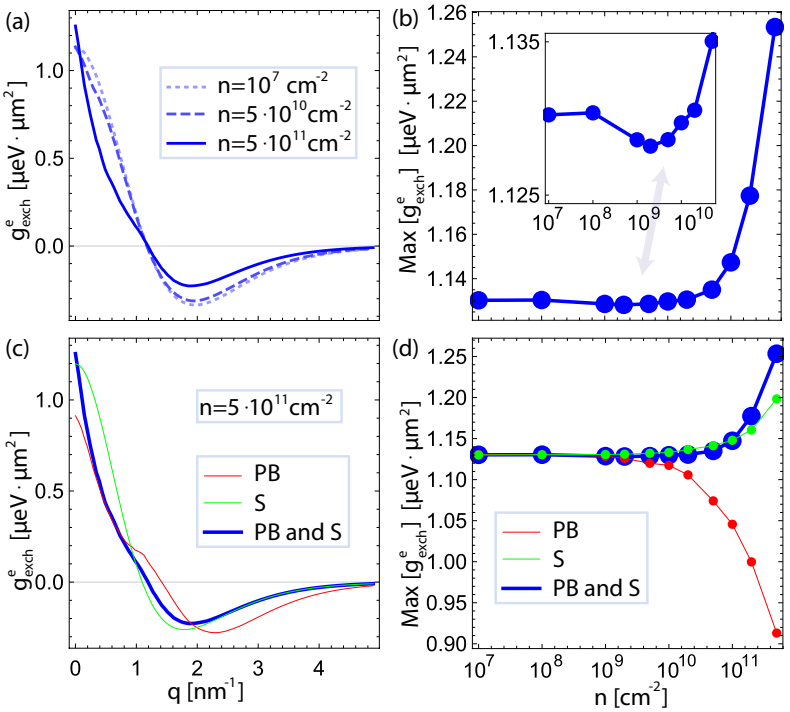

Figure 7.3: Exciton-exciton exchange interaction. (a) The dependence of interaction constant on transfer momenta at different densities of free electron gas. While the interaction maxima demonstrates a moderate and non-monotonous shift with the increase of the free electron gas density, the shape for transfer momenta dependence is nearly unaltered. (b) The maxima of interaction constant as a function of free electron gas density. The inset illustrates zoomed-in region with the non-monotonous dependence. (c) The impact of screening and Pauli blocking factors on momentum dependence of exciton-exciton interaction at high density of free electron gas. Here the green curve corresponds to the absence of Pauli blocking, the red curve to the absence of interaction screening by electron gas, and blue solid curve accounts both effects. (d) The influence of screening and Pauli blocking factors on the maxima of exchange interaction vs the density of free electrons. Colors are the same as in panel (c).

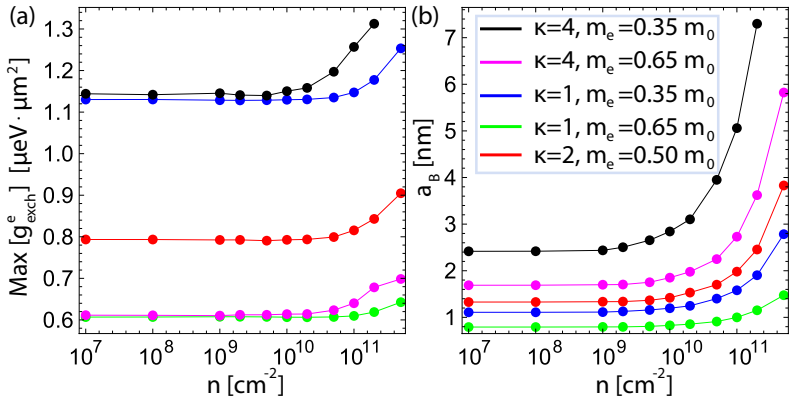

Figure 7.4: (a) The maximum of exciton-exciton exchange interaction and (b) exciton Bohr radius shown as a function of the free electron gas density for different material parameters. Colors in both panels correspond to parameters shown in panel (b). The increase of the dielectric constant κ for surrounding media leads to the growth of exciton Bohr radius, which is nearly compensated by the reduction of interaction potential between excitons. Instead, the reduction of effective mass leads to the increase of Bohr radius, which is not compensated by change in interaction potential. This shows that for the fixed effective mass the interaction constant has weak dependence on the dielectric environment properties.

7.4 Saturation effects and quenching of the Rabi splitting

We proceed with the discussion of impact of free electron gas on the coupling between exciton and cavity photon modes. For a TMD monolayer put in a microcavity this corresponds to the electron density-dependent Rabi frequency. It can be expressed as

$$\Omega_0(n) = \sqrt{\frac{E_C}{\kappa\varepsilon_0 L_C}}|\psi_n(0)|d_{cv}, \tag{7.8}$$

where E_C is the cavity resonance energy, $L_C = \pi\hbar c/(\sqrt{\kappa}E_C)$ is the cavity length, and c is the speed of light. Here $\psi_n(0)$ is the real space exciton wavefunction at the origin that depends on the free electron gas density. We note that the latter cannot be approximated via conventional relation $\psi_n(0) \propto a_B^{-1}$ due to the Pauli blocking, leading to the mixing of exciton ground and excited states. Finally, d_{cv} denotes the dipole matrix element for the optical interband transition.

We consider the case of the optical cavity being resonant to the exciton transition in the absence of electron gas, $E_C = E_{\mathrm{X}}^0(0)$. The exciton transition energy in the presence of electron gas reads $E_{\mathrm{X}}^0(n) = E_g + \Sigma_g(n) - E_b(n)$, where we recall that $E_b = |E_{\mathrm{X}} - \Sigma_g|$ is the exciton binding energy. It should be noted, that the position of excitonic transition varies very slowly with the increase of n, as the reduction of binding energy is largely compensated by the corresponding bandgap renormalization. The latter is in good agreement with experimental [202, 229, 230] and theoretical evidence [200].

The value of the dipole matrix element of interband transition is set to $d_{cv} = 7$ D, leading to Rabi splitting of ~ 30 meV, in agreement with existing experimental results [176]. Here we assume that the dependence of the interband transition matrix element on the density of free electron gas is negligible. Hence, the density of electron gas affects on the efficiency light-matter coupling only via the exciton wave function [see Eq. (7.8)]. The dependence of light-matter coupling $\Omega_0(n)$ on the density of free electron gas is presented in Fig. 7.5(a). The reduction of coupling with the increase of electron density stems from the impact of Pauli blocking, and the detailed analysis is presented in Section 7.7.

Next we study the nonlinear part of light-matter interaction that is represented by optical saturation coming from the phase space filling. Recently it was shown to provide a significant nonlinear response contribution for TMD polaritons [178, 221]. Together with nonlinear exciton-exciton interaction, the optical saturation effect leads to the energy blueshift for the lower polariton mode, coming from the renormalization of Rabi splitting. It depends on the density of excitons n_{X} and the excitonic wavefunction. The generalized Rabi frequency can be written as [214]

$$\Omega(n_{\mathrm{X}}, n) \approx \Omega_0(n)\sqrt{1 - 2s(n)n_{\mathrm{X}}}, \tag{7.9}$$

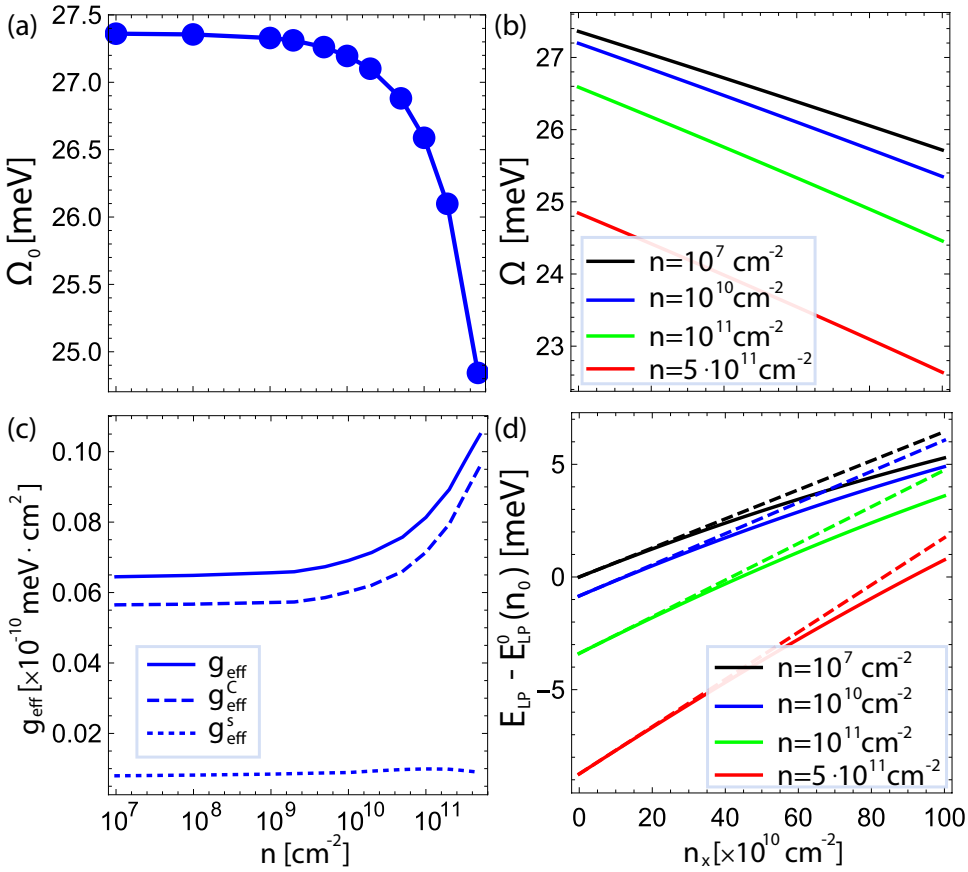

Figure 7.5: (a) Rabi splitting as a function of the free electron density in the weak excitation regime. (b) Light-matter coupling as a function of exciton density shown for different electron gas concentration. (c) Polariton nonlinearity coefficient and its contributions shown as a function of the free electron density. (d) Energy of the lower polariton branch relative to the reference value $E^0_{\mathrm{LP}}(n_0)$ as a function of the exciton density at different n. Here the solid curves correspond to Eq. (7.11)*, and the dashed curves to Eq.* (7.12)*.*

where the saturation factor

$$s(n) = \frac{\sum_{\mathbf{k}} |C_{\mathbf{k}}|^2 C_{\mathbf{k}}}{\sum_{\mathbf{k}'} C^*_{\mathbf{k}'}} \tag{7.10}$$

accounts for the phase space filling arising from multiple exchange diagrams. In particular, in the case of effectively hydrogenic wavefunctions, this yields $s^{\mathrm{hyd}} = 8\pi a_B^2/7$, meaning that the larger Bohr radius provides larger nonlinearity. Here, however, the presence of Pauli blocking leads to a moderate dependence of the saturation factor on the density of free electron gas, discussed in Section 7.7. As stated in Eq. (7.9), for growing density of excitons the Rabi splitting effectively shrinks. The corresponding dependence is illustrated in Fig. 7.5 (b) for various values of free electron gas density.

The energy of lower polariton branch reads as

$$\begin{aligned} E_{\mathrm{LP}}(n_{\mathrm{X}}, n) = \frac{1}{2}\Big[& E_C + E_{\mathrm{X}}(n, n_{\mathrm{X}}) \\ & - \sqrt{\left[E_C - E_{\mathrm{X}}(n, n_{\mathrm{X}})\right]^2 + \Omega^2(n_{\mathrm{X}}, n)}\Big], \end{aligned} \tag{7.11}$$

where the exciton energy is $E_{\mathrm{X}}(n, n_{\mathrm{X}}) = E^0_{\mathrm{X}}(n) + g_{\mathrm{tot}(n)} n_{\mathrm{X}}/2$. Introducing the detuning between cavity and exciton modes as $\Delta(n) = E_C - E_{\mathrm{X}}(n)$, and taking the limit of low exciton density, the energy for the lower polariton mode reads

$$E_{\mathrm{LP}}(n_{\mathrm{X}}, n) \approx E^0_{\mathrm{LP}}(n) + g_{\mathrm{eff}}(n) n_{\mathrm{X}}, \tag{7.12}$$

which consists of the linear part equal to

$$E^0_{\mathrm{LP}}(n) = E_C - \frac{\Delta + \sqrt{\Delta^2 + \Omega_0^2}}{2}, \tag{7.13}$$

and nonlinear blueshift $g_{\mathrm{eff}}(n) n_{\mathrm{X}}$. Here $g_{\mathrm{eff}}(n)$ is an effective polariton nonlinearity coefficient that is a sum of Coulomb-based interaction and saturative nonlinearity contributions,

$$\begin{aligned} g_{\mathrm{eff}}(n) &= \left(1 + \frac{\Delta}{\sqrt{\Omega_0^2 + \Delta^2}}\right) \frac{g_{\mathrm{tot}}}{4} + \frac{\Omega_0^2}{2\sqrt{\Omega_0^2 + \Delta^2}} s \\ &=: g^C_{\mathrm{eff}}(n) + g^s_{\mathrm{eff}}(n). \end{aligned} \tag{7.14}$$

For the compactness we omitted the electron density dependence of the quantities Δ, Ω_0, s etc.

Polaritonic nonlinearity coefficient and its parts are shown in the Fig. 7.5(c) as a function of free electron gas density. Notably we observe that while the saturation coefficient s increases more than the Coulomb interaction, the electron density dependence of its pre-factor diminishes its enhancement, making it nearly flat (dotted curve). Instead, the increase of Coulomb nonlinearity is further boosted by the corresponding growth of its pre-factor (the dashed curve).

In Fig. 7.5(d) the dependence of the lower polariton energy on the exciton density is shown, where we plot its nonlinear contribution (as compared to $E^0_{\rm LP}(n_0)$ with $n_0 = 10^7$ cm^{-2}). At fixed density of free electrons the increase of the exciton density leads to both reduction of light-matter interaction, and the blueshift of the exciton energy. In each this leads to the blueshift of the lower polariton energy. With the increase of free electron gas density both the exciton-exciton interaction constant $g^e_{\rm exch}$ and the saturation factor s are enhanced, leading to the corresponding growth of the nonlinear optical response. It should be mentioned that relation $E_{\rm LP}(n_{\rm X}, n) \approx E^0_{\rm LP}(n) + g_{\rm eff}(n) n_{\rm X}$ is valid in the moderate excitation regime $n_{\rm X} \leq 10^{12}$ cm^{-2}, as for higher intensities the quadratic terms $\propto n^2_{\rm X}$ become relevant.

Finally, we discuss the impact of trion on the exciton-polariton nonlinear optical response. As stated in Section II, the trion resonance is far detuned from the exciton and cavity modes, and thus has limited impact on resulting polariton modes at higher energy. Indeed, the estimate for the trion binding energy for the considered case of freestanding monolayer is about 50 meV, and it mixing with polariton branches is small (see Section 7.8 for the details). The detailed analysis of the electron density dependence of trion nonlinear response for the case of near-resonant cavity is a separate research question, and will be studied in future works.

7.5 Expansion of an exciton wavefunction in terms of basis functions

We analyze the impact of Pauli blocking factor on the excitonic wavefunction that results in the reduction of the exciton-exciton interaction for increasing electron gas density. First, we simulate Eq. (7.5) of the main text in the absence of both interaction screening and the Pauli blocking. We find wavefunctions for ground and excited exciton states ($1s$, $2s$, $3s$). Their real space distributions are shown in Fig. 7.6(a). Next, for each value of n we expand calculated wavefunctions in the presence of Pauli blocking (but non screening) in terms of bare basis functions. This procedure yields

$$\psi_n(r) = a_1(n)\psi_{1s}(r) + a_2(n)\psi_{2s}(r) + a_3(n)\psi_{3s}(r), \tag{7.15}$$

where coefficients $a_i(n)$ are found from

$$\begin{aligned}
&\psi_n(0) = a_1(n)\psi_{1s}(0) + a_2(n)\psi_{2s}(0) + a_3(n)\psi_{3s}(0),\\
&\psi_n(r_1) = a_1(n)\psi_{1s}(r_1) + a_2(n)\psi_{2s}(r_1) + a_3(n)\psi_{3s}(r_1),\\
&1 = |a_1(n)|^2 + |a_2(n)|^2 + |a_3(n)|^2,
\end{aligned} \tag{7.16}$$

and r_1 corresponds to the first root of ψ_n. The results of fitting for large density of the electron gas are shown in Fig. 7.6(b, c). We find that the fit is nearly exact at small r, but strongly deviates at large distances (not shown). Correspondingly,

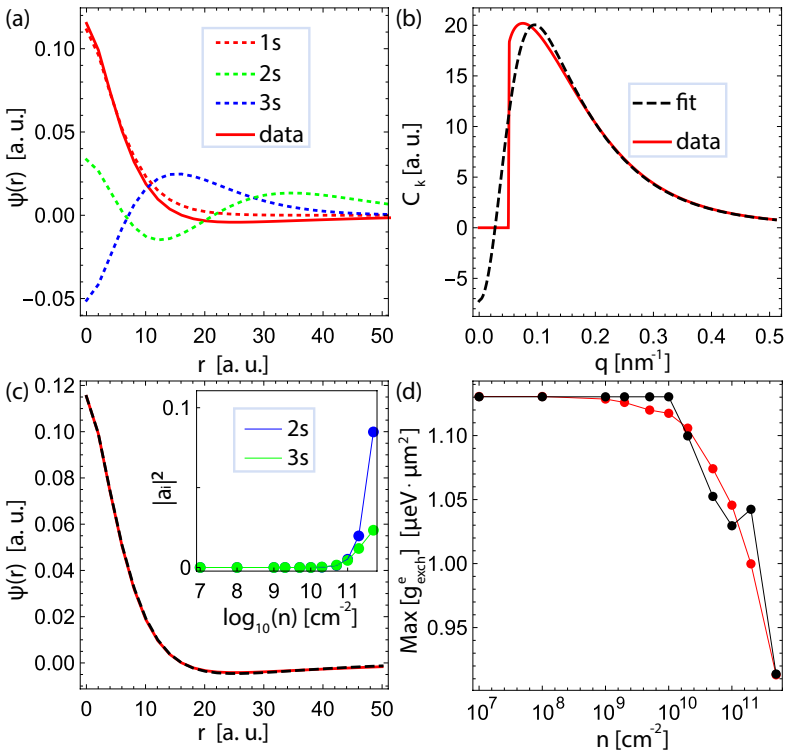

Figure 7.6: (a) The real space dependence of exciton wave function in the presence of Pauli blocking at density of free electrons $n = 5 \cdot 10^{11}$ cm^{-2} (red solid curve), and the exciton ground and excited states wavefunctions in its absence. Here we neglect the impact of the interaction screening by free electrons. (b) Real and (c) momentum space dependence of wave function (red solid curve) and its expansion in terms of basis functions (black dashed curve). The inset in panel (c) demonstrates the contribution of excited states versus the density of free electron gas. (d) The maxima of exciton-exciton interactions as a function of free electron density. The red dots correspond to calculation using the actual wave functions, and the black dots is calculated using the wavefunctions expanded in terms of basis functions. The mismatch in the values is attributed to the imperfection of the fitting procedure.

for the small momenta there is a strong deviation, while for larger values there is a good agreement. Finally, in Fig. 7.6(d) we provide the comparison of the exciton-exciton interaction coefficient calculated from exact wave functions (red dots), and the wave functions defined by the (7.15). Evidently, with the increase of electron gas density Pauli blocking leads to larger contribution of excited states [see the inset in Fig. 7.6(c)], which interact attractively [209, 228], resulting in corresponding reduction of the ground state exciton-exciton repulsive interaction.

7.6 The dependence of exciton-exciton interaction on electron/hole effective mass ratio

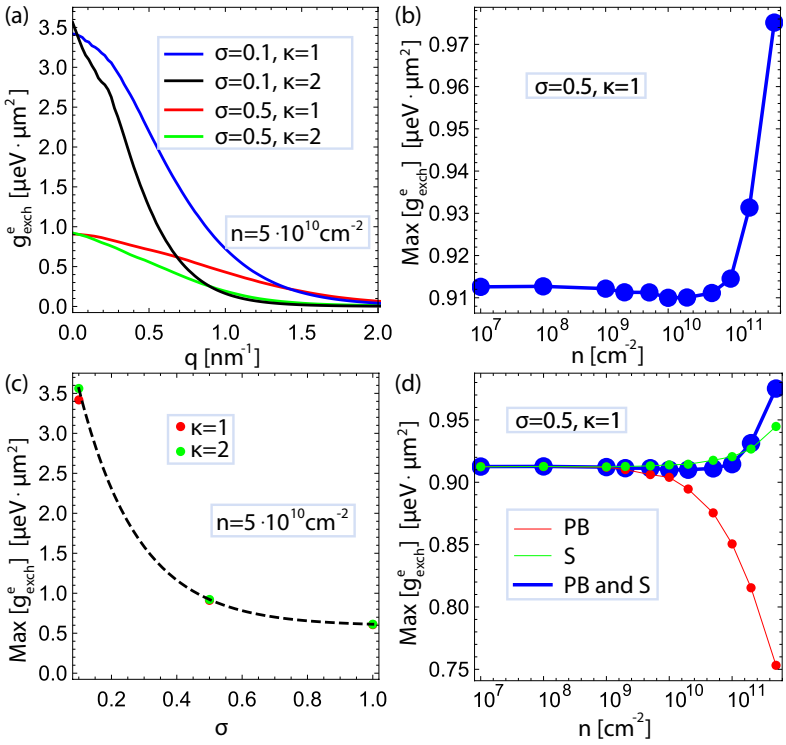

Figure 7.7: Exciton-exciton exchange interaction. (a) The dependence of interaction constant on transfer momenta for different dielectric screening and effective mass ratio σ. (b) The maxima of interaction constant as a function of free electron density. (c) The effective mass ratio dependence of exchange interaction constant. Dashed black curve corresponds to an exponential fit. (d) The influence of screening and Pauli blocking factors on the maxima of exchange interaction vs the density of free electrons.

The effective masses of conduction and valence bands in TMD monolayer typically differ from each other [231]. Here we study the impact of mass ratio $\sigma = m/m_v$ on the exciton-exciton interaction strength. To do so, we fix the effective mass of hole as $m_v = 0.65m_0$, and consider the cases when $\sigma = 0.5$, $\sigma = 0.1$. We also consider two values of surrounding dielectric constant, $\kappa = 1$ and $\kappa = 2$. The results of calculations are shown in Fig. 7.7. It is evident, that the absolute values of interaction are strongly dependent on the effective masses, and weakly dependent on the dielectric screening [Fig. 7.7 (a)]. Moreover, the maximum of interaction constant demonstrates

an exponential behavior on the effective mass ratio σ [Fig. 7.7 (c)]. However, the impact of Pauli blocking and the interaction screening by free electrons together with the nonmonotonous dependence of interaction on the free electron gas density are qualitatively independent on the structure parameters [Fig. 7.7 (b) and (d)].

7.7 The dependence of Rabi splitting saturation rate on the free electron gas density

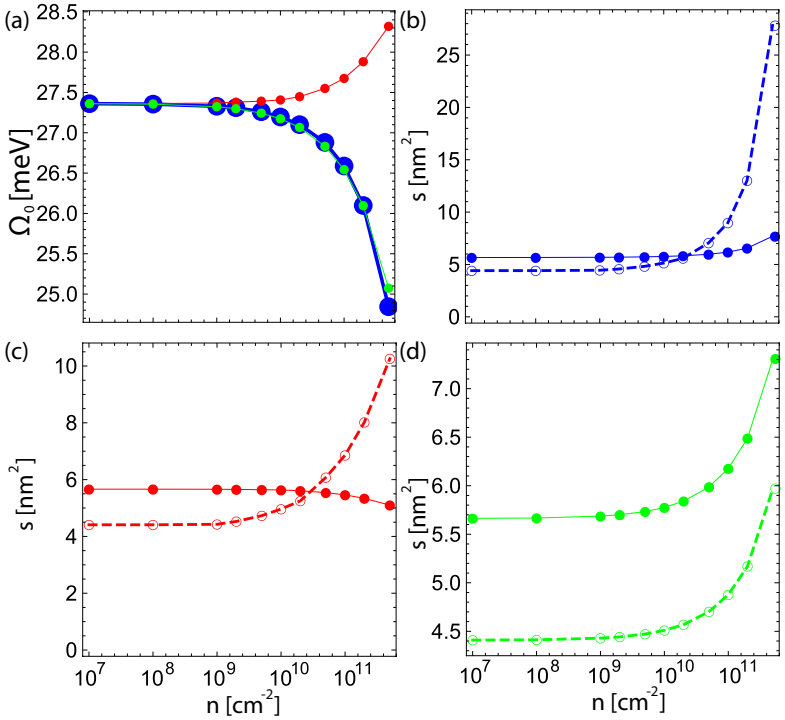

Figure 7.8: (a) Light-matter coupling as a function of the free electron gas density at low excitation regime. Here green curves correspond to the absence of Pauli blocking, red curves correspond to the absence of interaction screening, and blue curves account both effects. (b), (c), (d) The saturation factor $s(n)$ (solid curves) and its hydrogen-like estimate $s^{\mathrm{hyd}}(n)$ (dashed curves) versus the free electron gas density. Panel (b) corresponds to the presence of both Pauli blocking and the interaction screening; panel (c) stands for the absence of the interaction screening; panel (d) illustrates the absence of Pauli blocking.

In Fig. 7.8(a) we present light-matter coupling at small exciton densities, $n_{\mathrm{X}} a_B^2 \ll 1$,

as a function of free electron gas density n. In the absence of the Pauli blocking the screening of Coulomb interaction leads to weaker binding of excitons, so that the wavefunction is less concentrated around the origin. The latter results in the quenching of light-matter coupling [Fig. 7.8(a), green curve]. On the contrary, in the absence of screening the Pauli blocking leads to mixing with excited exciton states, leading to the increase of wavefunction amplitude at the origin [see Fig. 7.6(a)]. This results in the corresponding enhancement of light-matter coupling [Fig. 7.8(a), red curve]. Yet, the impact of screening is much stronger, so that the interplay of this counteracting effects leads to overall reduction of light-matter coupling with the increase of free electron gas density [Fig. 7.8(a), blue curve].

We further analyze the Rabi splitting saturation factor $s(n)$. Fig. 7.8(b) illustrates its dependence on the density of free electron gas. We observe a moderate enhancement of the saturation rate with the growth of the electron gas density. On the other hand, the estimate of saturation factor for the hydrogen-like exciton $s^{\mathrm{hyd}}(n)$ grows much faster [dashed curve in Fig. 7.8(b)]. To get a better insight, we study the impacts of the screening of interaction and Pauli blocking separately.

In Fig. 7.8(c) we present the free electron gas density dependence of saturation factor and its estimate in the absence of interaction screening. As the density increases, the saturation factor moderately reduces, while its estimate enhances. This discrepancy with the hydrogen-based estimate stems from the Pauli blocking, which leads to emergence of strongly non-hydrogenic wavefunctions.

Fig. 7.8(d) illustrates the case of the absence of Pauli blocking and the presence of interaction screening. Here both the saturation factor and its estimate increase nearly on equal footing, indicating that in the absence of Pauli blocking effect the hydrogen-like model is valid up to a constant. In total, the interplay of these two counteracting impacts results in the moderate enhancement of saturation efficiency, as depicted in Fig. 7.8(b).

7.8 The impact of trion state on the exciton-polariton spectra

The binding energy of trion can be estimated using the variational energy minimization with Chandrasekhar-type trial function in momentum space [178, 232]

$$\Phi^{\mathrm{T}}_{k_1,k_2} = \mathcal{N}\left[\Phi_{k_1}(\lambda_1)\Phi_{k_2}(\lambda_2) + \Phi_{k_2}(\lambda_1)\Phi_{k_1}(\lambda_2)\right], \tag{7.17}$$

where $\Phi_{k_i}(\lambda_j) = \sqrt{8\pi\lambda_j^2}\left[1+(\lambda_j k_i)^2\right]^{-3/2}$, $\mathcal{N} = \left[2(1+\chi^2)\right]^{-1/2}$ and $\chi = 4\lambda_1\lambda_2/(\lambda_1+\lambda_2)^2$. The results for the considered parameters of freestanding monolayer are $E_b^{\mathrm{T}} = 52.83$ meV, $\lambda_1 = 1.21$ nm, $\lambda_2 = 3.06$ nm. For an estimate we neglect the screening of

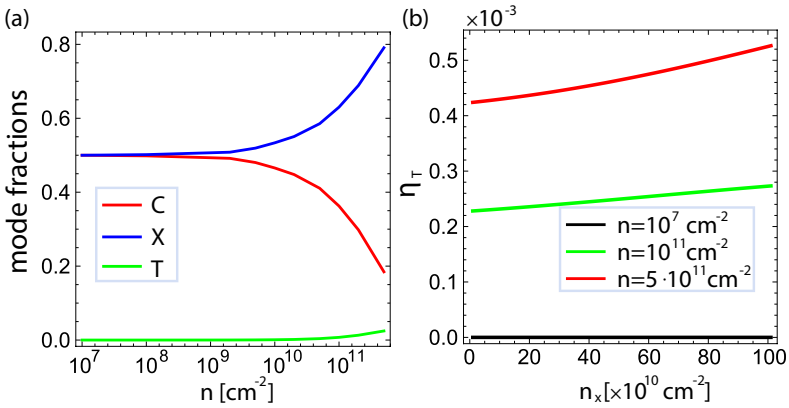

Figure 7.9: (a) The fractions of photon (C), exciton (X) and trion (T) modes in the middle polariton branch as a function of free electron gas density. (b) Correction of middle polariton branch energy by trions, plotted as a function of the exciton density.

Coulomb interactions by free electron gas, meaning that the position of trion resonance remains unaltered when the free electron density changes. Though this treatment is simplistic, it allows to get in the first approximation the impact of trions on exciton-polariton spectra.

The contribution of the trion resonance can be analysed within the model of three coupled modes, where together with dominant exciton-photon coupling there is an admixture of the far-detuned trion mode. Polariton eigenmodes can be obtained diagonalizing

$$\hat{H}^{\mathrm{T}} = \begin{pmatrix} E_{\mathrm{C}} & \Omega_{\mathrm{X}}(n, n_{\mathrm{X}}) & \Omega_{\mathrm{T}}(n, n_{\mathrm{X}}) \\ \Omega_{\mathrm{X}}(n, n_{\mathrm{X}}) & E_{\mathrm{X}}(n, n_{\mathrm{X}}) & 0 \\ \Omega_{\mathrm{T}}(n, n_{\mathrm{X}}) & 0 & E_{\mathrm{T}} \end{pmatrix}, \tag{7.18}$$

where $E_{\mathrm{T}} = E_{\mathrm{C}} - E_b^{\mathrm{T}}$, and the trion-photon coupling is calculated as [178]

$$\Omega_{\mathrm{T}}(n, n_{\mathrm{X}}) = 4\mathcal{N}\left(\frac{\lambda_1}{\lambda_2} + \frac{\lambda_2}{\lambda_1}\right)\frac{\sqrt{n}}{|\psi_n(0)|}\Omega_{\mathrm{X}}(n, n_{\mathrm{X}}). \tag{7.19}$$

The eigenmodes of Hamiltonian (7.18) correspond to three polariton branches. Here we focus on the middle polariton branch $E_{\mathrm{MP}}^{\mathrm{T}}$, as it is dominated by exciton mode with a small admixture of trion, as depicted in Fig. 7.9(a). As the electron density increases, the trion contribution slowly increases due to reduction of detuning and the enhancement of trion-photon coupling. Fig. 7.9(b) demonstrates the exciton density dependence of spectrum correction caused by trions. The latter is defined as

$$\eta_{\mathrm{T}} = \frac{E_{\mathrm{MP}}^{\mathrm{T}} - E_{\mathrm{LP}}}{E_{\mathrm{LP}}}. \tag{7.20}$$

We observe that even for large concentration of free electrons the correction is minor and thus can be neglected in the description of the middle polariton branch.

7.9 Conclusions

In this chapter we analyzed the behavior of exciton polaritons in a TMD monolayer in the presence of a gas of free electrons. We revealed that the Fermi sea has a strong effect on the nonlinear optical response of the system. We found that the role of free electrons is twofold. First, doping leads to screening of the Coulomb interaction, and results in the increase of exciton Bohr radius and simultaneously the reduction of exciton-exciton interaction potential. Our calculations show that the overall impact of the screening leads to the enhancement of exciton-exciton interaction coefficient. Second, due to the Pauli exclusion principle, the presence of the free electrons also dramatically modifies the structure of the excitonic wave functions, suppressing the contribution of the harmonics corresponding to small electron wavevectors. Surprisingly the impact of the Pauli blocking factor leads to the reduction of exciton-exciton interaction. We found that the latter can be attributed to mixing of exciton ground and excited states, caused by the Pauli blocking factor. It is known that the interaction between excited exciton states is of attractive type, which explains the reduction of exciton-exciton repulsive interaction caused by Pauli principle. Finally, we showed that the combined impact of interaction screening and Pauli blocking leads to the non-monotonous dependence of the exciton-exciton interaction constant as a function of free electron gas density.

The presence of Fermi sea substantially modifies also the statistics-based renormalization of the Rabi splitting at high exciton densities, which gives another contribution to the enhancement of the optical nonlinearity. It is important to note that both Coulomb nonlinearity and saturation-based nonlinearity generally grow with the increase of the free electron gas density. As the latter can be easily controlled by application of the external gate voltage, our findings pave the way to accessible and experimental friendly tuning of the degree of optical nonlinearity in TMD based samples.

8 Conclusions

In conclusion, in the current thesis, we studied various phenomena that take place in the regime of strong coupling between light and matter. We studied the transport properties of electrons in low-dimensional semiconductor nanostructures under the influence of high-frequency radiation. We investigated the transport of magneto-excitons in semiconductor quantum wells and proposed a new physical phenomenon, which allows for the separation of dark and bright excitons. We studied the optical nonlinearity in the regime of strong light-matter coupling in a TMD monolayer, embedded in a microcavity and demonstrated, that this nonlinearity can be efficiently controlled by applying the gate voltage. We studied theoretically and experimentally the nonequilibrium properties of a polariton BEC in ring-shaped microcavities. We discovered, that a 2D lattice formed from interconnected polariton rings, may host topologically protected edge states at its boundaries in the presence of a magnetic field. And finally, as one of the main results of the current thesis, we discovered a new class of quantum Hamiltonians, that are effectively describe the behavior of harmonically trapped atoms in the vicinity of a chiral waveguide. These models demonstrate self-organization, quantum phase transitions, and the emergence of the multicomponent Schrödinger cat ground states.

List of publications

(**Relevant to the current Thesis**:)

[A1] S. Mukherjee, V. K. Kozin, A. V. Nalitov, I. A. Shelykh, Z. Sun, D. M. Myers, B. Ozden, J. Beaumariage, M. Steger, L. N. Pfeiffer, K. West, D. W. Snoke, Dynamics of spin polarization in tilted polariton rings, *Phys. Rev. B* (2021) **103**, 165306 (2021)

[A2] V. K. Kozin, V. A. Shabashov, A. V. Kavokin, I. A. Shelykh, Anomalous Exciton Hall Effect, *Phys. Rev. Lett.* **126**, 036801 (2021)

[A3] D. D. Sedov, V. K. Kozin, and I. V. Iorsh, Chiral waveguide optomechanics: First order quantum phase transitions with $\mathbb{Z}_3$ symmetry breaking, *Phys. Rev. Lett.* **125**, 263606 (2020)

[A4] V. Shahnazaryan, V. K. Kozin, I. A. Shelykh, I. V. Iorsh, and O. Kyriienko, Tunable optical nonlinearity for transition metal dichalcogenide polaritons dressed by a Fermi sea, *Phys. Rev. B* **102**, 115310 (2020)

[A5] V. K. Kozin, I. A. Shelykh, A. V. Nalitov, and I. V. Iorsh, Topological metamaterials based on polariton rings, *Phys. Rev. B* **98**, 125115 (2018)

[A6] V. K. Kozin, I. V. Iorsh, O. V. Kibis, and I. A. Shelykh, Quantum rings with the Rashba spin-orbit interaction in the regime of strong light-matter coupling, *Phys. Rev. B* **97**, 155434 (2018)

[A7] V. K. Kozin, I. V. Iorsh, O. V. Kibis, and I. A. Shelykh, Periodic array of quantum rings strongly coupled to circularly polarized light as a topological insulator, *Phys. Rev. B* **97**, 035416 (2018).

(**Other related publications**:)

[A8] Valerii K. Kozin and Oleksandr Kyriienko, Quantum Time Crystals from Hamiltonians with Long-Range Interactions, *Phys. Rev. Lett.* **123**, 210602 (2019), (*Editor's Suggestion, Featured in Physics*)

[A9] A. V. Yulin, V. K. Kozin, A. V. Nalitov, and I. A. Shelykh, Resonant excitation of acoustic waves in one-dimensional exciton-polariton systems, *Phys. Rev. A* **100**, 043610 (2019)

[A10] V. K. Kozin, A connection between $\mathcal{R}$-invariants and Yang-Baxter R-operators

in $\mathcal{N} = 4$ super-Yang-Mills theory, *JHEP* **09** (2019) 077

[A11] Albert A. Shirinyan, Valerii K. Kozin, Johan Hellsvik, Manuel Pereiro, Olle Eriksson, and Dmitry Yudin, Self-organizing maps as a method for detecting phase transitions and phase identification, *Phys. Rev. B* **99**, 041108(R) (2019)

[A12] S.A. Kolodny, V.K. Kozin and I.V. Iorsh, Enhancement of Second-harmonic Generation in Micropillar Resonator due to the Engineered Destructive Interference, JETP Lett. (2021).

[A13] L. S. Ricco, V. K. Kozin, A. C. Seridonio, I. A. Shelykh, Accessing the degree of Majorana nonlocality with photons, arXiv:2105.05925 (submitted to NJP)

[A14] D. Zvyagintseva, H. Sigurdsson, V. K. Kozin, I. V. Iorsh, I. A. Shelykh et al., Machine learning of phase transitions in nonlinear polariton lattices, arXiv:2104.12921 (submitted to Communications Physics)

[A15] C. E. Whittaker, T. Isoniemi, S. Lovett, P. M. Walker, S. Kolodny, V. Kozin, I. V. Iorsh et al., Exciton-polaritons in GaAs-based slab waveguide photonic crystals (submitted to APL)

[A16] V. A. Shabashov, V. K. Kozin, and L. P. Pryadko, QDistRnd: A GAP package for computing the distance of quantum codes (submitted to JOSS)

(**Conference papers**:)

[A17] Valerii K. Kozin and Oleksandr Kyriienko, Effective Hamiltonians for Discrete Time Crystals, *AIP Conference Proceedings* 2241, 020024 (2020)

[A18] V. K. Kozin, A. V. Yulin, A. V. Nalitov, I. V. Iorsh and I. A. Shelykh, Acoustic waves in polariton wires, *J. Phys.: Conf. Ser.* 1331 012023 (2019)

[A19] O. V. Kibis, V. K. Kozin, I. V. Iorsh and I. A. Shelykh, Quantum Rings Dressed by a High-Frequency Electromagnetic Field, *Semiconductors* 52 (14), 1806-1808 (2018)

[A20] O. V. Kibis, V. K. Kozin, I. V. Iorsh and I. A. Shelykh, Electronic properties of quantum rings dressed by a high-frequency electromagnetic field, *Journal of Physics: Conference Series* 1092 (1), 012055 (2018)

(**Textbooks**:)

[A21] V. K. Kozin, V. A. Pivovarov, F. A. Smirnov, Textbook on Classical Electrodynamics, ITMO University (2020) https://books.ifmo.ru/file/pdf/2666.pdf

Bibliography

[1] Z. I. Alferov, "The history and future of semiconductor heterostructures", Semiconductors **32**, 3 (1998).

[2] T. F. Gallagher, *Rydberg Atoms* (Cambridge University Press, New York, 1994).

[3] T. Kazimierczuk, D. Fröhlich, S. Scheel, H. Stolz and M. Bayer, "Giant Rydberg excitons in the copper oxide Cu_2O", Nature (London) **514**, 343 (2014).

[4] J. Thewes, J. Heckötter, T. Kazimierczuk, M. Aßmann, D. Fröhlich, M. Bayer, M. A. Semina, and M. M. Glazov, "Observation of High Angular Momentum Excitons in Cuprous Oxide", Phys. Rev. Lett. **115**, 027402 (2015).

[5] S. Zielinska-Raczynska, G. Czajkowski, and D. Ziemkiewicz, "Optical properties of Rydberg excitons and polaritons", Phys. Rev. B **93**, 075206 (2016).

[6] J. Heckötter, M. Freitag, D. Fröhlich, M. Aßmann, M. Bayer, M. Semina, M. Glazov, "High-resolution study of the yellow excitons in Cu_2O subject to an electric field", Phys. Rev. B **95**, 035210 (2017).

[7] J. Heckötter, M. Freitag, D. Fröhlich, M. Aßmann, M. Bayer, M. Semina, M. Glazov, "Scaling laws of Rydberg excitons", arXiv:1704.00974 (2017).

[8] D. G. W. Parfitt and M. E. Portnoi, "The two-dimensional hydrogen atom revisited", J. Math. Phys. **43**, 4681 (2002).

[9] J. Inoue, T. Brandes, and A. Shimizu, "Renormalized bosonic interaction of excitons", Phys. Rev. B **61**, 2863 (2000).

[10] S. B. de-Leon and B. Laikhtman, "Exciton-exciton interactions in quantum wells: Optical properties and energy and spin relaxation", Phys. Rev. B **63**, 125306 (2001).

[11] S. Okumura and T. Ogawa, "Boson representation of two-exciton correlations: An exact treatment of composite-particle effects", Phys. Rev. B **65**, 035105 (2001).

[12] M. Combescot, O. Betbeder-Matibet, and R. Combescot, "Exciton-exciton scattering: Composite boson versus elementary boson" Phys. Rev. B **75**, 174305 (2007).

[13] J. Zhang, Y. Ning, X. Zhang, J. Zhang, Y. Zeng, X. Shan, L. Qin, and L. Wang, "High-peak-power vertical-cavity surface-emitting laser quasi-array realized using optimized large-aperture single emitters", Japanese Journal of Applied Physics **53**, 070303 (2014).

[14] S. I. Pekar, "Theory of electromagnetic waves in a crystal in which excitons arise", Exp. Teor. Fiz. USSR **33**, 1022 (1957).

[15] V. M. Agranovich, "On the influence of reabsorption on the decay of fluorescence in molecular crystals", Optika i Spectr. textbf3, 84 (1957).

[16] J. J. Hopfield, "Theory of the Contribution of Excitons to the Complex Dielectric Constant of Crystals", Physical Review **112**, 1556 (1958).

[17] C. Weisbuch, M. Nishioka, A. Ishikawa, and Y. Arakawa, "Observation of the coupled exciton-photon mode splitting in a semiconductor quantum microcavity", Phys. Rev. Lett. **69**, 3314 (1992).

[18] H. Deng, H. Haug, and Y. Yamamoto, "Exciton-polariton Bose-Einstein condensation", Rev. Mod. Phys. 82, 1489 (2010).

[19] A. V. Kavokin, J. J. Baumberg, G. Malpuech, and F. P. Laussy, *Microcavities* (Oxford University Press, New York, 2007).

[20] T. C. H. Liew, I. A. Shelykh, and G. Malpuech, "Polaritonic devices", Physica E **43**, 1543 (2011).

[21] A. Amo, J. Lefrére, S. Pigeon, C. Adrados, C. Ciuti, I. Carusotto, R. Houdré, E. Giacobino, and A. Bramati, "Superfluidity of polaritons in semiconductor microcavities", Nature Phys. **5**, 805 (2009).

[22] A. Amo, D. Sanvitto, F. P. Laussy, D. Ballarini, E. del Valle, M. D. Martin, A. Lemaître, J. Bloch, D. N. Krizhanovskii, M. S. Skolnick, C. Tejedor, and L. Viña, "Collective fluid dynamics of a polariton condensate in a semiconductor microcavity", Nature **457**, 291-295 (2009).

[23] Q. Duan, D. Xu, W. Liu, J. Lu, L. Zhang, J. Wang, Y. Wang, J. Gu, T. Hu, W. Xie, X. Shen, and Z. Chen, "Polariton lasing of quasi-whispering gallery modes in a ZnO microwire", Appl. Phys. Lett. **103**, 022103 (2013).

[24] F. Li, L. Orosz, O. Kamoun, S. Bouchoule, C. Brimont, P. Disseix, T. Guillet, X. Lafosse, M. Leroux, J. Leymarie, M. Mexis, M. Mihailovic, G. Patriarche, F. Reveret, D. Solnyshkov, J. Zuniga-Perez, and G. Malpuech, "From Excitonic to Photonic Polariton Condensate in a ZnO-Based Microcavity", Phys. Rev. Lett. **110**, 196406 (2013).

[25] W. Xie, H. Dong, S. Zhang, L. Sun, W. Zhou, Y. Ling, J. Lu, X. Shen, and Z. Chen, "Room-Temperature Polariton Parametric Scattering Driven by a One-Dimensional Polariton Condensate", Phys. Rev. Lett. **108**, 166401 (2012).

[26] A. Kavokin, G. Malpuech, M. Glazov, "Optical Spin Hall Effect", Phys. Rev. Lett. **95**, 136601 (2005).

[27] H. Flayac, D.D. Solnyshkov, I.A. Shelykh, and G. Malpuech, "Transmutation of skyrmions to half-solitons driven by the nonlinear optical spin hall effect", Phys. Rev. Lett. **110**, 016404 (2013).

[28] S. Morina, T. C. H. Liew, and I. A. Shelykh, "Magnetic field control of the optical spin Hall effect", Phys. Rev. B **88**, 035311 (2013).

[29] Yu. E. Lozovik and V. I. Yudson, "On the possibility of superfluidity of spatially separated electrons and holes due to their coupling: new mechanism of superfluidity", JETP Lett. **22**, 26 (1975).

[30] Yu. E. Lozovik and V. I. Yudson, "New mechanism of superconductivity: coupling between spatially separated electrons and holes", Sov. Phys. JETP **44**, 389 (1976).

[31] L. V. Butov, "Cold exciton gases in coupled quantum well structures", J. Phys.: Condens. Matter, **19**, 295202, 2007.

[32] A. A. High, J. R. Leonard, A. T. Hammack, M. M. Fogler, L. V. Butov, A. V. Kavokin, K. L. Campman, and A. C. Gossard, "Spontaneous Coherence in a Cold Exciton Gas", Nature (London) **483**, 584 (2012).

[33] D. Snoke, S. Denev, Y. Liu, L. Pfeiffer, and K. West, "Long-range transport in excitonic dark states in coupled quantum wells", Nature **418**, 754 (2002).

[34] L. V. Butov, A. C. Gossard, and D. S. Chemla, "Macroscopically ordered state in an exciton system", Nature **418**, 751 (2002).

[35] O. Kyriienko, E. B. Magnusson, and I. A. Shelykh, "Spin dynamics of cold exciton condensates", Phys. Rev. B **86**, 115324 (2012).

[36] G. Christmann, A. Askitopoulos, G. Deligeorgis, Z. Hatzopoulos, S. I. Tsintzos, P. G. Savvidis, and J. J. Baumberg, "Oriented polaritons in strongly-coupled asymmetric double quantum well microcavities", Appl. Phys. Lett. **98**, 081111 (2011).

[37] P. Cristofolini, G. Christmann, S. I. Tsintzos, G. Deligeorgis, G. Konstantinidis, Z. Hatzopoulos, P. G. Savvidis, and J. J. Baumberg, "Coupling quantum tunneling with cavity photons", Science **336**, 704 (2012).

[38] O. Kyriienko, A. V. Kavokin, and I. A. Shelykh, "Superradiant Terahertz Emission by Dipolaritons", Phys. Rev. Lett. **111**, 176401 (2013).

[39] K. Kristinsson, O. Kyriienko, T. C. H. Liew, and I. A. Shelykh, "Continuous terahertz emission from dipolaritons", Phys. Rev. B **88**, 245303 (2013).

[40] K. Kristinsson, O. Kyriienko, and I. A. Shelykh, "Terahertz laser based on dipolaritons", Phys. Rev. A **89**, 023836 (2014).

[41] C. Cohen-Tannoudji, J. Dupont-Roc, and G. Grynberg, *Atom-Photon Interactions: Basic Processes and Applications* (Wiley, Chichester, 1998).

[42] D. A. Steck, "Quantum and Atom Optics", available online at http://steck.us/teaching

[43] D. D. Solnyshkov, I. Shelykh, M. Glazov, G. Malpuech, T. Amand, P. Renucci, X. Marie, A. Kavokin, "Nonlinear effects in spin relaxation of cavity polaritons", *Semiconductors*, vol. 41, p. 1099, 2007.

[44] M. Combescot, O. Betbeder-Matibet, and R. Combescot, "Bose-Einstein Condensation in Semiconductors: The Key Role of Dark Excitons", *Phys. Rev. Lett.*, vol. 99, p. 176403, 2007.

[45] Andras Suto, Bose-Einstein condensation and symmetry breaking, *Phys. Rev. A* **71**, 023602 (2005)

[46] Andras Suto, Equivalence of Bose-Einstein Condensation and Symmetry Breaking, *Phys. Rev. Lett.* **94**, 080402 (2005)

[47] Andrey R. Kolovsky, Quantum entanglement and the Born-Markov approximation for an open quantum system, *Phys. Rev. E* **101**, 062116 (2020)

[48] N. Goldman and J. Dalibard, Periodically Driven Quantum Systems: Effective Hamiltonians and Engineered Gauge Fields, *Phys. Rev. X* **4**, 031027 (2014)

[49] David Tong, Lectures on the Quantum Hall Effect, arXiv:1606.06687 [hep-th]

[50] O. V. Kibis 2014 EPL **107** 57003

[51] Phys. Rev. A **44**, 7439 (1991)

[52] Luca D'Alessio and Marcos Rigol, Phys. Rev. X **4**, 041048 (2014)

[53] Takashi Oka and Hideo Aoki, Phys. Rev. B **79**, 081406(R) (2009)

[54] O. V. Kibis, Phys. Rev. B 81, 165433 (2010)

[55] J. W. McIver, B. Schulte, F.-U. Stein, T. Matsuyama, G. Jotzu, G. Meier, and A. Cavalleri, Nature Physics 16, pages38–41(2020)

[56] Simon A. Weidinger and Michael Knap, Scientific Reports volume **7**, Article number: 45382 (2017)

[57] D. Braak, Phys. Rev. Lett. **107**, 100401 (2011)

[58] D. G. Thomas, J. J. Hopfield, Phys. Rev. **124**, 657 (1961).

[59] M. Lafrentz, D. Brunne, B. Kaminski,V. V. Pavlov, A.V.Rodina, R. V. Pisarev, D. R. Yakovlev, A. Bakin, and M. Bayer, Phys. Rev. Lett. **110**, 116402 (2013).

[60] Y. J. Chen, E. S. Koteles, B. S. Elman, and C. A. Armiento, Phys. Rev. B **36**, 4562 (1987).

[61] P. Andreakou, A. V. Mikhailov, S. Cronenberger, D. Scalbert, A. Nalitov, A. V. Kavokin, M. Nawrocki, L. V. Butov, K. L. Campman, A. C. Gossard, and M. Vladimirova, Phys. Rev. B **93**, 115410 (2016).

[62] A. Imamoglu, Phys. Rev. B **85**, 14285 (1996).

[63] H-T. Lim, E. Togan, M. Kroner, J. Miguel-Sanchez and A. Imamoglu, Nature Communications **8**, 14540 (2017).

[64] M. Onga, Y. Zhang, T. Ideue & Y. Iwasa, Nature Materials **16**, 1193 (2017).

[65] Jean Dalibard, Fabrice Gerbier, Gediminas Juzeliūnas, and Patrik Öhberg, Rev. Mod. Phys. **83**, 1523 (2011).

[66] K. Fang, Z. Yu, S. Fan, Nat. Photon. **6**, 782 (2012).

[67] F. Liu, T. Xu, S. Wang, Z. H. Hang, J. Li, Adv. Opt. Mater. **7**, 1801582 (2019).

[68] I. V. Lerner, Y.E. Lozovik, Zh. Eksp. Theor. Phys. **78**, 1167 [Sov. Phys. JETP **51**, 588] (1978)

[69] L. V. Butov, C. W. Lai, D. S. Chemla, Yu. E. Lozovik, K. L. Campman, and A. C. Gossard Phys. Rev. Lett. **87**, 216804 (2001)

[70] Yu. E. Lozovik, I. V. Ovchinnikov, S. Yu. Volkov, L. V. Butov, and D. S. Chemla Phys. Rev. B **65**, 235304 (2002)

[71] Arseev, P.I., Dzyubenko, A.B. Exciton, J. Exp. Theor. Phys. 87, 200–209 (1998)

[72] L. P. Gor'kov and I. E. Dzyaloshinskii, Zh. Eksp. Teor. Fiz. 53, 717 (1967) [Sov. Phys. JETP 26, 449 (1968)].

[73] Denisov, K. S., Rozhansky, I. V., Averkiev, N. S. et al., Sci Rep 7, 17204 (2017).

[74] K. S. Denisov, I. V. Rozhansky, N. S. Averkiev, and E. Lähderanta, Phys. Rev. Lett. **117**, 027202 (2016)

[75] K. S. Denisov, I. V. Rozhansky, N. S. Averkiev, and E. Lähderanta Phys. Rev. B **98**, 195439 (2018)

[76] S. Fraizzoli, F. Bassani, and R. Buczko Phys. Rev. B **41**, 5096 (1990)

[77] Alexander B. Dzyubenko and Gerrit E. W. Bauer Phys. Rev. B **51**, 14524 (1995)

[78] Bychkov Yu. A., Iordanskii S. V., Eliashberg G. M., Pis'ma Zh. Eksp. Teor. Fiz. **33**, No. 3, 152-155 (5 February 1981)

[79] Thomas G. Pedersen, Exact polarizability of low-dimensional excitons, Solid State Communications, Volume 141, Issue 10, 2007

[80] S. I. Shevchenko, Pis'ma Zh. Eksp. Teor. Fiz. 28, No. **3**, 112-116 (5 August 1978)

[81] D. V. Fil and S. I. Shevchenko, Low Temperature Physics **46**, 420 (2020)

[82] S. I. Shevchenko Phys. Rev. Lett. **75**, 3312 (1995)

[83] K. B. Arnardottir, O. Kyriienko, and I. A. Shelykh Phys. Rev. B **86**, 245311 (2012)

[84] P. Schwab et al. 2010 EPL **90** 67004

[85] C. Schneider, A. Rahimi-Iman, N. Y. Kim, J. Fischer, I. G. Savenko, M. Amthor, M. Lermer, A. Wolf, L. Worschech, V. D. Kulakovskii, I. A. Shelykh, M. Kamp, S. Reitzenstein, A. Forchel, Y. Yamamoto, and S. Höfling, Nature (London) **497**, 348 (2013).

[86] D. Ballarini, D. Caputo, C. S. Muñoz, M. De Giorgi, L. Dominici, M. H. Szymaǹska, K. West, L. N. Pfeiffer, G. Gigli, F. P. Laussy, and D. Sanvitto, Phys. Rev. Lett. **118**, 215301 (2017).

[87] Naoto Nagaosa, Jairo Sinova, Shigeki Onoda, A. H. MacDonald, and N. P. Ong Rev. Mod. Phys. **82**, 1539 (2010)

[88] Monique Combescot, Roland Combescot, Mathieu Alloing and François Dubin, EPL, **105** 4 (2014) 47011

[89] Yotam Mazuz-Harpaz, Kobi Cohen, Michael Leveson, Ken West, Loren Pfeiffer, Maxim Khodas, Ronen Rapaport, Proceedings of the National Academy of Sciences Sep 2019, 116 (37) 18328-18333

[90] C.-K. Chiu, J. C. Y. Teo, A. P. Schnyder, and S. Ryu, Classification of topological quantum matter with symmetries, Rev. Mod. Phys. **88**, 035005 (2016).

[91] M. Z. Hasan and C. L. Kane, Topological insulators, Rev. Mod. Phys. **82**, 3045 (2010).

[92] X.-L. Qi and S.-C. Zhang, Topological insulators and superconductors, Rev. Mod. Phys. **83**, 1057 (2011).

[93] A. M. Chang, Chiral Luttinger liquids at the fractional quantum Hall edge, Rev. Mod. Phys. **75**, 1449 (2003).

[94] F. Haldane, and S. Raghu, Possible Realization of Directional Optical Waveguides in Photonic Crystals with Broken Time-Reversal Symmetry, Phys. Rev. Lett. **100**, 013904 (2008).

[95] A. B. Khanikaev, S. H. Mousavi, W.-K. Tse, M. Kargarian, A. H. MacDonald, and G. Shvets, Photonic topological insulators, Nat. Mater. **12**, 233-239 (2013).

[96] A. V. Nalitov, D. D. Solnyshkov, and G. Malpuech, Polariton Z Topological Insulator, Phys. Rev. Lett. **114**, 116401 (2015).

[97] T. Karzig, C.-E. Bardyn, N. H. Lindner and G. Refael, Topological Polaritons, Phys. Rev. X **5**, 031001 (2015).

[98] C.-E. Bardyn, T. Karzig, G. Refael and T. C. H. Liew, Topological polaritons and excitons in garden-variety systems, Phys. Rev. B **91**, 161413 (2015).

[99] D. R. Gulevich, D. Yudin, I. V. Iorsh, and I. A. Shelykh, Kagome lattice from an exciton-polariton perspective, Phys. Rev. B **94**, 115437 (2016).

[100] O. V. Kibis, Dissipationless Electron Transport in Photon-Dressed Nanostructures, Phys. Rev. Lett. **107**, 106802 (2011).

[101] H. Sigurdsson, O. V. Kibis, and I. A. Shelykh, Optically induced Aharonov-Bohm effect in mesoscopic rings, Phys. Rev. B **90**, 235413 (2014).

[102] O. V. Kibis, H. Sigurdsson and I. A. Shelykh, Aharonov-Bohm effect for excitons in a semiconductor quantum ring dressed by circularly polarized light, Phys. Rev. B **91**, 235308 (2015).

[103] M. Hasan, I. V. Iorsh, O. V. Kibis, and I. A. Shelykh, Optically controlled periodical chain of quantum rings, Phys. Rev. B **93**, 125401 (2016).

[104] Fomin V. M., Physics of Quantum Rings (Springer, Berlin, 2014).

[105] S. Morina, O. V. Kibis, A. A. Pervishko, and I. A. Shelykh, Transport properties of a two-dimensional electron gas dressed by light, Phys. Rev. B **91**, 155312 (2015).

[106] O. V. Kibis, S. Morina, K. Dini, and I. A. Shelykh, Magnetoelectronic properties of graphene dressed by a high-frequency field, Phys. Rev. B **93**, 115420 (2016).

[107] Y. V. Pershin and C. Piermarocchi, Laser-controlled local magnetic field with semiconductor quantum rings, Phys. Rev. B **72**, 245331 (2005).

[108] E. Räsänen, A. Castro, J. Werschnik, A. Rubio, and E. K. U. Gross, Optimal Control of Quantum Rings by Terahertz Laser Pulses, Phys. Rev. Lett. **98**, 157404 (2007).

[109] A. Matos-Abiague and J. Berakdar, Photoinduced Charge Currents in Mesoscopic Rings, Phys. Rev. Lett. **94**, 166801 (2005).

[110] K. L. Koshelev, V. Yu. Kachorovskii, M. Titov, and M. S. Shur, Plasmonic shock waves and solitons in a nanoring, Phys. Rev. B **95**, 035418 (2017).

[111] M. Buttiker, Y. Imry, and M. Y. Azbel, Quantum oscillations in one-dimensional normal-metal rings, Phys. Rev. A **30**, 1982 (1984).

[112] I. A. Shelykh, N. T. Bagraev, N. G. Galkin, and L. E. Klyachkin, Interplay of h/e and h/2e oscillations in gate-controlled Aharonov-Bohm rings, Phys. Rev. B **71**, 113311 (2005).

[113] A. Lorke, J. R. Luyken, A. O. Govorov, J. P. Kotthaus, J. M. Garcia, P. M. Petroff, Spectroscopy of Nanoscopic Semiconductor Rings, Phys. Rev. Lett. **84**, 2223 (2000).

[114] F. Nagasawa, D. Frustaglia, H. Saarikoski, K. Richter and J. Nitta, Control of the spin geometric phase in a semiconductor quantum ring, Nat. Commun. **4**, 2526 (2013).

[115] O. V. Kibis, How to suppress the backscattering of conduction electrons?, Europhys. Lett. **107**, 57003 (2014).

[116] D. D. Awschalom, D. Loss, N. Samarth, *Semiconductor Spintronics and Quantum Computation* (Springer-Verlag, Berlin, 2002).

[117] I. Zutic, J. Fabian and S. D. Sarma, Spintronics: Fundamentals and applications, Rev. Mod. Phys. **76**, 323 (2004).

[118] D. D. Awschalom and M. E. Flatté, Challenges for semiconductor spintronics, Nat. Phys. **3**, 153 (2007).

[119] M. Cahay, Spin transistors: Closer to an all-electric device, Nat. Nanotechnol. **10**, 21 (2015).

[120] S. Morina, O. V. Kibis, A. A. Pervishko, and I. A. Shelykh, Transport properties of a two-dimensional electron gas dressed by light, Phys. Rev. B **91**, 155312 (2015).

[121] A. Amo, J. Lefŕe, S. Pigeon, C. Adrados, C. Ciuti, I. Carusotto, R. Houdré, E. Giacobino, and A. Bramati, Nature Phys. **5**, 805 (2009).

[122] A. Amo, S. Pigeon, D. Sanvitto, V. G. Sala, R. Hivet, I. Carusotto, F. Pisanello, G. Leménager, R. Houdré, E. Giacobino, C. Ciuti, and A. Bramati, Science **332**, 1167 (2011).

[123] H. Terças, H. Flayac, D. D. Solnyshkov, and G. Malpuech, Phys. Rev. Lett. **112**, 066402 (2014).

[124] I. Carusotto and C. Ciuti, Rev. Mod. Phys. 85, 299 (2013).

[125] M. Sich, D. N. Krizhanovskii, M. S. Skolnick, A. V. Gorbach, R. Hartley, D. V. Skryabin, E. A. Cerda-Méndez, K. Biermann, R. Hey, and P. V. Santos, Nature Photonics **6**, 50 (2012).

[126] R. Hivet, H. Flayac, D. D. Solnyshkov, D. Tanese, T. Boulier, D. Andreoli, E. Giacobino, J. Bloch, A. Bramati, G. Malpuech, and A. Amo, Nature Phys. **8**, 724 (2012).

[127] J. K. Chana, M. Sich, F. Fras, A. V. Gorbach, D. V. Skryabin, E. Cancellieri, E. A. Cerda-Méndez, K. Biermann, R. Hey, P. V. Santos, M. S. Skolnick, and D. N. Krizhanovskii, Phys. Rev. Lett. **115**, 256401 (2015).

[128] A. Opala, M. Pieczarka, N. Bobrovska, and M. Matuszewski, Phys. Rev. B **97**, 155304 (2018).

[129] K. G. Lagoudakis, M. Wouters, M. Richard, A. Baas, I. Carusotto, R. Andre, L. S. Dang, and B. Deveaud-Pledran, Nature Phys. **4**, 706 (2008).

[130] G. Tosi, G. Christmann, N. G. Berloff, P. Tsotsis, T. Gao, Z. Hatzopoulos, P. G. Savvidis, and J. J. Baumberg, Nat. Commun. **3**, 1243 (2012).

[131] T. Boulier, H. Tercas, D. D. Solnyshkov, Q. Glorieux, E. Giacobino, G. Malpuech, and A. Bramati, Sci. Rep. **5**, 9230 (2015).

[132] M.-S. Kwon, B. Y. Oh, S.-H. Gong, J.-H. Kim, H. K. Kang, S. Kang, J. D. Song, H. Choi, and Y.-H. Cho, Phys. Rev. Lett. **122**, 045302 (2019).

[133] D. Caputo, N. Bobrovska, D. Ballarini, M. Matuszewski, M. De Giorgi, L. Dominici, K. West, L. N. Pfeiffer, G. Gigli, and D. Sanvitto, Nature Photon. **13**, 488 (2019).

[134] N. A. Gippius, I. A. Shelykh, D. D. Solnyshkov, S. S. Gavrilov, Y. G. Rubo, A. V. Kavokin, S. G. Tikhodeev, and G. Malpuech, Phys. Rev. Lett. **98**, 236401 (2007).

[135] R. Cerna, Y. Léger, T. K. Paraïso, M. Wouters, F. Morier-Genoud, M. T. Portella-Oberli, and B. Deveaud, Nature Commun. **4**, 2008 (2013).

[136] S. S. Gavrilov, A. V. Sekretenko, S. I. Novikov, C. Schneider, S. Höfling, M. Kamp, A. Forchel, and V. D. Kulakovskii, Appl. Phys. Lett. **102**, 011104 (2013).

[137] O. Kyriienko, E. A. Ostrovskaya, O. A. Egorov, I. A. Shelykh, and T. C. H. Liew, Phys. Rev. B **90**, 125407 (2014).

[138] M. Klaas, H. Sigurdsson, T. C. H. Liew, S. Klembt, M. Amthor, F. Hartmann, L. Worschech, C. Schneider, and S. Höfling, Phys. Rev. B **96**, 041301(R) (2017).

[139] E. Z. Tan, H. Sigurdsson, and T. C. H. Liew, Phys. Rev. B **97**, 075305 (2018).

[140] A. Askitopoulos, H. Ohadi, A. V. Kavokin, Z. Hatzopoulos, P. G. Savvidis, and P. G. Lagoudakis, Phys. Rev. B **88**, 041308(R) (2013).

[141] H. Ohadi, A. J. Ramsay, H. Sigurdsson, Y. delValle-InclanRedondo, S. I. Tsintzos, Z. Hatzopoulos, T. C. H. Liew, I. A. Shelykh, Y. G. Rubo, P. G. Savvidis, and J. J. Baumberg, Phys. Rev. Lett. **119**, 067401 (2017).

[142] H. Sigurdsson, A. J. Ramsay, H. Ohadi, Y. G. Rubo, T. C. H. Liew, J. J. Baumberg, and I. A. Shelykh, Phys. Rev. B **96**, 155403 (2017).

[143] T. Gao, O. A. Egorov, E. Estrecho, K. Winkler, M. Kamp, C. Schneider, S. Höfling, A. G. Truscott, and E. A. Ostrovskaya, Phys. Rev. Lett. **121**, 225302 (2018).

[144] H. Sigurdsson, O. Kyriienko, K. Dini, and T. C. H. Liew, ACS Photonics **6**, 123 (2018).

[145] P. Mietki and M. Matuszewski, Phys. Rev. B **98**, 195303 (2018).

[146] O. Kyriienko, H. Sigurdsson, and T. C. H. Liew, Phys. Rev. B **99**, 195301 (2019).

[147] For a review on early results see: T. C. H. Liew, I. A. Shelykh, and G. Malpuech, Physica E **43**, 1543 (2011).

[148] A. Amo, T. C. H. Liew, C. Adrados, R. Houdré, E. Giacobino, A. V. Kavokin, and A. Bramati, Nature Photon. **4**, 361 (2010).

[149] T. C. H. Liew, A. V. Kavokin, T. Ostatnický, M. Kaliteevski, I. A. Shelykh, and R. A. Abram, Phys. Rev. B **82**, 033302 (2010).

[150] H. Ohadi, A. Dreismann, Y. G. Rubo, F. Pinsker, Y. delValle-InclanRedondo, S. I. Tsintzos, Z. Hatzopoulos, P. G. Savvidis, and J. J. Baumberg, Phys. Rev. X **5**, 031002 (2015).

[151] A. Dreismann, H. Ohadi, Y. del Valle-Inclan Redondo, R. Balili, Y. G. Rubo, S. I. Tsintzos, G. Deligeorgis, Z. Hatzopoulos, P. G. Savvidis, and J. J. Baumberg, Nature Mater. **15**, 1074 (2016).

[152] A. Askitopoulos, A. V. Nalitov, E. S. Sedov, L. Pickup, E. D. Cherotchenko, Z. Hatzopoulos, P. G. Savvidis, A. V. Kavokin, and P. G. Lagoudakis, Phys. Rev. B **97**, 235303 (2018).

[153] A. Opala, S. Ghosh, T. C. H. Liew, and M. Matuszewski, Phys. Rev. Applied **11**, 064029 (2019).

[154] C. Ciuti, V. Savona, C. Piermarocchi, A. Quattropani, and P. Schwendimann, Phys. Rev. B **58**, 7926 (1998).

[155] F. Tassone, and Y. Yamamoto, Phys. Rev. B **59**, 10830 (1999).

[156] M. M. Glazov, H. Ouerdane, L. Pilozzi, G. Malpuech, A. V. Kavokin, and A. D'Andrea, Phys. Rev. B **80**, 155306 (2009).

[157] M. Vladimirova, S. Cronenberger, D. Scalbert, K. V. Kavokin, A. Miard, A. Lemaître, J. Bloch, D. Solnyshkov, G. Malpuech, and A. V. Kavokin, Phys. Rev. B **82**, 075301 (2010).

[158] A. S. Brichkin, S. I. Novikov, A. V. Larionov, V. D. Kulakovskii, M. M. Glazov, C. Schneider, S. Höfling, M. Kamp, and A. Forchel, Phys. Rev. B **84**, 195301 (2011).

[159] E. Estrecho, T. Gao, N. Bobrovska, D. Comber-Todd, M. D. Fraser, M. Steger, K. West, L. N. Pfeiffer, J. Levinsen, M. M. Parish, T. C. H. Liew, M. Matuszewski, D. W. Snoke, A. G. Truscott, and E. A. Ostrovskaya, Phys. Rev. B **100**, 035306 (2019).

[160] J. Levinsen, G. Li, and M. M. Parish, Phys. Rev. Research **1**, 033120 (2019).

[161] G. Munoz-Matutano, A. Wood, M. Johnsson, X. Vidal, B. Q. Baragiola, A. Reinhard, A. Lemaitre, J. Bloch, A. Amo, G. Nogues, B. Besga, M. Richard, and T. Volz, Nature Mater. **18**, 213 (2019).

[162] A. Delteil, T. Fink, A. Schade, S. Hofling, C. Schneider, and A. Imamoglu, Nature Mater. **18**, 219 (2019).

[163] H. Deng, H. Haug, and Y. Yamamoto, Rev. Mod. Phys. **82**, 1489 (2010).

[164] C. Schneider, M. M. Glazov, T. Korn, S. Höfling, and B. Urbaszek, Nat. Commun. **9**, 2695 (2018).

[165] P. A. D. Gonçalves, N. Stenger, J. D. Cox, N. A. Mortensen, and S. Xiao, Adv. Optical Mater. **8**, 1901473 (2020).

[166] K. F. Mak, C. Lee, J. Hone, J. Shan, T. F. Heinz, Phys. Rev. Lett. **105**, 136805 (2010).

[167] A. Chernikov, T. C. Berkelbach, H. M. Hill, A. Rigosi, Y. Li, O. B. Aslan, D. R. Reichman, M. S. Hybertsen, and T. F. Heinz, Phys. Rev. Lett. **113**, 076802 (2014).

[168] J. A. Miwa, S. Ulstrup, S. G. Sørensen, M. Dendzik, A. G. Cabo, M. Bianchi, J. V. Lauritsen, and P. Hofmann, Phys. Rev. Lett. **114**, 046802 (2015).

[169] P. Steinleitner, P. Merkl, P. Nagler, J. Mornhinweg, C. Schüller, T. Korn, A. Chernikov, and R. Huber, Nano Lett. **17**, 1455 (2017).

[170] H. Rostami, R. Roldán, E. Cappelluti, R. Asgari, and F. Guinea, Phys. Rev. B **92**, 195402 (2015).

[171] S. Schwarz, S. Dufferwiel, P. M. Walker, F. Withers, A. A. P. Trichet, M. Sich, F. Li, E. A. Chekhovich, D. N. Borisenko, N. N. Kolesnikov, K. S. Novoselov, M. S. Skolnick, J. M. Smith, D. N. Krizhanovskii, A. I. Tartakovskii, Nano Lett. **14**, 7003 (2014).

[172] G. Wang, A. Chernikov, M. M. Glazov, T. F. Heinz, X. Marie, T. Amand, and B. Urbaszek, Rev. Mod. Phys. **90**, 021001 (2018).

[173] U. Wurstbauer, B. Miller, E. Parzinger, and A. W. Holleitner, J. Phys. D: Appl. Phys. **50**, 173001 (2017).

[174] X. Liu, T. Galfsky, Z. Sun, F. Xia, E. Lin, Y.-H. Lee, S. Kéna-Cohen, and V. M. Menon, Nat. Photon. **9**, 30 (2015).

[175] S. Dufferwiel, S. Schwarz, F. Withers, A. A. P. Trichet, F. Li, M. Sich, O. Del Pozo-Zamudio, C. Clark, A. Nalitov, D. D. Solnyshkov, G. Malpuech, K. S. Novoselov, J. M. Smith, M. S. Skolnick, D. N. Krizhanovskii and A. I. Tartakovskii, Nature Commun. **6**, 8579 (2015).

[176] S. Dufferwiel, T. P. Lyons, D. D. Solnyshkov, A. A. P. Trichet, F. Withers, S. Schwarz, G. Malpuech, J. M. Smith, K. S. Novoselov, M. S. Skolnick, D. N. Krizhanovskii, and A. I. Tartakovskii, Nature Photon. **11**, 497 (2017).

[177] M. Sidler, P. Back, O. Cotlet, A. Srivastava, T. Fink, M. Kroner, E. Demler and A. Imamoglu, Nature Physics **13**, 255 (2017).

[178] R. P. A. Emmanuele, M. Sich, O. Kyriienko, V. Shahnazaryan, F. Withers, A. Catanzaro, P. M. Walker, F. A. Benimetskiy, M. S. Skolnick, A. I. Tartakovskii, I. A. Shelykh, and D. N. Krizhanovskii, Nature Commun. **11**, 3589 (2020).

[179] N. Lundt, A. Marynski, E. Cherotchenko, A. Pant, X. Fan, S. Tongay, G. Sek, A. V. Kavokin, S. Höfling, and C. Schneider, 2D Materials **4**, 015006 (2017).

[180] L. Zhang, R. Gogna, W. Burg, E. Tutuc, and H. Deng, Nat. Commun. **9**, 713 (2018).

[181] V. Kravtsov, E. Khestanova, F. A. Benimetskiy, T. Ivanova, A. K. Samusev, I. S. Sinev, D. Pidgayko, A. M. Mozharov, I. S. Mukhin, M. S. Lozhkin, Y. V. Kapitonov, A. S. Brichkin, V. D. Kulakovskii, I. A. Shelykh, A. I. Tartakovskii, P. M. Walker, M. S. Skolnick, D. N. Krizhanovskii, and I. V. Iorsh, Light Sci. Appl. **9**, 56 (2020).

[182] M.-E. Kleemann, R. Chikkaraddy, E. M. Alexeev, D. Kos, C. Carnegie, W. Deacon, A. Casalis de Pury, C. Grosse, B. de Nijs, J. Mertens, A. I. Tartakovskii, and J. J. Baumberg, Nature Commun. **8**, 1296 (2017).

[183] P. A. D. Gonçalves, L. P. Bertelsen, S. Xiao, and N. A. Mortensen, Phys. Rev. B **97**, 041402(R) (2018).

[184] M. Geisler, X. Cui, J. Wang, T. Rindzevicius, L. Gammelgaard, B. S. Jessen, P. A. D. Gonçalves, F. Todisco, P. Bøggild, A. Boisen, M. Wubs, N. A. Mortensen, S. Xiao, and N. Stenger, ACS Photonics **6**, 994 (2019).

[185] T. J. Antosiewicz, S. P. Apell, and T. Shegai, ACS Photonics **1**, 454 (2014).

[186] M. Stüuhrenberg, B. Munkhbat, D. G. Baranov, J. Cuadra, A. B. Yankovich, T. J. Antosiewicz, E. Olsson, and T. Shegai, Nano Lett. **18**, 9, 5938 (2018).

[187] K. F. Mak, K. He, C. Lee, G. H. Lee, J. Hone, T. F. Heinz, and J. Shan, Nature Materials **12**, 207 (2013).

[188] J. S. Ross, S. Wu, H. Yu, N. J. Ghimire, A. M. Jones, G. Aivazian, J. Yan, D. G. Mandrus, D. Xiao, W. Yao, and X. Xu, Nature Commun. **4**, 1474 (2013).

[189] A. Singh, G. Moody, K. Tran, M. E. Scott, V. Overbeck, G. Berghäuser, J. Schaibley, E. J. Seifert, D. Pleskot, N. M. Gabor, J. Yan, D. G. Mandrus, M. Richter, E. Malic, X. Xu, and X. Li, Phys. Rev. B **93**, 041401(R) (2016).

[190] E. Courtade, M. Semina, M. Manca, M. M. Glazov, C. Robert, F. Cadiz, G. Wang, T. Taniguchi, K. Watanabe, M. Pierre, W. Escoffier, E. L. Ivchenko, P. Renucci, X. Marie, T. Amand, and B. Urbaszek, Phys. Rev. B **96**, 085302 (2017).

[191] N. Lundt, E. Cherotchenko, O. Iff, X. Fan, Y. Shen, P. Bigenwald, A. V. Kavokin, S. H́ofling, and C. Schneider, Appl. Phys. Lett. **112**, 031107 (2018).

[192] Y. You, X.-X. Zhang, T. C. Berkelbach, M. S. Hybertsen, D. R. Reichman, and T. F. Heinz, Nature Phys. **11**, 477 (2015).

[193] G. Wang, C. Robert, M. M. Glazov, F. Cadiz, E. Courtade, T. Amand, D. Lagarde, T. Taniguchi, K. Watanabe, B. Urbaszek, and X. Marie, Phys. Rev. Lett. **119**, 047401 (2017).

[194] M. Manca, M. M. Glazov, C. Robert, F. Cadiz, T. Taniguchi, K. Watanabe, E. Courtade, T. Amand, P. Renucci, X. Marie, G. Wang, and B. Urbaszek, Nature Commun. **8**, 14927 (2017).

[195] N. Lundt, L. Dusanowski, E. Sedov, P. Stepanov, M. M. Glazov, S. Klembt, M. Klaas, J. Beierlein, Y. Qin, S. Tongay, M. Richard, A. V. Kavokin, S. Höfling, and C. Schneider, Nature Nanotech. **14**, 770 (2019).

[196] M. Kulig, J. Zipfel, P. Nagler, S. Blanter, C. Schüller, T. Korn, N. Paradiso, M. M. Glazov, and A. Chernikov, Phys. Rev. Lett. **120**, 207401 (2018).

[197] J. Zipfel, M. Kulig, R. Perea-Causin, S. Brem, J. D. Ziegler, R. Rosati, T. Taniguchi, K. Watanabe, M. M. Glazov, E. Malic, and A. Chernikov, Phys. Rev. B **101**, 115430 (2020).

[198] F. Hüser, T. Olsen, and K. S. Thygesen, Phys. Rev. B **88**, 245309 (2013).

[199] S. Latini, T. Olsen, and K. S. Thygesen, Phys. Rev. B **92**, 245123 (2015).

[200] V. Shahnazaryan, O. Kyriienko, and H. Rostami, Phys. Rev. B **100**, 165303 (2019).

[201] A. Chernikov, C. Ruppert, H. M. Hill, A. F. Rigosi, and T. F. Heinz, Nature Photonics **9**, 466 (2015).

[202] A. Chernikov, A. M. van der Zande, H. M. Hill, A. F. Rigosi, A. Velauthapillai, J. Hone, and T. F. Heinz, Phys. Rev. Lett. **115**, 126802 (2015).

[203] F. Withers, O. Del Pozo-Zamudio, A. Mishchenko, A. P. Rooney, A. Gholinia, K. Watanabe, T. Taniguchi, S. J. Haigh, A. K. Geim, A. I. Tartakovskii, and K. S. Novoselov, Nature Mater. **14**, 301 (2015).

[204] A. Raja, A. Chaves, J. Yu, G. Arefe, H. M. Hill, A. F. Rigosi, T. C. Berkelbach, P. Nagler, C. Schüller, T. Korn, C. Nuckolls, J. Hone, L. E. Brus, T. F. Heinz, D. R. Reichman, and A. Chernikov, Nature Commun. **8**, 15251 (2017).

[205] S. Kumar, M. Brotons-Gisbert, R. Al-Khuzheyri, A. Branny, G. Ballesteros-Garcia, J. F. Sanchez-Royo, and B. D. Gerardot, Optica **3**, 882 (2016).

[206] A. Branny, S. Kumar, R. Proux, and B. D. Gerardot, Nature Commun. **8**, 15053 (2017).

[207] C. Palacios-Berraquero, D. M. Kara, A. R.-P. Montblanch, M. Barbone, P. Latawiec, D. Yoon, A. K. Ott, M. Loncar, A. C. Ferrari, and M. Atatüre, Nature Commun. **8**, 15093 (2017).

[208] L. C. Flatten, L. Weng, A. Branny, S. Johnson, P. R. Dolan, A. A. P. Trichet, B. D. Gerardot, and J. M. Smith, Appl. Phys. Lett. **112**, 191105 (2018).

[209] V. Shahnazaryan, I. Iorsh, I. A. Shelykh, and O. Kyriienko, Phys. Rev. B **96**, 115409 (2017).

[210] F. Barachati, A. Fieramosca, S. Hafezian, J. Gu, B. Chakraborty, D. Ballarini, L. Martinu, V. Menon, D. Sanvitto, S. Kéna-Cohen, Nature Nanotechnology **13**, 906 (2018).

[211] M. Combescot, O. Betbeder-Matibet, and F. Dubin, Physics Reports **463**, 215 (2008).

[212] M. Combescot, O.Betbeder-Matibet, and F. Dubin, Eur. Phys. J. B **52**, 181 (2006).

[213] K. S. Daskalakis, S. A. Maier, R. Murray, and S. Kéna-Cohen, Nature Mater. **13**, 271 (2014).

[214] T. Yagafarov, D. Sannikov, A. Zasedatelev, K. Georgiou, A. Baranikov, O. Kyriienko, I. Shelykh, L. Gai, Z. Shen, D. G. Lidzey, and P. G. Lagoudakis, Communications Physics **3**, 1 (2020).

[215] S. Betzold, M. Dusel, O. Kyriienko, C. P. Dietrich, S. Klembt, J. Ohmer, U. Fischer, I. A. Shelykh, C. Schneider, and S. Höfling, ACS Photonics **7**, 384 (2020).

[216] Y.-C. Chang, S.-Y. Shiau, and M. Combescot, Phys. Rev. B **98**, 235203 (2018).

[217] S.-Y. Shiau, M. Combescot, and Y.-C. Chang, Eur. Phys. Lett. **117**, 57001 (2017).

[218] D. K. Efimkin and A. H. MacDonald, Phys. Rev. B **95**, 035417 (2017).

[219] S. Ravets, P.Knüppel, S. Faelt, O. Cotlet, M. Kroner, W. Wegscheider, and A. Imamoglu, Phys. Rev. Lett. **120**, 057401 (2018).

[220] L. B. Tan, O. Cotlet, A. Bergschneider, R. Schmidt, P. Back, Y. Shimazaki, M. Kroner, and A. Imamoglu, Phys. Rev. X **10**, 021011 (2020).

[221] O. Kyriienko, D. N. Krizhanovskii, and I. A. Shelykh, arXiv:1910.11294 (2019).

[222] F. Stern, Phys. Rev. Lett. **18**, 546 (1967).

[223] M. Glazov, and A. Chernikov, Phys. Status Solidi B **255**, 1800216 (2018).

[224] L. V. Keldysh, JETP Lett. **29**, 658 (1979).

[225] D. Y. Qiu, F. H. da Jornada, and S. G. Louie, Phys. Rev. Lett. **111**, 216805 (2013); D. Y. Qiu, F. H. da Jornada, and S. G. Louie, Phys. Rev. Lett. **115**, 119901(E), 2015.

[226] A. V. Stier, N. P. Wilson, K. A. Velizhanin, J. Kono, X. Xu, and S. A. Crooker, Phys. Rev. Lett. **120**, 057405 (2018).

[227] S. Larentis, H. C. P. Movva, B. Fallahazad, K. Kim, A. Behroozi, T. Taniguchi, K. Watanabe, S. K. Banerjee, and E. Tutuc, Phys. Rev. B **97,** 201407(R) (2018).

[228] V. Shahnazaryan, I. A. Shelykh, and O. Kyriienko, Phys. Rev. B **93**, 245302 (2016).

[229] M. M. Ugeda, A. J. Bradley, S.-F. Shi, F. H. da Jornada, Y. Zhang, D. Y. Qiu, W. Ruan, S.-K. Mo, Z. Hussain, Z.-X. Shen, F. Wang, S. G. Louie and M. F. Crommie, Nature Materials **13**, 1091–1095 (2014).

[230] Y. Lin, X. Ling, L. Yu, S. Huang, A. L. Hsu, Y.-H. Lee, J. Kong, M. S. Dresselhaus, and T. Palacios, Nano Lett. **14**, 5569 (2014).

[231] D. W. Kidd, D. K. Zhang, and K. Varga, Phys. Rev. B **93**, 125423 (2016).

[232] G. Ramon, A. Mann, and E. Cohen, Phys. Rev. B **67**, 045323 (2003).

[233] K. v. Klitzing, G. Dorda, and M. Pepper, Phys. Rev. Lett. **45**, 494 (1980).

[234] R. B. Laughlin, Phys. Rev. B **23**, 5632 (1981).

[235] X.-G. Wen, Y.-S. Wu, and Y. Hatsugai, Nuclear Physics B **422**, 476 (1994).

[236] J. K. Jain, *Composite Fermions* (Cambridge University Press, 2007).

[237] X. G. Wen, Phys. Rev. Lett. **66**, 802 (1991).

[238] C. L. Kane and E. J. Mele, Phys. Rev. Lett. **95**, 226801 (2005).

[239] C. Beenakker, Annual Review of Condensed Matter Physics **4**, 113 (2013), https://doi.org/10.1146/annurev-conmatphys-030212-184337 .

[240] S. M. Huang, S. Y. Xu, I. Belopolski, C. C. Lee, G. Chang, B. Wang, N. Alidoust, G. Bian, M. Neupane, C. Zhang, S. Jia, A. Bansil, H. Lin, and M. Z. Hasan, Nature Communications **6**, 7373 (2015), arXiv:1501.00755 .

[241] H. Min, J. E. Hill, N. A. Sinitsyn, B. R. Sahu, L. Kleinman, and A. H. MacDonald, Phys. Rev. B **74**, 165310 (2006).

[242] M. König, S. Wiedmann, C. Brüne, A. Roth, H. Buhmann, L. W. Molenkamp, X.-L. Qi, and S.-C. Zhang, Science (2007), 10.1126/science.1148047, http://science.sciencemag.org/content/early/2007/09/20/science.1148047.full.pdf .

[243] J. Kasprzak, M. Richard, S. Kundermann, A. Baas, P. Jeambrun, J. M. J. Keeling, F. M. Marchetti, M. H. Szymanska, R. André, J. L. Staehli, V. Savona, P. B. Littlewood, B. Deveaud, and L. S. Dang, Nature **443**, 409 EP (2006), article.

[244] C. Schneider, A. Rahimi-Iman, N. Y. Kim, J. Fischer, I. G. Savenko, M. Amthor, M. Lermer, A. Wolf, L. Worschech, V. D. Kulakovskii, I. A. Shelykh, M. Kamp, S. Reitzenstein, A. Forchel, Y. Yamamoto, and S. Höfling, Nature **497**, 348 EP (2013).

[245] A. Kavokin, G. Malpuech, and F. P. Laussy, Physics Letters A **306**, 187 (2003).

[246] A. V. Nalitov, D. D. Solnyshkov, and G. Malpuech, Phys. Rev. Lett. **114**, 116401 (2015).

[247] D. Zezyulin, D. Gulevich, D. Skryabin, and I. A. Shelykh, Phys. Rev. B **97**, 161302(R) (2018) (2018).

[248] I. A. Shelykh, G. Pavlovic, D. D. Solnyshkov, and G. Malpuech, Phys. Rev. Lett. **102**, 046407 (2009).

[249] Y. Aharonov and D. Bohm, Phys. Rev. **115**, 485 (1959).

[250] O. V. Kibis, H. Sigurdsson, and I. A. Shelykh, Phys. Rev. B **91**, 235308 (2015).

[251] M. Z. Hasan and C. L. Kane, Rev. Mod. Phys. **82**, 3045 (2010).

[252] E. Tang and L. Fu, Nature Physics **10**, 964 EP (2014), article.

[253] F. E. Meijer, A. F. Morpurgo, and T. M. Klapwijk, Phys. Rev. B **66**, 033107 (2002).

[254] M. Büttiker, Y. Imry, and M. Y. Azbel, Phys. Rev. A **30**, 1982 (1984).

[255] J. S. Griffith, Trans. Faraday Soc. **49**, 345 (1953).

[256] B. Bernevig and T. Hughes, *Topological Insulators and Topological Superconductors* (Princeton University Press, 2013).

[257] V. K. Kozin, I. V. Iorsh, O. V. Kibis, and I. A. Shelykh, Phys. Rev. B **97**, 035416 (2018).

[258] C. L. Kane and E. J. Mele, Phys. Rev. Lett. **95**, 146802 (2005).

[259] F. D. M. Haldane and S. Raghu, Phys. Rev. Lett. **100**, 013904 (2008).

[260] M. Hafezi, E. A. Demler, M. D. Lukin, and J. M. Taylor, Nature Physics **7**, 907 EP (2011), article.

[261] M. C. Rechtsman, J. M. Zeuner, Y. Plotnik, Y. Lumer, D. Podolsky, F. Dreisow, S. Nolte, M. Segev, and A. Szameit, Nature **496**, 196 EP (2013).

[262] A. B. Khanikaev, S. Hossein Mousavi, W.-K. Tse, M. Kargarian, A. H. MacDonald, and G. Shvets, Nature Materials **12**, 233 EP (2012), article.

[263] A. V. Nalitov, D. D. Solnyshkov, and G. Malpuech, Phys. Rev. Lett. **114**, 116401 (2015).

[264] T. Karzig, C.-E. Bardyn, N. H. Lindner, and G. Refael, Phys. Rev. X **5**, 031001 (2015).

[265] C.-E. Bardyn, T. Karzig, G. Refael, and T. C. H. Liew, Phys. Rev. B **91**, 161413 (2015).

[266] O. Bleu, D. D. Solnyshkov, and G. Malpuech, Phys. Rev. B **93**, 085438 (2016).

[267] Y. V. Kartashov and D. V. Skryabin, Phys. Rev. Lett. **119**, 253904 (2017).

[268] P. St-Jean, V. Goblot, E. Galopin, A. Lemaître, T. Ozawa, L. Le Gratiet, I. Sagnes, J. Bloch, and A. Amo, Nature Photonics **11**, 651 (2017).

[269] D. C. Tsui, H. L. Stormer, and A. C. Gossard, Phys. Rev. Lett. **48**, 1559 (1982).

[270] D. J. Thouless, M. Kohmoto, M. P. Nightingale, and M. den Nijs, Phys. Rev. Lett. **49**, 405 (1982)
.

[271] R Balili, V Hartwell, D Snoke, L Pfeiffer, and K West, "Bose-einstein condensation of microcavity polaritons in a trap," Science **316**, 1007–1010 (2007).

[272] Yongbao Sun, Patrick Wen, Yoseob Yoon, Gangqiang Liu, Mark Steger, Loren N. Pfeiffer, Ken West, David W. Snoke, and Keith A. Nelson, "Bose-einstein condensation of long-lifetime polaritons in thermal equilibrium," Phys. Rev. Lett. **118**, 016602 (2017).

[273] Davide Caputo, Dario Ballarini, Galbadrakh Dagvadorj, Carlos Sánchez Muñoz, Milena De Giorgi, Lorenzo Dominici, Kenneth West, Loren N Pfeiffer, Giuseppe Gigli, Fabrice P Laussy, Marzena H. Szymańska, and Daniele Sanvitto, "Topological order and thermal equilibrium in polariton condensates," Nature Materials **17**, 145 (2017).

[274] Mark Steger, Chitra Gautham, David W. Snoke, Loren Pfeiffer, and Ken West, "Slow reflection and two-photon generation of microcavity exciton–polaritons," Optica **2**, 1–5 (2015).

[275] Mark Steger, Gangqiang Liu, Bryan Nelsen, Chitra Gautham, David W Snoke, Ryan Balili, Loren Pfeiffer, and Ken West, "Long-range ballistic motion and coherent flow of long-lifetime polaritons," Physical Review B **88**, 235314 (2013).

[276] Alexey V. Kavokin, Jeremy J. Baumberg, Guillaume Malpuech, and Fabrice P. Laussy, *Contemporary Physics*, 2nd ed. (Oxford University Press, 2017).

[277] David Snoke, *Solid state physics: Essential concepts* (Cambridge University Press, 2020).

[278] Charles Leyder, Marco Romanelli, J Ph Karr, Elisabeth Giacobino, Tim CH Liew, Mikhail M Glazov, Alexey V Kavokin, Guillaume Malpuech, and Alberto Bramati, "Observation of the optical spin hall effect," Nature Physics **3**, 628–631 (2007).

[279] Elena Kammann, Timothy Chi Hin Liew, Hamid Ohadi, Pasquale Cilibrizzi, Panayiotis Tsotsis, Zacharias Hatzopoulos, Pavlos G Savvidis, Alexey V Kavokin, and Pavlos G Lagoudakis, "Nonlinear optical spin hall effect and long-range spin transport in polariton lasers," Physical Review Letters **109**, 036404 (2012).

[280] Gangqiang Liu, David W. Snoke, Andrew Daley, Loren N. Pfeiffer, and Ken West, "A new type of half-quantum circulation in a macroscopic polariton spinor ring condensate," Proceedings of the National Academy of Sciences **112**, 2676–2681 (2015).

[281] Mark Steger, Brian Fluegel, Kirstin Alberi, David W Snoke, Loren N Pfeiffer, Ken West, and Angelo Mascarenhas, "Ultra-low threshold polariton condensation," Opt. Lett. **42**, 1165–1168 (2017).

[282] D. M. Myers, J. K. Wuenschell, B. Ozden, J. Beaumariage, D. W. Snoke, L. Pfeiffer, and K. West, "Edge trapping of exciton-polariton condensates in etched pillars," Applied Physics Letters (2017).

[283] D. M. Myers, S. Mukherjee, J. Beaumariage, D. W. Snoke, M. Steger, L. N. Pfeiffer, and K. West, "Polariton-enhanced exciton transport," Phys. Rev. B **98**, 235302 (2018).

[284] S Mukherjee, DM Myers, RG Lena, B Ozden, J Beaumariage, Z Sun, M Steger, LN Pfeiffer, K West, AJ Daley, *et al.*, "Observation of nonequilibrium motion and equilibration in polariton rings," Physical Review B **100**, 245304 (2019).

[285] ES Sedov and AV Kavokin, "Artificial gravity effect on spin-polarized exciton-polaritons," Scientific Reports **7**, 1–10 (2017).

[286] F. Tassone, C. Piermarocchi, V. Savona, A. Quattropani, and P. Schwendimann, "Bottleneck effects in the relaxation and photoluminescence of microcavity polaritons," Phys. Rev. B **56**, 7554–7563 (1997).

[287] D. A. Zezyulin, D. R. Gulevich, D. V. Skryabin, and I. A. Shelykh, "Chiral solitons in spinor polariton rings," Phys. Rev. B **97**, 161302 (2018).

[288] VK Kozin, IA Shelykh, AV Nalitov, and IV Iorsh, "Topological metamaterials based on polariton rings," Physical Review B **98**, 125115 (2018).

[289] Chuanyi Zhang and Guojun Jin, "Rotation of exciton-polariton condensates with te-tm splitting in a microcavity ring," New Journal of Physics **19**, 093002 (2017).

[290] A. V. Yulin, V. K. Kozin, A. V. Nalitov, and I. A. Shelykh, "Resonant excitation of acoustic waves in one-dimensional exciton-polariton systems," Phys. Rev. A **100**, 043610 (2019).

[291] H. Flayac, I. A. Shelykh, D. D. Solnyshkov, and G. Malpuech, "Topological stability of the half-vortices in spinor exciton-polariton condensates," Phys. Rev. B **81**, 045318 (2010)
.

[292] D. Roy, C. M. Wilson, and O. Firstenberg, Rev. Mod. Phys. **89**, 021001 (2017).

[293] D. E. Chang, J. S. Douglas, A. González-Tudela, C.-L. Hung, and H. J. Kimble, Rev. Mod. Phys. **90**, 031002 (2018).

[294] A. F. van Loo, A. Fedorov, K. Lalumiere, B. C. Sanders, A. Blais, and A. Wallraff, Science **342**, 1494 (2013), URL `https://doi.org/10.1126/science.1244324`.

[295] M. Mirhosseini, E. Kim, X. Zhang, A. Sipahigil, P. B. Dieterle, A. J. Keller, A. Asenjo-Garcia, D. E. Chang, and O. Painter, Nature **569**, 692 (2019).

[296] N. V. Corzo, J. Raskop, A. Chandra, A. S. Sheremet, B. Gouraud, and J. Laurat, Nature **566**, 359 (2019).

[297] A. Foster, D. Hallett, I. Iorsh, S. Sheldon, M. Godsland, B. Royall, E. Clarke, I. Shelykh, A. Fox, M. Skolnick, et al., Physical review letters **122**, 173603 (2019).

[298] S. Barik, A. Karasahin, S. Mittal, E. Waks, and M. Hafezi, Phys. Rev. B **101**, 205303 (2020), URL `https://link.aps.org/doi/10.1103/PhysRevB.101.205303`.

[299] M. J. Mehrabad, A. P. Foster, R. Dost, A. M. Fox, M. S. Skolnick, and L. R. Wilson, arXiv preprint arXiv:1912.09943 (2019).

[300] A. F. Kockum, A. Miranowicz, S. D. Liberato, S. Savasta, and F. Nori, Nature Reviews Physics **1**, 19 (2019).

[301] P. Forn-Díaz, L. Lamata, E. Rico, J. Kono, and E. Solano, Rev. Mod. Phys. **91**, 025005 (2019), URL `https://link.aps.org/doi/10.1103/RevModPhys.91.025005`.

[302] T. H. Kyaw, S. Felicetti, G. Romero, E. Solano, and L.-C. Kwek, Scientific Reports **5**, 1 (2015).

[303] C. S. Colley, J. C. Hebden, D. T. Delpy, A. D. Cambrey, R. A. Brown, E. A. Zibik, W. H. Ng, L. R. Wilson, and J. W. Cockburn, Review of Scientific Instruments **78**, 123108 (2007).

[304] M. Ruggenthaler, N. Tancogne-Dejean, J. Flick, H. Appel, and A. Rubio, Nature Reviews Chemistry **2**, 1 (2018).

[305] S. Felicetti and A. Le Boité, Phys. Rev. Lett. **124**, 040404 (2020), URL `https://link.aps.org/doi/10.1103/PhysRevLett.124.040404`.

[306] D. E. Chang, J. I. Cirac, and H. J. Kimble, Physical review letters **110**, 113606 (2013).

[307] M. T. Manzoni, L. Mathey, and D. E. Chang, Nature communications **8**, 1 (2017).

[308] D. Braak, Phys. Rev. Lett. **107**, 100401 (2011).

[309] S. Bravyi, D. P. DiVincenzo, and D. Loss, Annals of Physics **326**, 2793 (2011), ISSN 0003-4916, URL `http://www.sciencedirect.com/science/article/pii/S0003491611001059`.

[310] A. P. Burgers, L. S. Peng, J. A. Muniz, A. C. McClung, M. J. Martin, and H. J. Kimble, Proceedings of the National Academy of Sciences **116**, 456 (2019).

[311] J. R. Anglin and W. Ketterle, Nature **416**, 211 (2002).

[312] M. Pletyukhov and V. Gritsev, New Journal of Physics **14**, 095028 (2012).

[313] D. Kornovan, M. Petrov, and I. Iorsh, Physical Review B **96**, 115162 (2017).

[314] C. Emary and T. Brandes, Physical Review A **69**, 053804 (2004).

[315] *Supplemental Material* (2020).

[316] R. Barnett, G. R. Boyd, and V. Galitski, Physical review letters **109**, 235308 (2012).

[317] W. Han, X.-F. Zhang, S.-W. Song, H. Saito, W. Zhang, W.-M. Liu, and S.-G. Zhang, Phys. Rev. A **94**, 033629 (2016), URL `https://link.aps.org/doi/10.1103/PhysRevA.94.033629`.

[318] S. Sachdev, Handbook of Magnetism and Advanced Magnetic Materials (2007).

[319] M.-J. Hwang, R. Puebla, and M. B. Plenio, Phys. Rev. Lett. **115**, 180404 (2015), URL `https://link.aps.org/doi/10.1103/PhysRevLett.115.180404`.

[320] B. Vlastakis, G. Kirchmair, Z. Leghtas, S. E. Nigg, L. Frunzio, S. M. Girvin, M. Mirrahimi, M. H. Devoret, and R. J. Schoelkopf, Science **342**, 607 (2013).

[321] P. Nataf and C. Ciuti, Phys. Rev. Lett. **107**, 190402 (2011), URL https://link.aps.org/doi/10.1103/PhysRevLett.107.190402.

[322] Y. Wang, J. Zhang, C. Wu, J. You, and G. Romero, Physical Review A **94**, 012328 (2016).

[323] L. Bakemeier, A. Alvermann, and H. Fehske, Phys. Rev. A **85**, 043821 (2012), URL https://link.aps.org/doi/10.1103/PhysRevA.85.043821.

[324] S. Ashhab, Phys. Rev. A **87**, 013826 (2013), URL https://link.aps.org/doi/10.1103/PhysRevA.87.013826.

[325] R. Puebla, M.-J. Hwang, J. Casanova, and M. B. Plenio, Physical Review Letters **118**, 073001 (2017).